Numerical and Experimental Investigations on the Stress Distribution of Bolted Glass Connections under In-Plane Loads

Iris Maniatis

Vollständiger Abdruck der von der Fakultät für Bauingenieur- und Vermessungswesen
der Technischen Universität München zur Erlangung des akademischen Grades eines

Doktor-Ingenieurs (Dr.-Ing.)

genehmigten Dissertation.

Abstract

To calculate the loadbearing of bolted connections in glass panels under the application of in-plane loads exact knowledge of the contact mechanisms and the parameters which influence the stress distribution around the hole is necessary. At first analytical and numerical solutions of contact between a bolt and a conforming hole in a panel are formulated to determine the stress distribution. An approach for verifying the numerical model with the analytical solutions is developed. To determine relevant results for design the verified FEM-model is used to examine the influences of different parameters on the stress distribution around the hole. In addition experimental investigations are carried out in order to check the results of the FEM-calculations and the analytical solutions.

Kurzfassung

Um Lastabtragungen in Scheibenebene über Punkthalter oder Bolzen aus Stahl in Glasbohrungen rechnerisch abbilden zu können, sind genaue Kenntnisse über die Kontaktmechanismen notwendig. Darüber hinaus sind die Parameter zu untersuchen, die Einfluss auf die Spannungsverteilung am Bohrloch haben. Daher werden zunächst analytische und numerische Methoden aufgezeigt, um den Kontakt zwischen Glas und Halterung abzubilden und die Spannungsverteilung zu ermitteln. Mit Hilfe der analytischen Lösungen wird eine Vorgehensweise zur Verifikation des Finite-Elemente-Modells entwickelt. Des Weiteren werden mit dem verifizierten FE-Modell die Einflüsse unterschiedlicher Parameter auf die Spannungsverteilung am Bohrloch untersucht, um letztendlich bemessungsrelevante Erkenntnisse zu gewinnen. Zusätzlich werden experimentelle Untersuchungen durchgeführt, um die numerischen und analytischen Ergebnisse zu überprüfen.

Acknowledgements

Contents

1 Introduction

1.1 Cause

For several years there has been a trend in architecture, to use glass not only as a part of the building envelope, but also to build the loadbearing elements of glass. This represents a special challenge because of the material behaviour of glass. In the most frequent cases glass columns or so-called glass fins (see Figure 1.1) are used and the loads are transferred via compound point-supports or bolts of steel to the glass drill hole. To avoid any contact between steel and glass a suitable interlayer or bushing material, such as plastic or aluminium, has to be applied.
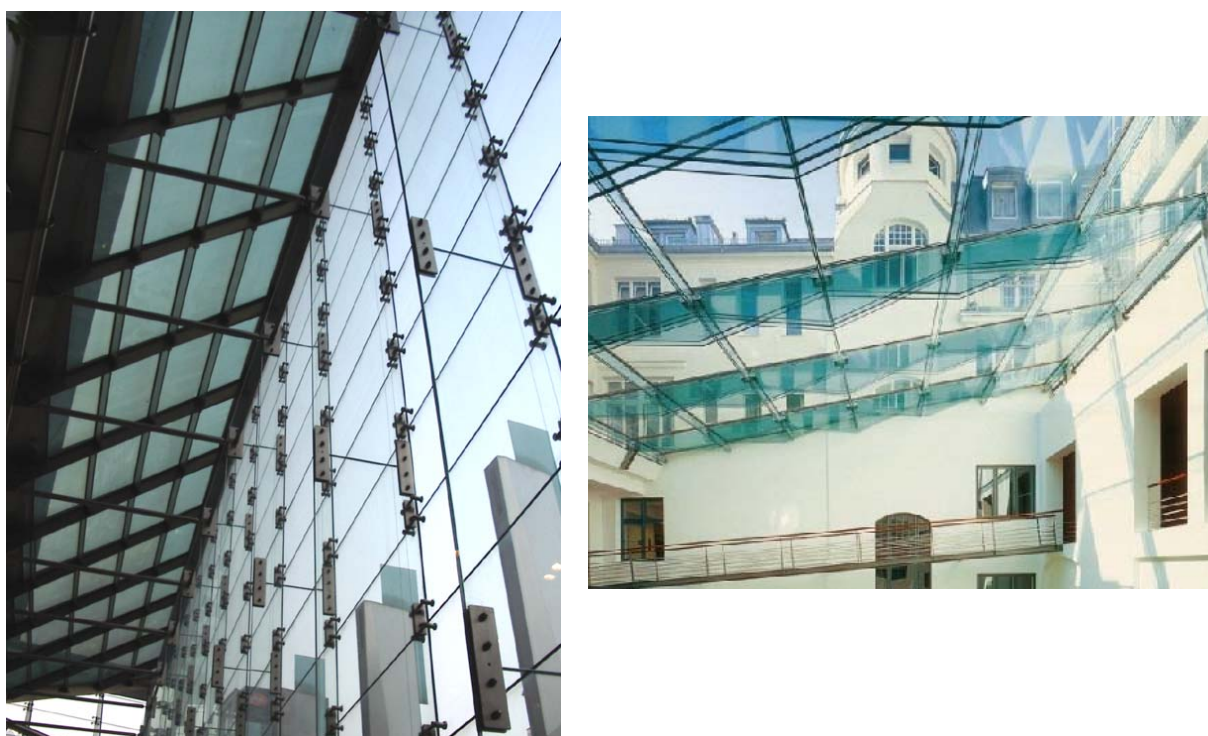
Figure 1.1   Examples of loadbearing glass structures

Special care is required with the design and the structural detailing of point-supported glazing. High local stresses can occur around the drill hole, if the loads are transferred via screws, bolts or point-supports to the glass holes. The design has to be done in a way which insures that forces are distributed uniformly, in order to keep stress concentrations at a minimum.

Using the material steel local stress-peaks can be reduced by local plastification due to the elasto-plastic material behaviour. Applying glass as a material this is impossible because of its brittle material behaviour.

The kind of the support, the geometry of the components, the quality of the glass edges and surfaces as well as the interlayer material influence the stress distribution around the drill hole. Due to the complexity of the calculation of point-supported glazing the design is usually carried out by means of finite element method (FEM). However, to get reasonable results, a very good understanding of the FEM-program is required. Dependant on complexity and parameter selection of the FEM-calculation the stresses and deformations in the glazing are registered more or less precise. Mostly extensive FEM-models with contact approaches are

necessary. In order to exclude unsuitable static models and to be able to evaluate a FEM-model in a qualified way, verifications of the corresponding programs are indispensable.

Up to now technical rules only exist for the design of line supported glass structures.

Scientific investigations that were carried out so far in the field of point-supported glazing are not yet sufficient in order to transform the design into a standard.

In particular, very few research which deals with the loadbearing of bolted glass connections under the application of in-plane loads exists up to now.

In case of so-called bolted connections the loads are transmitted only by contact perpendicular to the bolt axis to the panel plane. The compressive forces interact normal to the contact surface. To find the correct computational model precise knowledge about the contact mechanisms and the parameters that influence the stress distribution is necessary. This thesis should achieve a contribution on this.

1.2 Aims and Structure of the Thesis

From the problems outlined in chapter 1.1, the aims of the thesis can be derived as follows.

The primary aims of this work are to find the correct analytical and numerical model for the contact between glass and bolt as well as for the stress distribution around the hole. Furthermore the influences of different parameters on the stress distribution at the drill hole area should be examined. Finally, conclusions that are relevant to the design, should be gained.

To verify the correctness of the numerical approach, analytical solutions based on contact mechanics are formulated initially. Afterwards experimental examinations are carried out.

After verifying the FEM-model, it will be used to examine the influences of different parameters on the stress distribution around the hole. The following parameters are examined in particular:

- Different bushing materials
- Clearance between bolt and drill hole
- Boundary surface friction between bolt and drill hole
- Eccentric loading
- Variation of hole diameter and panel width
- Variation of distance between hole and panel edge

According to the aims of this thesis its content is divided in as follows:

In chapter 2 the most important glass properties are explained and the distribution of the surface compression of tempered glass panes as well as the strength in the drill hole and edge area is stated. This is followed by a short summary of the design concepts of structural glass.

Chapter 3 contains a detailed description of point supported-glazing including their components, as for example the bushing material.

Based on the theory of panels and the analytical solution for the panel with a hole (Chapter 4), the analytical solutions for the panel with an enclosed bolt are formulated in chapter 5 by means of contact mechanics.

Chapter 6 starts with a description of the numerical approach of the contact by means of finite elements and program-specific solution algorithms of the programs MSC.visualNastran for Windows and the extra module Nonlinear+, which is based on the program MSC.Marc. Thereafter chapter 7 deals with the creation of the FEM-model, which is being verified along the analytical solutions. After that a detailed examination of different parameters and their influence on the stress distribution at the drill hole follows.

In order to check the results of the FEM-calculation and the analytical solution, experimental investigations are carried out, which are described in chapter 8. Based on the numerical parameter study in chapter 7, a variety of parameters such as drill hole diameter, panel width, distance between hole and panel edge as well as thickness and bushing material are examined. The appendix contains the detailed results.

Chapter 9 completes the thesis with a conclusion and an outlook on continuing scientific investigations.

2   Glass Properties

2.1   Introduction

For the design of a material the strength is of central importance. Various investigations showed that the strength in a flat glass panel is not constant. A differentiation between glass surface, edge, corner and drill hole area is required. Local surface damages that occur due to processing of holes and edges can lead to a reduction of the strength. Considering point supported glazing, examination of the holes is especially important because, besides possible surface defects, additional stress concentrations in these areas can cause a failure. However, the qualitative capturing of these influencing parameters is quite difficult. Mostly, experimental investigations are carried out in order to receive reliable values for the design of point supported glass elements. The best way to describe the material glass is to utilize the probability of failure and basic principles of fracture mechanics. Taking into account the partial safety factors and influencing coefficients, these principles are used to develop a design concept.

Due to the existence of extensive literature in the field of glass-manufacturing and -processing this thesis is not covering these, but refers to [Lohmeyer 1987, 2001], [Scholze 1988], [Doremus 1994], [Sedlacek et al. 1999], [Siebert 1999], [Siebert 2001], [Woerner et al. 2001]. In the following section only the most important material properties will be named. A more detailed look will be taken on the pre-stress and stress distribution of thermal pre-stressed glass, since stress concentrations at the drill hole are of central interest for point supported glass panes.

2.2   Composition and Physical Properties of Glass

The basic module of all silicates is the SiO_4-tetrahedron that is based on a central silicon atom with 4 surrounding oxygen atoms. While these tetrahedron are regularly ordered in the mono crystalline form, they form an irregular net in the glass. Glass is an amorphous, homogeneous and isotropic material with linear elastic material behaviour which fails in case of overload with a brittle fracture.

Most of the commonly used glasses contain numerous components with SiO_2 as the main component. Mainly two types of basic glasses are used for building materials: soda lime silicate glass [DIN EN 572-1] and borosilicate glass [DIN EN 1748-1].

Soda lime silicate glass has by far the greater share and is used especially for float glass [DIN EN 572-2], [DIN 1249-3, -10, -11].

Borosilicate glass is used in special applications such as fire protection glass, because of its high chemical resistance as well as high resistance to alternating temperatures. Table 2.1 lists the chemical compositions of these two types of glass.

Table 2.1   Chemical composition of silicate glass

Components	Soda lime silicate glass [DIN EN 572-1]	Borosilicate glass [DIN EN 1748-1]
SiO_2	69 - 74%	70 - 87 %
CaO	5 - 12%	-
B_2O_3	-	7 - 15 %
Na_2O/K_2O	12 - 16%	0 - 16%
MgO	0 - 6%	-
Al_2O_3	0 - 3%	0 - 8%
others	-	0 - 8%

The chemical composition has an essential influence on the melting temperature and the thermal expansion coefficient α_t. Table 2.2 lists the most important physical properties of soda lime silicate glass and borosilicate glass.

Table 2.2   Physical properties

Property	Symbol [Unit]	Soda lime silicate glass [DIN EN 572-1]	Borosilicate glass [DIN EN 1748-1]
Density (at 18°C)	ρ [kg/m³]	2500	2200 - 2500
Hardness (Knoop)	[GPa]	6	4,5 - 6
Young's modulus	E [MPa]	70.000	60.000-70.000
Poisson's ratio	ν [-]	0,20*)	0,20
Specific heat capacity	c [J/(kg$\cdot$K)]	$0,72\cdot 10^3$	$0,8\cdot 10^3$
Average thermal expansion coefficient	α_t [1/K]	$9\cdot 10^{-6}$	$3,1 - 6,0\cdot 10^{-6}$
Thermal conductivity	λ [W/(m$\cdot$K)]	1,0	1,0
Average refraction index for visible wavelength	N [-]	1,5	1,5

*) according to DIN 1249-10 in Germany currently ν=0,23 is used for design

Terms for glass types and glass groups are listed in [DIN 1259-1], terms for glass products are listed in [DIN 1259-2].

2.3 Pre-Stressing of Glass

2.3.1 Introduction

The mechanical strength of glass and the resistance to alternating temperatures can be improved considerably by heating up the glass to a few degrees before reaching the softening point (approx. 650°C) and subsequent rapid cooling down (thermal pre-stressing). A bulged structure in the surface layer is frozen by this quenching, which leads to a compressive pre-stress in the surface layer and a tensile pre-stress in the core.

A compressive pre-stress in the glass can be achieved as well by ion exchange in a silicate glass that contains Li_2O or Na_2O (chemical pre-stress). The Li^+- or the Na^+-ions are replaced by larger K^+-ions below the transformation temperature and the network structure of the layer with ion-exchange is bulged. The compressive pre-stress that can be achieved by ion exchange in a surface layer of 30 to 300 µm thickness is about 300 to 500 MPa [Lohmeyer 2001]. However, compared to thermal toughened glass, chemical pre-stressed glass is more sensitive for surface damages because the compressive stress layer is much thinner across glass thickness.

The durable compressive pre-stress on the glass surface increases the resistance capacity, since locations for initial failure (micro and macro cracks, notches) become compressed. Crack-propagation can only occur if there is a tensile stress on the surface.

The pre-stressed glass products are divided as follows:

Thermally toughened glass

is regulated according to [DIN 1249-12] and [DIN EN 12150-1]. Compared to annealed glass thermally toughened glass has a considerably higher resistance against mechanical and thermal stress. In case of breakage numerous small and rounded pieces arise. The fragments are namely less sharp and smaller than those of annealed glass but not less dangerous if they are falling from a certain height.

Heat strengthened glass

is regulated according to [DIN EN 1863-1]. The properties of the heat strengthened glass are comparable with those of thermally toughened glass. However, the thermal pre-stress on the surface is smaller compared to thermally toughened glass because of the slower cooling rate. Heat strengthened glass breaks into larger fragments than thermally toughened glass. The fracture pattern is comparable with that from annealed glass.

Chemically strengthened glass

is regulated according to [DIN EN 12337-1]. Higher resistance against mechanical and thermal stress is achieved by ion exchange. Ions of smaller diameter are replaced against such of larger diameter and they expand the structure in the surface layer. On the surface a thin compressive layer is formed.

The fracture pattern corresponds to that of annealed glass.

In the following this thesis focuses on glasses with thermal pre-stress since these are most commonly used in building-relevant areas.

2.3.2 Thermally Pre-Stressed Glass

The thermal pre-stress can be either determined numerically by finite elements or experimentally, for example with photoelasticity. Various investigations have already been made in this field. Recently, [Hof 2005] made computational and experimental investigations with the aid of digital image correlation method, which is quite new for glass. Using this method a picture is taken with a CCD-camera (charge-coupled device) with the help of white light. This light creates an irregular pattern of the surface structure. The procedure consists of making one reference picture before and a second one after tempering or loading. These pictures are compared and the displacement is determined. The method is described in detail in [Hof 2005].

By comparison of photoelastically measured values e.g. [Bernard, Daudeville 2003], [Bernard, Daudeville 2004], [Schneider 2001], [Laufs 2000] and [Carré, Daudeville 1999] showed, that the process of pre-stressing glass can be represented numerically. Therefore the viscoelastic behaviour of glass as well as the other physical properties have to be modelled realistically. Especially the correct representation of the heat transfer between glass and the cooling medium is important. Dependent on the utilized pre-stress furnace the glass properties can vary.

2.3.3 Distribution of Pre-Stress in Glass Panels

[Guesgen 1998] and in particular [Laufs 2000] showed that the distribution of pre-stress in glass panels is not constant. The parabolic shape of the stress distribution due to thermal pre-stress can only be achieved in areas that had the quenching from both sides of the glass surface. Dependant on the possibilities of the heat dissipation during the quenching, the glass panel can be divided into 4 zones. These are the glass surface (zone 1), the edges (zone 2), the corners (zone 3) and the drill hole area (zone 4), (see Figure 2.1).
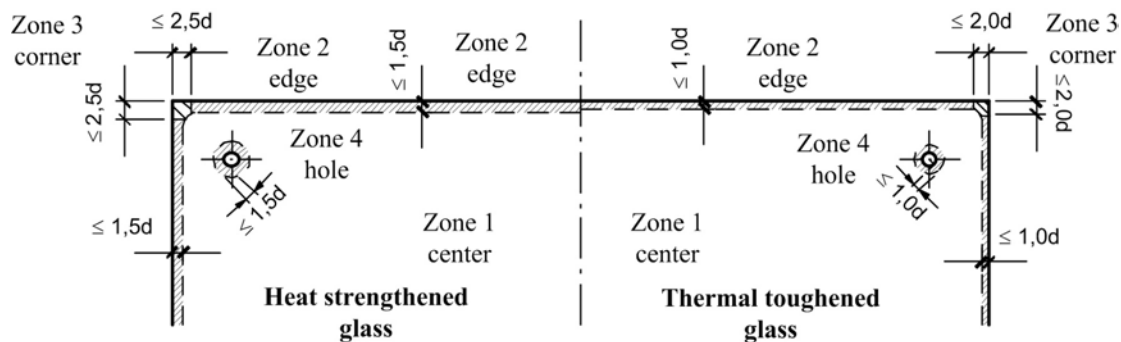
Figure 2.1   Partitioning of the glass panel into 4 zones for thermally toughened glass and
heat strengthened glass according to [Siebert 2001]

The pre-stress profiles of zone 2 and zone 4 do influence each other if the drill hole is too close to the edge. In the scope of the thesis of [Laufs 2000] minimum distances are indicated to avoid an interaction of the pre-stress profiles between drill hole and edge area. For heat strengthened glass the distance between drill hole and edge should be at least 3 times the glass thickness d. For thermally toughened glass the distance should be at least 2,0 d.

Qualitative curves of thermally introduced pre-stress for the zones 1 to 4 are shown in Figure 2.2. In the central area, stress distribution in normal direction (across thickness) has a parabolic shape. The ratio between surface stress to maximum tensile stress is about 1 : 2,0 to 2,2. Zero-crossing of the parabolic curve is at about 20% of glass thickness d. The edge area is represented by a three dimensional residual stress state. Due to the fact that the

surface cools down on three sides. The compressive stress σ_2 parallel to the edges is a membrane stress that compresses the entire edge surface.

The influence of the edge reaches to a depth of about 1 to $2d$. Since the corner area cools down on 4 sides, the pre-stress follows continuously along the surfaces. For equilibrium reasons there is no membrane stress at the free edge of the corner. The influence of the corner is about 2 to $3d$.
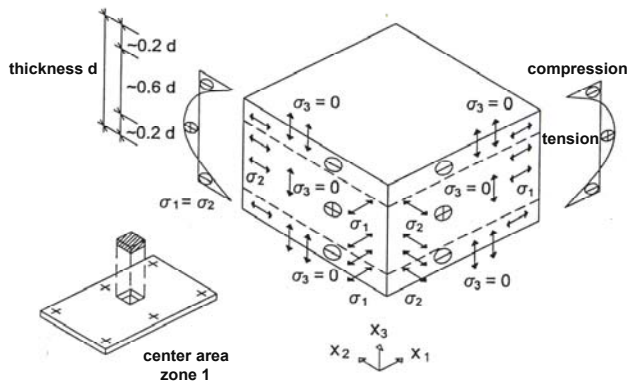
Zone 1, center   Zone 2, edge
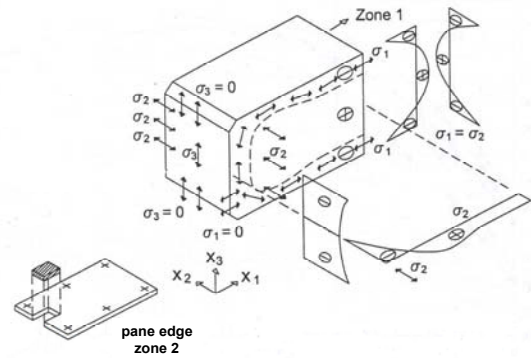
Zone 3, corner
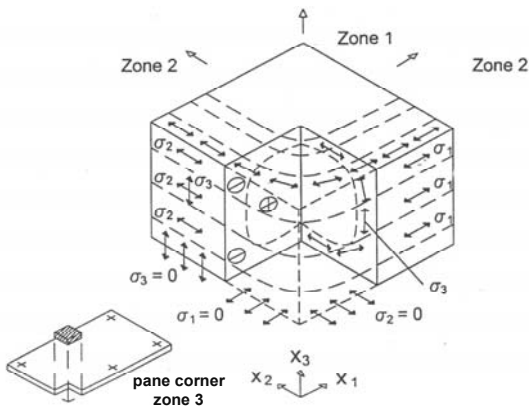
Zone 4, cylindric drill hole   Zone 4, conical drill hole
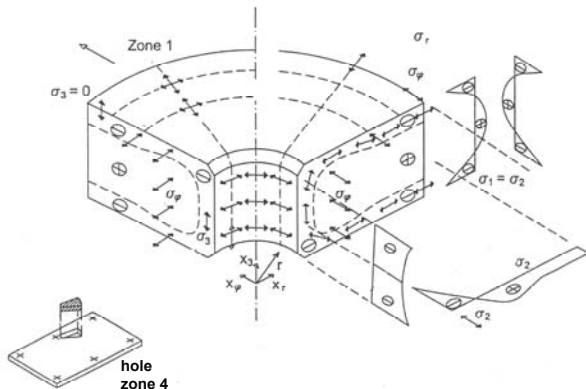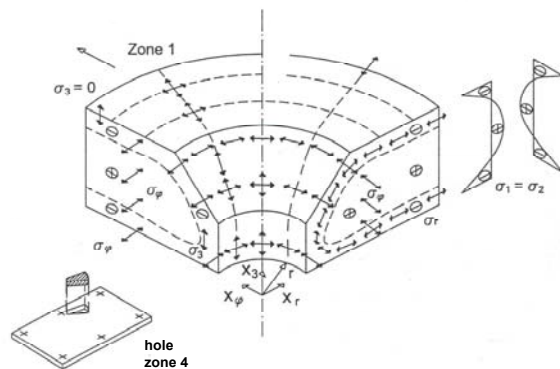
Figure 2.2   Qualitative curves of the thermally introduced pre-stress for zones 1 to 4 [Laufs 2000]

Heating temperature in the pre-stress furnace as well as cooling and orientation of the panel in the furnace have an influence on thermal pre-stress. In practice these influences can lead to a considerable variability. Investigations carried out by *Laufs* show as well that thicker glasses have a higher pre-stress than thinner ones by taking a uniformly heat transfer coefficient α_k.

In his thesis *Laufs* indicates characteristic values (95 % confidence level, 5 % fractile) of pre-stress for heat strengthened and thermally toughened glass in the respective zones (see Table 2.3). The listed values were determined with a sufficient margin of safety and are valid for all nominal glass thickness not depending on glass manufacturer and pre-stress furnace.

Table 2.3   Characteristic values of pre-stress in MPa in the four zones

Zone	Plate loadbearing		Panel loadbearing	
	Heat strengthened glass	Thermally toughened glass	Heat strengthened glass	Thermally toughened glass
1) surface	-30	-84	-30	-84
2) edge	-43	-75	-45	-63
3) corner	0	0	0	0
4) drill hole	-40	-68	-37	-57

Laufs results show that the pre-stress in the surface, the edge and the drill holes are in the same order of magnitude, while at the corners there is virtually no pre-stress at all. The slightly higher pre-stress at the edges and the drill holes of heat strengthened glass in comparison to the surface can be explained by the multi-dimensional cooling behaviour. Due to the edgewise cooling a high temperature gradient is build up, which, after pre-stressing results in a higher membrane compressive pre-stress at the edges [Sedlacek et al. 1999].

2.4 Glass Strength

2.4.1 Basics

Under mechanical stress glass behaves linear elastic in almost any composition and fails with a brittle fracture.

There is a difference between the theoretical and practical tensile strength. Due to molecular bonding forces the theoretical strength is in the range of 10.000 to 30.000 MPa [Siebert 1999]. However experimental measured strength values of glass are in several orders of magnitude below the theoretical ones. The practical tensile strength as well as the ultimate strength of glass is not a constant material value, but depends on the degree and size of damage of the surface that is under tension, on the type and duration of loading as well as on the environmental conditions.

The strength values of glass are determined by the four point bending test or the coaxial double ring test. The corresponding experiments are regulated in [DIN EN 1288-1 to -5]. Strictly speaking experimentally determined bending strength values can only be obtained on components which are free from residual stresses or pre-stresses. If the strength of pre-stressed glass is determined experimentally, the result is a "test bending strength" $\sigma_{test,Be}$. The bending strength σ_{Be} consists of the "test bending strength" $\sigma_{test,Be}$ and the residual stress σ_{Re} [Exner 2001 A]:

$$\sigma_{Be} = \sigma_{test,Be} + \sigma_{Re} \qquad\qquad (2.1)$$

The evaluation of the experiments is usually done with the Weibull distribution [DIN 55303-7]. For the most commonly used glass products Table 2.4 lists the characteristic minimum bending tensile strength (= test bending strength) at 95 % confidence level and 5% fractile including the current product standards.

Table 2.4   Characteristic values of bending tensile strength

Product	Standard	Bending tensile strength [MPa]
Float glass	DIN 1249-10 DIN EN 572-2	45 MPa
Thermally toughened glass	DIN 1249-12 DIN EN 12150-1	120 MPa
Heat strengthened glass	DIN EN 1863-1	70 MPa

Detailed investigations on bending tensile strength of glass can be taken from the corresponding literature such as [Wilikins et al. 1976], [Schmitt et al. 1983], [Exner 2001 a, b, c], [Siebert 1999] and [Siebert 2001]. Basic principles and experimental methods for the strength of glass are described in detail in [HVG 1987] for example.

Except for glass fins or columns, where the loadbearing is in-plane compressive, compressive strength does not play such an important role in constructive glass design, where, in most cases, elements are used that are stressed by bending. So far only compressive strength values for float glass are available in [DIN 1249-10], which are noted to 700 to 900 MPa.

To examine the fatigue resistance of float glass under continuous loading [Fink 2000] performed longtime experiments with glass stressed by bending and compressive load. He found out that under a continuous load the strength is significantly below the "minimum test strength".

2.4.2 Glass Strength at the Edge and in the Hole Area

The quality of the edges and the drill hole are of essential importance for the strength of glass. Potential weak points of the glass are at the drill holes and the edges due to possible surface damages or micro cracks that can occur during the machine-made manufacture. Additionally, regarding point supported glasses, the highest stress concentration occurs in the rim of the drill holes.

[Weißmann 2004] performed investigations of the strength and the quality of the edges. The strength is determined by the four point bending test. The glass stripes are installed upright on edges in the test rig to stress only the edges with tension. [Weißmann 2004] examined annealed float glass and thermally toughened glass of different thickness and different edge qualities. The essential results of his investigations are represented in Figure 2.3.

sample no.	glass type / edge treatment
1	float glass / cutting edge
2	thermally toughened glass / cutting edge
3	float glass / C-grinding
4	thermally toughened glass / C- grinding
5	float glass / double-sided vordered
6	thermally toughened glass / double-sided vordered
7	float glass / water jet, vordered
8	thermally toughened glass / water jet, vordered
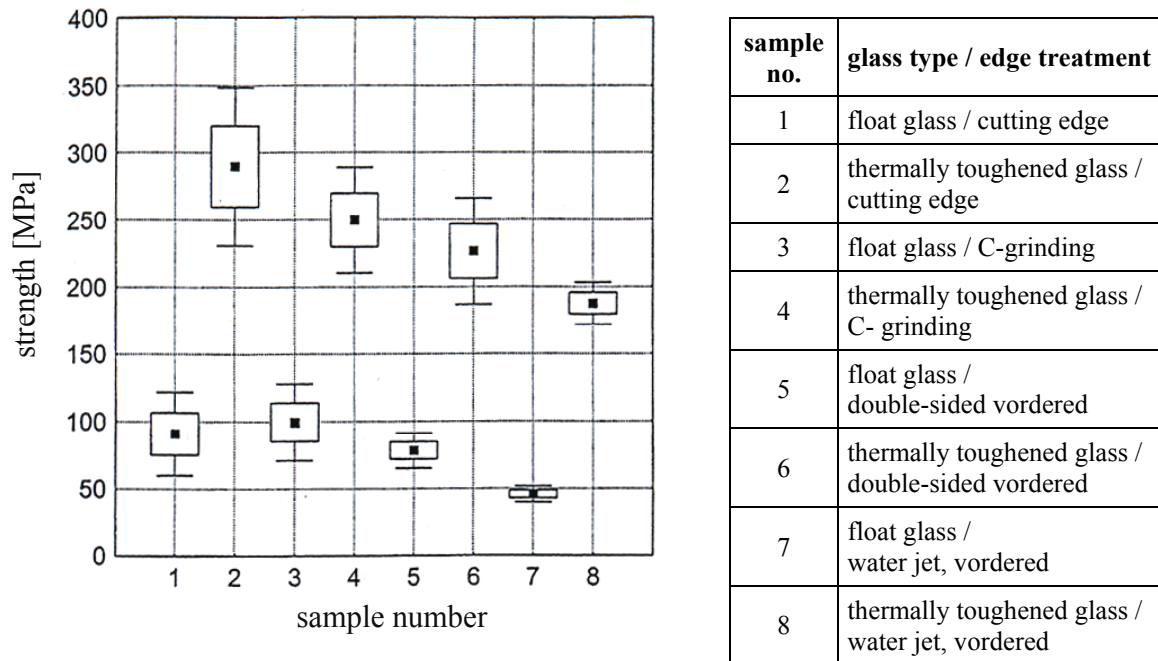
Figure 2.3   Strength of the edges [Weißmann 2004]

One of the most interesting results is that the edges cut by water jet show the least strength values. For float glass no significant differences in strength can be found between cutting edges (test no. 1) and grinded edges (test no. 3). For thermally toughened glass the cutting edges (test no. 2) show a higher strength than the vordered edges (test no. 4).

[Hess 2000] carried out strength investigations at glass-beams with different geometry and glass set-ups. Using the four point bending test he compared the strength of glass fins mounted upright and horizontally in the test-up. Among other things he observed that the strength values for upright mounted fins were lower than the values for horizontal mounted fins. The reason for this is that in contrast to horizontally mounted panes, the edges of upright mounted panes are under tension. Due to edge processing the probability of a surface damage initiating a crack is higher there.

[Kutterer, Goerzig 1997] carried out experimental strength investigations of drilled float glass and drilled thermally toughened glass panes, both under tension in-plane. Milled holes, conventionally drilled with a diamond equipped cylindrical drill and holes drilled by water jet were examined. In addition polished drill holes were examined. As a result, the surface damages of the water jet holes were slightly higher, so their failure load was slightly lower than the others. Nevertheless, considering the design, no relevant losses in strength were observed.

The initial micro-crack always appeared in the midplane of the panel at the edge of the drill hole. No significant difference in failure loads was detected between the milled and the polished drill holes.

Investigations on the strength of drilled float glass and thermally toughened panes according to the ring to ring test were carried out by [Schneider, Shen 1998] and [Schneider 2001a, b]. In [Schneider 2001a, b] different drill hole diameters and geometries (conical and cylindrical) were examined. Here as well, the water jet drilled float glass had a smaller failure load whereas thermally toughened glass had nearly the same failure load, no matter whether the holes were drilled by water jet method or by a diamond drill. It was presumed that, by the process of pre-stress, crack "healing" effects reduce the surface damage. The experiments

confirmed a minimum bending tensile strength of 120 MPa according to [DIN 1240-12] and [DIN EN12150-1].

Another interesting aspect is that not only the method of cutting and drilling, but also the applied coolant decisively influence the surface quality. Therefore extensive research was carried out by [Gulati et al. 2001], [Emonds et al. 2003] and [Emonds et al. 2005]. During the drilling of holes and cutting of the glass edges coolants are used to reduce the heat generated by friction and to remove the glass waste. To improve the lubrication between the tip of the drill and the glass, chemical additives are compounded to the cooling water. The above mentioned authors examined the influences of different chemical coolants and pure water on the strength of drill holes and edges. The grinding strength can be reduced by 16% with chemical additions compared to pure water. As a result more holes can be drilled in the same time. The evaluation of strength experiments (four point bending test and ring to ring test) resulted in an increase in strength of 4 to 10% at the edges and up to 35% at the drill holes by using chemical additives in comparison with pure water. An increase of the concentration of the chemical additives led to a further increase in strength. This leads to the conclusion, that dependant on the composition and concentration of the chemical coolants the surface damages can be reduced significantly.

The strength values do not only depend on the degree of surface damage, but as well on various other influencing parameters such as the load rate and the geometry of the specimen. For the statistical evaluation of the strength values as well, the number of tests and the type of applied statistical distribution have an influence. [Siebert 2004] lists a crucial comparison of strength values gathered from different series of experiments.

2.4.3 Crack Formation and Propagation

There is extensive literature available about crack formation and crack propagation by using the theory of fracture mechanics such as [Kerkhof 1970], [Kerkhof 1977], [Richter 1974], [Jebsen-Marwendel 1980], [Siebert 2001]. Therefore, within the scope of this work, only the most important basics are mentioned.

As already mentioned, the bending strength of glass is not a material constant factor, but depends on microscopic or macroscopic surface defects. Essential for crack propagation are the conditions at the tip of the crack. With the aid of fracture mechanics the progressing process can be described. With appropriate models based on the theory of elasticity quantitative relations between the external loads, the crack size and specific material constants are derived.

In general a crack in a real workpiece is subject to complex stress fields consisting of the superposition of three break modes. These three basic modes are shown in Figure 2.4.

Mode I   Mode II   Mode III
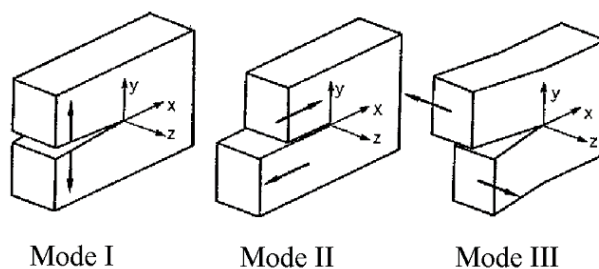
Figure 2.4   Basic cases of loading possibilities of an edge crack

Loading a crack with a tensile stress normal to the crack surface (Mode I) is essential for a brittle crack propagation. The so-called stress concentration factors (SCF) K_I, K_{II} and K_{III}, are dependent on the above mentioned three basic cases, on the geometry of the loaded body, the crack geometry, as well as the magnitude and direction of the loading.

Although the determination of the stress concentration factors is based on extensive mathematical methods these can approximately be calculated for elementary crack problems in a quite simple way [Rossmanith 1982]. For Mode I the calculation according to the theory of elasticity results in the following relationship:

$$K_I = \sigma_0 \sqrt{a}\, f \qquad\qquad (2.2)$$

Where a is the depth of the crack, σ_0 is the tensile stress resulting from the applied load at the place of the crack normal to the crack-plane, assuming a crack would not exist. f is a correcting function dependent on the specimen and crack geometry as well as on the kind of load. Assuming a long, straight crack of small depth, it is allowed to calculate with a constant value $f = 1,99$ for pure bending- as well as for pure tension. As soon as the stress concentration factor K_I exceeds the resistance of the material against crack propagation (= critical stress concentration factor K_{Ic}) the crack starts to grow [Siebert 2001].

With the help of the basic equations of fracture mechanics as well as the corresponding material parameters and the pre-stress of glass a realistic design of glass can be accomplished. For example concepts of [Guesgen 1998], [Shen 1997] or [Siebert 1999] are available, but will not be explained in more detail within the scope of this thesis.

The following section covers briefly the current and future design situation in Germany and Europe.

2.5 Design of Glass Structures

2.5.1 Current Situation

In Germany the concept of global safety factors or - according to the analysis of "old" standards - the allowable stresses are applied so far for the design of glass. Depending on the glass type and the application (vertical or overhead area) allowable stress values are directly stated by dividing experimentally determined strength values by the means of a global safety factor. The global safety factor covers all uncertainties concerning actions, values of resistance and model creation. For verification, the characteristic values of actions are applied without partial safety factors.

Using this method the extremely simple application is of advantage. However, the values used for the design have different uncertainties which are not covered by a global safety factor. Furthermore the concept is not transparent. Therefore transferring the concept on applications without experience is hardly possible.

The concept of the allowable stresses is used especially in [TRLV 1998] und [TRAV 2003]. Both technical rules are valid only for plate bearing elements.

2.5.2 Future Situation

At present, a new design standard for glass is in progress on European level [prEN 13474-1, -3] and on German level [E DIN V 18008-1, -2]. Both approaches are based on the current concept of partial safety factors, as it is applied in the Eurocodes and based on fracture mechanics (see also chapter 2.4)

The fundamentals of the design of [prEN 13474-3] and [E DIN V 18008-1] are based on [DIN EN 1990]. The actions are determined according to [DIN EN 1990], [DIN EN 1991] and [DIN 1055-100].

The resistance verification of glass plates as described in [E DIN V 18008-1] is done on the verification of the maximum principle tensile stress at the glass surface. Residual stresses of thermal pre-stress are considered on the resistance side.

It has to be verified that the condition:

$$E_d \leq R_d \qquad (2.3)$$

is fulfilled, where E_d is the design value of the load and R_d the design value of the resistance.

According to [E DIN V 18008-1] the design value of the resistance versus stress failure for thermally pre-stressed glass, in simplified terms, is set by:

$$R_d = \frac{f_k}{\gamma_M} \qquad (2.4)$$

where f_k is the characteristic value of the bending strength and γ_M is the material partial factor for resistance.

For glass without thermal pre-stress (e.g. float glass) the following formula

$$R_d = \frac{k_{\mathrm{mod}} f_k}{\gamma_M} \qquad (2.5)$$

is valid.

The coefficient k_{mod} is considering the dependence of the duration of load bearing on the glass strength.

The above mentioned design concepts are starting from a basic strength (residual strength) of glass under certain conditions (test conditions). To cope with the planned application conditions and the properties of the member that needs to be designed, the basic strength is modified with different influencing factors. The surface size stressed under tension, the stress distribution on the surface as well as the load duration and the pre-stress of the glass are taken into consideration. The approach of a partial compound-effect when using laminated safety glass is considered as well.

3 Point-Supported Glass Elements

3.1 Introduction

High local stress occurs at the edge of the drill hole, if loads will be applied via screws, bolts or point-supports that are mounted in drill holes of panels. Designs that are loaded in-plane and that carry the load via screws, bolts or point-supports are called bolted connections. In case of so-called bolted connections the loads are transmitted only by contact perpendicular to the bolt axis into the panel plane. The compressive forces interact normal to the contact surface.

In steel construction local stress-peaks can be reduced by local plastification due to the elasto-plastic material behaviour. Considering glass, this is impossible because of its brittle material behaviour. By applying appropriate material, such as plastic or aluminium, between the steel-bolt and the glass hole peaks in stress are avoided and the forces are distributed uniformly over the contact area. The size of the contact surface and hence the size of the loadbearing area as well as the stress distribution depend on several parameters whose influences are examined in chapter 7 and 8.

The kind of the support, the geometry of the components, the quality of the glass edges and surfaces as well as the interlayer material influence the stress distribution around the drill hole. Due to the complexity of the calculation of point-supported glazing, the design is usually carried out by means of the finite element method (FEM).

In order to find the correct computational model precise knowledge about the contact mechanisms and the parameters that influence the stress distribution is necessary. To exclude unsuitable static models and to be able to evaluate a FEM-model in a qualified way, verifications of the corresponding programs are indispensable. To verify this, the FEM-model is compared with an analytical solution or experimental investigations.

No technical rules or standards are available up to now that regulate the manufacturing, the design and the usage of point-supported vertical and overhead glazing.

3.1.1 Loadbearing Types

The load depends on the respective mounting situation and area of application. In general there is the differentiation between vertical and overhead glazing [TRLV 1998]. Next to the actions from dead load and wind as well as an additional snow load at overhead glazing, further influences are to be considered according to the type of use and the area of application. These are, for example, impact load (anti drop glazing) [TRAV 2003] or additional variations in pressure in the spacing of insulating glazing units (climate loads).

In some cases overhead glazing needs to be accessible for cleaning and maintenance purpose or for public traffic. Therefore additional requirements need to be considered, which in case of Germany are [DIN 4416], [GS-Bau 18 2001], [DIBt 2001]. Another important factor for overhead glazing is the residual load-carrying capacity. Only the appropriate glass types and constructions, which are approved for a respective area of application, have to be used.

All additional actions which may lead to an increase in stress have to be considered. These are, for example, temperature, deformation of the substructure, eccentricities, constraints from the assembly or manufacturing inaccuracies of the components.

Forces in, or perpendicular to the plane of the panel accordingly result from the above mentioned actions. These forces, dependant on the supporting type at the bearing point, can result in additional bending moments.

3.1.2 Force Transmission

In general, there is the distinction between point bearing and line bearing. Line bearing is used if the glazing is supported at least on two opposite sides on a continuous line-shaped clamping strip [TRLV 1998], [E DIN V 18008-2].

Bonded connections represent an alternative to the mechanical fixing. However, there are no standards for these so far. Up to now, in Europe bonded connections are only possible within the framework of a technical approval for bonded facades (SSGS - Structural Sealant Glazing Systems). The European guideline ETAG no. 2 [ETAG Nr. 002 1998] controls the requirements for the approval of SSGS-systems.

In case of point supported glazing there is a distinction between point-supports which are carried through glass drill holes and clamping strips, which are arranged without drill holes in the corners or at the edges of the glazing [DIN 18516-1, -4].

In the following paragraphs point-supported glazing that carry the loads via bolted connections in the drill holes are covered. Essentially, three different ways of transmitting forces between glass and point-support are possible:

-   Bonded connections

-   Connection by friction

-   Bolted connections

A combination of those actions outlined in Figure 3.1 and Figure 3.2 represent the possible stressing. In most cases point supported glazing can not be definitely assigned to one of these connection types, since in most applications a combination of different actions occur.
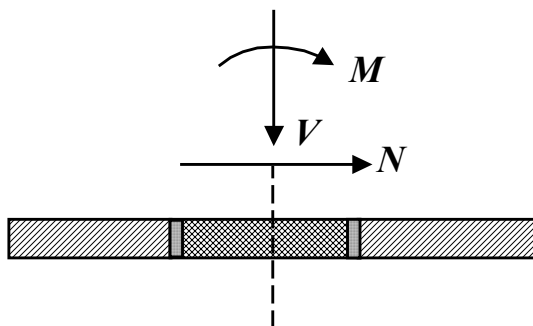
Figure 3.1 Force transmission by contact   **Figure 3.2** Force transmission by friction
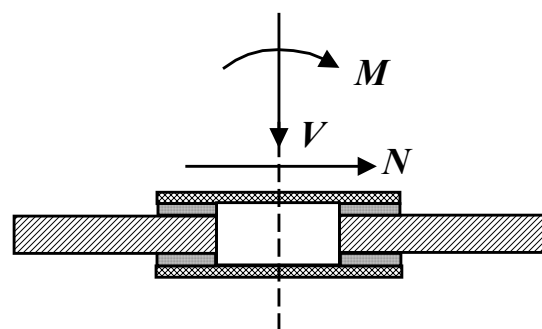
[Techen 1997] for example explicitly covered the connection techniques above mentioned. He explains each connection in detail and examines various interlayer materials.

Numerical and experimental investigations on bonded connections were carried out for example by [Overend 2002]. The thesis of [Panait 2004] covers frictional connections stressed by in-plane loads.

3.1.3 Types of Point-Supports and Bearings

Numerous supporting systems are available for point supported glazing. Because of the brittle material behaviour of glass, special attention has to be paid on the usage of appropriate materials in order to distribute the forces uniformly over the contact area of the glazing. This is particularly important for construction, dimensioning and the design of point-supports.

Below the essential distinction criteria of point-supports are explained with regard to geometry and types of bearing.

In principle, there is the differentiation between cylindrical- and conical drill hole geometry (see chapter 2). Accordingly two corresponding point-support models are existing for these geometries: countersunk support and supports with discs (see Figure 3.3 und Figure 3.4).
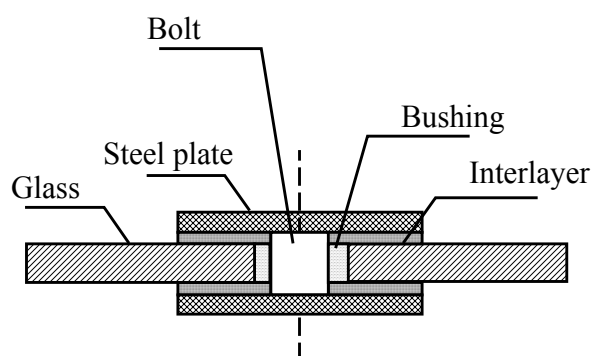
Figure 3.3 Principle sketch of supports with discs (steel plates)
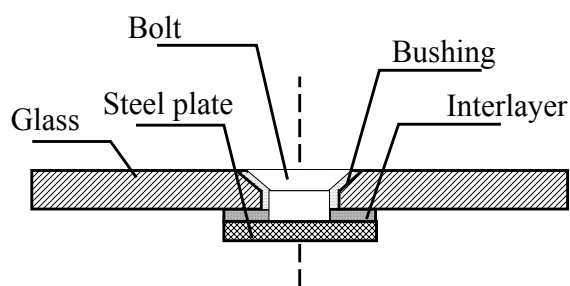
Figure 3.4 Principle sketch of countersunk support

Dependent on their type of bearing above two types of point supports can be further divided into two more categories:

- rigid joint

- hinge joint

Corresponding examples are shown in Figure 3.5. In case that a rotation is possible, the place of the hinge leads to further differentiation (see Figure 3.6).

Rigid joint   Movable elastic joint   Ideal ball-and-socket joint
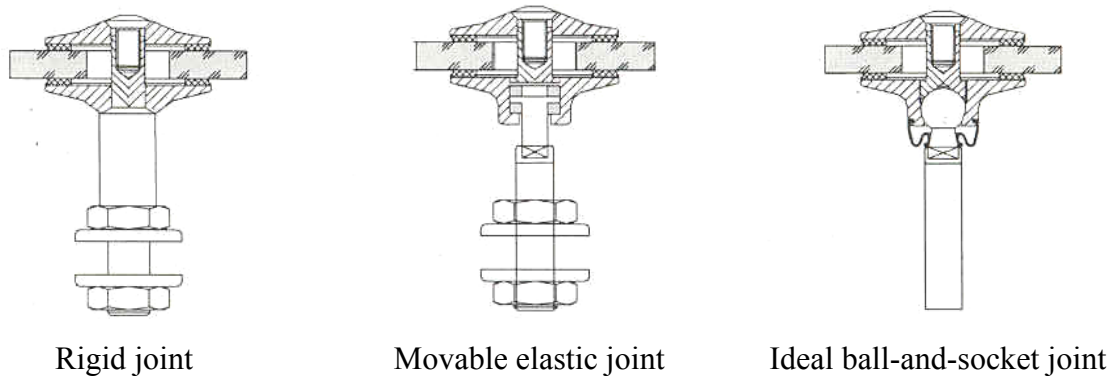
Figure 3.5   Rotation of the supports [Albrecht 2004]

In panel plane   Behind panel plane   At the connection to the
substructure
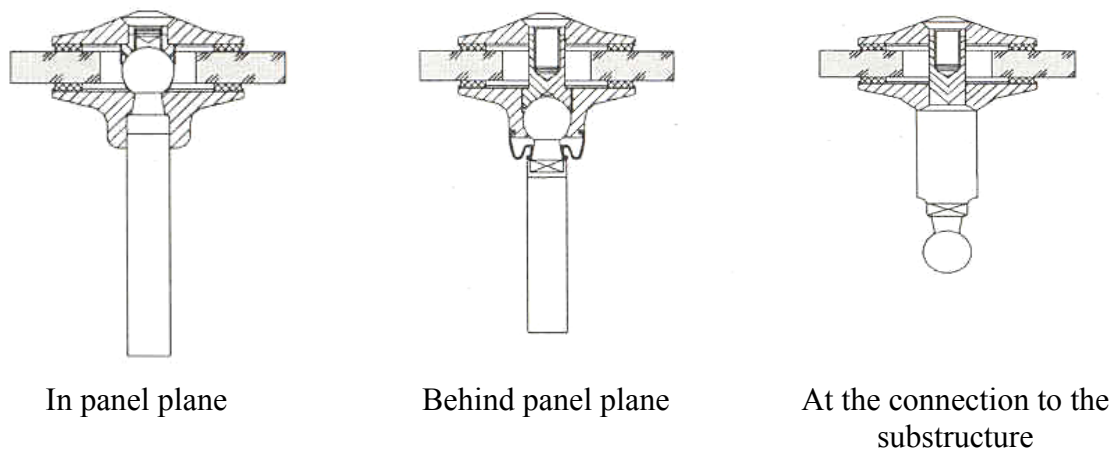
Figure 3.6   Location of the hinge [Albrecht 2004]

In case of eccentricities of the hinge, additional stress is inserted by a bending moment in the glazing. If the hinge is in-plane, this additional stress is avoided. A bending moment can occur as well in combination with constraints, such as variation in temperatures or assembly inaccuracies of the substructure.

For dimensioning and constructive design manufacturing inaccuracies of the point support, the substructure as well as the glazing [DIN 1249-12], [DIN EN 572-2], [DIN EN12150-1], [DIN EN 1863-1] have to be considered. An overview of the limits for drill holes in thermally toughened glass and heat strengthened glass is given in Table 3.1.

Table 3.1   Allowed tolerances for drill holes

Type of glass	Nominal diameter ∅ [mm]	Allowed tolerance [mm]	Source
thermally toughened glass heat strengthened glass	$4 \leq \varnothing \leq 20$	$\pm\ 1{,}0$	DIN 1249-12 DIN EN12150-1 DIN EN 1863-1
	$20 < \varnothing \leq 100$	$\pm\ 2{,}0$	
	$100 < \varnothing$	Request manufacturer	

For laminated safety glass (LSG) the allowed misalignment of the drill holes has to be considered [DIN EN 12543-5]. Table 3.2 lists the allowed maximum values.

Table 3.2   Allowed misalignment for LSG

Nominal value B or H [mm]	Maximum misalignment [mm]
B, H ≤ 1000	2,0
1000 < B, H ≤ 2000	3,0
2000 < B, H ≤ 4000	4,0
B, H > 4000	6,0

Due to the cylindrical shape of the drill hole, supports with steel discs can more easily compensate inaccuracies or tolerances in manufacturing. The drill holes simply needs to be a few millimeters larger than the bolt of the point-support. Remaining spaces can be filled with suitable filling material [DASt 2004], [Techen 1997]. Using countersunk supports inaccuracies in the drill hole or the support geometry cause concentrated inhomogeneous introductions of load. These can lead to the fracture of the glass pane. Accordingly, any compensation of tolerances is hardly possible.

The size of the influence of constraints basically depends on the flexibility and the possibilities of compensation of the point-support construction as well as on the substructure. Deformations of the substructure particularly influence soft support-structures. In the same way changing stiffness are critical, for example local supports at a stiff substructure [Burmeister 1998a, 1998b]. Ideally, any constraints should be avoided and a statically determined bearing should be aspired (see Figure 3.7).
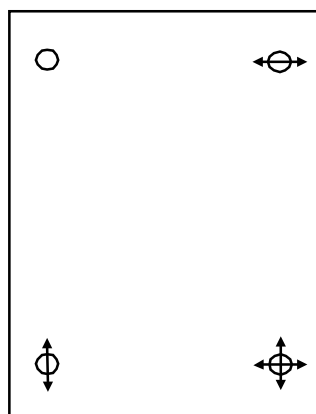
Figure 3.7   Glazing, statically determined bearing

In order to attain any in-plane displacements, compensation elements (slotted holes) between point support and substructure may be installed (see Figure 3.8). Sliding films or "teflon" (polytetrafluoroethylene) panes are used at the contact surfaces between the bolting and the substructure in order to guarantee the swaying of the support, e.g. [Albrecht 2004]. Polytetrafluoroethylene (PTFE) as a friction-partner of metals is quite favourable due to its low coefficient of friction $\mu_{PTFE/Metal}$ of 0,05 to 0,1.
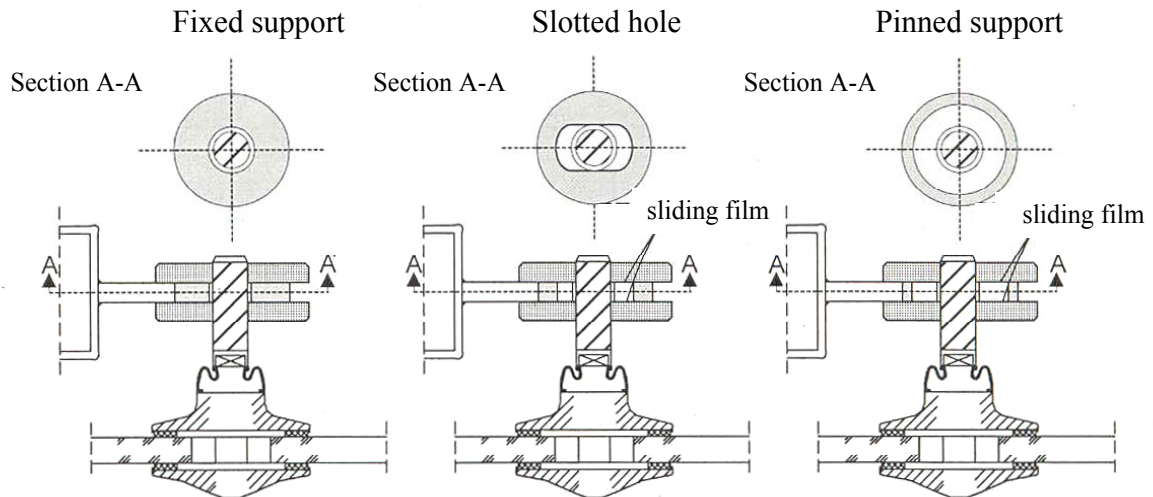
Figure 3.8   Compensating elements to ensure displacements [Albrecht 2004]

So-called "spiders" are also used frequently for large-area facades. They provide one point of support for four adjacent panes (see Figure 3.9). To compensate tolerances the spider can have one fixed support, one slotted hole and two pinned supports.
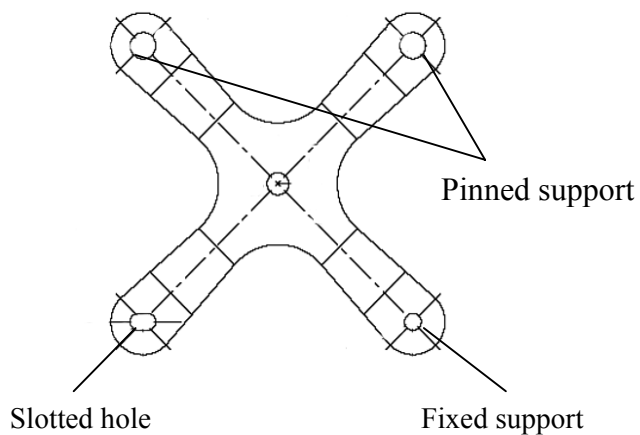
Figure 3.9   Example of a "spider" point-support system

However, to design ideal hinges and to provide durable displacements, a high structural and technical effort is required, which results in high costs. In particular the intrusion of moisture and corrosion needs to be prevented. Practice shows that the assurance of durable displacements and by this a constraint-free support during the entire service life of a building often are a problem. Therefore, for a design with sufficient margin of safety, limit state investigations should be carried out (see chapter 3.3), which means that under worst case conditions a rigid connection of the point support with the substructure has to be assumed. In spite of that uneconomical constructions can be avoided if elastic flexibility of the structure or stiffness of the support are considered [Brendler, Schneider 2004].

3.1.4 Materials of the Point-Supports

The material properties of the individual components have to be known for the design of structural members as well as for the assessment of the loadbearing capacity and operational suitability.

In particular the following parameters are of importance:

- Force-displacement behaviour (tensile- and compressive strength, Young's modulus)

- Durability:
  Weather resistance
  (UV-light, temperature, humidity, other environmental influences)

- Force-displacement behaviour under long-term influence (creeping, relaxation)

The material properties for glass and metals are known. The metal parts of the support (bolt, washer, etc.) either consist of steel according to [DIN 18800-1] or in most cases of stainless steel in accordance with the technical approval [AbZ Z-30.3-6] or [DIN EN 10088-1]. Within these standards and the technical approval the strength values and mechanical properties are contained.

Next to aluminium, mainly plastics are utilized for bushing and interlayer materials. The usage of plastics is continuously increasing. They are particularly employed more and more in high-quality application fields. With the increasing demands the exact determination of material properties becomes more and more important. However, the determination of all material properties is quite time- and cost intensive, as for example creeping tests. Hence frequently material specifications for bushing and interlayer materials are missing for the design of point supports.

Modelling the components by finite elements it is important to utilize characteristic material values for the interlayer and bushings that are close to reality because - as already explained - the uniform distribution of the force is of central importance. Limit value investigations have to be carried out for the finite element calculation, in case material data is missing. The selection of sensitive limit value is not always possible without any issues. An enormous requirement for investigation is needed to be able to judge on the influence of the material behaviour. Material investigations on different bushing materials under in-plane loads in bolted connections were carried out for example in [Techen 1997] and [DASt 2004].

Suitable interlayer are placed between point supports and the glass to avoid any direct contact between steel and glass (see Figure 3.3 and Figure 3.4). Between steel discs and glass, elastic interlayer are used. These are mainly ethylen-propylene-diene rubber (EPDM), polyamide (PA), polyvinyl chloride (PVC), silicone, soft aluminium or epoxy resins. The various interlayer-materials will not be covered here in more detail. The thesis of [Siebert 2004] contains a detailed disquisition of different interlayer-materials.

In general, preprocessed bushings of aluminium or plastic are inserted between the bolt and the glass drill hole. Alternatively, the empty space between bolt and glass can be squirted with a compound material, such as reaction resins. The usage of these filling materials simplifies the compensation of manufacturing tolerances (see chapter 3.1.3 and 3.2.1), but the processing of these fillings is more extensive than insertion of pre-processed bushings.

The following part of this thesis covers suitable materials for pre-processed bushings, since these are of central importance for in-plane loadbearing. In addition experimental investigations for two different bushing materials are carried out (see chapter 8).

3.2 Material Properties of the Bushings

3.2.1 Grouting Materials

For point supports grouted in glass drill holes, a reaction resin with technical approval for fixing-systems, is often used as filling material [Mauthe 1999]. The filling material is a two component hybrid mortar consisting of an organic binder (urethane methyl acrylate) and cement. Also epoxy resins are used. Table 3.3 exemplary lists several material properties for the hybrid mortar as well as for an epoxy resin.

Table 3.3   Properties of grouting materials

Grouting material	Hybrid mortar [Mauthe 1999]	Epoxy resin [Epple 2001]
Comp. strength acc. to DIN 53458 after 1 day after 28 days permissible compressive strength	49,3 MPa 69,0 MPa 20,0 MPa	65 MPa
Tensile strength	n.a.	40 MPa
Tensile shear strength	n.a.	n.a.
Bending tensile strength	n.a.	18 MPa
Young's modulus acc. DIN 53452	2780 MPa	1700 MPa
Elongation at break [%]	n.a.	10
Thermal expansion coefficient α_t	$38 \cdot 10^{-6}$ K^{-1}	n.a.
PVB-film compatible	84 (Shore D)	97 (Shore A)
EPDM compatible Silicone profile compatible UV resistant	yes yes yes	yes yes yes
Water proof Water absorption according to DIN 53495 in [%] Temperature resistance cleaning agent cleaning agent	yes yes 4,3 % $\leq$ 80°C 1% tenside solution with no influence	n.a. yes n.a. $\leq$ 120°C alkali proof
Suitable for outdoor use	yes	yes
Reaction behaviour (work life at 20°C)	4 minutes	3 minutes
Hardening time at 20°C/ Post hardening time	60 minutes / 28 days	3 hours
Storing duration (cool/dry environment, in original package)	9 months	12 months
Viscosity at 20°C	60-80 Pa·s	after 30 minutes at 23 °C 55 Pa·s

To avoid inclusion of air during the grouting of the filling material special point supports with two holes can be utilized. While injecting the mortar in the big hole it fills the empty space and comes out at the small hole indicating the filling is complete. Figure 3.10 shows an example of this type of point support.

Figure 3.10 Example of a point-support for grouting materials with special filling holes

Such type of grouting allows a good compensation of tolerances between drill hole and bolt. A drawback is the high precision which is required to assure a consistent distribution of the filling material in the drill hole. Furthermore, some filling materials are difficult to process and provide a strong gluing between glass and bolt, which can possibly lead to additional constraints. Attention has to be paid as well to allow a sufficient hardening time for most of the reaction resins. Figure 3.11 shows a drill hole filled with mortar.
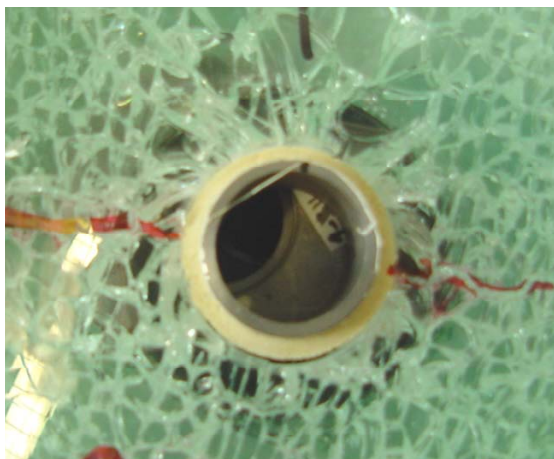
Figure 3.11 Example of a drill hole filled with mortar

Investigations on five different reaction resins can be taken from the thesis of [Techen 1997]. Results from tensile tests done by [Techen 1997] and [DASt 2004] show that the determined ultimate loads are subject to big dispersion, which can be explained by the above mentioned disadvantages of grouting.

3.2.2 Thermoplastic Synthetics

If pre-processed plastic bushings are applied, thermoplastics are used in general. In particular polyamide (PA) and polyacetal (POM), with different additives are employed. These are characterized by high surface hardness, wear-resistance and retaining of shape. They are mainly used as bearing elements and gears in mechanical engineering.

Thermoplastics are polymeric materials [DIN 7724] which consist of a line up or chain of monomer elements. The bonding forces that keep together the atoms chain are known (primary forces). The state of order, or in other words, the physical state of the chains towards each other is of relevance for the forces which connect one chain to another (secondary forces). Although these forces are only in the range of one hundredth of the primary strength, the secondary strength is influencing the mechanical behaviour of thermoplastic decisively.

This difference in bonding forces is typical for thermoplastics. They soften in the heat and then can be deformed in almost any way. If cooled down, the melted thermoplastic becomes solid again. In theory, this can be repeated unlimited times. The molecular chains of thermoplastics can be straight or they can show several branches. A high number of branches and a bulky arrangement decrease the intermolecular forces and enlarge the concatenation distance, which leads to a high light transparency. In the same way these soften in a broad temperature range and freeze intricately in complete disorder, which is the amorphous state (see Figure 3.12). If the molecule chains show at least some order in partial areas, then they are partial crystalline thermoplastics (see Figure 3.13). Polyacetal and polyamid are semi-crystalline thermoplastics.
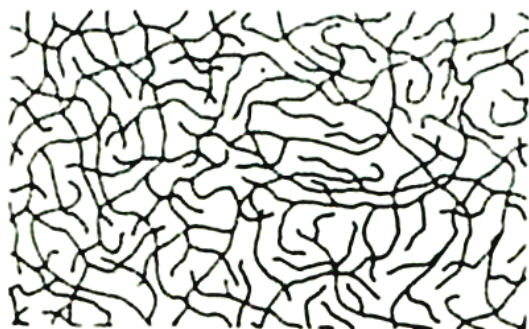
Figure 3.12 Amorphous state   **Figure 3.13** Semi-crystalline state
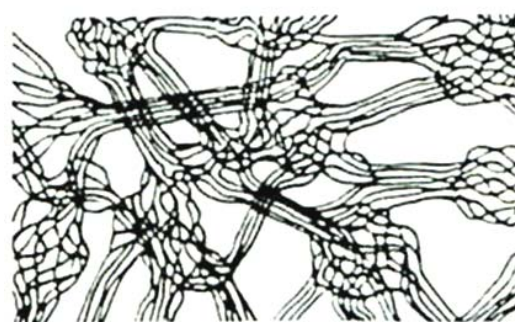
Mechanical and thermal properties

In case of mechanical stress polymers show a strongly visco-elastic behaviour, which means that the occurring deformations are partly elastic (reversible) and partly plastic (non-reversible). This results in the consequence that important material properties such as the Young's modulus and shear modulus are not only dependant on temperature but also on time and the speed of load. Other factors of influence are humidity and radiation as well as the kind of stress and the amount of stress. Besides, the stress-history of the plastic is of great importance. This type of material behaviour can be visualized in the stress-strain-diagram as a function of temperature. The spectrum reaches from brittle, almost ideally elastic glassy solid state at temperatures below the glass transition temperature up to the ductile material, which already deforms at a minimum of stress.

Figure 3.14 shows the schematic temperature dependency of the shear modulus G of partial crystalline thermoplastics. The shear modulus is determined according to [DIN EN ISO 6721-2].
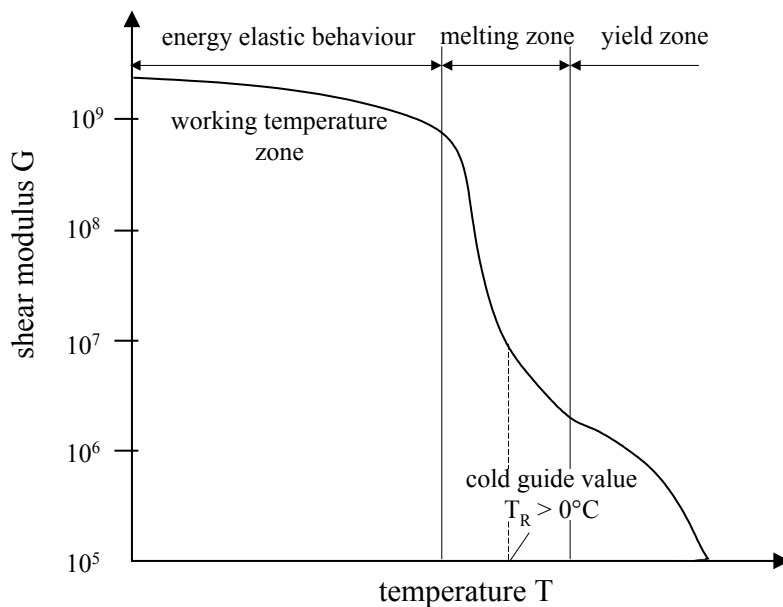
Figure 3.14 Shear modulus G as a function of temperature T of semi-crystalline thermoplastics [DIN 7724]

All thermoplastics plasticise already at room temperature for loads which are significantly below the elastic limit. For the description of the material properties this means that time has to be considered as additional parameter.

For the design of components subjected to permanent loading the long time behaviour of plastics has to be considered. [DIN EN ISO 899-1] is covering a procedure for the definition of the creep behaviour (increase in deformation at constant load) of plastics under tensile stress.

A description of test specimen as well as an overview to define every single property of thermoplastic mold compounds made of polymeric mixtures is contained in the standard [DIN 16780-2].

Polyacetal (POM)

Polyacetal (POM) and acetal-coplymere (POM-C) have a linear composition and a high degree of crystallinity. In particular these are favourable qualities of POM:

- High hardness and rigidity
- Shape stability at heat
- Minimal water absorption
- High resistance against solvents
- Resistance against initiations of stress cracks
- Favourable slide and wear behaviour

For polyacetals functional additives play an important role. Specific properties can be corrected by addition of various ingredients. For example, by adding PTFE (Polytetrafluoroethylene) the sliding behaviour can be improved and by adding glass fibers the shape stability can be enhanced.

Ultraviolet radiation damages polyacetal. The thinner material is, the faster the changes in properties caused by radiation occur. By adding light stabilizers the destruction can be delayed. Active soot proves as a most effective stabilizer.

The standard [DIN 16781-2] contains a description of test specimen as well as an overview on the definition of the individual properties of POM. The most important mechanical properties are listed in Table 3.4.

Table 3.4   Mechanical properties of acetal-homo- and copolymers

		POM	**POM-C**	**POM GF30*)**
Density ρ		1,42 g/cm^3	1,41 g/cm^3	1,56 g/cm^3
Tensile strength according to [DIN EN ISO 527-1, -2]		65 to 70 MPa	67 to 72 MPa	140 MPa
Elongation at break according to DIN EN ISO 527-1		25 to 70%	25 to 70%	3%
Young's modulus E**) (tension) according to DIN EN ISO 527-1		ca. 1600 to 2800 MPa	ca. 1600 to 3200 MPa	ca. 9000 to 10000 MPa
Service temperature:	Max. short term	110 to 140°C	110 to 140°C	110 to 150°C
	Max. enduring	90 to 110°C	90 to 110°C	90 to 110°C
	Min. enduring	-60°C	-60°C	-60°C
Melting area		175°C	164 to 167°C	164 to 167°C
Coefficient of thermal expansion α_t		$90 \cdot 10^{-6}$ /K	$110 \cdot 10^{-6}$ /K	$30 \cdot 10^{-6}$ /K
Water absorption saturation at 23°		0,5 to 0,7%		

*)   GF30: 30% glass fiber reinforced
**) The values for the Young's modulus vary depending on the composition of the material as well
     as whether determined in dry or moist state

For decreasing temperatures the area around -60° C represents the embrittlement limit and is designated as freezing or glass temperature. Figure 3.15 shows, that the mechanical strength of POM is superior to various other thermoplastics.
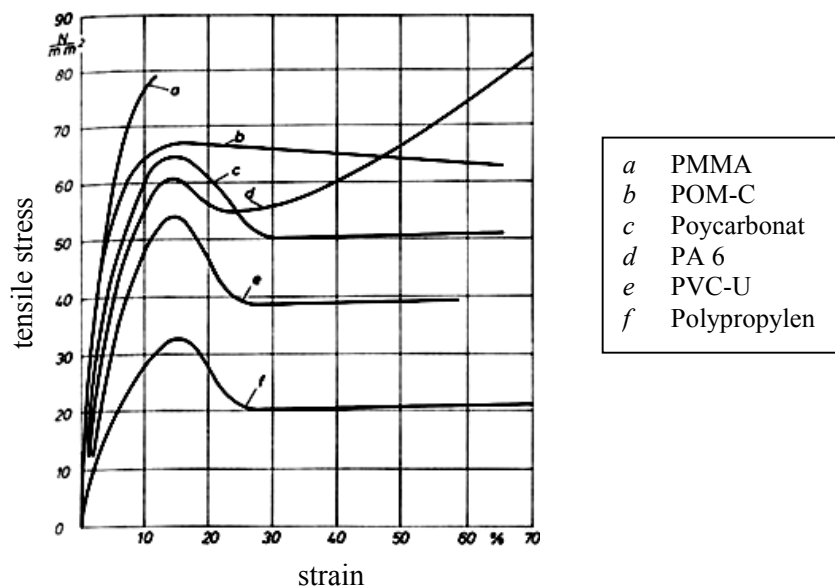
Figure 3.15 Stress-strain-diagram of different thermoplastics [Domininghaus 1997]

Figure 3.16 shows the stress-strain behaviour as a function of constant times (isochrones). These are determined with creep tests, which are long-term tests under constant load in accordance with DIN EN ISO 899-1.
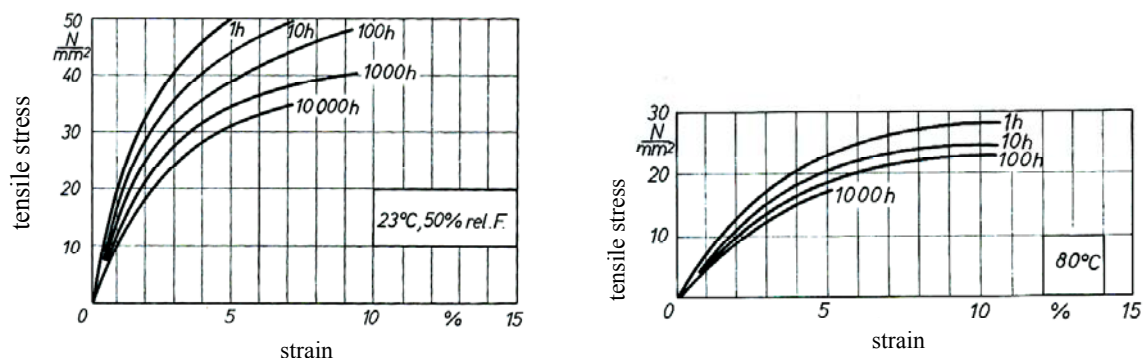
Figure 3.16 Isochrone stress-strain-diagrams for POM-C at different temperatures, [Domininghaus 1997]

The water absorption of polyacetal is quite small. Figure 3.17 shows the time dependency of the water absorption in the temperature range of 20 up to 60°C.
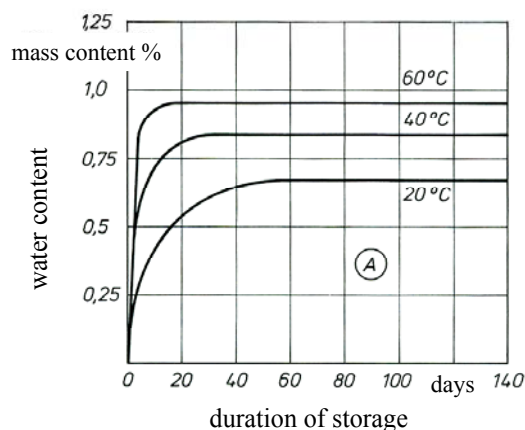
Figure 3.17 Water absorption of polyacetal, [Domininghaus 1997]

Furthermore, polyacetal is resistant against weak acids and leaches as well as against gasoline, alcohols, fat and oils. Besides, copolymers are resistant against strong leaches.

Polyamide (PA)

Polyamides belong to the most important thermoplastic condensation polymers. Their positive properties include in particular:

- High strength, rigidity and hardness
- High shape stability at heat
- High resistance against solvents
- Favourable sliding and wear behaviour

One of their negative qualities is the fact that the mechanical properties of polyamides depend on the humidity of the component and the reversible water absorption comes along with a change in volume. Also for polyamides, functional additives for improvement of specific

parameters are of importance. A high life time for outdoor use is achieved with stabilization with soot.

An important material for strengthening of polyamides are glass fibers. They cause an improvement of the mechanical properties. At the same time they also reduce the water absorption.

In civil engineering mainly partial crystalline PA 6 and PA 66 polyamides are used. They show a very high resistance against deformation in the heat, high rigidity and hardness as well as strength versus abrasion.

The most important mechanical ratings of PA 6 and PA 66 are listed in Table 3.5.

Table 3.5   Mechanical properties of PA 6 and PA 66 polyamides

		PA 6	**PA 6 GF30*)**	**PA 66**
Density ρ		1,13 g/cm^3	1,36 g/cm^3	1,14 g/cm^3
Tensile strength according to [DIN EN ISO 527-1, -2]		70 to 85 MPa	100 MPa	77 to 84 MPa
Elongation at break according to DIN EN ISO 527-1		200%	-	150%
Young's modulus E**) (tension) according to DIN EN ISO 527-1		ca. 1400 to 3000 MPa	ca. 5000 to 8500 MPa	ca. 2000 to 3100 MPa
Service temperature:	Max. short term	140 to 180°C	180 to 220°C	170 to 200°C
	Max. enduring	80 to 100°C	100 to 130°C	80 to 120°C
	Min. enduring	-30°C	-30°C	-30°C
Melting area		220°C	220°C	255°C
Coefficient of thermal expansion α_t		$80 \cdot 10^{-6}$ /K	$30 \cdot 10^{-6}$ /K	$80 \cdot 10^{-6}$ /K
Water absorption saturation at 23°		2,5 to 3,5%	1,6 to 2,2%	2,5 to 3,1%

*) GF30: 30% glass fiber reinforced
**) The values for the Young's modulus vary depending on the composition of the material as well as whether determined in dry or moist state

Further properties of thermoplastics can be taken from the corresponding literature: Extensive investigations for the long term behaviour under static and vibration loading of the thermoplastics POM and PA 66 were carried out by [Becker 1984]. [Lewen 1991] investigated in the non-linear vicious-elastic behaviour of plastics. Explanations about the material behaviour of plastics are contained for example in [Menges 1990].

3.2.3 Aluminium

Aluminium alloys as well are frequently used for the bushings. The advantage in using aluminium is that the material properties such as density, Young's modulus and thermal expansion only change in a small bandwidth for different alloy components. Thus, the values of the material properties in Table 3.6 can be used for the design without having to consider limit value investigations for the finite element calculation, as it is often required for plastics.

Table 3.6   Material properties

Density ρ	2,7 g/cm^3
Young's modulus E	70.000 MPa
Poisson's ratio ν	0,3
Coefficient of thermal expansion α_t	$24 \cdot 10^{-6}$ /K
Melting point	ca. 650°C

Material information, in particular minimum values of the strength for different semi-finished products, are to be taken from the design standard for aluminium [DIN 4113-1].

Aluminium alloys show with sufficient ductility minimum values for the tensile strength (R_m) of 200 MPa. In comparison, "pure aluminium" can only reach maximum strength of 150 MPa. The most important alloying elements are silicon (Si), copper (Cu), magnesium (Mg), manganese (Mn) and zinc (Zn).

Aluminium has its lowest strength in the untreated state after casting. The strength of aluminium and aluminium alloys can be increased by cold-work hardening or tempered hardening. Cold-work hardening means a plastic deformation for example through cold-rolling. This leads to displacements in the crystal network, which increasingly hinder each other and by that enlarge the resistance versus deformations (strength, etc.). By cold-work hardening, especially the proof strain ratio $R_{p0,2}/R_m$ is being increased whereas the elongation at fracture strongly decreases. For tempered hardening the material needs to be heated to a temperature where most of the impurities leading to the hardening are dissolved in the mixed crystal. A rapid cooling down to room temperature (quenching) follows. By this the impurities remain unbalanced in solution. Hardening is only possible with specific alloys.

A preceded hardening can be reversed by thermal treatment (spheroidise annealing).

Enlarging the strength increases the proof strain ratio $R_{p0,2}/R_m$ and the brittleness. Increasing the temperature reduces the tensile strength, the strength against cyclic loads, the proof limit and the hardness, whereas elongation at fracture and reduction in area at the breaking point are increasing.

3.3 Previous Design Concepts

No technical rules or standards that control the manufacturing, the design and the usage of point-supported facades and overhead glazing are available up to now. This means that in Germany such designs are not regulated and require a technical approval or an approval on an individual basis. Within the framework of these approvals various proofs are required in general.

In most cases the bearing capacity of supports has to be verified by experiments, since the glass supports often consist of a great number of single components and especially supports with hinges show quite complex load carrying- and deformation-mechanism. The ideal hinge-movement can be constrained for example by a rubber seal or a soft interlayer. Therefore these types of supports can only be transferred in realistic static models after experimental investigation. For the determination of the basic data the support is stressed with static and perhaps also cyclic actions. Under different bearing conditions, the load carrying behaviour is examined and the required material ratings are determined.

The verification of stability for point-supported glazing can be done numerically by means of a finite element calculation. However, this is no simple task. Investigations on the quality of different FEM-models [Schneider 2001], [Siebert 2004], [Albrecht 2004] show that depending on the complexity and the choice of the parameters the tensions and deformations in the glazing can be determined more or less exactly. Every detail of the point support has an influence on the local state of stress at the edge of the drill hole. In most cases extensive FEM-models with contact approaches are required in order to capture the reaction of point supported designs realistically. Depending on the level of knowledge and possibilities of the applied FEM-program, the quality of static models of the FEM-users varies. A verification is necessary to exclude unsuitable static models and to be able to evaluate a FEM-model in a qualified way. The aim of a verification is to limit the calculations of different program systems.

Next to an extensive FEM-modelling with volume and contact approaches a verification as well should allow simplified modelling with sufficient margins of safety that consider the decisive influences. The framework of technical approvals [AbZ Z-70.2-99; AbZ Z-70.2-112] defines determinations for verification of the FEM-program including the required verification for every type of point support. This procedure allows the utilization of variable glass dimensions and different configurations of point supports.

The verification can either be performed by means of an analytical solution - if available - or by experiment. It is required to accomplish the verification of the FEM-model step by step, which means separated by every value in order to be able to evaluate their respective influence on the total result of a system. Currently two different procedures exist [Siebert 2004], [Brendler, Schneider 2004], that are applied within the framework of approval procedures and that also serve as a basis of the national design standard for point supported glazing [E DIN 18008-2] which is currently in progress.

For "simple" supported glazing in facades and overhead area, which are well proved in the practice, the "technical rules for design and implementation of point supported glazing" are currently elaborated in Germany [eTRPV 2005]. Since September 2005 the draft is available to the community of experts for commenting. These rules assume a design without verified FEM-model. Therefore only laminated safety glass of thermally toughened glass as well as heat strengthened glass are supposed to be allowed. In the same way the span width for overhead glazing are limited to certain values for reasons of the residual load carrying capacity.

4 Stress Distribution in an Isotropic Panel

4.1 Basics

A thin plane plate structure is called panel, if it is loaded by forces applied at the boundary, parallel to the plane and distributed uniformly over the thickness. In case of any deformation the midplane of the panel has to stay plane. Additionally, it is assumed that the panel thickness t is constant.

4.2 Fundamental Equations for the Panel

In a panel the deflected state can be described with the deflection components u *(x,y)* and w *(x,y)*. The stresses are denoted with σ_x^0, σ_y^0 and τ_{xy}^0. If the thickness t of the panel is very small, the stress components σ_z^0, τ_{zx}^0 and τ_{zy}^0 are zero on both faces of the panel and it may be assumed that they are zero also within the panel. It also may be assumed that these three components are independent of z, i.e. they do not vary through the thickness t. They are then functions of x and y only. All differential elements of the area, which are parallel to the midplane, are stress-free and a plane stress state is obtained. The remaining stress components σ_x^0, σ_y^0 und τ_{xy}^0 of the cross sections, which are perpendicular to the midplane, are all directed parallel to the midplane. Knowing the stress components at any point x and y of a panel, the stress for any different direction can be calculated. φ meaning the angle between the normal and the *x*-axis (see Figure 4.1), the components σ_ξ^0, σ_η^0 and $\tau_{\xi\eta}^0$ result:

$$\sigma_\xi^0 = \frac{\sigma_x^0 + \sigma_y^0}{2} + \frac{\sigma_x^0 - \sigma_y^0}{2}\cos 2\varphi + \tau_{xy}^0 \sin 2\varphi$$

$$\sigma_\eta^0 = \frac{\sigma_x^0 + \sigma_y^0}{2} - \frac{\sigma_x^0 - \sigma_y^0}{2}\cos 2\varphi - \tau_{xy}^0 \sin 2\varphi \qquad (4.1)$$

$$\tau_{\xi\eta}^0 = -\frac{\sigma_x^0 - \sigma_y^0}{2}\sin 2\varphi + \tau_{xy}^0 \cos 2\varphi$$
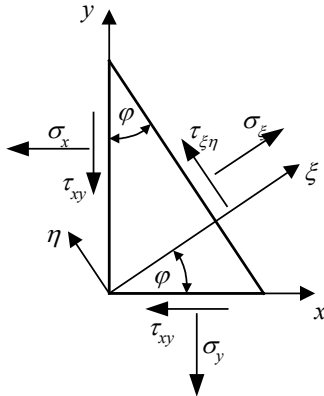
Figure 4.1   Conditions for transformation

The extreme values of σ_{ξ}^0, the principal stresses result in the cross sections which are described through the equation:

$$\tan 2\varphi^* = \frac{2\tau_{xy}^0}{\sigma_x^0 - \sigma_y^0} \qquad (4.2)$$

Equation (4.2) gives two solutions that are $\varphi_1^* = \varphi$ and $\varphi_2^* = \varphi_1^* \pm \dfrac{\pi}{2}$.

The corresponding extreme values σ_1^0 and σ_2^0 are

$$\sigma_{1,2}^0 = \frac{\sigma_x^0 + \sigma_y^0}{2} \pm \sqrt{\left(\frac{\sigma_x^0 - \sigma_y^0}{2}\right)^2 + \tau_{xy}^{0\,2}} \qquad (4.3)$$

The shearing stress becomes zero in these plane cross sections.

The extreme values of $\tau_{\xi\eta}^0$, the principal shearing stresses are calculated as following:

$$\tau_1^0 = \pm\frac{\sigma_2^0}{2}; \qquad \tau_2^0 = \pm\frac{\sigma_1^0}{2}; \qquad \tau_3^0 = \pm\frac{\left(\sigma_1^0 - \sigma_2^0\right)}{2} \qquad (4.4)$$

and

$$\tau_{\max}^0 = \tau_3^0 = \pm\sqrt{\left(\frac{\sigma_x^0 - \sigma_y^0}{2}\right)^2 + \tau_{xy}^{0\,2}} \qquad (4.5)$$

The principal shearing stresses $\tau_{\max}^0$ act in the cross sections perpendicular to the midplane of the panel and build an angle of 45° with the planes of the principal normal stresses, $\varphi^{**} = \varphi^* \pm \dfrac{\pi}{4}$.

The plane stress state of the panel is described by:

$$\begin{bmatrix} \sigma_x^0 \\ \sigma_y^0 \\ \tau_{xy}^0 \end{bmatrix} = \frac{E}{1-v^2} \begin{bmatrix} 1 & v & 0 \\ v & 1 & 0 \\ 0 & 0 & \dfrac{1-v}{2} \end{bmatrix} \cdot \begin{bmatrix} \varepsilon_x^0 \\ \varepsilon_y^0 \\ \gamma_{xy}^0 \end{bmatrix} \qquad (4.6)$$

with G: shear modulus $G = \dfrac{E}{2 \cdot (1+v)}$

The strain can be determined from the displacements by derivation. For the panel the equations are:

$$
\begin{bmatrix} \varepsilon_x^0 \\ \varepsilon_y^0 \\ \gamma_{xy}^0 \end{bmatrix} = \begin{bmatrix} \dfrac{\partial}{\partial x} & 0 \\ 0 & \dfrac{\partial}{\partial y} \\ \dfrac{\partial}{\partial y} & \dfrac{\partial}{\partial x} \end{bmatrix} \cdot \begin{bmatrix} u \\ v \end{bmatrix}
\tag{4.7}
$$
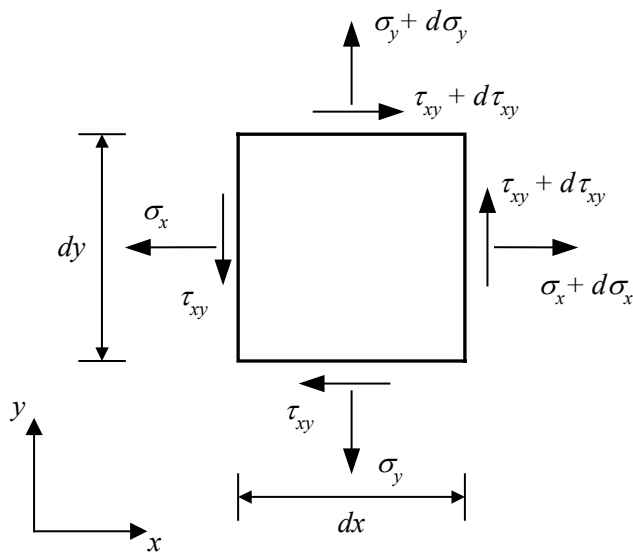
Figure 4.2   Conditions of equilibrium of a panel

The conditions of equilibrium can be represented as following (Figure 4.2):

$$
\Sigma X = 0: \quad \frac{\partial \sigma_x^0}{\partial x} + \frac{\partial \tau_{xy}^0}{\partial y} + \frac{p_x}{t} = 0
\tag{4.8}
$$

$$
\Sigma Y = 0: \quad \frac{\partial \sigma_y^0}{\partial y} + \frac{\partial \tau_{xy}^0}{\partial x} + \frac{p_y}{t} = 0
\tag{4.9}
$$

with: p_x: surface load in x-direction
      p_y: surface load in y-direction
      t: panel thickness

4.3 Panel with a Circular Hole

If a circular hole is made in the middle of the panel, the stress distribution in the neighbourhood of the hole will change. Instead of the basic stress state σ_x^0, σ_y^0 and τ_{xy}^0 of the panel without hole, a new stress distribution σ_x, σ_y and τ_{xy} is obtained.

The origin of the system of coordinates may be placed in the geometrical center of the hole. The new stress state σ_x, σ_y and τ_{xy} can be represented in the following form:

$$\sigma_x = \sigma_x^0 + \sigma_x^*$$
$$\sigma_y = \sigma_y^0 + \sigma_y^* \qquad (4.10)$$
$$\tau_{xy} = \tau_{xy}^0 + \tau_{xy}^*$$

σ_x^*, σ_y^* and τ_{xy}^* are the additional stress components which result from the existing hole [Savin 1956].

4.3.1 Uniaxial Compression or Tension

If a panel without a hole is submitted to a uniform tension of magnitude σ_1 in x-direction, the basic state of the panel is described with the following stress components:

$$\sigma_x^0 = \sigma_1 \cos^2 \theta$$
$$\sigma_y^0 = \sigma_1 \sin^2 \theta \qquad (4.11)$$
$$\tau_{xy}^0 = -\sigma_1 \sin \theta \cos \theta$$

At first, the infinite panel under uniform tensile stress σ_1 in x-direction, given in Figure 4.3, is taken into consideration.
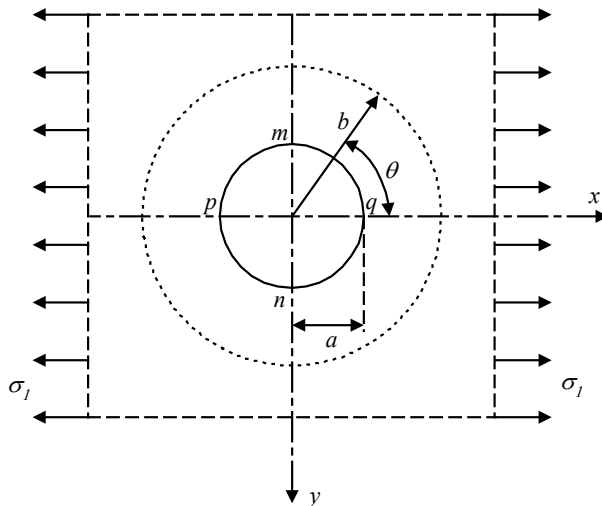
Figure 4.3 Infinite panel with a circular hole under uniform tensile stress σ_1 in x-direction

As shown in Figure 4.3, the panel is weakened by a hole with the radius a. At first, the portion of the panel within a concentric circle of radius b, large in comparison with a, is considered. The stresses at the radius b are effectively the same as in the panel without the hole and are therefore given by:

$$(\sigma_r)_{r=b} = \sigma_1 \cos^2 \theta = \frac{1}{2}\sigma_1(1 + \cos 2\theta)$$

$$(\tau_{r\theta})_{r=b} = -\sigma_1 \sin \theta \cos \theta = -\frac{1}{2}\sigma_1 \sin 2\theta$$

(4.12)

The forces acting around the outside of the ring, having the inner radii $r=a$ and $r=b$, give a stress function Φ of the form:

$$\Phi = f(r)\cos 2\theta$$

(4.13)

Substituting this into compatibility equation

$$\left(\frac{\partial^2}{\partial r^2} + \frac{1}{r}\frac{\partial}{\partial r} + \frac{1}{r^2}\frac{\partial^2}{\partial \theta^2}\right)\left(\frac{\partial^2 \Phi}{\partial r^2} + \frac{1}{r}\frac{\partial \Phi}{\partial r} + \frac{1}{r^2}\frac{\partial^2 \Phi}{\partial \theta^2}\right) = 0$$

(4.14)

the following differential equation to determine $f(r)$ will be found:

$$\left(\frac{d^2}{dr^2} + \frac{1}{r}\frac{d}{dr} - \frac{4}{r^2}\right)\left(\frac{d^2 f}{dr^2} + \frac{1}{r}\frac{df}{dr} - \frac{4f}{r^2}\right) = 0$$

(4.15)

The general solution is:

$$f(r) = Ar^2 + Br^4 + C\frac{1}{r^2} + D$$

(4.16)

The stress function is therefore:

$$\Phi = \left(Ar^2 + Br^4 + C\frac{1}{r^2} + D\right)\cos 2\theta$$

(4.17)

The corresponding stress components are:

$$\sigma_r = \frac{1}{r}\frac{\partial \Phi}{\partial r} + \frac{1}{r^2}\frac{\partial^2 \Phi}{\partial \theta^2} = -\left(2A + \frac{6C}{r^4} + \frac{4D}{r^2}\right)\cos 2\theta$$

$$\sigma_\theta = \frac{\partial^2 \Phi}{\partial r^2} = \left(2A + 12Br^2 + \frac{6C}{r^4}\right)\cos 2\theta \qquad\qquad (4.18)$$

$$\tau_{r\theta} = -\frac{\partial}{\partial r}\left(\frac{1}{r}\frac{\partial \Phi}{\partial \theta}\right) = \left(2A + 6Br^2 - \frac{6C}{r^4} - \frac{2D}{r^2}\right)\sin 2\theta$$

The constants of integration *A, B, C* and *D* are now to be determined from conditions (4.12) for the outer boundary and from the condition that the edge of the hole is free from external forces:

$$2A + \frac{6C}{b^4} + \frac{4D}{b^2} = -\frac{1}{2}\sigma_1$$

$$2A + \frac{6C}{a^4} + \frac{4D}{a^2} = 0$$

$$\qquad\qquad (4.19)$$

$$2A + 6Bb^2 - \frac{6C}{b^4} - \frac{2D}{b^2} = -\frac{1}{2}\sigma_1$$

$$2A + 6Ba^2 - \frac{6C}{a^4} - \frac{2D}{a^2} = 0$$

Assuming an infinitely large panel and putting $b \to \infty$, the equations (4.19) show these results:

$$A = -\frac{\sigma_1}{4} \qquad\qquad B = 0 \qquad\qquad C = -\frac{a^4}{4}\sigma_1 \qquad\qquad D = \frac{a^2}{2}\sigma_1$$

Putting these values in equations (4.18), the following equations are found:

$$\sigma_r = \frac{\sigma_1}{2}\left(1 - \frac{a^2}{r^2}\right) + \frac{\sigma_1}{2}\left(1 + \frac{3a^4}{r^4} - \frac{4a^2}{r^2}\right)\cos 2\theta$$

$$\sigma_\theta = \frac{\sigma_1}{2}\left(1 + \frac{a^2}{r^2}\right) - \frac{\sigma_1}{2}\left(1 + \frac{3a^4}{r^4}\right)\cos 2\theta \qquad\qquad (4.20)$$

$$\tau_{r\theta} = -\frac{\sigma_1}{2}\left(1 - \frac{3a^4}{r^4} + \frac{2a^2}{r^2}\right)\sin 2\theta$$

At the edge of the hole: $r = a$. This means $\sigma_r = \tau_{r\theta} = 0$ and $\sigma_\theta = \sigma_1 - 2\sigma_1 \cos 2\theta$.

The distribution of the stresses σ_θ (Figure 4.4) shows that the effect resulting from the hole is limited to a small area. The stress concentration can be found at the edge of the hole.
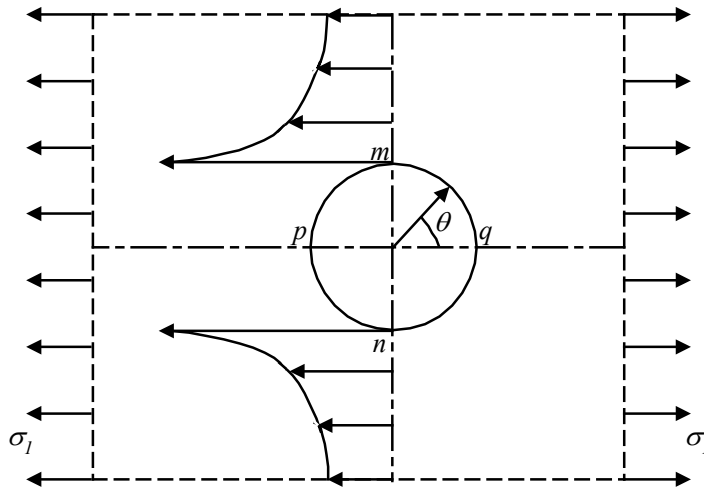
Figure 4.4 Distribution of σ_θ

It is easy to show that σ_θ is greatest when $\theta = \pm 90°$, i.e. at the ends m and n of the diameter perpendicular to the direction of the tension (Figure 4.4). At these points the maximum tensile stress is $\sigma_\theta \max = 3\sigma_1$ and it is three times the uniform stress σ_1. The compressive stress $\sigma_\theta = -\sigma_1$ is obtained at the points p and q ($\theta = 0°$ and $180°$). The corresponding stress distribution is shown in Figure 4.5
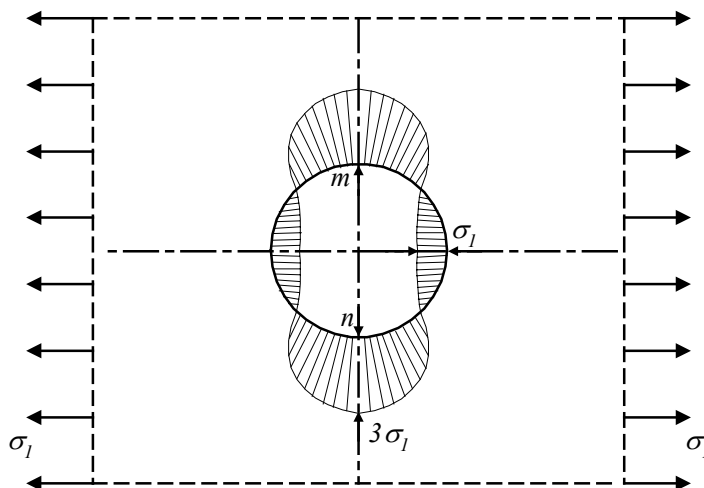
Figure 4.5 Stress distribution σ_θ at the hole edge

What is interesting is the deviation, which is caused by the hole, compared with the basic stress state without the hole. As a result the corresponding coefficient of stress concentration can be determined.

The stress concentration factor (SCF) is defined as the ratio of one component of the stress tensor at a certain point in the hole area and the same component of the stress tensor without the hole. As a result, in case of the plane stress state, three concentration factors exist in each point.

In the case $\theta = \pm\, 90°$, the result is $K = 3$. This is only valid, if the panel thickness is very thin compared to the hole radius. If the values of panel thickness and hole diameter are approximately of the same magnitude, then K is slightly greater than 3 in the midplane and on the surface of the panel K is slightly smaller than 3 [Flügge 1962], [Timoshenko, Goodier 1951].

4.3.2 Biaxial Stress State

If an infinite panel with a circular hole is submitted to a uniform tension of magnitude σ_l in x- and y-direction, the following tangential stresses result from equation (4.20) at the edge of the hole for $r = a$:

$$\sigma_\theta = \sigma_1 - 2\sigma_1 \cos 2\theta + \left(\sigma_1 - 2\sigma_1 \cos\left(2\theta - \pi\right)\right) \qquad (4.21)$$

With $r = a$ the result at the boundary is $\sigma_\theta = 2\sigma_1$, for all values of θ.

By taking a tensile stress σ_l in x-direction under and a compressive stress σ_l in y-direction, the case of pure shear is obtained and the tangential stresses σ_θ at the boundary of the hole are:

$$\sigma_\theta = \sigma_1 - 2\sigma_1 \cos 2\theta - \left(\sigma_1 - 2\sigma_1 \cos\left(2\theta - \pi\right)\right) \qquad (4.22)$$

For $\theta = 90°$ and $270°$, i.e., at the points m and n (see Figure 4.3), the maximum tensile stress $\sigma_\theta = 4\sigma_1$ occurs. For $\theta = 0°$ and $180°$, i.e., at the points p and q, the maximum compressive stress $\sigma_\theta = -4\sigma_1$ occurs.

4.3.3 Semi-Finite Panel with a Circular Hole

In the last sections the effects of a circular hole on the stress distribution of an infinite panel were examined. In the engineering practice it is not very common that holes are positioned in infinite areas. Like in many glass structures with in-plane loading (e.g. glass fins), the structures are planes with finite width. Therefore the question has to be proposed, in which cases the solution (dependent on the postulated precision) for an infinite panel can be applied for the finite panel.

That is why a direct comparison of the exact solutions for an infinite and a finite panel are necessary. This is impossible because an exact solution for the finite panel does not exist. In the following an approximate solution for the semi-finite panel with a finite width is explained.

A semi-finite panel with a finite width of *2b* and a thickness *t* is taken into consideration (see Figure 4.6). In *x*-direction a tensile force *p* (force per unit length) is applied.
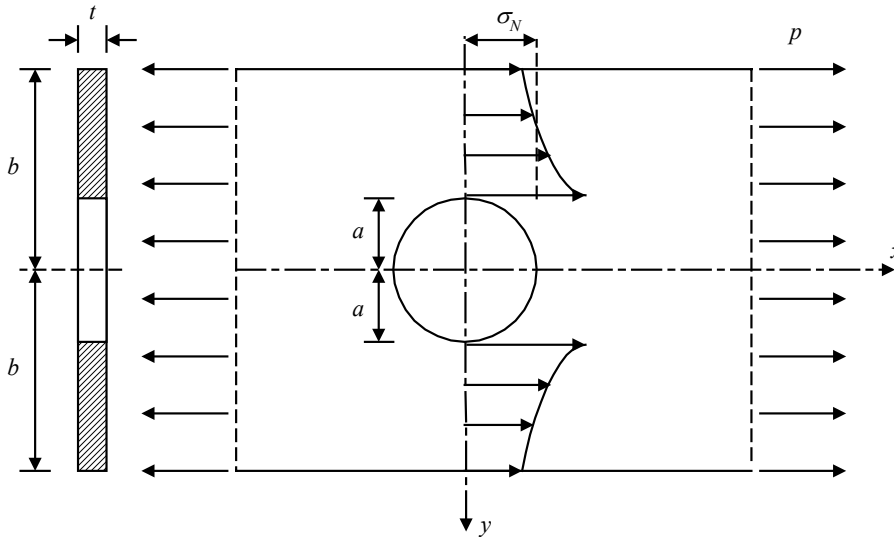
Figure 4.6 Panel with a width of *2b* and a hole of radius *a* under tensile stress

The nominal stress σ_N is defined as:

$$\sigma_N = \frac{p \cdot 2b}{2(b-a)t} \qquad (4.23)$$

As already shown, the stresses in the hole area are considerably higher than in the area without a hole and equation (4.23) there is not valid.

If $a \ll b$, equation (4.20) for the infinite panel can be used. In the case that *a* is only slightly smaller than *b*, [Peterson 1953] gives a formula which was developed by *Howland* and is now just rendered:

$$\sigma_\theta \max = K\sigma_N \qquad (4.24)$$

whereas the stress concentration factor *K* is

$$K = 3,00 - 3,13\left(\frac{a}{b}\right) + 3,66\left(\frac{a}{b}\right)^2 - 1,53\left(\frac{a}{b}\right)^3 .$$

In Figure 4.7 the stress concentration factors are indicated as a function of the ratio *a/b* for the semi-finite panel with a circular hole.
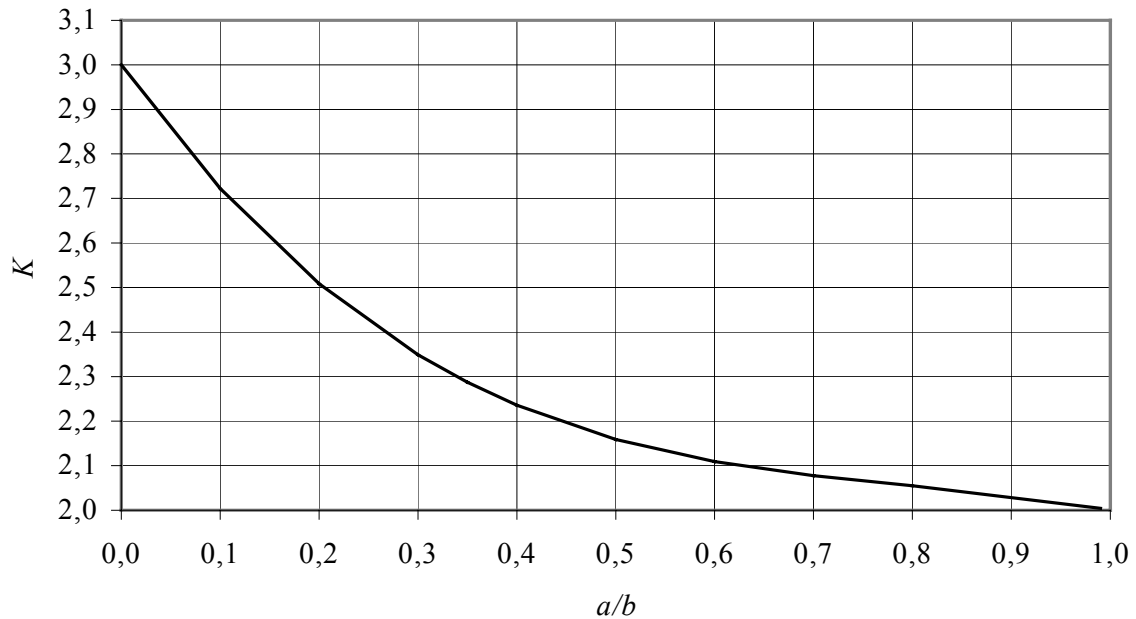
Figure 4.7   Stress concentration factors as a function of the ratio *a/b*

The curves in Figure 4.8 show a parameter study for different values of *b* as a function of the hole radius a, using equations (4.23) and (4.24). For the panel thickness $t = 10$ mm and for the load $P = 30$ kN are chosen constantly.
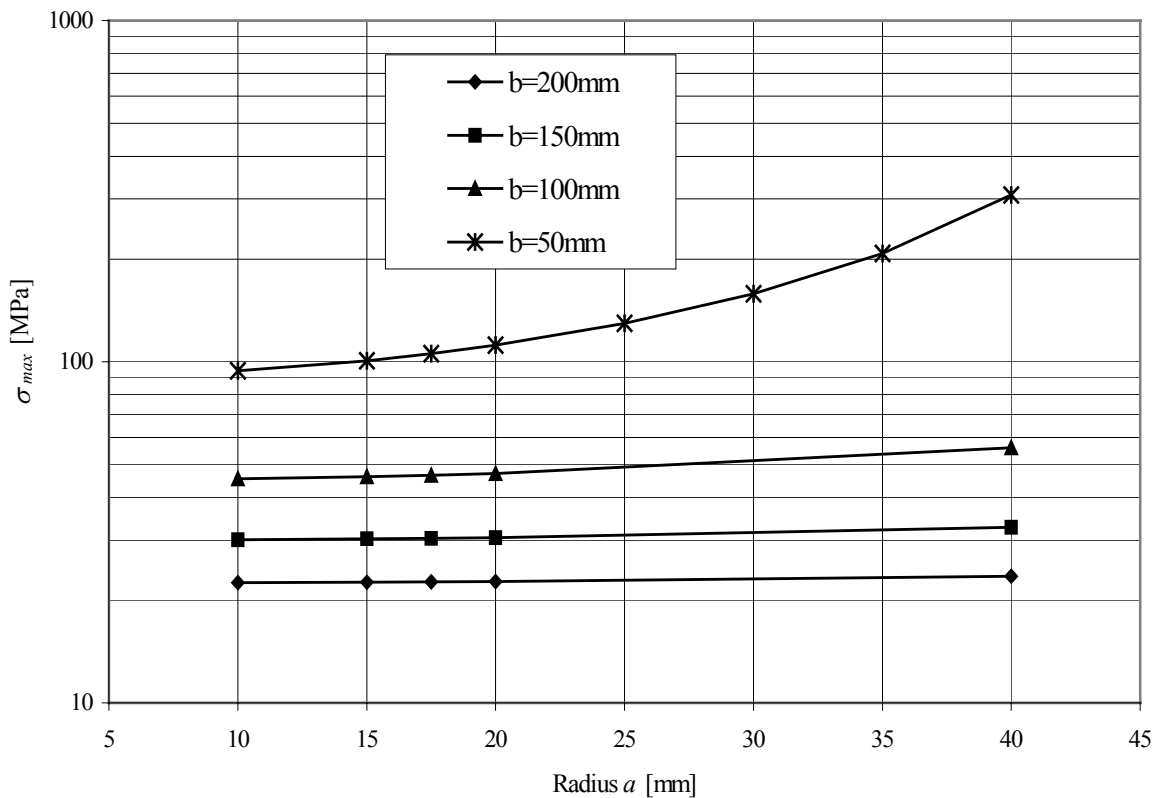
Figure 4.8   Maximum tensile stresses at the boundary of the hole as a function of radius *a* and semi-width *b*

As it can be seen in Figure 4.8, the stresses σ_θ increase at the boundary of the hole with an increasing radius a. The stresses also increase with a decreasing panel width. A comparison between Figure 4.7 and Figure 4.8 shows that with an increasing ratio a/b the stress concentration factor decreases indeed, but the nominal stress and the maximum stress at the edge of the hole increase.

Figure 4.9 shows a comparison of the maximum tensile stresses at the boundary of the hole for the infinite ($\sigma_\theta\,\mathrm{max} = 3\sigma_N$) and the finite panel. The diagram indicates that with a decreasing ratio a/b and increasing panel width the stress values of the semi-finite panel approach asymptotically to the stress values of the infinite panel. With a panel width of 400 mm or 300 mm and a ratio $a/b = 0,1$ the values conform to each other.
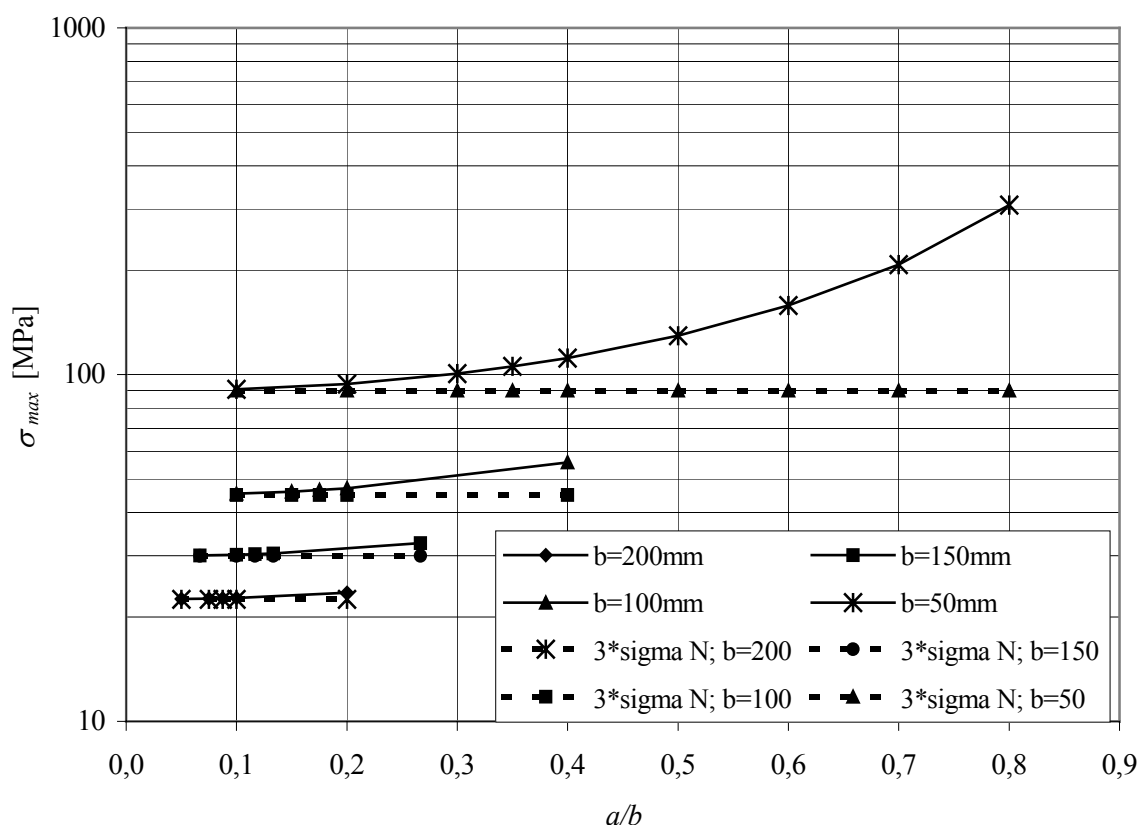
Figure 4.9   Maximum tensile stresses at the boundary of the hole as a function of ratio a/b

If the hole is not situated symmetrically in the center of the panel strip, [Peterson 1953] gives the following stress concentration factor K, according to *Sjöström*:

$$K = 3,00 - 3,13\left(\frac{a}{c}\right) + 3,66\left(\frac{a}{c}\right)^2 - 1,53\left(\frac{a}{c}\right)^3 .$$

c is defined as the shorter distance between panel edge and hole center.

The nominal stress σ_N is determined with:

$$\sigma_N = \frac{P}{2bt} \frac{\sqrt{1-\left(\dfrac{a}{c}\right)^2}}{1-\left(\dfrac{a}{c}\right)} \frac{1-\left(\dfrac{c}{2b}\right)}{1-\left(\dfrac{c}{2b}\right)\left(2-\sqrt{1-\left(\dfrac{a}{c}\right)^2}\right)}$$

(4.25)

5 Analytical Definition of the Contact Problem

5.1 Introduction

Contact mechanics describes the stress state of two elastic bodies in contact. The first satisfactory analysis of the contact of two elastic solids (elastic half spaces) was developed by *Heinrich Hertz* in 1882 [Hertz 1882]. Until today extensive development of this theory is taking place.

Referring to the geometry of contact bodies, the loading and the kinematics (static, sliding, rolling), the geometry of the contact area and its stress distribution is being calculated. The contact stresses consist of a normal and a tangential part. Closed solutions are available only for simple cases.

In this chapter the theory according to *Hertz* will be explained at first. Afterwards the question will be examined in which cases this theory is suitable for bolted connections under the application of in-plane loads.

5.2 Hertz Theory

5.2.1 Basic Equations

If two elastic bodies which have opposite surface curvatures in the contact area are brought into contact at a single point O, they have a common tangent plane and a common normal (see Figure 5.1).

If collinear forces are now applied so as to press the two bodies together, deformation takes place and with ascending forces the contact area increases and will replace the contact point of the unloaded state.
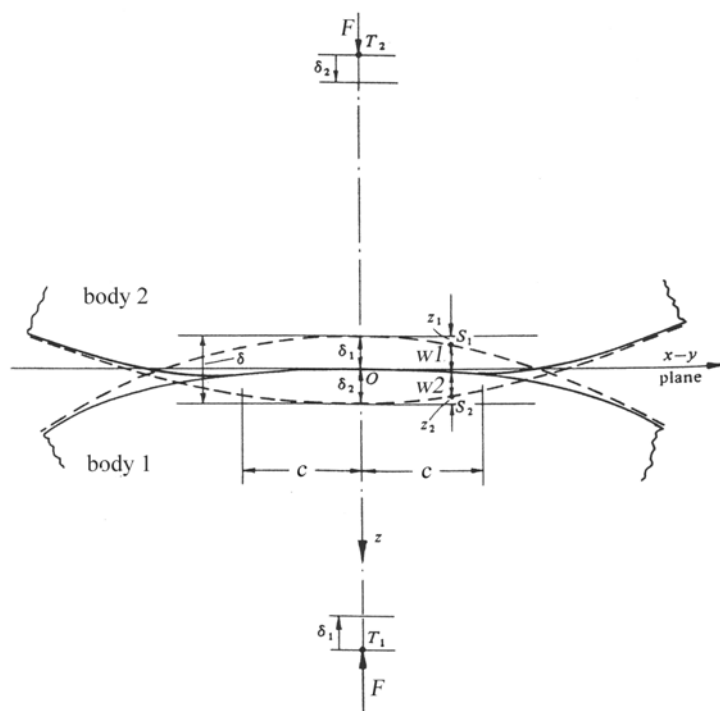
Figure 5.1   Contact between two elastic solids

The first step is to find the size and shape of this contact area and the distribution of normal pressure arising on it. Having investigated these, the stresses and deformations can be calculated.

Hertz starts by assuming that the contacting bodies are isotropic linear elastic and the dimensions of the contact area are very small compared to the various radii of curvature of the undeformed bodies. This leads to a further assumption: The shape of the two touching bodies close to the zone of contact can be described almost perfectly accurate by polynomials of second order:

$$z_i = A_i x^2 + B_i y^2 + H_i xy \tag{5.1}$$

with $i = 1, 2$ for body 1 and 2.

The Cartesian coordinates x and y are lying in the common tangent. Finally, he assumes that the two bodies are perfectly smooth which means that only the normal pressures, which arise during the contact, are taken into consideration. Relative displacements in the plane of x and y and any shearing tractions, which might arise from there, are neglected as effects of higher order.

The separation between the two bodies is given by $h = z_1 + z_2$ (see Figure 5.1). With equation (5.1) it follows

$$h = z_1 + z_2 = Ax^2 + By^2 + Hxy \tag{5.2}$$

z_1 and z_2, can be represented with sufficient accuracy by the following equations (5.3). It is assumed that the distance to the z_1- and z_2-axis is very small.

$$
\begin{aligned}
z_1 &= \frac{1}{2R_1} x_1^{\,2} + \frac{1}{2R_1'} y_1^{\,2} \\
z_2 &= \frac{1}{2R_2} x_2^{\,2} + \frac{1}{2R_2'} y_2^{\,2}
\end{aligned}
\tag{5.3}
$$

R_i, R_i' with $i=1,2$, are the principal radii of curvature of the bodies in the origin.

The axis of each body can be chosen in a way that the term containing the term xy disappears. The distance h of two points S_1 and S_2 is then:

$$h = Ax^2 + By^2 = z_1 + z_2 = \frac{1}{2R} x^2 + \frac{1}{2R'} y^2 \tag{5.4}$$

A und *B* are positive constants. *R* and *R'* are defined as the principal relative radii of curvature. In equation (5.4) it can be shown that all points with the same distance *h* lie on one ellipse. If the bodies are pressed together, the surface of contact will have an elliptical boundary. As a result the general form of the contact area is an ellipse.

If the axis of principal relative radii of curvature *R* and *R'* of each surface, i.e. the x_1- and the x_2-axis, are inclined to each other by an angle α, then equation (5.5) is valid [Timoshenko, Goodier 1951]:

$$A + B = \frac{1}{2}\left(\frac{1}{R} + \frac{1}{R'}\right) = \frac{1}{2}\left(\frac{1}{R_1} + \frac{1}{R_1'} + \frac{1}{R_2} + \frac{1}{R_2'}\right)$$

$$B - A = \frac{1}{2}\left\{\left(\frac{1}{R_1} - \frac{1}{R_1'}\right)^2 + \left(\frac{1}{R_2} - \frac{1}{R_2'}\right)^2 + 2\left(\frac{1}{R_1} - \frac{1}{R_1'}\right)\left(\frac{1}{R_2} - \frac{1}{R_2'}\right)\cos 2\alpha\right\}^{\frac{1}{2}}$$

$$\text{(5.5)}$$

In equation (5.5) convex relative radii of curvature have a positive radius. Equation (5.5) equally applies to concave surfaces by ascribing a negative sign to the concave curvatures.

Before a load *F* is applied on the two bodies, the distance *h* of two points lying on the surfaces of the bodies, such as S_1 *(x,y,z₁)* and S_2 *(x,y,z₂)*, is given by equation (5.4). If the two bodies are pressed together, they move towards *O*, parallel to the *z*-axis and the points T_1 and T_2 are moving towards each other by displacement of δ_1 and δ_2. Due to the contact pressure the surface of each body is displaced by an amount of w_1 and w_2 (measured positive into each body) relative to the distant points T_1 and T_2 (see Figure 5.1).

If, after deformation, the points S_1 and S_2 are coincident within the contact area then

$$w_1 + w_2 + h = \delta \qquad\qquad (5.6)$$

with $\delta = \delta_1 + \delta_2$.

Making use of equation (5.4) and (5.6) follows for the elastic displacement:

$$w_1 + w_2 = \delta - Ax^2 - By^2 \qquad\qquad (5.7)$$

If the points S_1 and S_2 lie outside the contact area so that they do not touch each other, the result is:

$$w_1 + w_2 > \delta - Ax^2 - By^2 \qquad\qquad (5.8)$$

where *x* and *y* are the common coordinates of S_1 and S_2 projected onto the *x-y*-plane.

According to [Timoshenko, Goodier 1951] the sum of the displacements w_1 and w_2 for points of the surface of contact is:

$$w_1 + w_2 = \left(\frac{1 - v_1^2}{\pi E_1} + \frac{1 - v_2^2}{\pi E_2} \right) \iint \frac{pdA}{r} = \delta - Ax^2 - By^2 \qquad (5.9)$$

with E_i $i=1,2$; Young's modulus of the bodies

$\quad$ v_i $i=1,2$: Poisson's ratio of the bodies

Where pdA is the pressure acting on an infinitely small element of the surface of contact, r is the distance of this element to the point under consideration. The integration must be extended over the whole contact surface. The problem is to find a distribution of pressure p, which satisfies equation (5.9). As already mentioned, *Hertz* showed that this condition will be satisfied if the stress distribution p of the contact area is represented by an ellipse with the semi-axes j and k. The maximum pressure p_0 then appears in the center of the contact surface.

The contact load F is calculated by:

$$F = \iint pdA = \frac{2}{3} \pi jkp_0$$
$$p_0 = \frac{3}{2} \frac{F}{\pi jk} \qquad (5.10)$$

To calculate the contact pressure p_0, the values of the semi-axes j and k must be known.

Knowing the stress distribution p, at any point of the contact surface the contact pressure can be calculated. If the semi-axes j and k are defined in x- and y-direction, then the stresses are:

$$p(x,y) = p_0 \left(1 - \left(\frac{x}{j} \right)^2 - \left(\frac{y}{k} \right)^2 \right)^{\frac{1}{2}} \qquad (5.11)$$

There are only compressive stresses due to this stress function within the contact area inside the two bodies. At the boundary of the contact surface there are tensile stresses, with a maximum magnitude.

The stresses within the bodies can be calculated in the origin O (center of the contact surface) by the following equation:

$$\sigma_x = -p_0\left(2v + \frac{(1-2v)k}{(j+k)}\right)$$

$$\sigma_y = -p_0\left(2v + \frac{(1-2v)j}{(j+k)}\right) \qquad (5.12)$$

$$\sigma_z = -p_0$$

with $j > k$.

At the boundary of the contact area, at the ends of the semi-axes j and k, the compressive and the tensile stresses are of the same magnitude in radial and tangential direction. At the point $x = \pm j, y = 0$ the result is:

$$\sigma_x = -\sigma_y = p_0(1-2v)\frac{k}{je^2}\left(\frac{1}{e}\tanh^{-1}e - 1\right) \qquad (5.13)$$

and at the point $x = 0, y = \pm k$

$$\sigma_y = -\sigma_x = p_0(1-2v)\frac{k}{je^2}\left(1 - \frac{k}{je}\tan^{-1}e\left(\frac{ej}{k}\right)\right)$$

where $e = \frac{1}{j}(j^2 - k^2)^{\frac{1}{2}}$

By increasing the ratio j/k, the elliptical shape of the contact surface is getting more narrow and in case of $j/k \to \infty$ two cylinders with parallel axis arise. The contact area has now a rectangular shape.

5.2.2 Two-Dimensional Contact of Cylindrical Bodies

When two cylindrical bodies, with their axes lying parallel to the y-axis are brought into contact by a load F^* (load per unit length), the problem is two-dimensional. The shape of the contact area is then a long strip of width $2\overline{b}$ lying parallel to the y-axis.

When equation (5.5) is now used for cylindrical bodies, with $R_1' = \infty$, $R_2' = \infty$ and $\alpha = 0°$ the constants are: $A = \frac{1}{2}\left(\frac{1}{R_1} + \frac{1}{R_2}\right)$ and $B = 0$.

For cylindrical bodies equation (5.4) is simplified to

$$h = z_1 + z_2 = Ax^2 = \frac{1}{2}\left(\frac{1}{R_1} + \frac{1}{R_2}\right)x^2 \qquad (5.14)$$

The sum of the displacements w_1 and w_2 for points of the surface of contact is:

$$w_1 + w_2 = \delta - Ax^2 = \delta - \frac{1}{2}\left(\frac{1}{R}\right)x^2 \qquad (5.15)$$

where $\dfrac{1}{R} = \dfrac{1}{R_1} + \dfrac{1}{R_2}$.

According to the *Hertz* approximation, the displacements w_1 and w_2 can be calculated by considering the bodies elastic half spaces. In case of two cylindrical bodies no solution in closed form is available. Indeed, for a cylinder with the length L and a cylindrical half space (see Figure 5.2), the contact pressure $p(x)$ can be determined by a satisfying approximation [Johnson 1996].

The load F^*, the contact pressure p_0, and the semi-width $\bar{b}$ of the contact surface can be calculated with the following equations:

$$F^* = \frac{1}{2}\pi \bar{b} p_0$$

$$p_0 = \frac{2F^*}{\pi \bar{b}} \qquad (5.16)$$

$$\bar{b} = \left(\frac{4F^*\left(\left(\frac{1-v_1^2}{\pi E_1}\right) + \left(\frac{1-v_2^2}{\pi E_2}\right)\right)R_1 R_2}{\left(R_1 + R_2\right)}\right)^{\frac{1}{2}}$$

The distribution of the contact compressive stress $p(x)$ is

$$p(x) = \frac{2F^*}{\pi \bar{b}^2}\left(\bar{b}^2 - x^2\right)^{\frac{1}{2}} \qquad (5.17)$$

At the boundary of the contact area the function $p(x)$ is zero. Within the contact area $\sigma_x = \sigma_y = -p(x)$.

In a different notation [Young 1989] also determines the maximum contact pressure p_0 for a cylinder with the length L and a cylindrical half space with approximately:

$$p_0 \approx 0,798 \sqrt{\dfrac{F^*}{\left(\dfrac{D_1 D_2}{D_1 - D_2}\right)\left(\dfrac{1-v_1^2}{E_1} + \dfrac{1-v_2^2}{E_2}\right)}} \qquad (5.18)$$

Where F^* is the load per unit length, $F^* = \dfrac{F}{L}$.

The formula for the width $2\bar{b}$ of the contact area is:

$$2\bar{b} \approx 1,6 \sqrt{F^*\left(\dfrac{D_1 D_2}{D_1 - D_2}\right)\left(\dfrac{1-v_1^2}{E_1} + \dfrac{1-v_2^2}{E_2}\right)} \qquad (5.19)$$
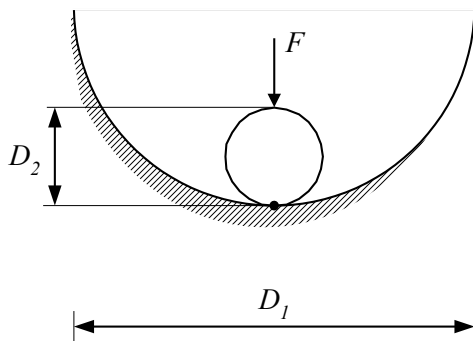
Figure 5.2   Cylinder in a cylindrical half space according to [Young 1989]

The equations (5.16) to (5.19) are based on the *Hertz* theory (linear elastic material behaviour, absence of friction) and are valid only if the length L of the cylinder is significant bigger than the diameter D_2 of the cylindrical body.

Taking equation (5.18) Figure 5.3 shows the maximum contact pressure p_0 as a function of $\varDelta D$ for exemplary values, where $\varDelta D = D_1 - D_2$. With growing $\varDelta D$ the stresses approach the values of contact between cylinder and plane. As it can be seen from equation (5.19), with growing $\varDelta D$ the contact width $2\bar{b}$ is getting smaller and therefore the contact pressure p_0 is getting bigger.
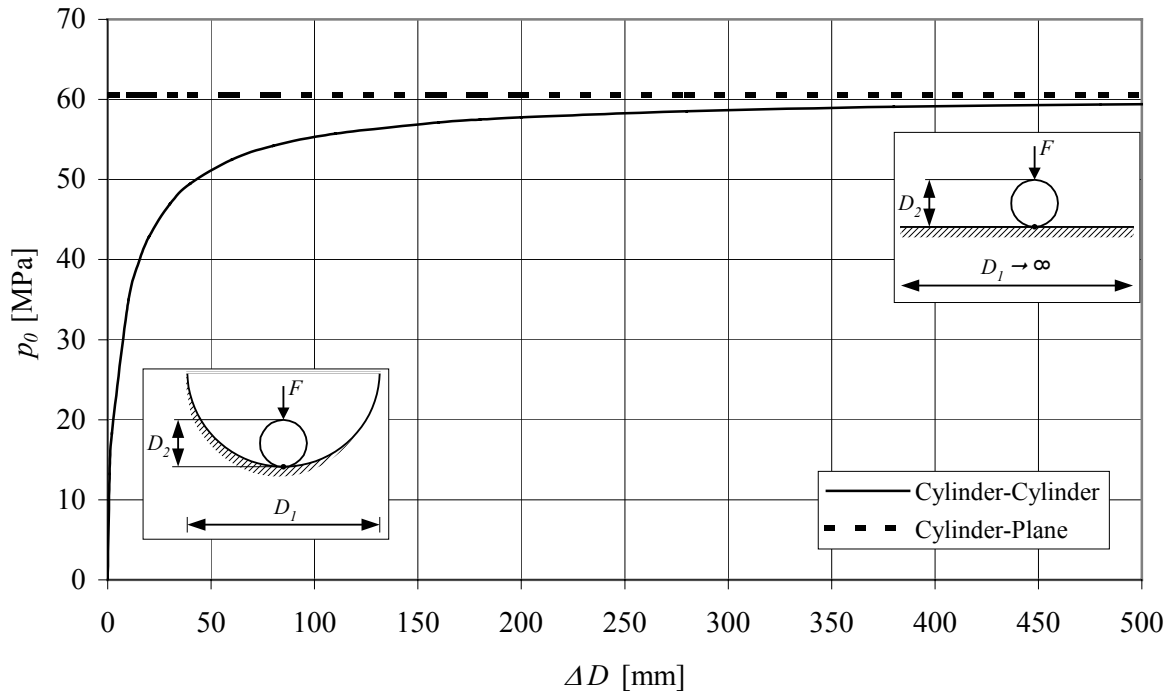
Figure 5.3   Maximum compressive stress p_0 as a function of ΔD

5.3   "Non-Hertzian" Normal Contact of Elastic Bodies

5.3.1 Introduction

Further analytical approaches have to be applied to find appropriate stress distributions for both bolt and panel with a conforming hole:

As already explained in the previous chapter, the mentioned equations are valid only if the cylindrical bodies are of a certain length L. This means that the approach is not valid for a thin glass panel with a bolt of approximately the same length than the glass thickness. Furthermore, *Hertz* assumed that the two bodies in contact are elastic half-spaces and the contact area is small compared to the dimensions of each body and to the relative radii of curvature of the surfaces. With this simplification he put forward the hypotheses that the contact area is elliptical and can therefore be described by a polynomial of second order. In addition the surfaces are assumed to be frictionless so that only a normal pressure is transmitted between them. Relative displacements in the *x-y*-plane and possible resultant tangential forces are neglected. This approximation is complied as long as the radii of curvature of the bodies are appreciable bigger than the size of the contact area. If the contacting bodies have approximately similar surface geometries (bolt in a hole) under the application of load, the size of the contact area grows rapidly and the arc of contact occupies a main part of the circumference of the hole. Therefore, *Hertz's* treatment is invalid.

5.3.2 Contact between Bolt and Conforming Hole in an Infinite Panel

Under the application of load, the size of contact area grows rapidly and the arc of contact occupies a main part of the circumference of the hole. When the "contact arc" subtends an angle α which is not small, neither the bolt nor the hole can be assumed as elastic half spaces. The geometry for a bolt (body 1) in a conforming hole of an infinite panel (body 2) is shown in Figure 5.4.
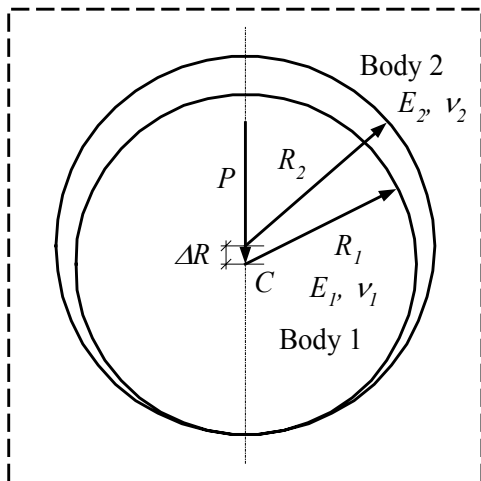
Figure 5.4 Bolt in a conforming hole   **Figure 5.5** Deformation in the contact area
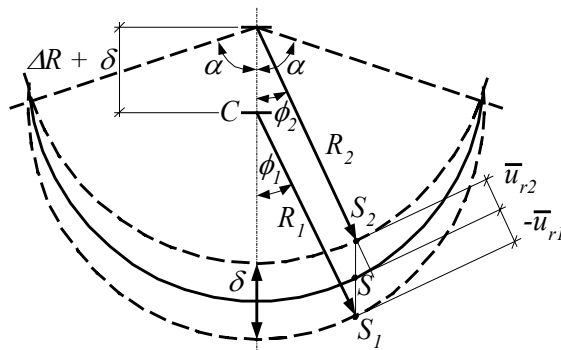
It is assumed that the difference in radii $\Delta R = R_2 - R_1$ is small compared to either R_1 or R_2. The external load P is applied to the bolt on its center C. The deformation is represented in Figure 5.5. The points S_1 and S_2 on the surfaces which come into contact on the interface at S, experience both radial and tangential displacements $\overline{u}_{ri}$ and $\overline{v}_{\theta i}$, where $i = 1, 2$.

Since ΔR and δ are both small compared to R_1 und R_2 and $\phi_1 = \phi_2 = \phi$, the result is:

$$\left(R_2 + \overline{u}_{r2}\right) - \left(R_1 + \overline{u}_{r1}\right) = \left(\Delta R + \delta\right)\cos\phi$$
$$\overline{u}_{r2} - \overline{u}_{r1} = \delta\cos\phi + \Delta R(\cos\phi - 1)$$

(5.20)

Analogous to the examined cases, the size of the "contact arcs" and the stress distribution along these arcs must be determined. The problem is now to find the stress distribution and the deformations of both bodies. Additionally, the relationship between the contact compressive stress $p_r(\phi)$, the angle ϕ and the displacement δ have to be derived.

Finding an appropriate analytical function for the contact stress distribution has been treated mathematically by many authors. The most precise analytical approximate solution is obtained for a linear-elastic connection in an infinite panel, whereas bolt and panel consist of identical materials and the contact is assumed to be frictionless.

[Girkmann 1963] for example based his work on investigations made by [Bickley 1928], assuming that both bolt and hole are of the same linear elastic material, that there is no clearance between bolt and hole ($R_1 \approx R_2$) and that the bolt fits in the hole (neat-fit condition), i.e. $\alpha = \pi$.

More comprehensive investigations where made by [Edwards 1951], [Noble, Hussain 1969], [Persson 1964] or [Gladwell 1980] examining different material properties of bolt and panel.

Within this thesis the investigations of [Persson 1964] are examined in particular, because they include the deformation conditions in the contact area between panel and bolt. The following equations are based on the assumption that only in-plane stresses result and that the surfaces are frictionless. *Persson's* approach is valid if there is clearance between bolt and hole $R_1 < R_2$ and if the bolt fits in the hole ($R_1 \approx R_2$). His calculations for the "neat-fit" condition agree with the investigations of *Girkmann*.
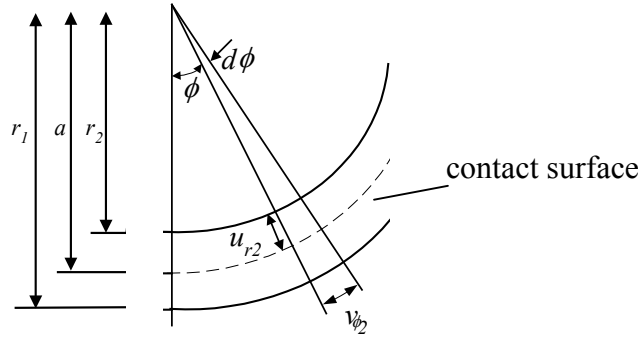
Figure 5.6   Contact of two elastic bodies

When the bodies are brought in contact

$$r = aF(\phi) \tag{5.21}$$

and according to Figure 5.6 follows the equation

$$r_2 + \overline{u}_{2r} = aF(\phi + d\phi) \approx aF(\phi + \frac{v_{\phi 2}}{r}) \tag{5.22}$$

If a *Taylor*-series is applied on the function $F(\phi)$, equation (5.22) becomes

$$\overline{u}_{2r} = aF(\phi) - r_2 F_2(\phi) + F'(\phi)\frac{av_{\phi 2}}{r} + \frac{F''(\phi)}{2!}\frac{av_{\phi 2}^2}{r^2} + \dots \tag{5.23}$$

If $F(\phi)=const=C_0$, i.e. the contact area is part of a cylinder, then $F'(\phi) = F''(\phi) = \dots = 0$ follows.

The result of the stress equation of the panel are the following expressions:

$$\int_0^a \varepsilon_{1r}dr = \int_0^a \frac{\partial u_{1r}}{\partial r}dr = \bar{u}_{1r}$$

$$\int_a^\infty \varepsilon_{2r}dr = \int_a^\infty \frac{\partial u_{2r}}{\partial r}dr = -\bar{u}_{2r}$$

(5.24)

where $R_1 \approx R_2 = a$ and $(u_{1r})_{r=0} = (u_{2r})_{r=\infty} = 0$, which is an arbitrary choice.

Thus from equation (5.20) and (5.24) the condition of deformation at all points on the surface of contact becomes

$$\bar{u}_{r2} - \bar{u}_{r1} = \delta \cos\phi + \Delta R(\cos\phi - 1) = -\int_0^a \varepsilon_{1r}dr - \int_a^\infty \varepsilon_{2r}dr$$

(5.25)

The contact pressure $p_r(\phi) = -\sigma_r(a,\phi)$ is distributed over the contact surface. If $r=a$, the boundary conditions required for the two bodies are:

$$\sigma_r = 0 \qquad\qquad \alpha \le |\psi| \le \pi$$

$$\sigma_r = -p_r(\psi) \qquad\qquad -\alpha \le \psi \le \alpha$$

$$\tau = 0$$

where (a,ψ) is a point on one of the boundaries. Thus for the inner body 1 (bolt)

$$\sigma_{r1} + \sigma_{\phi 1} = -2\int_{-\alpha}^\alpha p_r(\psi)Qd\psi + \frac{1+\nu_1}{2\pi}\frac{P}{r}\left(2\frac{r^2}{a^2} - 1\right)\cos\phi$$

$$\sigma_{r1} = -\int_{-\alpha}^\alpha p_r(\psi)Sd\psi - \frac{1+\nu_1}{4\pi}\frac{P}{r}\left(1 - \frac{r^2}{a^2}\right)\cos\phi$$

(5.26)

$$\tau_{r\phi 1} = -\int_{-\alpha}^\alpha p_r(\psi)Td\psi - \frac{1+\nu_1}{4\pi}\frac{P}{r}\left(1 - \frac{r^2}{a^2}\right)\sin\phi$$

where $0 \le r < a$

and for the outer body 2 (panel)

$$\sigma_{r2} + \sigma_{\phi2} = \frac{1}{\pi} \int\limits_{-\alpha}^{\alpha} p_r(\psi) d\psi + 2 \int\limits_{-\alpha}^{\alpha} p_r(\psi) Q d\psi + \frac{3-v_2}{2\pi} \frac{P}{r} \cos\phi$$

$$\sigma_{r2} = \frac{r^2 - a^2}{2\pi r^2} \int\limits_{-\alpha}^{\alpha} p_r(\psi) d\psi + \int\limits_{-\alpha}^{\alpha} p_r(\psi) S d\psi + \frac{3-v_2}{4\pi} \frac{P}{r} \left(1 - \frac{a^2}{r^2}\right) \cos\phi \qquad (5.27)$$

$$\tau_{r\phi2} = \int\limits_{-\alpha}^{\alpha} p_r(\psi) T d\psi + \frac{3-v_2}{4\pi} \frac{P}{r} \left(1 - \frac{a^2}{r^2}\right) \sin\phi$$

where $a < r < \infty$

and P load per unit thickness.

The appropriate condition of equilibrium is:

$$a \int\limits_{-\alpha}^{\alpha} p_r(\psi) \cos\psi d\psi = P$$

$$a \int\limits_{-\alpha}^{\alpha} p_r(\psi) \sin\psi d\psi = 0$$

$$(5.28)$$

The functions Q, S and T are determined as follows:

$$2\pi Q = \frac{a^2 - r^2}{a^2 + r^2 - 2\arccos\vartheta}$$

$$2\pi S = \frac{\left(a^2 - r^2\right)^2}{r} \frac{a\cos\vartheta - r}{\left(a^2 + r^2 - 2\arccos\vartheta\right)^2} \qquad (5.29)$$

$$2\pi T = \frac{a\left(a^2 - r^2\right)^2}{r} \frac{\sin\vartheta}{\left(a^2 + r^2 - 2\arccos\vartheta\right)^2}$$

where $\vartheta = \psi - \phi$.

To get the relationship between the load P, the radial difference ΔR and the dedicated angle α, the contact pressure has to be transformed and then denoted as $q(y)$. Hereby, a comparison according to *Hertz's* theory is possible.

At first the following new and dimensionless quantities are introduced:

$$y = \tan\frac{\phi}{2}; \qquad t = \tan\frac{\psi}{2}; \qquad b = \tan\frac{\alpha}{2}$$

$$q(y) = \frac{ap_r(\phi)}{P}$$

$$n = \frac{E_1}{E_2}$$

$$\lambda = 1 - v_1 - n(1 - v_2); \quad k = \frac{\pi}{2}\frac{2(1+n)-\lambda}{1+n}$$

(5.30)

α is the semi-angle of the contact segment. After executing some calculations the integral equation will become:

$$\int_{-b}^{b} q'(t)\left(\frac{1+y^2}{t-y}+y\right)dt + \frac{\lambda\pi}{1+n}q(y) = -\frac{4k}{\pi}\frac{1}{1+y^2}+B$$

(5.31)

for $-b < y < b$

where $B = \dfrac{2k}{\pi} - \dfrac{2n}{1+n}\displaystyle\int_{-b}^{b} q(t)\dfrac{dt}{1+t^2} - \dfrac{\pi E_1 \Delta R}{P(1+n)}$

As a result $q(t)=q(-t)$ and $q'(t)=-q'(-t)$. Thus $\displaystyle\int_{-b}^{b} q'(t)dt = 0$ and equation (5.31) becomes

$$\int_{-b}^{b}\frac{q'(t)}{t-y}dt + \frac{\lambda\pi}{1+n}q(y)+\frac{1}{1+y^2} = -\frac{4k}{\pi}\frac{1}{\left(1+y^2\right)^2}+\frac{B}{1+y^2}$$

(5.32)

for $-b < y < b$

after using the substitution, equations (5.30) and equations (5.28), it follows

$$\int_{-b}^{b} q(t)\frac{1-t^2}{\left(1+t^2\right)^2}dt = \frac{1}{2}.$$

(5.33)

Now, the unknown contact pressure function $q(y)$ can be calculated using the solution of equation (5.32) and the condition (5.33). Accordingly to this solution, the parameters $q(y)$ und b result. Using equation (5.31) the relationship between the load P, the radial difference ΔR and the parameter b is determined.

At first, the approach for the case $E_1 = E_2$ or $\nu_1 = \nu_2$ is examined, i.e. both bodies have the same material properties. A solution in closed form is possible here.

Substituting these conditions in the equations (5.30) and in the equations (5.31), (5.32) and (5.33), the dimensionless compressive stress function in the contact area results in:

$$q(y) = \frac{ap_r(\phi)}{P} = \frac{2}{\pi\sqrt{b^2+1}}\frac{\sqrt{b^2-y^2}}{1+y^2} + \frac{1}{2\pi b^2(1+b^2)}\ln\frac{\sqrt{b^2+1}+\sqrt{b^2-y^2}}{\sqrt{b^2+1}-\sqrt{b^2-y^2}} \qquad (5.34)$$

The relationship between the load P, the radial difference ΔR and the parameter b is determined as follows:

$$\frac{E\Delta R}{P} = \frac{2}{\pi}\frac{1-b^2}{b^2} - \frac{I}{\pi^2 b^2\left(1+b^2\right)} \qquad (5.35)$$

where $I = \displaystyle\int_{-b}^{b} \ln\frac{\sqrt{b^2+1}+\sqrt{b^2-t^2}}{\sqrt{b^2+1}-\sqrt{b^2-t^2}}\frac{dt}{1+t^2}$

Using equation (5.34) and $\phi = 0 = y = 0$ it is possible to calculate the dimensionless maximum contact compressive stress q_{max}:

$$q_{\max} = \frac{ap_r(\phi = 0)}{P} = \frac{2|b|}{\pi\sqrt{b^2+1}} + \frac{\ln\left(\sqrt{b^2+1}+|b|\right)}{\pi b^2\left(1+b^2\right)} \qquad (5.36)$$

The stress in any point of the two bodies can be determined by the equations (5.26) and (5.27).

According to [Ciavarella, Decuzzi 2001a, b] the following closed form solution is available for the tangential stresses $\sigma_\phi = p_\phi(\phi)$ on the contact surface of the panel (body 2):

$$\sigma_\phi = p_\phi(\phi) = \frac{P}{a}\left(-q(y) + \frac{3-\nu_2}{2\pi}\cos\phi + \frac{\ln(b^2+1)+2b^4}{\pi b^2(b^2+1)}\right) \qquad (5.37)$$

If the stress function is known, with the strains and, by integration, the displacements can be determined (see equation (5.24)).

Figure 5.7 shows the stress function $p_r(\phi)$ in dimensionless form, i.e. according to equation (5.34), for different contact angles α, where $R_1 \approx R_2 \approx a$. By increasing the contact angle α the distribution of the radial stresses is getting more regular. The maximum contact stress constantly arises at an angle of 0°.
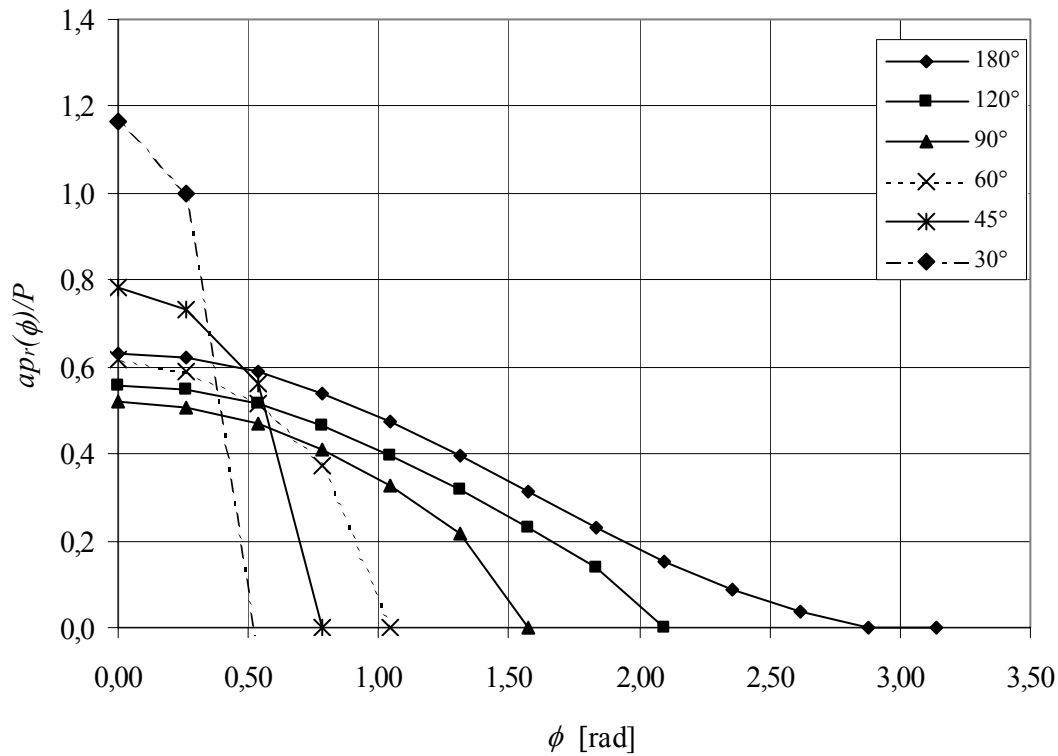
Figure 5.7 Dimensionless radial stress function for different contact angles α

By means of equation (5.36) Figure 5.8 contains the dimensionless contact compressive stress $q_{\max} = \dfrac{ap_r(\phi = 0)}{P}$ as a function of $b = \tan\dfrac{\alpha}{2}$. Where $r = a$ and $\phi = 0 = y = 0$. Figure 5.8 also contains a comparison with the approach according to *Hertz* (see chapter 5.2.2).
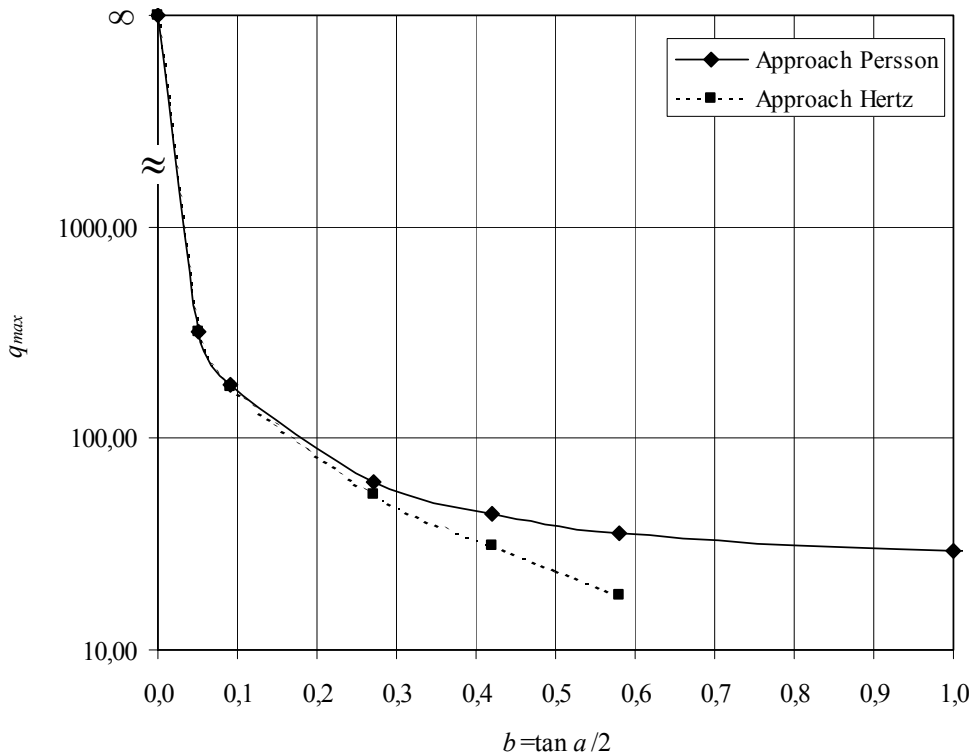
Figure 5.8   Comparison with the approach according to *Hertz*

When

– $\Delta R \rightarrow \infty$

– $\alpha \rightarrow 0$ or $b \rightarrow 0$ or

– $P \rightarrow 0$ or $\max p_0 \rightarrow 0$

the values of both approaches (*Persson, Hertz*) are identical. The maximum of both stress functions tend to infinity, whereas the range is very locally limited . When the "contact arcs" increase, the stresses will decrease vice versa and the difference between the two approaches is significantly. Then the contact stress is essentially underestimated according to *Hertz*'s theory, taking an angle of $\alpha = 60°$ the deviation amounts about 50%.

The dimensionless contact stress function $q_{\max}(\phi = 0)$ has its absolute minimum at $\alpha = 105,57°$ when $q_{max} = 0,5801$. Assuming absolute contact ($\alpha = 180°$), i.e. $b \rightarrow \infty$ the limit value $q_{\max} = \dfrac{2}{\pi}$ is reached.

Figure 5.9 shows the tangential stresses $p_\phi(\phi)$ at the hole boundary as a function of different contact angles according to equation (5.37). Thereby, the stresses are scaled again dependent on the load P and the hole radius a. *Poisson's* ratio was chosen as $v = 0,23$ (glass). As soon as the contact angle α increases, the distribution of the tangential stresses is getting more regular. Between 60° und 90° the curve shape changes significantly. As the curves show the tangential stresses increase till a contact angle of $\phi = 90°$ is reached and the maximum is reached at the boundary of the contact surface ($\phi = \alpha$). On the contrary, by taking contact angles of $\phi = 120°$ and 150° the maximum tangential stresses have their maximum at $\phi = 0°$.
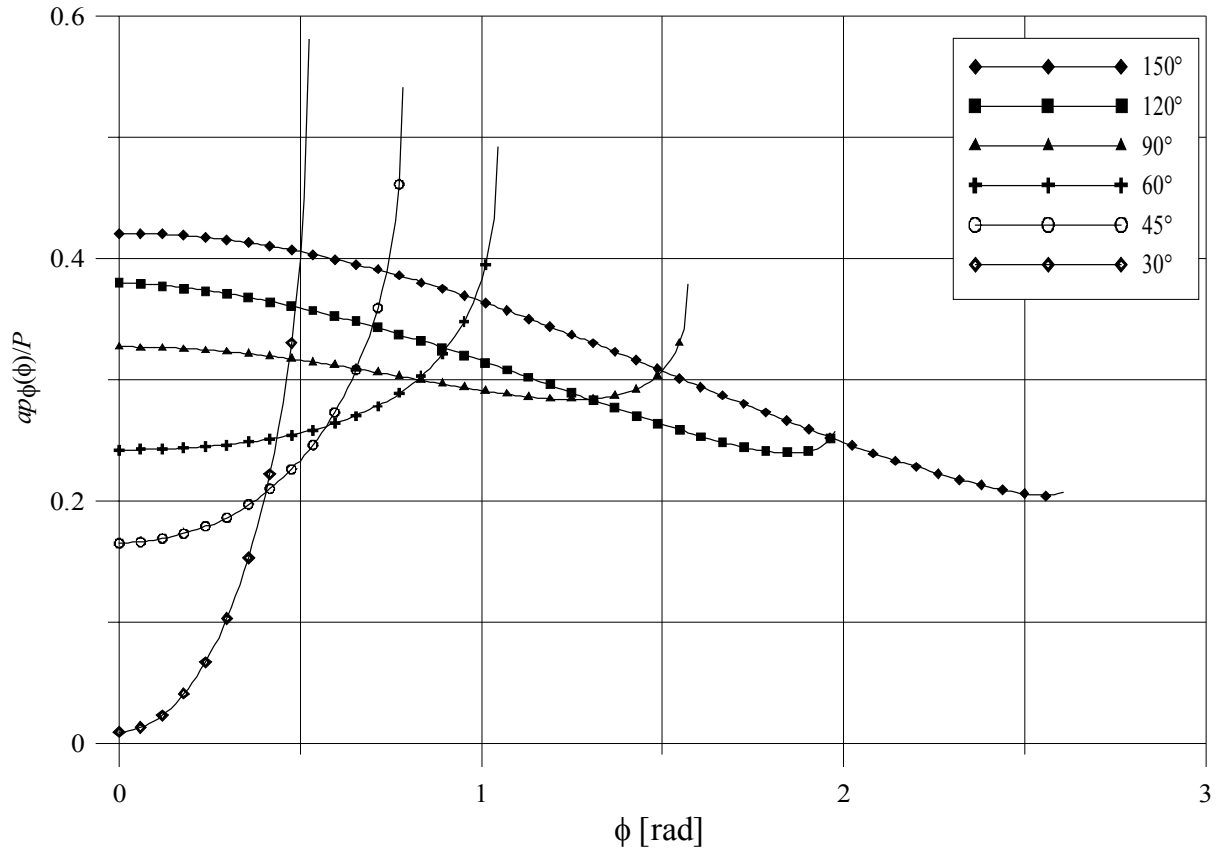
Figure 5.9   Dimensionless tangential stress function for different contact angles α, $\nu = 0{,}23$

By taking interface friction, different materials and a semi-finite width of the panel into consideration, the complexity of the analytical solution is increasing dramatically. Nevertheless, analytical approximate solutions exist (see chapter 5.3.3 and 5.3.4) the most accurate approximate solutions indeed only for the infinite panel with frictionless contact and identical linear material properties [Iyer 2001]. Therefore this solution should be used for verifying the FEM-model (see chapter 7).

The following equations are valid for contact bodies with different material properties, i.e. $E_1 \neq E_2$ and $\nu_1 \neq \nu_2$, and are only mentioned here. The approach is based on investigations carried out by [Ciavarella und Decuzzi 2001a, b], who based their research on [Persson 1964] and [Noble und Hussain 1969] and developed further these solutions.

At first the material parameters according to *Dundurs* [Dundurs 1975] are represented:

$$\alpha^* = \frac{E_2(1-\nu_1^2) - E_1(1-\nu_2^2)}{E_2(1-\nu_1^2) + E_1(1-\nu_2^2)}$$

$$\beta^* = \frac{E_2(1-2\nu_1)(1+\nu_1) - E_1(1-2\nu_2)(1+\nu_2)}{E_2(1-\nu_1^2) + E_1(1-\nu_2^2)}$$

(5.38)

Based on the formulas according to *Persson* the following context is determined:

$$\int_{-b}^{b}\frac{q'(t)}{t-y}dt+\frac{2\pi\beta^{*}}{1+y^{2}}q(y)=-\frac{4(1-\beta^{*})}{(1+y^{2})^{2}}+\frac{B^{*}}{1+y^{2}}$$

$$B^{*}=2(1-\beta^{*})-(1-\alpha^{*})\int_{-b}^{b}q(t)\frac{dt}{1+t^{2}}-\frac{\pi}{2}(1+\alpha^{*})\frac{E_{1}\Delta R}{P}$$

(5.39)

By using the contact stress function *Ciavarella* and *Decuzzi* found out that the material dissimilarity is negligible small. The maximum deviation is about 2%. Vice versa, the influence on the relationship between semi-contact angle α and the dimensionless parameter $E_{1}\Delta R/P$ is significant.

Because of these results, *q(y)* can be determined by equation (5.34). The dimensionless parameter $E_{1}\Delta R/P$ is determined by following approximation:

$$\frac{E_{1}\Delta R}{P}=\frac{(\alpha^{*}-1)(\ln(b^{2}+1)+2b^{4})+2}{\pi(1+\alpha^{*})(b^{2}+1)b^{2}}-\frac{4\beta^{*}}{\pi(1+\alpha^{*})}$$

(5.40)

5.3.3 Contact between Bolt and Conforming Hole in a Semi-Finite Panel

In the following section the most important investigations containing analytical solutions in closed form for contact between bolt and conforming hole in a semi-finite panel are discussed (see Figure 5.10). Examining the semi-finite panel, the problem is getting more complex and it is expected that a comparison with the FEM-calculation gives higher deviations than the comparison with an infinite panel. Nevertheless, the following approximate solutions are suited for a qualitative verification of the FEM-model, which will be examined in chapter 7.
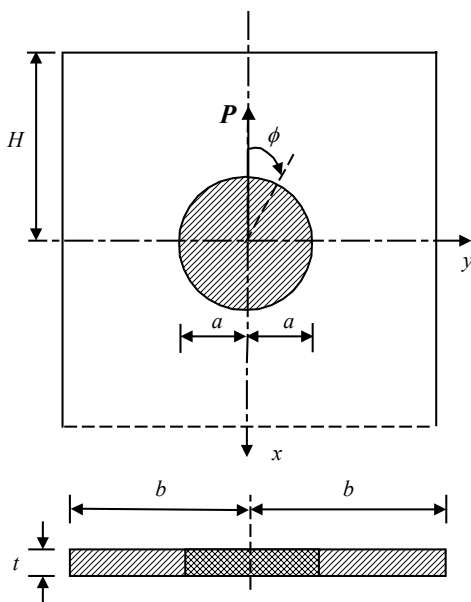
Figure 5.10 Bolted connection in a semi-finite panel

[Knight 1935] made a comparison of the stress distribution in an infinite panel and a panel of finite width with a bolt and a conforming hole in the center of the panel. The ratio a/b of the finite panel was 1/2. It was assumed that both bolt and hole are of the same linear elastic material, that there is no clearance between bolt and hole ($R_1 \approx R_2$) and that the bolt fits in the hole (neat-fit condition), i.e. $\alpha = \pi$. *Knight* successfully found approximations for the stress distribution. A comparison between infinite and finite panels showed that the maximum tangential stresses σ_ϕ arise at an angle of 90° at the boundary of the hole. To compare infinite and finite panel the tangential stresses increase by a ratio 2:5.

Further investigations containing the examinations of the stress distribution in a panel with finite width were made by [Theocaris 1956]. Using analytical approximate solutions, he determined the influence of the ratio a/b on the stress distribution. In particular, he examined the values a/b = 0,2, 0,4 and 0,5. He mainly observed that the maximum tangential stress or the maximum principal tensile stress σ_I arises at 90° in general and that the values have a maximum if a/b = 0,2. As soon as the value a/b increases the stresses decrease. After reaching a minimum between a/b = 0,4 and 0,5 the stresses increase again.

The maximum compressive stress or the maximum principal compressive stress σ_{II} arises at 0° and increases with a growing ratio a/b. He also found out that a variation of *Poisson*'s ratio ν has only a small influence on the stress distribution and is negligible when examining the maximum stress concentration (see also section 5.3.2, investigations of *Ciavarella* and *Decuzzi*).

Figure 5.11 shows the distribution of the principal stresses σ_I and σ_{II} at the hole boundary including different ratios $\lambda = a/b$.
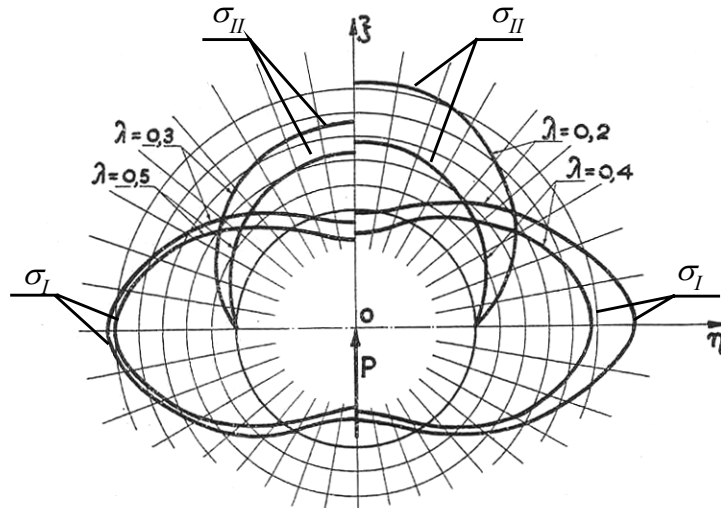
Figure 5.11 Qualitative distribution of the principal stresses σ_I and σ_{II} at the hole boundary including different ratios $\lambda = a/b$ [Theocaris 1956]

[Frocht, Hill 1940] examined experimentally panels of different widths with strain gauges and photoelastic measurements. They used aluminium panels with a hole in its center and aluminium and steel bolts. They also examined a possible clearance between bolt and hole ($\Delta R > 0$). *Frocht* and *Hill* determined the ratio a/b as a function of the stress concentration factors K. In the following the most important results will be summarized shortly. The detailed evaluation can be taken from [Frocht und Hill 1940].

Having a ratio $a/b = 0,7$ the stress concentration factors reach values of about $K = 2$. As soon as the ratio a/b decrease the stress concentration factors increase. If the ratio $a/b \rightarrow 0$, according to equation (5.41), the K-factors achieve a maximum value of about 13.

Figure 5.12 shows the stress concentration factors K_{tn} as a function of the ratio a/b according to [Theocaris 1956] and [Frocht und Hill 1949], in case the clearance $\Delta R = 0$ and the ratio $H/2b > 1,0$.

The stress concentration factor K_{tn} can be approximately determined with:

$$K_{tn} = 12,882 - 52,714\left(\frac{a}{b}\right) + 89,762\left(\frac{a}{b}\right)^2 - 51,667\left(\frac{a}{b}\right)^3 \qquad (5.41)$$

where $\sigma_\phi \max = K_{tn}\sigma_N$ and $\sigma_N = \dfrac{P}{2(b-a)t}$.
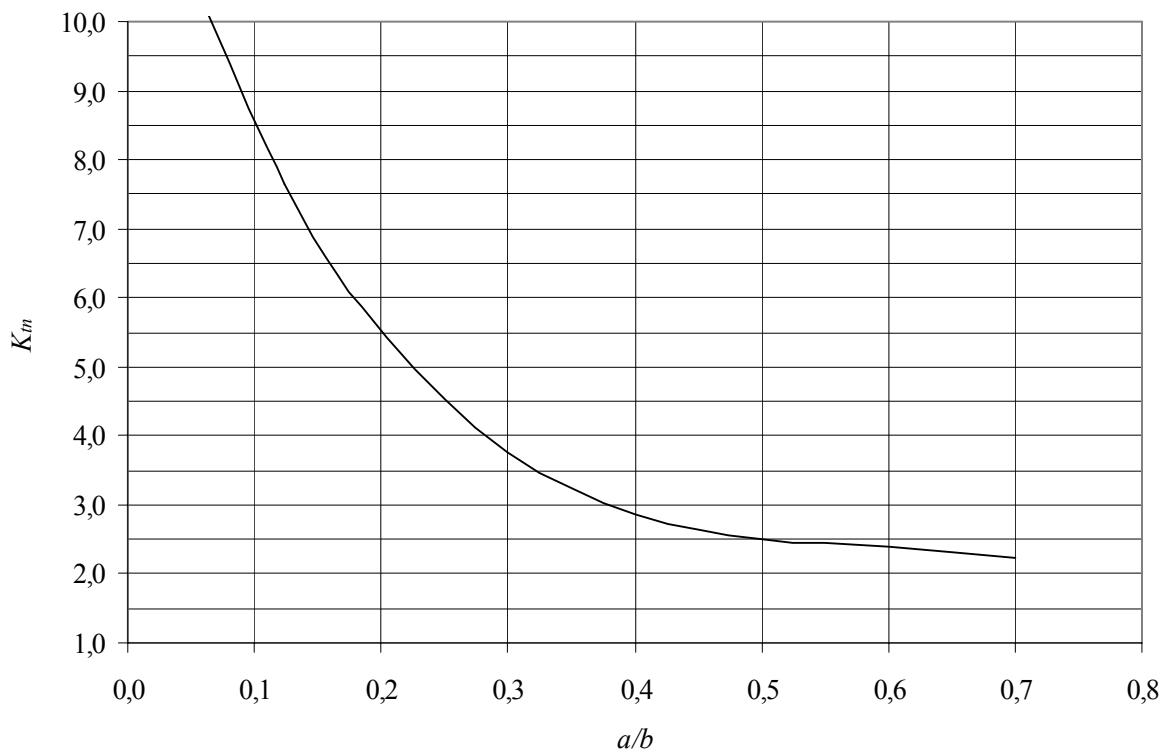
Figure 5.12 Stress concentration factors K_{tn} as a functions of a/b, where $\Delta R=0$ and $H/2b>1,0$

Furthermore, the investigations showed that by introducing a clearance between bolt and hole, the stress concentration factors increased. If the ratio $H/2b$ (see Figure 5.10) is getting smaller the influence of the clearance grows. On the contrary to fitted bolts the tangential stresses were not longer at 90° but dependent on the magnitude of clearance they moved a few degrees towards the direction of loadbearing.

Taking a clearance 0,2% of the hole diameter [Pilkey 1997] gives stress concentration factors as a function of a/b, where $\Delta R = 0,2\%$, $H/2b = 1,0$ and $t/2a < 0,5$ (see Figure 5.13).
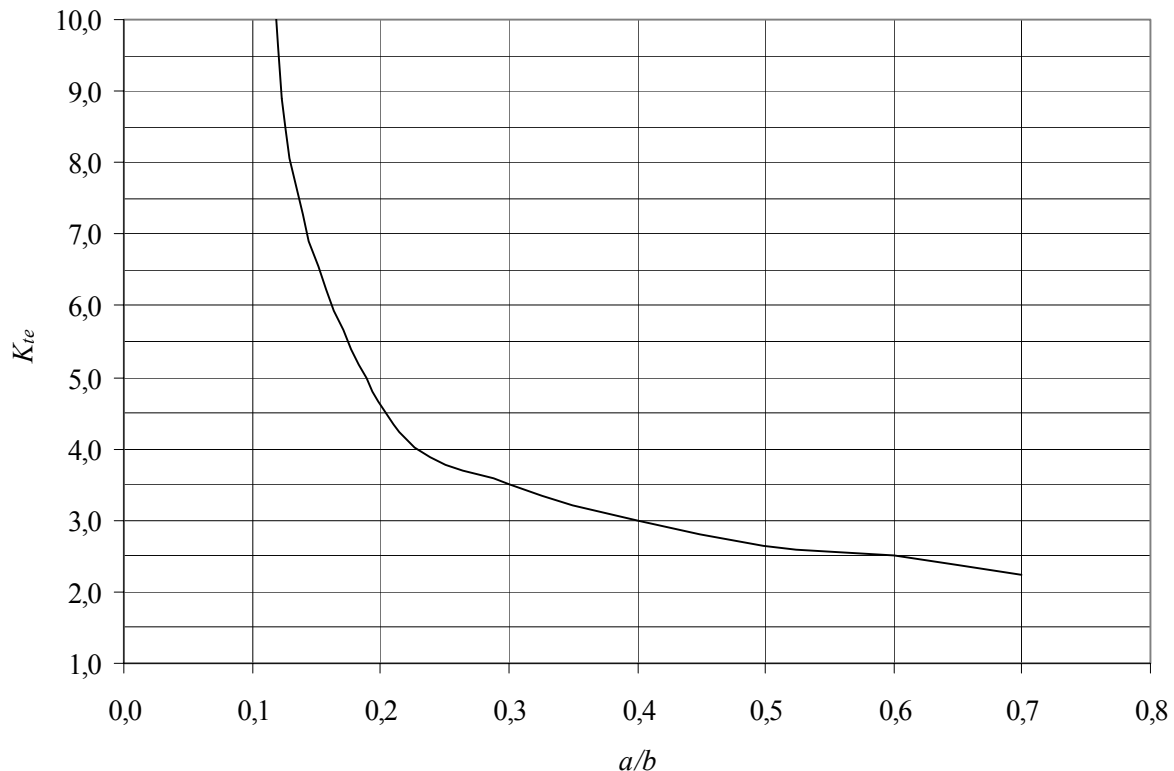
Figure 5.13 Stress concentration factors K_{te} as a function of a/b, for $\Delta R = 0,2\%$, $H/2b = 1,0$ and $t/2a < 0,5$

Pilkey also refers to studies which verify that, having a ratio $t/2a < 0,5$ and E_{bolt} / E_{panel} between 1 and 3, the influence of the different material properties (bolt and panel) on stress distribution is small.

By using the approximate solutions of this section within the parameter study of chapter 7, the numerical solutions will be compared.

5.3.4 Contact Considering Interfacial Friction

As already explained, in case the contact bodies are pressed together by a normal force at the interface of the two bodies, radial and tangential stresses arise and therefore friction at the interface may occur additionally. Friction is a complex physical phenomenon and affected by a variety of parameters. The most important ones are load-type and -duration, temperature as well as type of movement and duration. Relevant as well are the involved friction partners, the material properties in particular and their surface conditions (see chapter 7.3.4). Hence analytical and numerical modelling of friction has been simplified to idealistic models. The most popular friction model is the *Coulomb* friction model.

The physical laws describing friction were constituted by *Coulomb* in 1781:

  - The magnitude of the friction force R is independent on the contact area

  - The friction force R is proportional to the normal force N

  - The friction force R acts within the contact plane

  - The direction of the friction force R is reverse to the direction of relative motion.

The above mentioned rules can be described with the following equation (see Figure 5.14):

$$R = \mu N \qquad\qquad (5.42)$$

where μ is denoted as the friction coefficient [Gross et al. 1990].
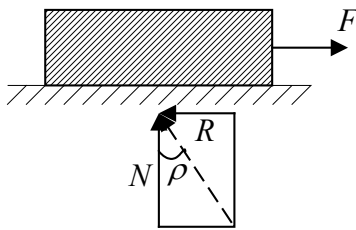
Figure 5.14 Definition of the forces considering friction

The direction of the resultant from N and R is:

$$\tan \rho = \mu = \frac{R}{N} \qquad\qquad (5.43)$$

Having contact between a bolt and a conforming hole in an infinite or finite panel with additional interface friction the calculation is very complex. [Ho und Chau 1997] determined an approximate solution in closed form for the stress distribution in an infinite panel with different material properties and friction. As described the approaches are less accurate due to the high complexity and not suited for a quantitative verification of the FEM-calculation.

Numerical investigations made by [Iyer 2001] showed that with an increasing friction coefficient μ the contact pressure p_0 decreases and the tangential stresses p_ϕ increase. If an infinite and finite panel is compared, the results for the infinite panels are higher contact stresses p_0. Vice versa the tangential stresses p_ϕ are lower for the semi-finite panel.

Within the parameter study of chapter 7 friction will be examined in detail by means of FEM.

6 Numerical Treatment of the Contact Using FEM

6.1 Introduction

In general simple framework, plate and panel models can be solved analytically, using an adequate differential equation. Systems which do not have any analytical solution must be solved numerical by approximations.

Using the finite element method (FEM) for calculating the framework, this will be discretisised in elements of finite size. The elements are linked with nodes. Therefore at the nodes the conditions of equilibrium of the nodal forces and the compatibility conditions of the displacements are satisfied. Considering the exact solution, the compatibility conditions of the displacements and the internal forces have to be satisfied not only at the nodes but also at every point of the framework. Therefore it is possible to build the basic equations, edge and compatibility conditions of an infinitesimal small element. These conditions can not be satisfied exactly by the finite element method. Finite elements are based on an assumption of the displacement distribution within the element. By using an adequate interpolation the displacements can then be calculated within the element. This means that the displacement conditions are satisfied at the supports and at the element boundaries. In spite of that the conditions of equilibrium of the element boundaries and free edges are only satisfied approximately. The principle of virtual displacements is used therefore. The conditions of equilibrium are satisfied within the chosen approximation [Werkle 2001].

The global stiffness matrix is

$$\mathbf{K} \cdot \mathbf{U} = \mathbf{P} \qquad (6.1)$$

where $\mathbf{K}$ stiffness matrix of the system

$\mathbf{U}$ vector of the nodal displacements

$\mathbf{P}$ vector of the external nodal loads

After the analysis of the system of equations (6.1) all internal forces, stresses and strains can be calculated from the derivatives of the displacements. The derivation of the finite element method is described in numerous literature, for example in [Bathe 1990], [Lee 1992], [Werkle 2001] and will therefore not be described within the scope of this thesis.

6.2 Modelling of the Structure

6.2.1 Singularities

A special problem, which may occur within the modelling of the structure, are singularities during the output of the results. This means an internal force or a displacements tending towards infinity at one boundary. Such a result is not close to reality and has to be interpreted by engineering experience.

Singularities are the result of insufficient modelling of the structure or load representation. An ordinary example is a panel with a width b and a thickness t loaded by a single force F, hence the stress of the panel is $\sigma_y = F/A$ where $A = bt$. The result at the transition point to a single load is $b \to 0$ and therefore the stress $\sigma_y \to \infty$ [Werkle 2001]. Singularities also occur at locations with a geometrical conspicuousness, for example sharp-edged openings. In these areas the two dimensional stress theory is not able to describe the occurring three-dimensional stress distributions. Using the finite element method at singularity locations, the stresses can only have finite values because of the displacement approach. With an increasing number of elements the stress values do not converge to a limit value but continue to increase. Such singularities can be avoided by an adequate load distribution or a suggestive filleting of sharp-edged corners. Referring to a hole in a panel the tensile stresses can increase rapidly at the hole boundaries as well, if the mesh size is getting finer. This is an indication of singularity locations, the results are then stress values which are lying above the analytical solution [Siebert 2004].

6.2.2 Element Options and Mesh Generating

When modelling plates and panels, most commonly 4-node-elements are used. On the one hand they suit to the geometry of the structure very well and on the other hand they are very precise. Taking the same number of degrees of freedom compared with triangular elements, quadrilateral elements have functions of higher order. Generally, a square is the most adequate shape for a finite element. It is followed by a rectangle, parallelogram and polygon.

By increasing the number of elements or reducing the size of elements (h-adaption), the more accurate the approximate solution by FEM becomes. Taking the same number of elements, elements with functions of higher order are also more precise than those with simpler approaches (p-adaption).

At the center of the element the stresses are obviously more exact than at the element boundary. Between two elements a stress step occurs because of the approximate calculation. The smaller this step gets the more accurate the result is. To get an uniform accuracy in areas of high stresses the elements should be condensed there. However, the size of adjacent elements should not change escalately. This would lead to a simulated stiffness change of the system. Therefore [Werkle 2001] suggests not to exceed a ratio in size of 1:1,5 for adjacent elements.

The quadrilateral elements for panels are divided in conforming (isoparametric) elements and elements which do not satisfy the conditions of conformance. These are elements with non conforming displacement approaches and hybride elements. Using an analytical approach for error estimations and convergence proofs, conforming elements are easier to handle. However, in practice, they behave quite "stiff". Essential differences result when panels are calculated, which are subjected to bending. For conforming elements a very fine mesh is needed. However, significantly less elements are necessary for non conforming elements. As long as in-plane loads are applied only, the differences are small between these two element types.

If the mesh is more refined, the system will get "softer", the deformations will increase and they will tend towards the exact solution.

6.3 Possibilities of Calculating the Contact

Having several bodies there is a possibility that they will touch each other and get into contact. Without considering the contact the bodies would penetrate one another during the FE-analysis and the different contact requirements, such as the contact between rigid and deformable bodies, multiple contact and separation would not be taken into consideration. Potential friction, static or kinetic friction, have to be considered as well.

The result is that not only a mathematically-mechanically approach is necessary but also an additional algorithm which is able to detect and model this contact. This is an exceeding nonlinear problem with unknown boundary conditions because they are dependent on the solution-variables itself. Therefore an incremental solution method is necessary:

In general it has to be distinguished between global and local algorithms:

Global algorithms:

1. Contact search
2. Solving of the different inequalities

Local algorithms:

1. Detecting of contact
2. Update of the essential equations and stresses

There are two different methods or global algorithms to model the contact numerically. The most common methods for linear contact problems are the *Lagrange*-Multiplier-Method and the Penalty-Method.

At first the two methods mentioned above are explained by the help of a discretised system, i.e. a system with a limited number of degrees of freedom. Therefore a minimizing function and the "constraints" is needed. Within a contact calculation, the "constraint" is the limiting of the movement. The calculation is based on the minimization of the total energy potential Π of two bodies in contact:

$$\Pi = U - W$$

$$\Pi = \frac{1}{2}\mathbf{U}^{\mathrm{T}}\mathbf{K}\mathbf{U} - \mathbf{U}^{\mathrm{T}}\mathbf{P} \rightarrow MIN$$

(6.2)

i.e. $\dfrac{\partial \Pi}{\partial U_i} = 0$ for all elements i

where   U strain energy

        W potential of all loads

        $\mathbf{K}$ stiffness matrix of the system

        $\mathbf{U}$ vector of the nodal displacements

        $\mathbf{P}$ vector of the external nodal loads

In detailed notation the equation of the two bodies is

$$\Pi = \frac{1}{2}\left\langle \mathbf{U}^1, \mathbf{U}^2 \right\rangle \begin{bmatrix} \mathbf{K}^1 & 0 \\ 0 & \mathbf{K}^2 \end{bmatrix} \begin{Bmatrix} \mathbf{U}^1 \\ \mathbf{U}^2 \end{Bmatrix} - \left\langle \mathbf{U}^1, \mathbf{U}^2 \right\rangle \begin{Bmatrix} \mathbf{P}^1 \\ \mathbf{P}^2 \end{Bmatrix} \qquad (6.3)$$

As seen from equation (6.3), the two bodies are not linked yet. This is done after a "gap"-function is introduced or added in every contact element Γ_i .

Using the *Lagrange*-Multiplier-Method the right side of equation (6.2) will be added in such a way that Π becomes:

$$\Pi^{LM}(\mathbf{U},\mathbf{\Lambda}) = \frac{1}{2}\mathbf{U}^\mathbf{T}\mathbf{K}\mathbf{U} - \mathbf{U}^\mathbf{T}\mathbf{P} + \mathbf{\Lambda}^\mathbf{T}\mathbf{C}^\mathbf{T}\mathbf{U} \qquad (6.4)$$

where $\mathbf{\Lambda}$ is the vector of the *Lagrange* Multipliers.

The "gap"-function is:

$$g_N = \widehat{\mathbf{C}}_\mathbf{i}^\mathbf{T}\mathbf{U} \qquad (6.5)$$

$\mathbf{C} = \begin{bmatrix} C_1 | C_2 | ... | C_n \end{bmatrix}$ is the vector of the constraints.

The demand $\partial \Pi^{LM} = 0$ leads to:

$$\begin{bmatrix} \mathbf{K} & \mathbf{C} \\ \mathbf{C}^\mathbf{T} & \mathbf{0} \end{bmatrix} \begin{bmatrix} \mathbf{U} \\ \mathbf{\Lambda} \end{bmatrix} = \begin{bmatrix} \mathbf{P} \\ \mathbf{0} \end{bmatrix} \qquad (6.6)$$

An auxiliary equation which contains the constraint condition is added to the conditions of equilibrium.

Compared with the *Lagrange*-Multiplier-Method the Penalty-Method only needs the discretisation of the displacement variables. The potential is

$$\Pi^P(\mathbf{U}) = \frac{1}{2}\mathbf{U}^\mathbf{T}\mathbf{K}\mathbf{U} - \mathbf{U}^\mathbf{T}\mathbf{P} + \frac{\varepsilon_N}{2}\mathbf{C}\mathbf{C}^\mathbf{T}\mathbf{U} \qquad (6.7)$$

where ε_N is the Penalty-parameter.

As a result the gap-function is:

$$g_N = \sum_I N_I(\xi)g_{NI} \qquad (6.8)$$

where N_I is a dimensionless form function.

With the condition $\partial\Pi^P = 0$ it results:

$$\left[\mathbf{K} + \varepsilon_N\mathbf{C}\mathbf{C}^\mathbf{T}\right]\mathbf{U} = \mathbf{P} \qquad (6.9)$$

The Penalty-Method is based on the addition of a large value to the element *i*. This means that in the diagonal of the stiffness matrix $\mathbf{K}$ an adequate force is added and that the required displacement is $\mathbf{U_i} \approx \mathbf{U_i^P}$. This method is very efficient because no additional equation is needed.

A detailed explanation of this method is described in [Wriggers 2002]. The two mentioned methods are limited on the node-to-node contact of two bodies and small deformations.

In a real contact calculation the number of contact constraints is unknown. Having a nonlinear problem, not only the displacements have to be determined but also the correct contact area. Having large displacements and multiple body contact the above mentioned equations, which are valid for linear problems, have to be generalized and extended. In most cases the Node-to-Segment (NTS)-approximation is used, which will be explained in more detail in chapter 6.4.3, together with the used contact discretisation of deformable bodies implemented in the program MSC.Marc. The geometrical contact conditions, which are necessary for the normal contact, in particular the function of penetration, will be explained.

6.4 MSC.visualNastran for Windows and the Additional Module Nonlinear+

6.4.1 Introduction

The calculations in this thisis are done with the finite element program MSC.visualNastran for Windows (N4W) version 2003 and version 2004 including the additional module Nonlinear+. The N4W Nonlinear+ module is the latest addition of MSC and can be implemented to an existing configuration as an add-on module of N4W. Nonlinear+ employs the MSC.Marc 2003 solver. Within the FE calculations of this thesis the Nonlinear+ module was used because it is specially adaptable for contact calculations of deformable bodies and the contact modelling itself is less time consuming than with GAP-elements (see chapter 6.4.6). Another disadvantage of GAP-elements is that only small deformations can be modelled sufficiently.

The following types of contact problems can be solved with Nonlinear+:

- Automated multi-body contact

- Contact between deformable bodies

- Self-contact

- 2-D and full 3-D contact

- Friction (*Coulomb*, shear or stick-slip friction laws)

- User-defined contact separation force or stress

- Modelling of large deformations

In the next sections some special features of the program system and the basics of contact discretisation are explained. Therefore only the virtually statical contact procedures which are needed within the scope of this thesis are explained.

The options of contact modelling by N4W without the additional module Nonlinear+ are described as well. In addition reference-calculations will be carried out.

6.4.2 Outline of the Used Element Types

N4W provides different isoparametric elements for calculating planes and bodies. The plane elements are used to represent membrane, shell and plate structures (see Figure 6.1). The simplest formulation of these elements are just a three-noded linear triangle and a four-noded linear quadrilateral. In addition, six-noded parabolic triangles and eight-noded parabolic quadrilaterals are also available.
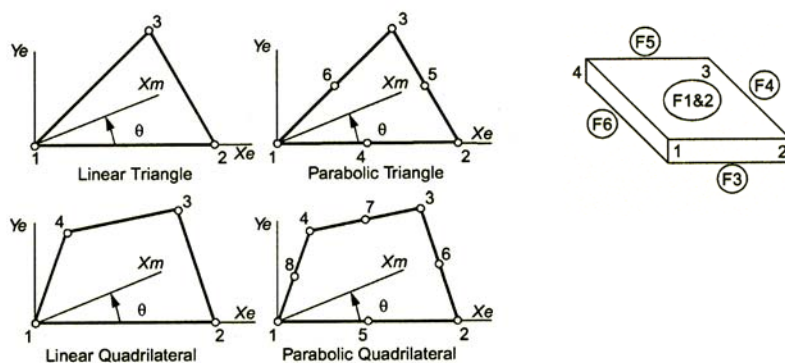
Figure 6.1 MSC.Nastran plane-elements [MSC.vN4W 2004a]

Volume elements are used to model three-dimensional solid structures. They can provide very detailed results but usually require additional modelling and analysis time and effort. Using SOLID-elements any three-dimensional structure can be modelled. They can consist of four or ten-noded tetrahedron, six or fifteen-noded wedge and eight or twenty-noded brick (hexahedron) elements, see Figure 6.2.
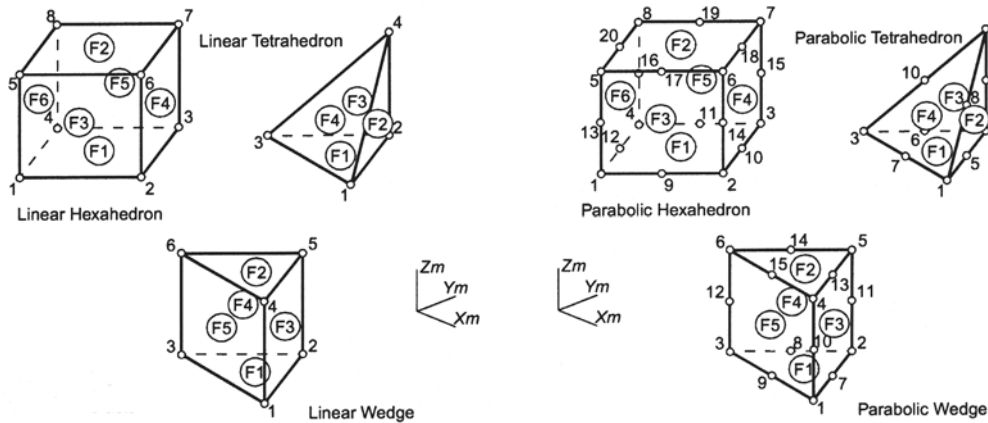
Figure 6.2 MSC.Nastran volume-elements [MSC.vN4W 2004a]

For nonlinear analysis, only solid elements without mid-edge nodes can be used (see Figure 6.1 and Figure 6.2).

Within the scope of this thesis only four-node-elements are used for modelling, because of the higher precision compared with the three-node-elements (see also chapter 6.2.2). Especially linear quadrilateral (CQUAD4) PLATE-elements are used. These elements are suited for thin plates and shells. SOLID-elements of the type linear hexahedral (CHEXA) are also used.

Within finite element modelling elements of lower order (h-adaption) should be used instead of elements of higher order (p-adaption). Having the same number of degrees of freedom, elements of higher order are more precise but because of the minor number of elements the real geometry cannot be modelled satisfactory. As already mentioned in chapter 6.2.2, having isoparametric elements of lower order the structure behaves stiffer than in reality and hence the displacement values are smaller. N4W provides several features to reduce or eliminate these effects. A detailed description of the background is given for example in [Lee 1992], [Macneal 1992], [Schieder 1998]. Additionally, these effects hardly arise when having only in-plane loadbearing (see chapter 6.2.2).

6.4.3 MSC.Marc CONTACT-Function (with friction)

Very often contact can only be modelled with special contact elements (e.g. GAP-elements, see chapter 6.4.6). Using MSC.Marc the contact is modelled "automatically" without the presence of contact elements. Only lines, surfaces and elements which should get into contact have to be defined. Therefore the direct constraint method is used. In this procedure, the motion of the bodies is tracked. In case that contact occurs, direct constraints are placed on the motion, using boundary conditions, both kinematic constraints on transformed degrees of freedom and nodal forces. This very accurate procedure is implemented in MSC.Marc through the CONTACT option [MSC.MARC 2003a, b, c, d, e], [MSC.vN4W 2004b, c].

Definition of the contact bodies

MSC.Marc offers two types of contact bodies, deformable and rigid. The disadvantage of MSC.N4W Nonlinear+ is that only deformable bodies are available. Deformable bodies are composed as shown below:

1. The finite elements which make up the body.

2. The nodes on the external surfaces which might contact another body or itself. These nodes are treated as potential contact nodes.

3. The edges (2-D) or faces (3-D) which describe the outer surface a node on another body (or the same body) might contact. These edges or surfaces are treated as potential contact segments.

The elements of a body are defined through the CONTACT option. It is not necessary to identify the nodes on the surface since this is done automatically.

When defining contact bodies for a deformable-to-deformable analysis it is important to define them in the proper order. As a general rule, a body with a finer mesh should be defined before a body with a coarser mesh. Contacting bodies should also have different mesh sizes because congruent nodes cause convergence problems.

Contact search

At first, all contact nodes are checked to see whether they are near to a contact segment. To simplify or to speed up the computation it is possible to use the CONTACT table option to indicate that a particular body will or will not contact another body. During the iteration process the motion of the nodes is checked to see whether they have penetrated a surface or crossed a segment after the iteration step.

It is unlikely that a node exactly contacts the surface during the contact process, therefore a contact tolerance is introduced (see Figure 6.3).
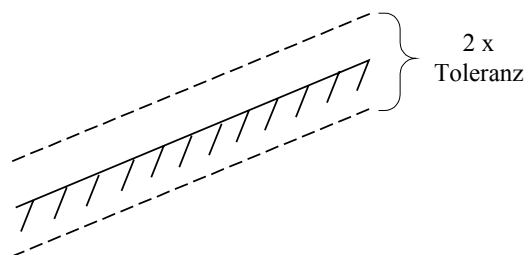
Figure 6.3   Contact tolerance

If a node is within the contact tolerance, it is considered to be in contact with the segment. The contact tolerance is calculated by MSC.MARC as 5% of the smallest volume (SOLID)-element side or 25% of the smallest SHELL-element thickness. It is also possible to define the contact tolerance through the input. The size of the contact tolerance influences the computational costs and the accuracy of the solution. If the contact tolerance is too small, detection of contact and penetration is difficult. This leads to higher computational costs. If the contact tolerance is too large, nodes are considered in contact prematurely, resulting in a loss of accuracy or more recycling due to separation. Therefore the default contact tolerance is recommended.

Often, there are areas in the model where nodes are almost touching a surface. In such cases the use of a biased tolerance area with a smaller distance on the outside and a larger distance on the inside is advised (see Figure 6.4). This avoids that close nodes are coming into contact and are separating again. The value of the bias factor should be between 0 and 0,99. The default is 0 or no bias. In analyses where a frictional contact is involved, a bias factor for the contact tolerance is recommended. The recommended bias factor value is 0,95.

(1-bias) x tolerance

(1+bias) x tolerance
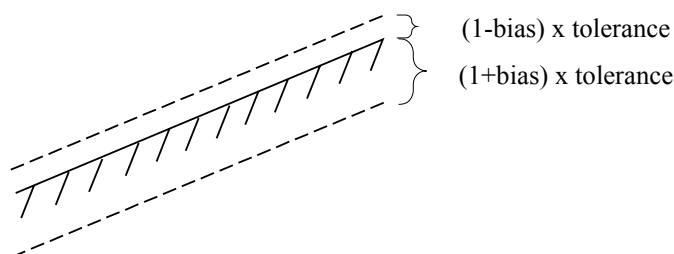
Figure 6.4   Contact tolerance with bias

Separation of the bodies

After contact occurs a reaction force, associated with the node in contact, balances the internal stress of the elements adjacent to this node. During separation, this reaction force behaves as a residual force (as the force on a free node should be zero). This requires a redistribution of the internal stresses in the deformable body. Depending on the magnitude of the force this might last several iterations. It should be noticed that a deformable body which is constrained only by other bodies (no explicit boundary conditions) and subsequently is separated from the other bodies, would then have rigid body motion. In static analysis this results in a singular or non-positive definite system. This problem can be avoided with the help of appropriate boundary conditions.

Friction modelling

The *Coulomb* friction model is depending on the normal force and the relative sliding velocity or displacement. Implementation in MSC.Marc has been done using a nonlinear spring model (see Figure 6.5).
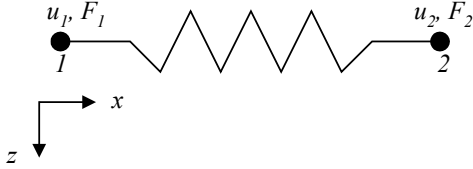
Figure 6.5   Spring model

The corresponding equation is given by:

$$\begin{bmatrix} K & -K \\ -K & K \end{bmatrix} \begin{bmatrix} u_1 \\ u_2 \end{bmatrix} = \begin{bmatrix} F_1 \\ F_2 \end{bmatrix} \qquad (6.10)$$

where K is the spring stiffness, u_1, u_2 the displacements and F_1 and F_2 the forces of points 1 and 2.

The equation can also be represented as a function of velocities v:

$$\begin{bmatrix} K & -K \\ -K & K \end{bmatrix} \begin{bmatrix} v_1 \\ v_2 \end{bmatrix} = \begin{bmatrix} F_{1x} \\ F_{2x} \end{bmatrix} \qquad (6.11)$$

Since K is a nonlinear function of the relative velocity, equation (6.11) is solved incrementally, where within each increment several iterations may be necessary.

Hence for the iteration i the following equation results:

$$\begin{bmatrix} K^i & -K^i \\ -K^i & K^i \end{bmatrix} \begin{bmatrix} \delta v_1^i \\ \delta v_2^i \end{bmatrix} = \begin{bmatrix} \triangle F_{1x}^i \\ \triangle F_{2x}^i \end{bmatrix} \qquad (6.12)$$

where δv_1^i and δv_2^i are used to update v_1^i and v_2^i by $v_n^1 = v_n^{i-1} + \delta v_n^i$, $n=1,2$.

The *Coulomb* friction model can either be used as a true stick- or a stick-slip-model. In this procedure a node sticks to the surface until the friction force F_x reaches the critical value μF_z.

To model the differences in static and dynamic friction analysis, an overshoot parameter α can be used additionally. MSC.Marc is based on the stick-slip-algorithm given in Figure 6.6.

```
                      ┌──────────────────┐
                      │  Initial Contact │
                      └──────────────────┘
                               │
                               ▼
                        ╱───────────╲
              ──No──── ⟨ Δu ≈ 0 ⟩ ────Yes──
              │         ╲───────────╱       │
              ▼                              ▼
       ┌──────────┐                   ┌──────────┐
       │ Slipping │                   │ Sticking │
       │   Mode   │                   │   Mode   │
       └──────────┘                   └──────────┘
              │                              │
              ▼                              ▼
              ┌──────────────────────────────┐
              │   Determine Solution of       │
              │     Next Iteration            │
              └──────────────────────────────┘
```

Remain in Slipping Mode if:
$$F_x \cdot \Delta u < 0 \quad and \quad \Delta u > \beta$$

Change to Sticking Mode if:
$$F_x \cdot \Delta u > 0 \quad and \quad \Delta u > \beta$$
or if
$$\Delta u \approx \varepsilon \beta$$

Remain in Sticking Mode if:
$$\|F_x\| \leq \alpha \mu F_z$$

Change to Slipping Mode if:
$$\|F_x\| > \alpha \mu F_z$$
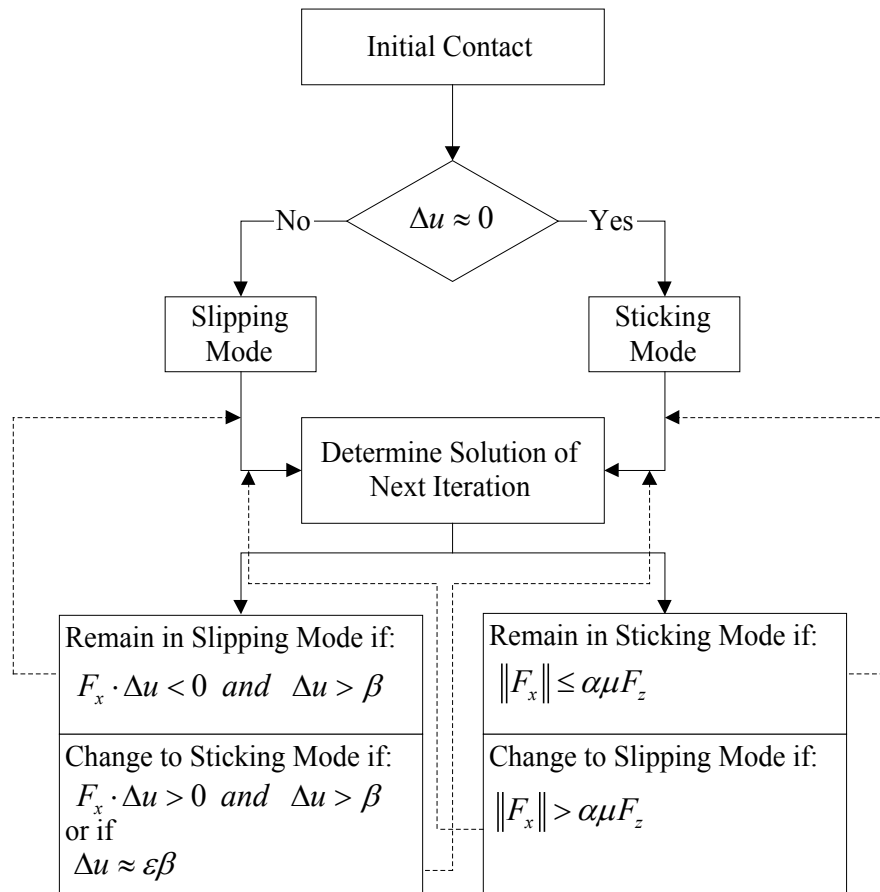
Where $\alpha = 1,05$ (default, can be user-defined)

$\beta = 1 \cdot 10^{-6}$ (default, can be user-defined)

$\varepsilon = 1 \cdot 10^{-6}$ (fixed, so that $\varepsilon \beta \approx 0$)

Figure 6.6 Stick-slip-algorithm [MSC.MARC 2003a]

MSC.Marc additionally provides a special type of friction model, the so called GLUE option. This option imposes that there is no relative tangential motion. Bodies with dissimilar meshes can be joined by specifying a very large SEPARATION FORCE and activating the GLUE option. The constraint equations are automatically written between the two meshes.

Mathematical representation of the contact

If the global contact search was successful, i.e. in case that contact is detected between a node and a deformable body, a tying relation (constraint condition) is formed between the contacting nodes and the nodes on the other body. The tying matrix is built in a way that the contacting node follows the surface. During the iteration process of finding an incremental solution a node can slide from one segment to another or can be linked with the surface. The algorithm has to be able to find all contact conditions during the solution process, in which the normal distance g_n between the bodies is zero. This discretisation is called "Node-to-Segment"(NTS)-method. To describe this process accurately the "Master-Slave" concept is used. The surface, which points are checked if penetrating into the other surface ("master"-surface), is called "slave"-surface.

The parts of "master" and "slave" can be permuted without changing the result. The "master"-segment is represented in 2D as a line and in 3D as a surface.
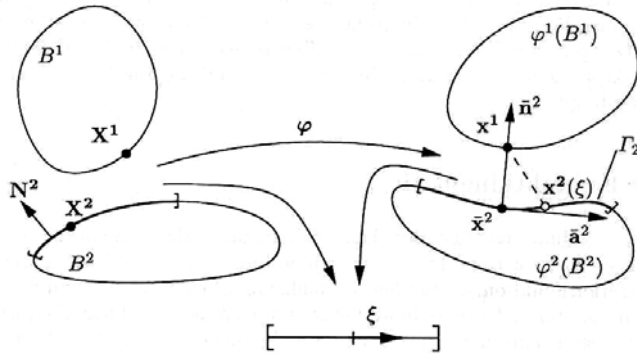
Figure 6.7   Geometry und geometrical approach of two bodies [Wriggers 2002]

The point $\bar{x}^2 = x^2(\xi)$ which has the minimum distance to a fixed point x^1 on the "slave"-surface can be determined with the following requirement (see Figure 6.7):

$$\left\| x^1 - \bar{x}^2 \right\| = \min_{x^2 \subseteq \Gamma^2} \left\| x^1 - x^2(\xi) \right\| \tag{6.13}$$

Equation (6.13) leads to the minimum of the distance function and to the fulfilling relation:

$$\frac{d}{d\xi^\alpha} \left\| x^1 - x^2(\xi^1, \xi^2) \right\| = \frac{x^1 - x^2(\xi^1, \xi^2)}{\left\| x^1 - x^2(\xi^1, \xi^2) \right\|} \cdot x^2_{,\alpha}(\xi^1, \xi^2) = 0 \tag{6.14}$$

in which the tangential vector of the "master"-surface is $x^2_{,\alpha} = a^2_\alpha$. In the solution point $\bar{x}^2$ of equation (6.13) the tangential vector must be perpendicular to the vector $x^1 - x^2(\xi^1, \xi^2)$ and perpendicular to the "master"-surface. If the point $\bar{x}^2$ is known the inequality conditions can be formed, which describe the non penetration of the body. As a result the following distance function is introduced:

$$g_N = \left[x^1 - x^2(\xi) \right] \cdot n^2(\bar{\xi}) \tag{6.15}$$

For:

$g_N > 0$ no contact

$g_N = 0$ perfect contact

$g_N < 0$ penetration.

The constraint condition of contact excluding penetration is

$$g_N = (x^1 - x^2) \cdot \overline{n}^2 \geq 0 \,. \qquad (6.16)$$

With the help of discretisation with the NTS-element it is assumed that the "slave"-node (s), coordinate x_s^2, comes into contact with the "master"-segment(1)-(2) which is defined by the nodal coordinates x_1^1 and x_2^1 (see Figure 6.8).
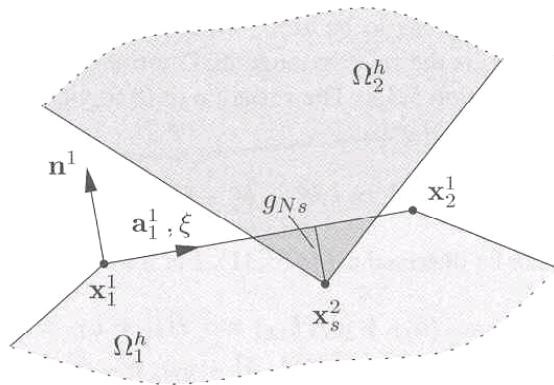
Figure 6.8   "Node-to-Segment"-(NTS) contact element [Wriggers 2002]

The mathematical representation of the NTS- discretisation is described in detail in [Wriggers 2002].

If a node touches the surface of a body, a "multipoint" constraint will be activated automatically. Assuming that the edges (2-D) or segments (3-D) which describe the outer surface are known, the constraint condition is determined. For the 2D-analysis, which uses elements of lower order, three nodes are retained, two for the boundary line and one for the point itself (see Figure 6.9). Having a 3D-analysis with SOLID-elements, which is based on hexahedral-elements, the segment is defined by a isoparametric four-node-element. That is why five points are needed in the whole (see Figure 6.10).
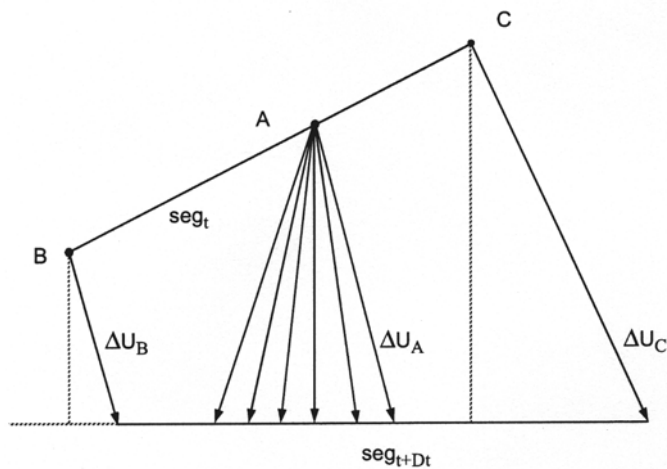
Figure 6.9 Links of 2D-contact with elements of lower order [MSC.MARC 2003a]
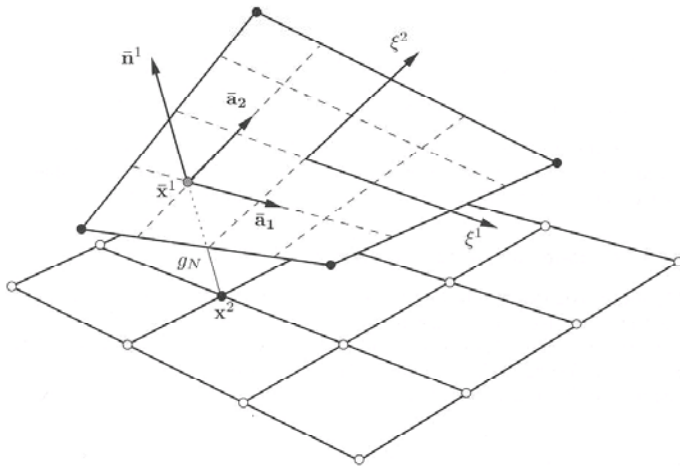
Figure 6.10 Geometry of the "five"-node contact element [Wriggers 2002]

Having elements of lower order, the normal is calculated with a piecewise linear representation of the element surface (see Figure 6.11). That is why the relation of the constraint conditions are not precise because of the constant distribution over the whole segment. If a node is sliding from one segment to the other a discontinuity, which obviously leads to numerical difficulties, arises in the normal.
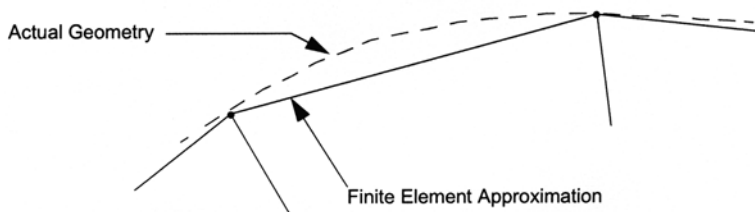
Figure 6.11 Linear representation using elements of lower order [MSC.MARC 2003a]

When smoothing the surface geometry a more precise calculation can be achieved. As a consequence optional discontinuity spots have to be localized in advance. Using elements of higher order these problems do not occur because the normal is calculated with a quadratic approach.

6.4.4 Solution Methods for Nonlinear Equation Systems

Nonlinear calculations need a good appraisal and also several calculation time and iterations. To solve nonlinear equation systems MSC.Marc provides several iterative methods. These are some versions of the "*Newton-Raphson* Iteration", which are applicable for contact calculations:

- Full *Newton-Raphson* Iteration

- Modified *Newton-Raphson* Iteration

- Secant-Method (Quasi *Newton* Method)

The default is "Full *Newton-Raphson* Iteration" using MSC.Marc. For the most nonlinear problems this methods provides satisfying results. Indeed, a high computation capacity is needed for 3D-calculations. Using the "Full *Newton-Raphson* Iteration" in every iteration step i the tangent stiffness matrix **K** will be redeveloped by taking the modified tangent stiffness into consideration.

In nonlinear calculations the following equation has to be solved at a time $t + \Delta t$:

$$^{t+\Delta t}\mathbf{F} - {}^{t+\Delta t}\mathbf{R} = \mathbf{0} \qquad (6.17)$$

where the vector $^{t+\Delta t}\mathbf{F}$ denotes the external nodal loads and $^{t+\Delta t}\mathbf{R}$ the vector of internal nodal loads. The internal nodal loads are equivalent to the element stresses, are calculated by the principle of virtual displacements and are nonlinearly dependent on the nodal displacements $\mathbf{U}$. Therefore equation (6.17) has to be solved by iteration.

At first, for a given load $\mathbf{F}^0$ with a linear initial tangential stiffness $\mathbf{K}^0$ the deformation will be calculated as for a linear system. Due to these nodal displacements the element strains are calculated and considering the physical nonlinear stiffness matrix the internal nodal forces $\mathbf{R}^{i-1}$ are determined. The internal nodal forces are now compared with the external forces $\mathbf{F}^{i-1}$ according to equation (6.17).
If the internal nodal forces are not in equilibrium with the external nodal forces, a difference vector (unbalanced load vector) $\Delta\mathbf{R}$ will be obtained:

$$\Delta\mathbf{R}^{i-1} = \mathbf{F}^{i-1} - \mathbf{R}^{i-1} \qquad (6.18)$$

where $i = 1,2,3,\ldots$ are the number of iteration steps.

In a second step, this vector $\Delta\mathbf{R}^{i-1}$ will be applied as an external load on the system, which is again assumed linear. The stiffness matrix is also recalculated. As a result the nodal displacement $\Delta\mathbf{U}^i$ is:

$$\Delta\mathbf{U}^i = \left[\mathbf{K}^{i-1}\right]^{-1} \cdot \Delta\mathbf{R}^{i-1} \qquad (6.19)$$

and the total displacements $\mathbf{U}^i$ can be calculated with $\mathbf{U}^i = \mathbf{U}^{i-1} + \Delta\mathbf{U}^i$. Resulting from this deformation the internal forces and the next difference vector can be calculated again. The calculation is repeated as long as the difference vector $\Delta\mathbf{R}$ or the displacement increments $\Delta\mathbf{U}$ tend towards zero.
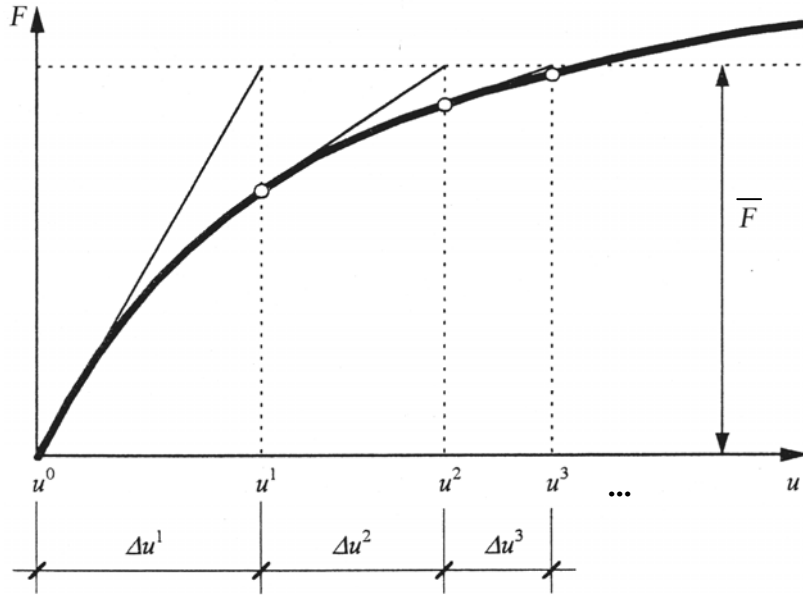
Figure 6.12   "Full *Newton-Raphson* Iteration"

Using the "Full *Newton-Raphson* Iteration" only a few iterations steps are necessary until the convergence criteria are fulfilled, which is of great advantage (see Figure 6.12). Further details of the "Full *Newton-Raphson* Iteration" are, for example, explained in [Bathe 1990] or [Schieder 1998].

Because of the factor decomposition of the tangent stiffness matrix the result are higher computational costs per iteration step. The "Modified *Newton-Raphson* Iteration" can be used as an alternative. This method differs from the "Full *Newton-Raphson* Iteration" because the tangent stiffness matrix is not calculated in every iteration step. Therefore the calculation steps are:

$$\mathbf{\Delta U}^{i} = \left[\mathbf{K}^{0} \right]^{-1} \cdot \mathbf{\Delta R}^{i-1}$$

$$\mathbf{\Delta R}^{i-1} = \mathbf{F}^{i-1} - \mathbf{R}^{i-1} \qquad\qquad (6.20)$$

$$\mathbf{U}^{i} = \mathbf{U}^{i-1} + \mathbf{\Delta U}^{i}$$

The process of calculation is faster in case the tangent stiffness matrix is only calculated once. However, more iterations steps are necessary to meet the convergence criteria (see Figure 6.13) and, having numerous nonlinearities or contact it can be time consuming until the solution converges. Therefore the "Full *Newton-Raphson* Iteration" is recommended [MSC.MARC 2003a].
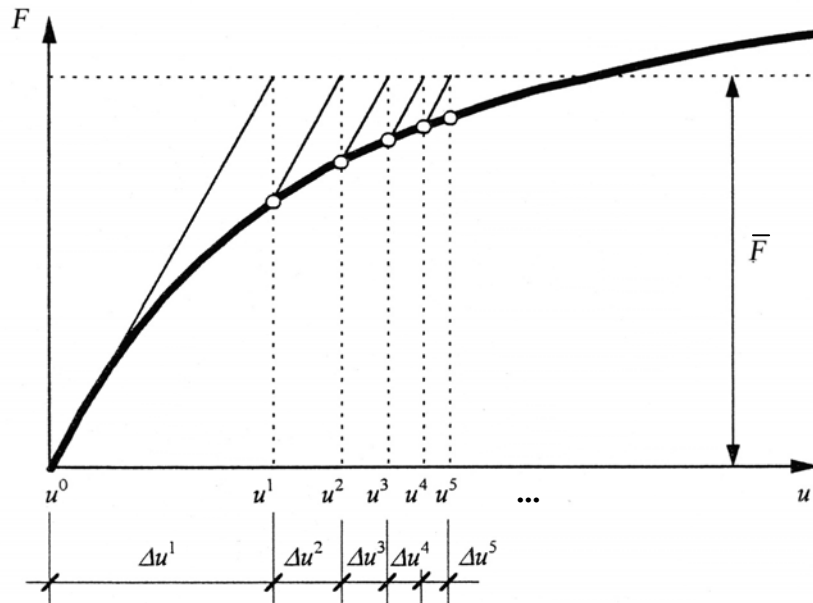
Figure 6.13 "Modified *Newton-Raphson* Iteration"

The "Secant-Method" can be used as well. This is a so called "Quasi *Newton* Method". The inverse of the stiffness matrix $\mathbf{K}_S$ is changed in every iteration step but not redeveloped like in the "Full *Newton-Raphson* Iteration".

$$\mathbf{\Delta U}^i = \left[\mathbf{K}_S^{i-1}\right]^{-1} \cdot (\mathbf{F} - \mathbf{R}^{i-1})$$
$$\mathbf{\Delta R}^{i-1} = \mathbf{F} - \mathbf{R}^{i-1}$$

(6.21)

Searching line by line towards the direction $\mathbf{\Delta U}^i$, the equilibrium must be fulfilled in this direction. Therefore the displacement vector $\mathbf{U}^i = \mathbf{U}^{i-1} + \beta \mathbf{\Delta U}^i$ is calculated, where β is a scalar vector. Subsequently the unbalanced loads $\mathbf{\Delta R}$, which comply with these displacements, are determined. The parameter β is varied as long as the convergence tolerance TOL meets the equation:

$$\mathbf{\Delta U}^i \mathbf{\Delta R}^i \le TOL \cdot \mathbf{\Delta U}^i \mathbf{\Delta R}^{i-1}$$

(6.22)

As soon as β complies with equation (6.22) it is possible to determine $\mathbf{U}^i$. During the next step the secant stiffness is calculated and then it is applied once more for the given load $\mathbf{F}$ (see Figure 6.14). As a consequence the value of the nodal displacement has to be improved in any iteration step.
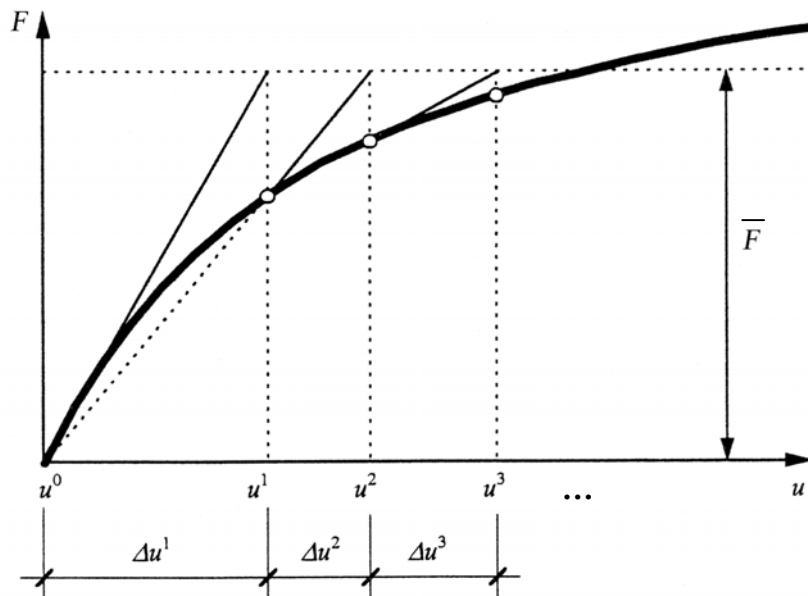
Figure 6.14 "Secant-Method" ("Quasi *Newton* Method")

6.4.5 Convergence Controls

Depending on the solution method an iterative calculation can only be efficient, if realistic convergence criteria are chosen to complete an iteration. At the end of every iteration it is therefore recommended to check whether the solution has already converged within given tolerances or whether there are still any divergences. It is also important to chose not too large convergence tolerances. Otherwise, the obtained results will not be very exact. Neither should the tolerances be chosen too small because the calculation might be unnecessary accurate and the computation time might increase rapidly as well.

Several criteria are available for convergence checking. Using MSC.Marc, three different checking criteria for the convergence are available:

1. RESIDUAL CHECKING (Default MSC.Marc)

This method measures the vector of the non balanced loads within a given tolerance. This difference between internal and external forces of the total system, has to be compared with a reference basis. This reference basis complies with the norm of the external loads, i.e. the load vector $F_{reaction}$ or $M_{reaction}$.

It has to be noticed that the criteria for termination of the computation does not consider displacements. Therefore a second criterion is provided, which is based on displacements:

2. DISPLACEMENT CHECKING

Using this method the convergence is achieved when the maximum displacement of the last iteration is very small compared to the actual displacement change of the increment.

If the forces and the displacements meet the conditions of equilibrium, a third convergence criterion can be used for evaluation:

3. STRAIN ENERGY CHECKING

This method can be compared to the displacement checking. Within this method a comparison of the strain energy of the last iteration and the strain energy of the increment is performed.

6.4.6 MSC.N4W GAP-Element with Friction

Using MSC.N4W without the additional module Nonlinear+ the contact modelling is done by GAP-elements. The GAP-element simulates a node-to-node contact. It is used to represent surfaces or points which can separate, close, or slide, relative to each other. The "Penalty-Method" is used for the numerical representation. The GAP coordinate system is shown in Figure 6.15. The x-axis points from the node G_A towards node G_B.
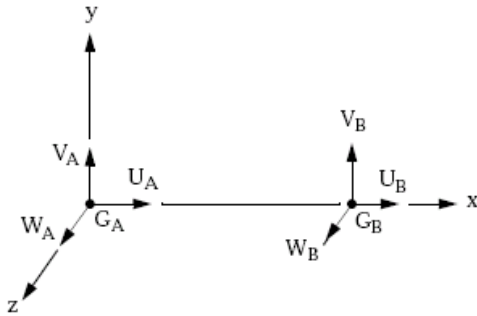
Figure 6.15 GAP-element coordinate system [MSC.vN4W 2004a]

If a load is applied, the GAP-element will change its status. The force components of the GAP-element in direction of the axis are the compressive force F_x and the frictional forces F_y and F_z in transverse direction regarding to the displacements u, v und w of the element coordinate system. These internal forces can be calculated by:

- If the GAP is open (no contact, no transverse stiffness) it follows:

$$F_x = K_b u \leq 0 \quad and \quad F_y = F_z = 0 \qquad (6.23)$$

where the stiffness K_b can be selected arbitrary.

- If the GAP is closed and sliding (without friction) occurs, it follows:

$$F_x = K_a u > 0 \quad and \quad F_y = F_z = 0 \qquad (6.24)$$

where K_a denotes the "Penalty"-value of the stiffness.

- If the GAP is closed and static friction occurs, it follows:

$$F_y^2 + F_z^2 \leq \left(\mu_s F_x \right)^2 \qquad (6.25)$$

where $F_x = K_a u$, $F_y = K_t v$ and $F_z = K_t w$. K_t denotes the "Penalty"-value of the transverse shear stiffness and is used when friction occurs.

The force-displacement-curve of the GAP-element is shown in Figure 6.16.
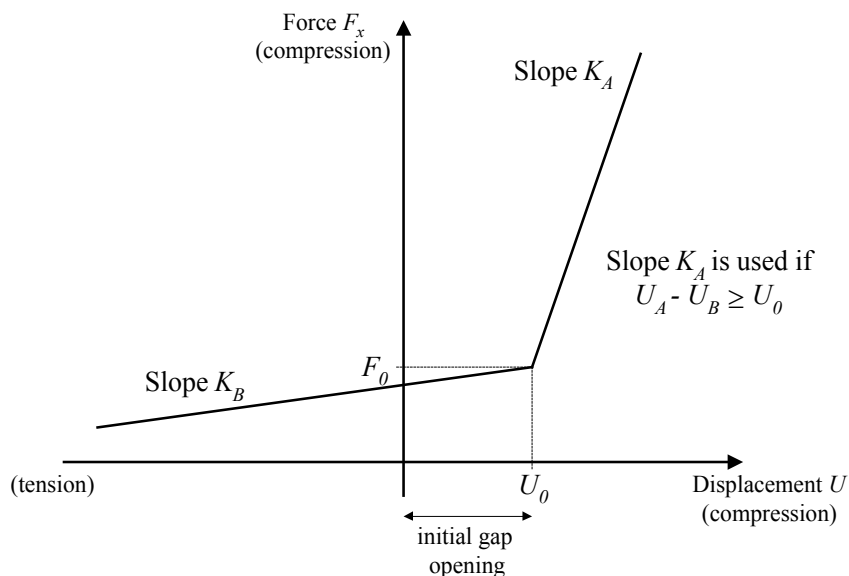
Figure 6.16   GAP-element force-displacement-curve

The initial GAP opening is defined by U_0 and the preload is defined by F_0. If the GAP is closed (U_A - $U_B \geq U_0$) the axial stiffness K_a has a large value relative to the adjacent structure. K_a should be chosen at least to be three orders of magnitude higher than the stiffness of the neighbouring grid points. A much larger K_a value may slow down convergence or cause divergence, while a much smaller value may result in an inaccuracy. If the GAP is open (U_A - $U_B < U_0$), there is a small stiffness K_b.

When using GAP-elements convergence problems occur very often in nonlinear analysis, especially if friction has to be considered additionally. The "Penalty"-Method is used to simulate the stiffness between two degrees of freedom, therefore a large stiffness value is added to them in order to get the same displacements for them. "Penalty"-values are introduced to avoid penetration and to cause friction between two points. Problems appear in case that the "Penalty"-values are not chosen correctly. The success of this method depends on the chosen "Penalty"-values and is a compromise between accuracy and numerical power [Lee 1992].

As already mentioned, when modelling the contact, the correct assumption of the stiffness values (compression stiffness, in case of friction, an additional transverse stiffness) is very important. Therefore it is recommended to execute a convergence examination, before the "Penalty"-values are determined (see chapter 7).

6.5 Discretisation of the FEM-Model (Glass-Bushing-Bolt)

Within the scope of this thesis the parameters of the FEM-model are systematically examined in order to check which elements and solution algorithms of the program N4W and Nonlinear+ module are suitable for solving the current problem. Additionally it is checked how complex the FEM-model have to be to obtain adequate results.

Based on [DASt 2003] and [Siebert 2004] the single parameters are determined first. Within these research works it was determined that a concentric mesh with 32 elements in circumference of the drill hole and an aspect ratio of the edge elements of at least 1:1 gives satisfying results which are in conformity with the analytical (theoretical) results.

Furthermore, a parameter study of different contact elements (MSC.Marc CONTACT option and N4W GAP-elements) will be done.

At first all components are modelled with linear quadrilateral (CQUAD4) PLATE-elements. After that the parameter study will be done predominantly with SOLID-elements of the type linear hexahedral (CHEXA). An overview of the used parameters is given in Table 6.1.

Table 6.1   Parameter overview

Used element type of all components (glass-bushing-bolt):	PLATE-elements (CQUAD) SOLID-elements (CHEXA)
Element mesh around the hole:	Concentric circle Aspect ratio radial 1:1
Elements in circumference of the drill hole:	32 64
Output-result:	Nodal stresses
Analysis without/with CONTACT or GAP:	Linear Nonlinear
Material behaviour:	Linear elastic
Friction:	without *Coulomb*

6.6 Evaluation of the Results

After solving the global system of equilibrium of the FEM-model the nodal displacements and rotations are available. Knowing these, all internal forces and displacements can be determined at every location of an element.

Using the PLATE- and SOLID- elements of N4W the nodal displacements and the rotations are calculated in the corner nodes and in the centroid of the element. Generally, the most accurate values are obtained in the center of the element. Having elements of higher order, the most accurate results are in the points of integration. The output in the center of the element is very stable but it is impossible to determine the internal forces at any location of the mesh. When examining the stress distribution around holes, it is necessary to determine the stresses at the edges of the elements because the maximum stresses occur there and with increasing distance from the hole they decrease very rapidly. Therefore the element stresses are significantly lower than the nodal values. Furthermore it is important not to use the averaged nodal stress values for the output. The program determines the element stresses of the elements, which are linked with the corresponding node, and calculates the mean value. If the maximum tensile stresses at the boundary hole are displayed, it is important to use the pure nodal values.

Within the parameter studies of chapter 7 and 8 the results of the FE-analyses are compared with the analytical solutions and the results of the experimental investigations.

7 Numerical Parameter Studies

7.1 Introduction

To verify the numerical FEM models the analytical solutions of the cases examined in chapter 4 and 5 are used at first. For the FE-analysis (FEA) the approaches explained in chapter 6 are used. After verifying the FEM model, it is used to examine the influences of different parameters, in particular the following ones:

- Different interlayer materials

- Clearance between bolt and hole

- Friction between bolt and hole

- Eccentric loading

- Variation of the hole diameter and the panel width

- Variation of the distance between hole and edge

Finally two examples of other research works are chosen in this chapter and they will be recalculated and evaluated with the FEM model developed in this thesis.

7.2 Semi-Finite Panel with a Circular Hole

To check whether the chosen parameters given in Table 7.1 are suited within the FE-analysis, the "most simple" case (panel with a circular hole), which has an analytical solution, will be numerically modelled in a first step. The analytical solutions of chapter 4.3.3 are used for the comparison (see Figure 4.9).

The calculations will be executed with MSC.N4W as well as with MSC.Marc in order to determine how big the differences in results are, using different programs. The assorted parameters in Table 7.1 are used for the FE-analyses.

Table 7.1   Parameter of the FE-analyses

Used element type of all components (glass-bushing-bolt):	PLATE-elements (CQUAD) SOLID-elements (CHEXA)
Element mesh around the hole:	Concentric circle Aspect ratio radial 1:1
Elements in circumference of the drill hole:	32 64
Output-result:	Nodal stresses
Analysis:	Linear Nonlinear
Material behaviour:	Linear elastic

As an example for two different panel widths the corresponding curves are shown below. PLATE-elements are used for modelling. Figure 7.1 and Figure 7.2 show the principal tensile stresses σ_{max} as a function of the hole diameter. The linear analyses using MSC.N4W and MSC.Marc are compared with the analytical solution (for input parameter see Table 7.2).

Table 7.2   Input parameter

Panel size (*2bxh*) [mm]	Hole diameter [mm]	Glass thickness *t* [mm]	Load *P* [kN]	Young's modulus *E* [MPa]	Poission's ratio *ν* [–]
variable	variable	10	30	70.000	0,23
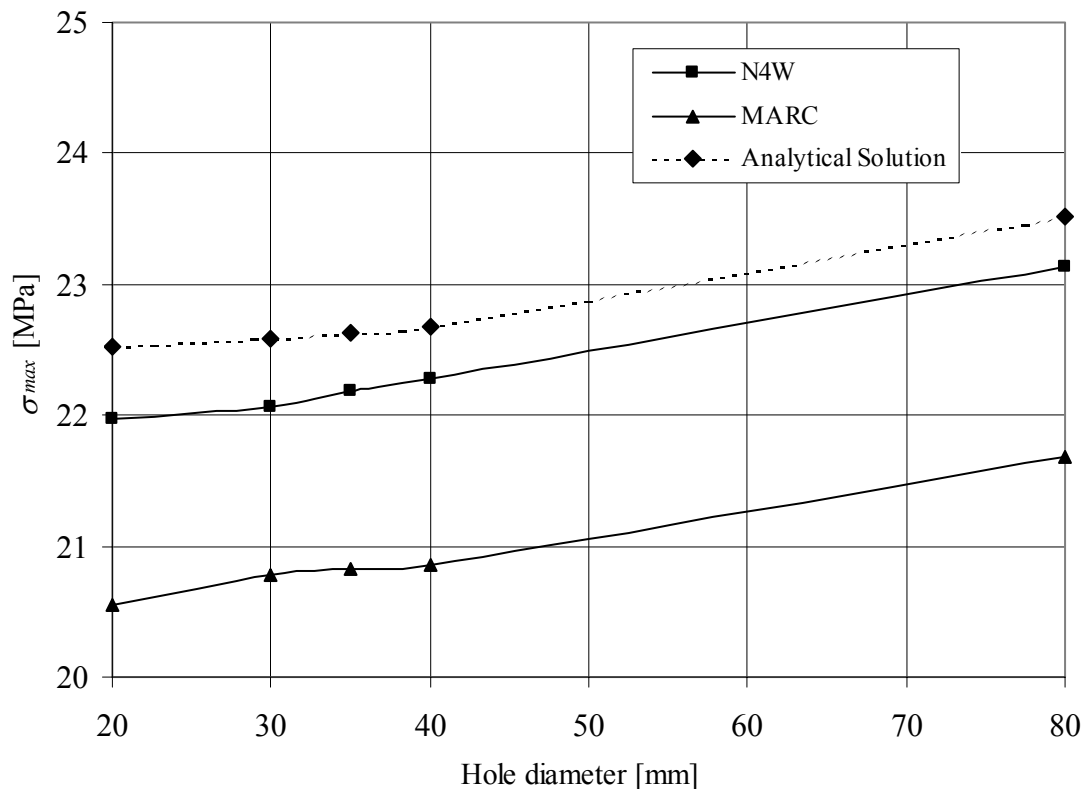
Figure 7.1   Maximum principal tensile stress σ_{max} at the hole boundary, comparison between FEA and analytical solution, panel size 400 mm x 600 mm
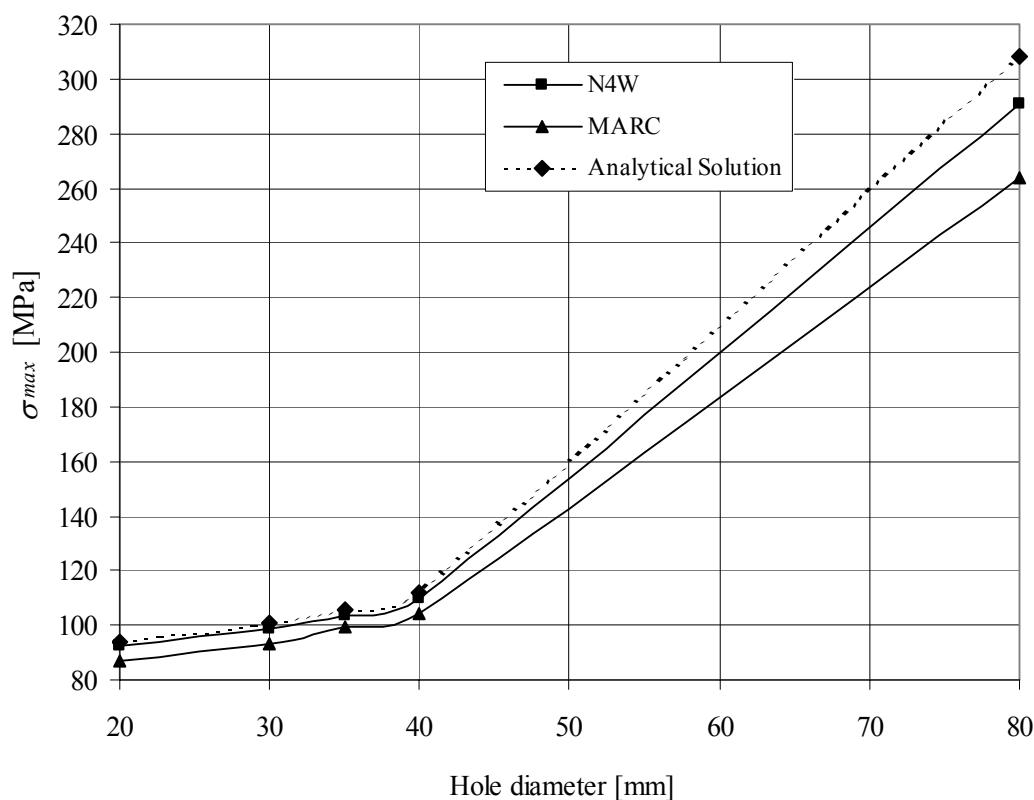
Figure 7.2   Maximum principal tensile stress σ_{max} at the hole boundary, comparison between FEA and analytical solution, panel size 100 mm x 600 mm

Using PLATE-elements for modelling the results of the FE-analysis correspond very well with the analytical solution. The deviation of the analytical value and the linear N4W-analysis amounts about 2% and the MARC-analysis between 5 to 8%. The maximum principal tensile stresses σ_{max} constantly occur perpendicular to the direction of loading.

Additionally it is examined if the accuracy of the calculation can be improved for a hole diameter of 40 mm and panel size 400 mm x 600 mm, if SOLID-elements are used. Whereas the analyses are executed linear and nonlinear. The influence of increasing the number of elements around the hole from 32 to 64 is studied as well. Table 7.3 summarizes the results.

Table 7.3   Results of the parameter study

Program	Element type	Elements across glass thickness	Analysis	σ_{max} [MPa]	
				Elements in circumference: 32	Elements in circumference: 64
N4W	PLATE	-	linear	22,10	22,59
N4W	PLATE	-	nonlinear	19,14	19,97
N4W	SOLID	4	linear	22,35	22,73
N4W	SOLID	4	nonlinear	22,32	22,71
MARC	PLATE	-	linear	21,17	21,66
MARC	SOLID	4	linear	21,28	21,77
Analytical result:				22,7	

The maximum principal tensile stresses σ_{max} constantly occur perpendicular to the direction of loading, which is in conformity with the analytical result. Using 64 elements instead of 32 elements in circumference of the hole, the results are slightly closer with the analytical solution (see Table 7.3).

In the examined case, when using PLATE-elements with the linear analysis, better results are obtained than with the nonlinear analysis. As explained in chapter 6, a nonlinear analysis should be applied only if there are large deformations, material nonlinearities or contact. Due to the iterative approach of the nonlinear analysis and the two-dimensional PLATE-elements, the stress values deviate more from the analytical results. However, using SOLID-elements no nameable difference between linear and nonlinear calculation is determined. It is assumed that, by using the SOLID-elements in general the stresses are determined more precisely.

Using the linear calculation with PLATE-elements the deviation amounts about 2,6% compared to the analytical value. SOLID-elements with 4 elements across thickness have a deviation of about 1,5%.

The examined example is alternatively modelled with 1, 2, 4 and 6 SOLID-elements across thickness. In circumference of the hole 32 elements are used. The analyses are carried out with MSC.N4W. As it can be seen in Figure 7.3, the stress distribution does not change significantly having 4 or more elements. The stress distribution also shows that the maximum occurs on the midplane of the panel and decreases towards the surfaces. This phenomenon is not detectable when modelling with PLATE-elements.
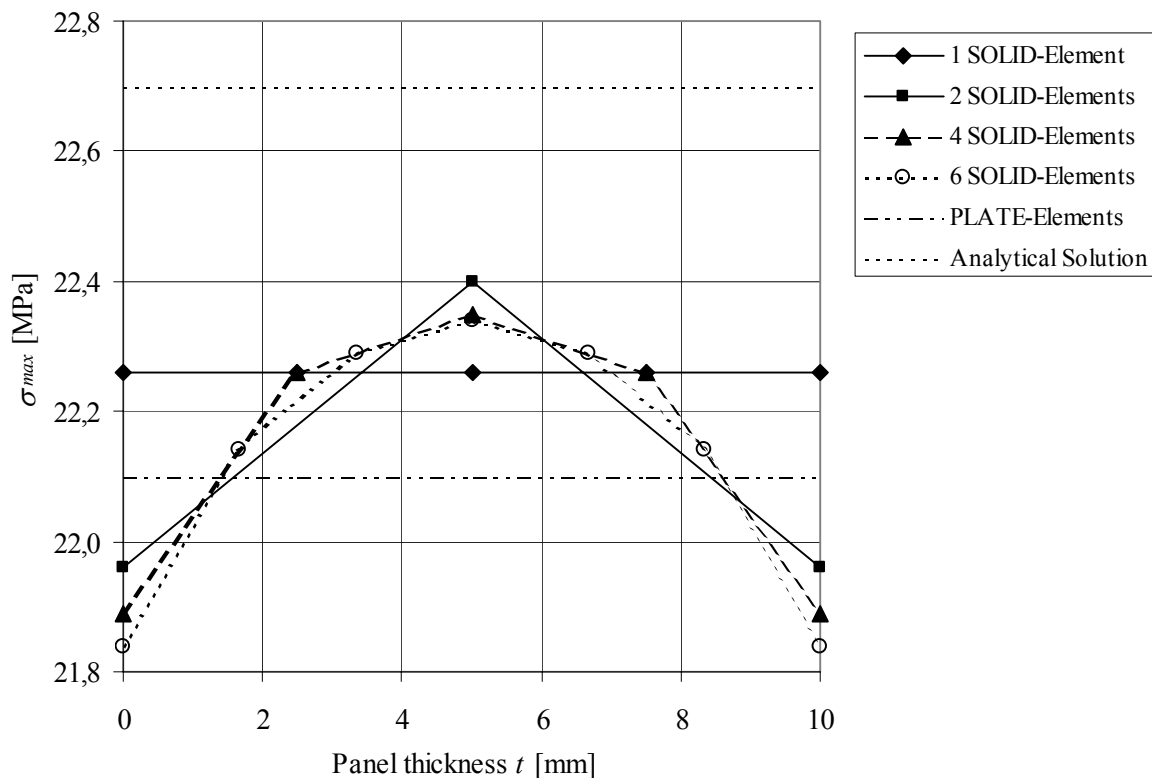
Figure 7.3 Maximum principal tensile stress σ_{max} stress distribution across thickness

The investigations show that using PLATE-elements and 32 elements in circumference of the hole, satisfying results for the examined case (semi-finite panel with a circular hole) can be achieved. The additional effort of computation time and amount of memory using SOLID-elements can be saved. Indeed, it is impossible to determine the stress distribution across thickness.

Whether PLATE-elements are suited for modelling panel and bolt or for contact modelling, will be examined in the following.

7.3 Infinite Panel with Bolt in a Conforming Hole

7.3.1 Verification of the FEM-Model

Now, the next step will be to model the panel with the bolt (see Figure 7.4). The parameters "elements" (PLATE and SOLID) and the type of contact modelling (GAP and CONTACT) will be examined and compared with the analytical result according to chapter 5.3.2. Because of the contact modelling in general the analyses are executed nonlinear (see chapter 6.4.6).

As a result of chapter 7.2, for modelling, 32 elements in circumference of the hole are used. Using SOLID-elements in the following calculations 4 elements across thickness are modelled.
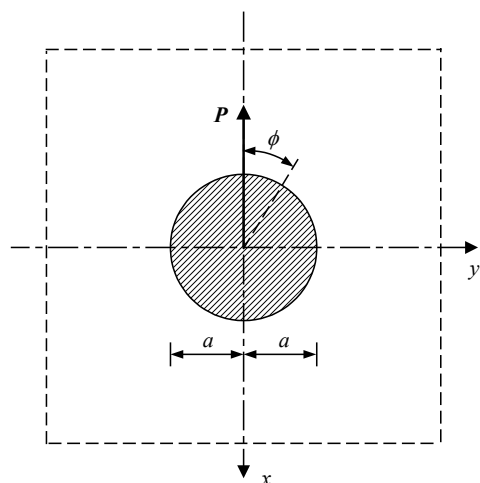
Figure 7.4   Infinite panel with conforming hole and bolt

The load is uniformly distributed over the bolt. Having a panel width of 400 mm and a hole diameter of 40 mm the stress distribution corresponds with the values of the infinite panel (see chapter 4.3, Figure 4.9) and can therefore be compared with the analytical solution. The geometry of the panel and the amount of the load is given in Table 7.4.

Table 7.4   Input parameters

Panel size (*2bxh*) [mm]	Hole diameter [mm]	Panel thickness *t* [mm]	Load *P* [kN]
400 x 600	40	10	30

Table 7.5   Material properties of the aluminium alloy

	AlMgSi0,5 F22
Density ρ	2,7 g/cm^3
Poisson's ratio ν	0,3
Young's modulus E	70.000 MPa

As explained in chapter 5.3.2, the most accurate analytical solution in closed form exists for a panel and bolt both consisting of the same material. For the numerical analysis aluminium according to Table 7.5 is chosen exemplary. It is further assumed that between bolt and hole no clearance occurs, i.e. $\Delta R = 0$.

Different compression stiffness values are studied at first whereas GAP-elements are used because they may influence the numerical results significantly (see chapter 6.4.6). As shown in Figure 7.5 the maximum compressive stresses σ_{min} finally approach the analytical solution asymptotically after attaining a certain value of compression stiffness of the GAP-elements. If the compression stiffness is chosen too small , the results may deviate up to 26%.
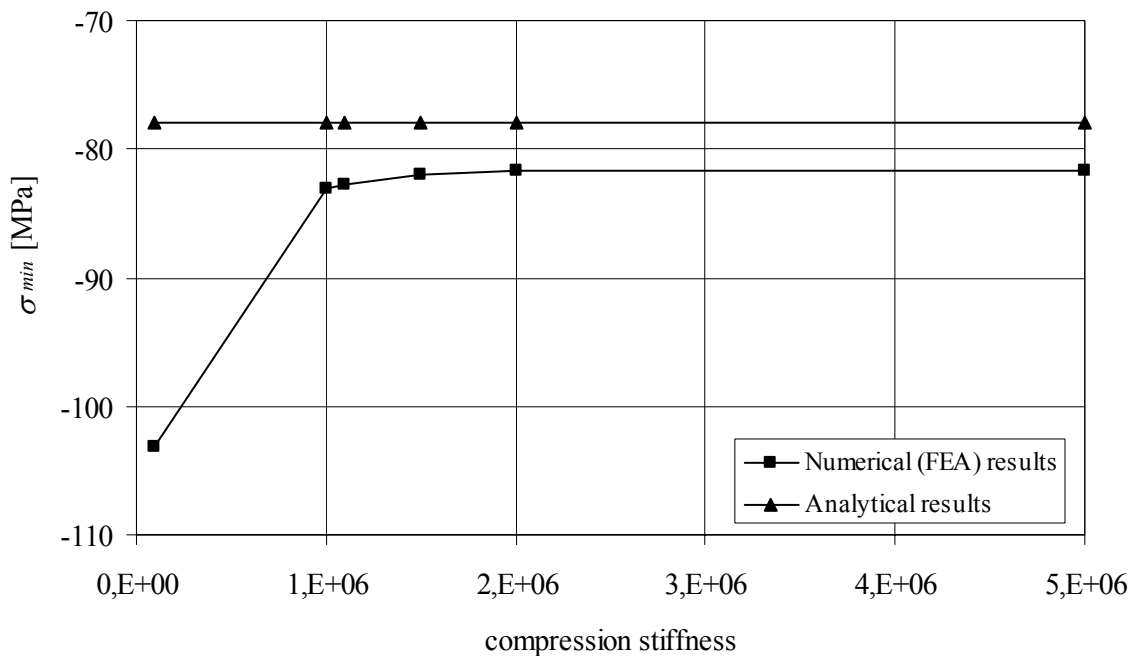
Figure 7.5   Influence of the compression stiffness of the GAP-elements, material combination aluminium-aluminium (Al-Al)

By increasing the compression stiffness the computation time increases as well and additionally convergence problems may occur. According to the results of Figure 7.5 a value of $2 \cdot 10^6$ is chosen for the following parameter study. Therefore, satisfying results are obtained and the computation time is not unnecessary high.

Table 7.6 contains a comparison of the numerical determined maximum tangential and radial stresses with the analytical results. Additionally the location of the maximum stresses are indicated (definition of the angle according to Figure 7.4).

Table 7.6   Maximum stresses of panel with bolt (material Al-Al), $\Delta R=0$

Program	Element type	Type of contact analysis	Max. $p_\phi(\phi)$ [MPa]	Angle ϕ	Max. $p_r(\phi)$ [MPa]	Angle ϕ
N4W	PLATE	GAP	54,57 / 90°		-80,53 / 0°	
N4W	SOLID	GAP	69,22 / 90°		-82,98 / 0°	
MARC	SOLID	CONTACT	68,59 / 90°		-82,19 / 0°	
Analytical result			64,5 / 90°		-78,0 / 0°	

In general the maximum principal tensile stresses occur at 90°, the maximum contact compressive stress at 0° at the midplane. The latter can only be determined in case that SOLID-elements are used.

The results of the FE-analyses are in good conformity with the analytical results: The maximum radial compressive stress value is slightly lower than the analytical solution, the deviation amounts between 3% or 5% depending on the used element type (PLATE or SOLID).

If modelling with PLATE-elements the value of the maximum tangential tensile stress is about 15 % lower than the analytical result. However, using SOLID-elements the deviation is very low: Using GAP-elements the deviation is about 7%, using MARC CONTACT the deviation is about 6%, compared with the analytical solution. Therefore, SOLID-elements are used for the following calculation.

7.3.2 Influence of Different Materials

In the next step the parameter "different materials" will be examined. The panel consists of glass. For the bolt either aluminium or POM-C is used, the material properties are given in Table 7.7. The remaining parameters are retained according to chapter 7.3.1.

Table 7.7   Material properties

	POM-C	AlMgSi0,5 F22	Glass
Density ρ	1,41 g/cm^3	2,7 g/cm^3	2,5 g/cm^3
Poisson's ratio ν	0,35*)	0,3	0,23
Young's modulus E	3200 MPa*)	70.000 MPa	70.000 MPa

*) according to specification of the manufacturer

First it is examined again, which compression stiffness of the GAP-elements are inter-balanced on the materials aluminium and glass as well as POM-C and glass.
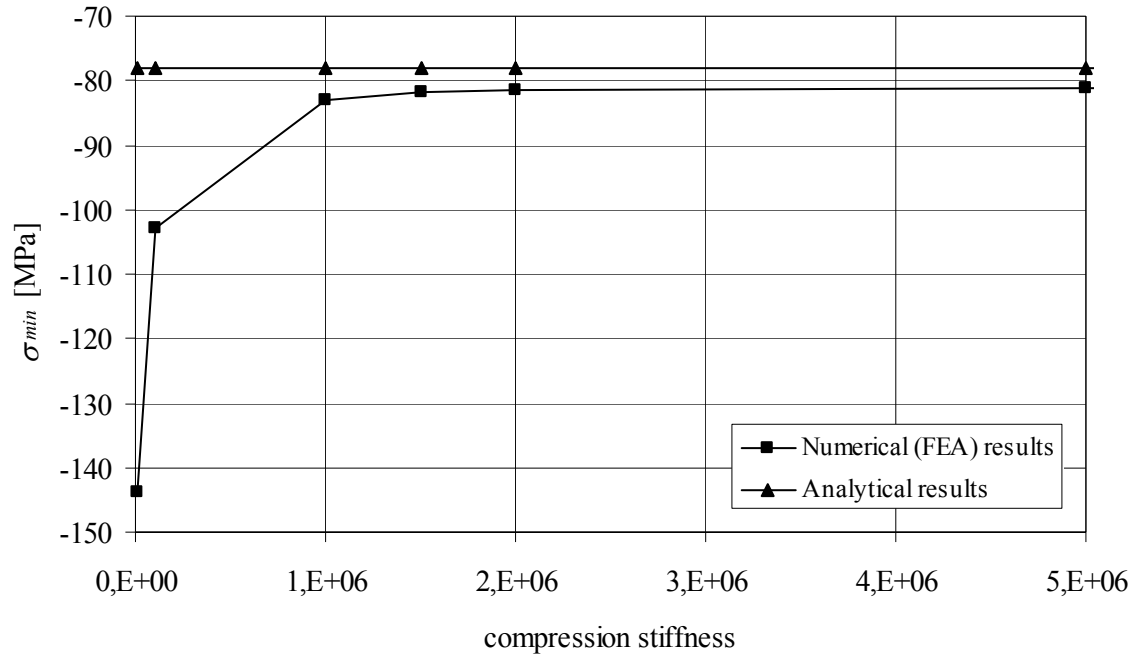
Figure 7.6 Influence of the compression stiffness of the GAP-elements, material combination glass-aluminium
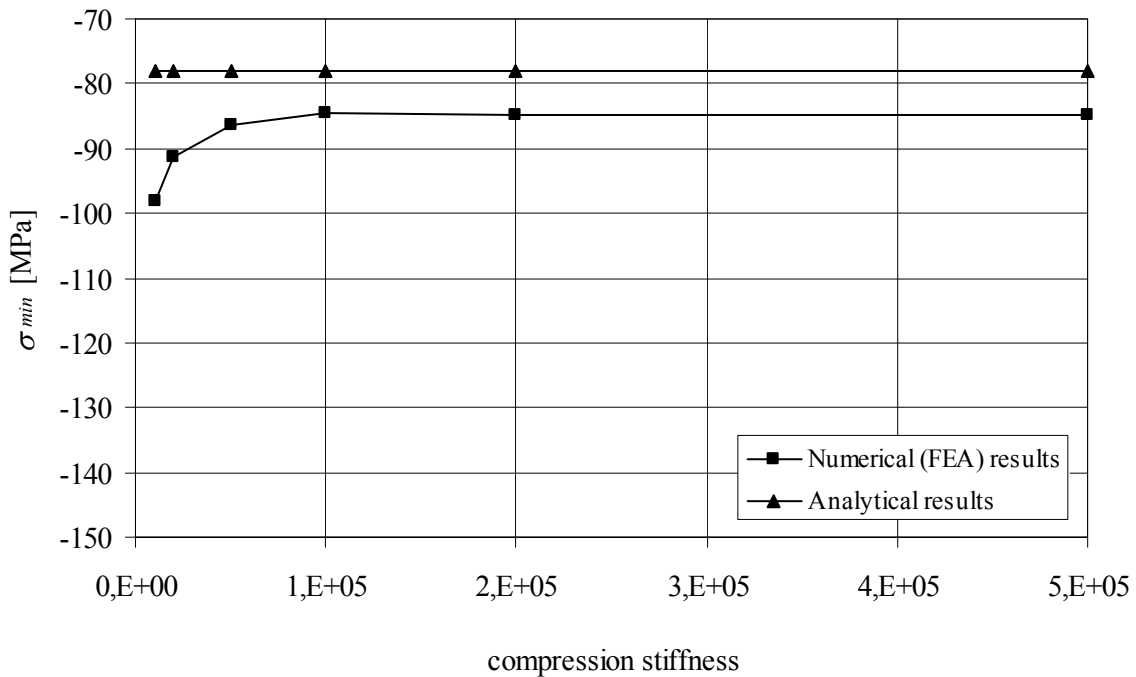
Figure 7.7 Influence of the compression stiffness of the GAP-elements, material combination glass-POM-C

Figure 7.6 shows the minimal principal compressive stresses for the material combination glass-aluminium as a function of the compression stiffness. Starting with a compression stiffness of $2 \cdot 10^6$ the numerical curve converges asymptotically to the analytical solution. Therefore the value $2 \cdot 10^6$ is taken for further calculations. Examining the material combination glass-POM-C, the numerical curve converges asymptotically, starting already with a compression stiffness of $2 \cdot 10^5$ (see Figure 7.7). As a result this value is used for the following analyses, for the material combination glass-POM-C.

Table 7.8   Principal stresses, panel-bolt (glass-Al), $\Delta R = 0$

Program	Element type	Type of contact analysis	σ_{max} [MPa]	Angle ϕ	σ_{min} [MPa]	Angle ϕ
N4W	PLATE	GAP	54,83 / 90°		-80,30 / 0°	
N4W	SOLID	GAP	71,48 / 101°		-83,20 / 0°	
MARC	SOLID	CONTACT	68,39 / 101°		-83,48 / 0°	

Table 7.9   Principal stresses, panel-bolt (glass-POM-C), $\Delta R = 0$

Program	Element type	Type of contact analysis	σ_{max} [MPa]	Angle ϕ	σ_{min} [MPa]	Angle ϕ
N4W	PLATE	GAP	52,81 / 90°		-81,87 / 0°	
N4W	SOLID	GAP	67,71 / 101°		-83,17 / 0°	
MARC	SOLID	CONTACT	64,12 / 101°		-83,36 / 0°	

A comparison of the principal stresses show (Table 7.8 and Table 7.9) that in spite of using different materials the values only differ slightly. Using SOLID-elements with the material combination glass-aluminium the maximum principal tensile stresses are 5,6% (N4W) or 6,3% (MARC) higher than the values for the material combination glass-POM-C.

If using PLATE-elements, the value of the compressive contact stress can be compared with the SOLID-element analysis. The principal tensile stress here is about 23% lower than the calculation using SOLID-elements.

As a result of the analysis using SOLID-elements, the maximum principal tensile stresses do not occur at an angle of 90° but at 101°. It should be noticed that, depending on the mesh size and geometry, the location of the maximum stress can be displaced a few degrees.

The contact modelling with MARC is more user friendly than modelling with GAP-elements but, because of the algorithm explained in chapter 6, very time consuming. In case that symmetries are used (modelling only half of the system), the analyses need still more time than with N4W GAP-elements. Convergence problems will occur, if nodes of contacting bodies (bolt and hole) are very close to each other. That is why the contacting bodies should have different mesh sizes and meshing should be done very accurate. It is also very important to define the contacting bodies in the proper order. As already explained in chapter 6.2, a body with a finer mesh should be defined before a body with a coarser mesh. If the contacting bodies are very close to each other, the application of a bias-factor is recommended (see chapter 6.4.3).

7.3.3 Influence of a Clearance

The examined example will now be modified by introducing a certain clearance between bolt and hole. Different clearance magnitudes will be examined. At first, the analyses are carried out with GAP-elements. The results for the bolt materials aluminium and POM-C are listed in Table 7.10 and Table 7.11.

Table 7.10 Principal stresses, panel-bolt (glass-Al), $\Delta R \geq 0$

Element type	Type of contact analysis	Clearance ΔR [mm]	σ_{max} [MPa]	Angle ϕ	σ_{min} [MPa]	Angle ϕ
SOLID	GAP	0,0	71,48 / 101°		-83,20 / 0°	
SOLID	GAP	0,2	94,60 / 67°		-119,50 / 0°	
SOLID	GAP	0,5	99,97 / 57°		-163,70 / 0°	
SOLID	GAP	1,0	107,60 / 45°		-218,30 / 0°	
SOLID	GAP	2,0	119,00 / 34°		-308,40 / 0°	

Table 7.11 Principal stresses, panel-bolt (glass-POM-C), $R \geq 0$

Element type	Type of contact analysis	Clearance ΔR [mm]	σ_{max} [MPa]	Angle ϕ	σ_{min} [MPa]	Angle ϕ
SOLID	GAP	0,0	67,71 / 101°		-83,17 / 0°	
SOLID	GAP	0,2	76,82 / 79°		-89,44 / 10°	
PLATE	GAP	0,2	62,92 / 68°-78°		-91,96 / 0°-10°	
SOLID	GAP	0,5	84,62 / 67°		-96,50 / 10°	
SOLID	GAP	1,0	87,99 / 56°		-108,34 / 10°	
SOLID	GAP	2,0	93,88 / 56°		-126,20 / 10°	

With increasing clearance the stresses increase significantly and the size of the contact angle reduces. That is why the location of the maximum principal tensile stresses displaces up to 67° towards the direction of loading. If aluminium is used for the bolt, the increase in stresses is higher than with POM-C. With a clearance of 2 mm for the aluminium bolt, the maximum principal tensile stress amounts 119 MPa at $\phi = 34°$ and for the POM-C bolt the value is 94 MPa at $\phi = 56°$. Compared to the neat-fit connection ($\Delta R = 0$) the increase in stresses is about 66% for aluminium and about 39% for POM-C (see Figure 7.8).

For both materials (aluminium, POM-C) and clearance $\Delta R = 0$ and $\Delta R = 2$ mm the dimensionless tangential stress distribution are clearly presented in Figure 7.8. With increasing clearance depending on the bolt material the tangential stresses attain negative values in a range of about 0° to 15°. However, if the bolt fits exactly in the hole ($\Delta R = 0$), the tangential stresses are constantly positive and the influence of different bolt materials are hardly ascertainable. This result corresponds to the analytical investigations (see chapter 5).

When $\Delta R > 0$, for the glass-aluminium combination the maximum compressive stress occurs at an angle of 0°. For the combination glass-POM-C the maximum occurs at 10° (Table 7.8 und Table 7.9).
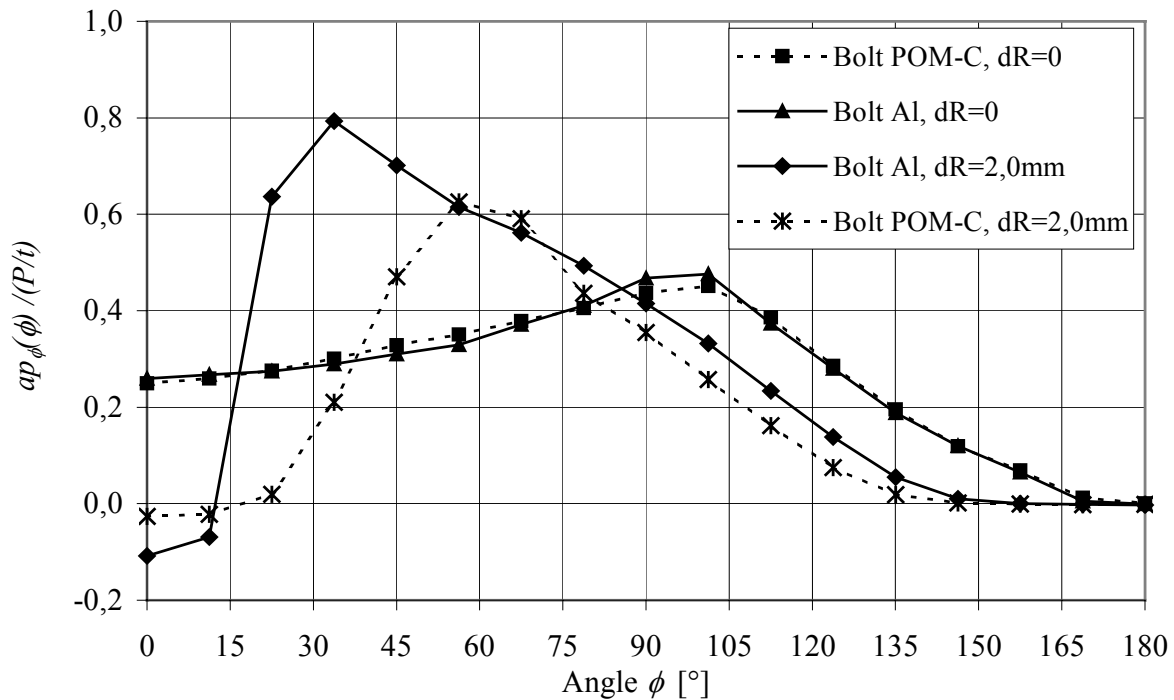
Figure 7.8   Dimensionless tangential stress distribution, influence of a clearance

Additionally, the analysis is carried out with PLATE-elements, taking a clearance of 0,2 mm and the material combination glass-POM-C. It is determined that the maximum principal tensile stress is significantly lower and that the maximum stress value is expanded on a larger area than with SOLID-elements. When using PLATE-elements, the maximum stresses can therefore only be determined roughly (see Figure 7.9 and Figure 7.10). The maximum tensile stress appears in a range of 68° to 78° and the maximum compressive stress appears in a range of 0° to 10°.
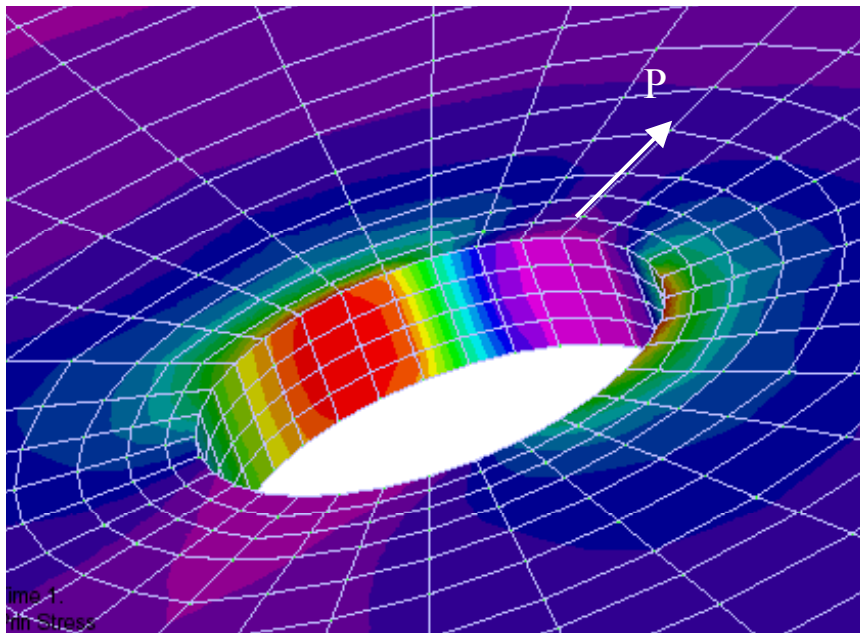
Figure 7.9   Distribution of the max. principal tensile stresses, SOLID-elements
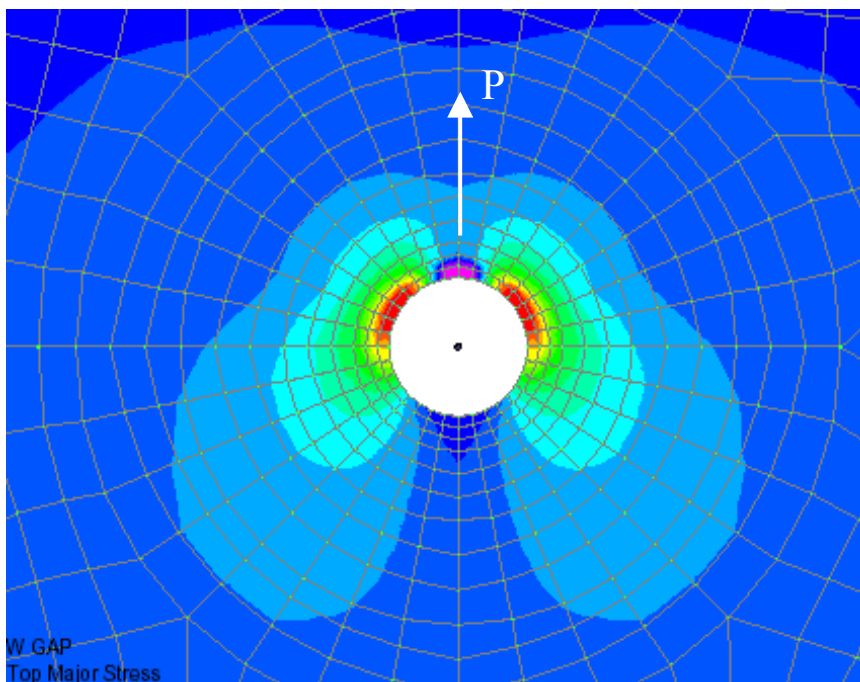
Figure 7.10 Distribution of the max. principal tensile stresses, PLATE-elements

The analyses with GAP-elements show that with increasing clearance the computation time increases. Partial convergence will only be obtained in case that the number of load increments and iteration steps are increased. Using MARC the extension of the clearance does not lead to convergence problems.

7.3.4 Influence of Friction

In the following the parameter "friction" will be examined (see also chapter 5.3.4, 6.4.3 and 6.4.6). The friction coefficient is influenced by a variety of parameters. Friction is a complex physical phenomenon that involves the characteristics of the surface, such as surface roughness, temperature, duration of loading and relative velocity. Furthermore, the materials of the contacting bodies and the surrounding medium such as the presence of lubricants have an influence on the friction parameter. In order to determine the exact friction coefficients experimental investigations are necessary. Very often, only limit values within certain ranges are given in literature. Indeed the friction coefficients could not be found in literature for the two different material combinations, glass-aluminium and glass-POM-C, which are examined within the scope of this thesis. In [Czichos, Habig 2003] only an inaccurate defined static friction coefficient $\mu_H = 0{,}6$ for the material combination glass-steel and for the combination glass-glass $\mu_H = 1{,}0$ is given.

As already mentioned, the influence of friction should be determined experimentally. The actual physics of friction and its experimental investigations continue to be topics of research and would exceed the scope of this thesis. Therefore different static friction coefficients μ_H are used to determine the influence of friction on the stress distribution.

In Figure 7.11 to Figure 7.14 the dimensionless tangential and radial stress distributions are shown for different friction coefficients μ_H and for the two different material combinations glass-aluminium and glass-POM-C. The clearance ΔR is assumed to be zero ($\Delta R = 0$).

In general it is determined that by increasing the friction coefficient μ_H the tangential stress p_ϕ increases and the contact compressive stress p_r decreases. These results correspond to the investigations made by [Iyer 2001], (see chapter 5.3.4). It is not dependent on the material combination in the examined case with a friction coefficient $\mu_H = 1{,}0$ that the tangential stresses are up to 30% higher compared with the frictionless connection. However, the radial stresses are 30% lower compared with the frictionless connection.
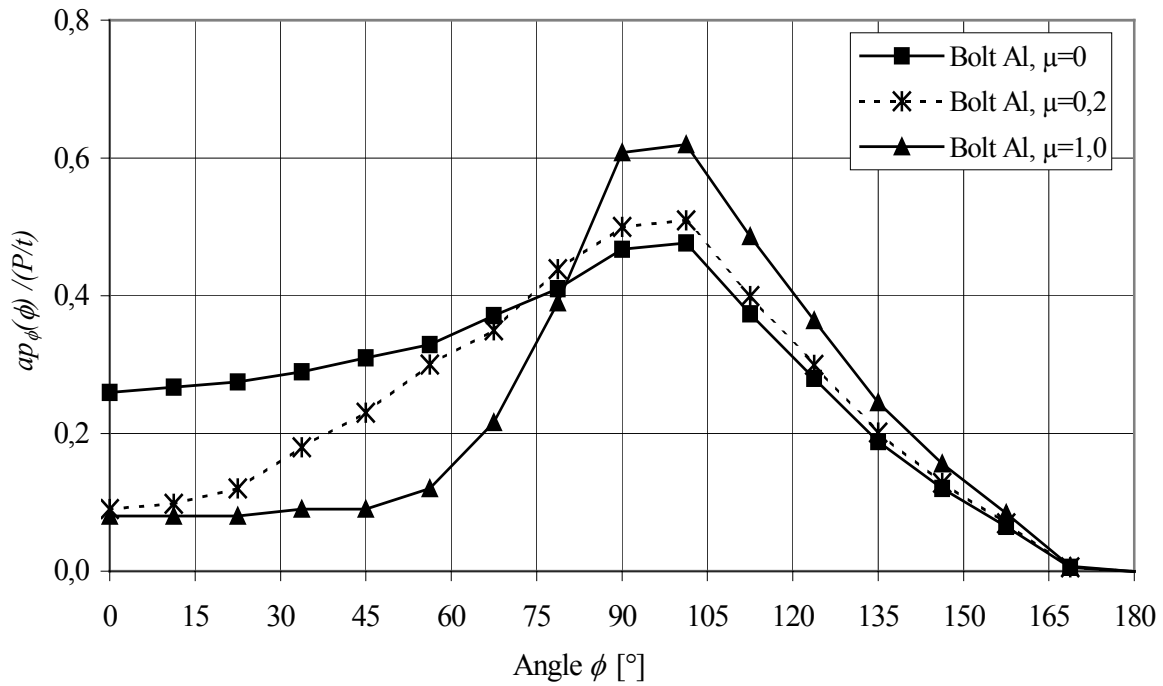
Figure 7.11 Dimensionless tangential stress distribution, influence of different friction coefficients, material combination glass-aluminium
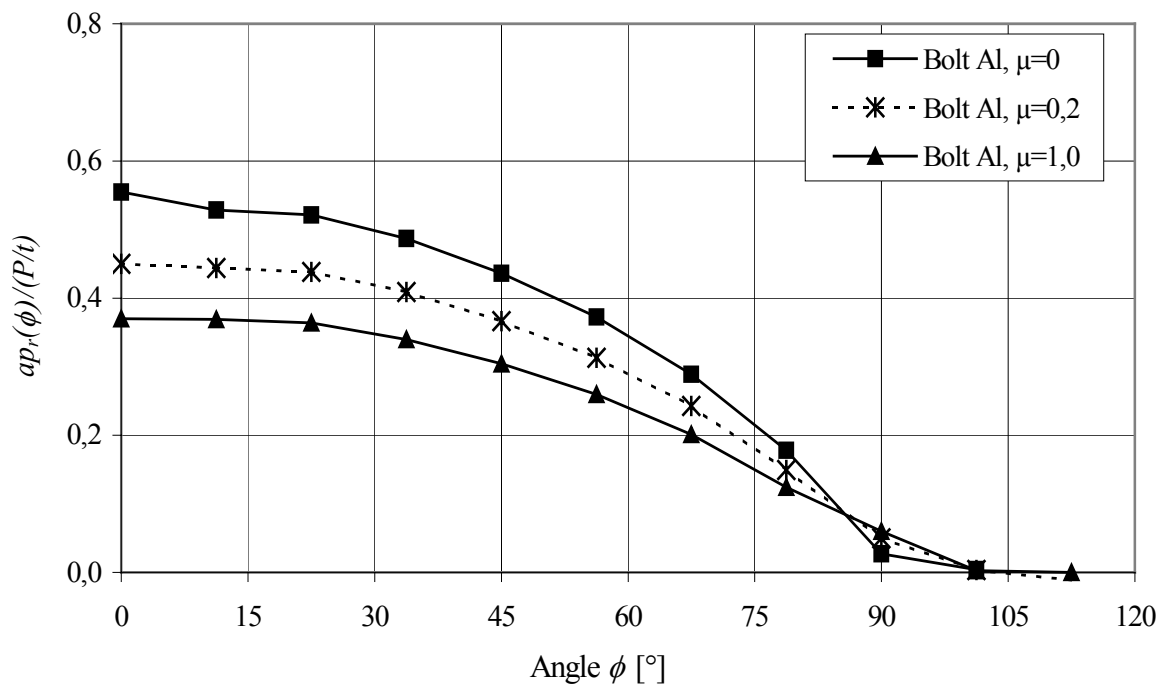
Figure 7.12 Dimensionless radial stress distribution, influence of different friction coefficients, material combination glass-aluminium
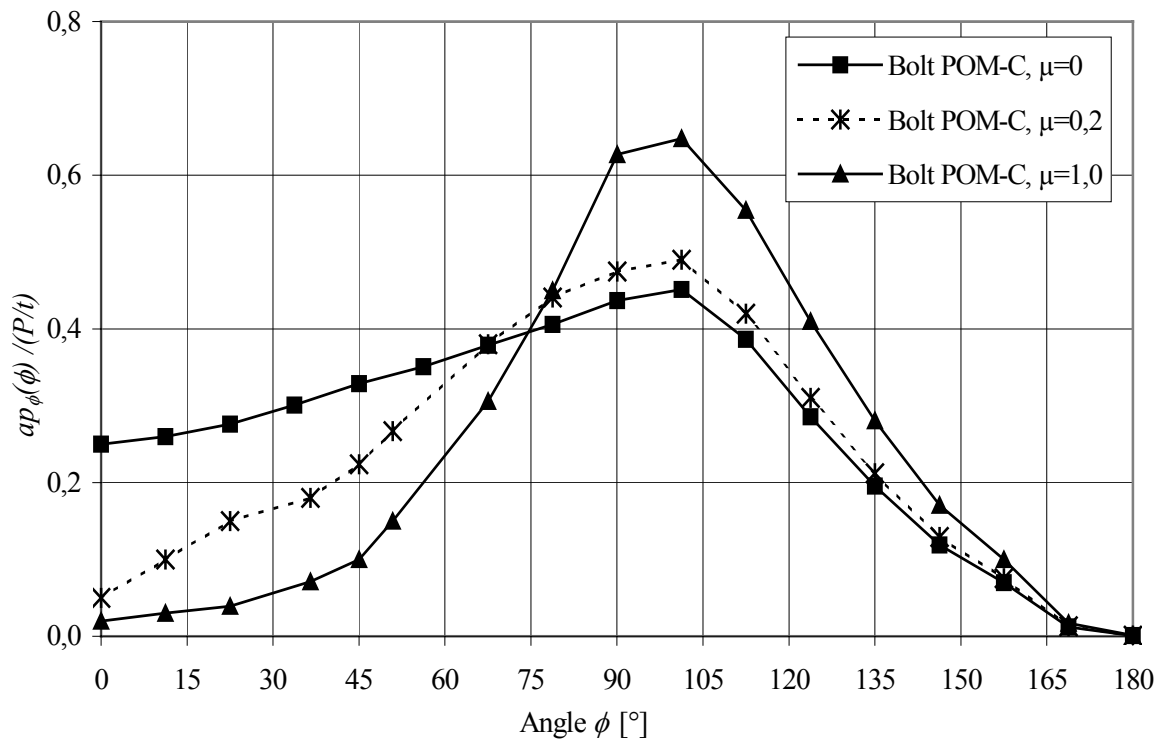
Figure 7.13 Dimensionless tangential stress distribution, influence of different friction
coefficients, material combination glass-POM-C
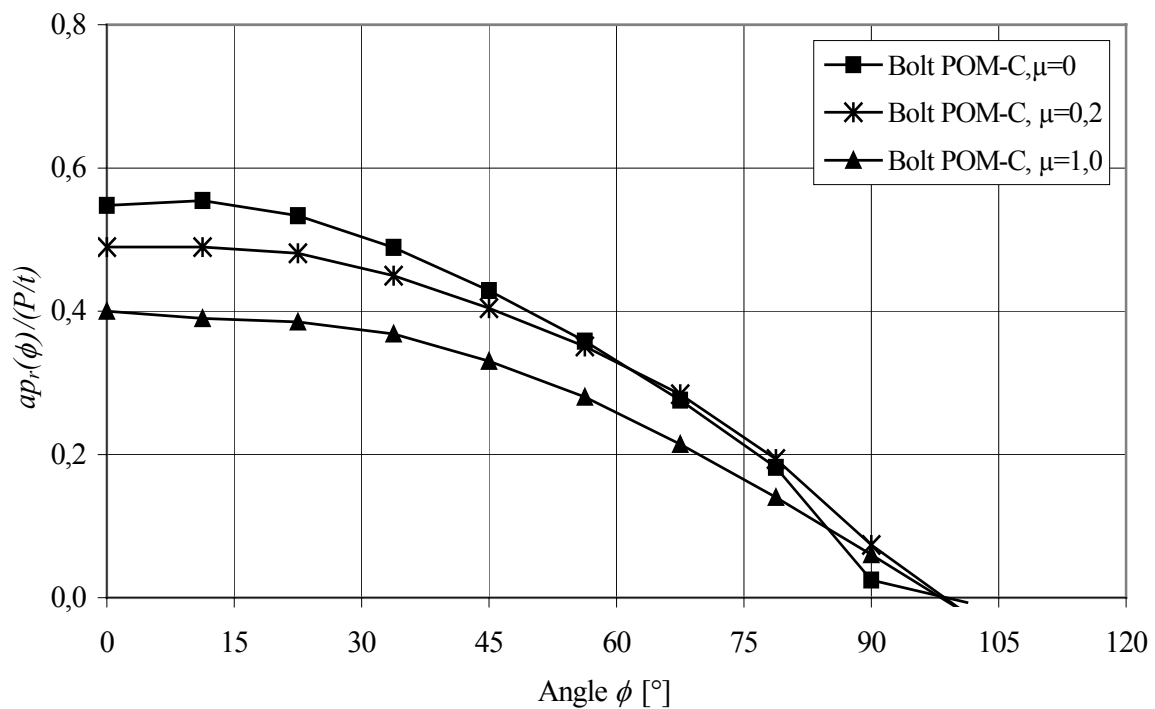
Figure 7.14 Dimensionless radial stress distribution, influence of different friction
coefficients, material combination glass-POM-C

The analyses are carried out with the MARC CONTACT function because, having higher friction coefficients, the N4W GAP-elements cause convergence problems. An other advantage is that investigations concerning the convergence controls of the GAP stiffness values (compression stiffness und transverse stiffness, see chapter 6 and 7.3.1) are dispensable.

7.3.5 Influence of an Eccentric Load Application

In practice, inaccuracies occur very often during the installation of a construction. Therefore the influence of an eccentric load application is of special interest. With the help of taking an example without clearance ($\Delta R = 0$) and one with clearance ($\Delta R = 0{,}2$ mm) this will be examined in the following. Then the load is distributed over the bolt in a non-uniform way, but only applied on one end of bolt. The example is calculated for an infinite panel with the material combination glass-aluminium.

Compared with the central loading the maximum stresses do not occur on the midplane anymore but, as expected, on the corresponding surface of load application. Without clearance the maximum principal tensile stress increases by 7,5%, the corresponding compressive stress increases by 7% compared with the central loading. Having an additional clearance of $\Delta R = 0{,}2$ mm, the principal tensile stress increases by approximately 35%. The principal compressive stress even increases by approximately 76%.

In Figure 7.15 to Figure 7.18 the distributions of the principal stresses are schematically represented for central and eccentric loading. The clearance amounts $\Delta R = 0{,}2$ mm.
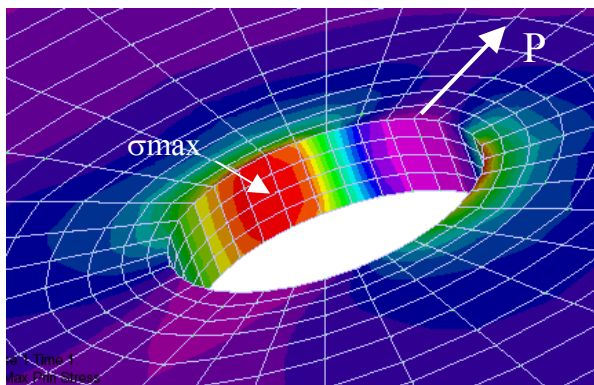
Figure 7.15 Max. principal tensile stress, central applied load, ΔR=0,2 mm
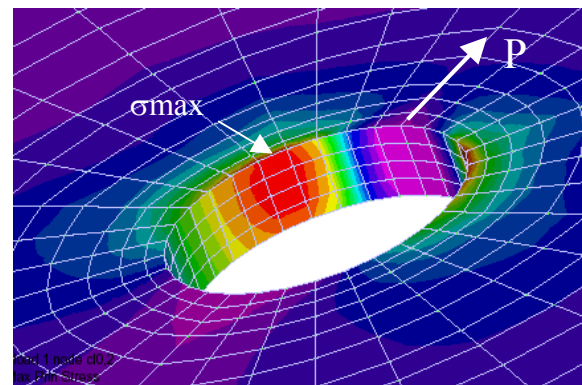
Figure 7.16   Max. principal tensile stress, eccentric applied load, ΔR=0,2 mm
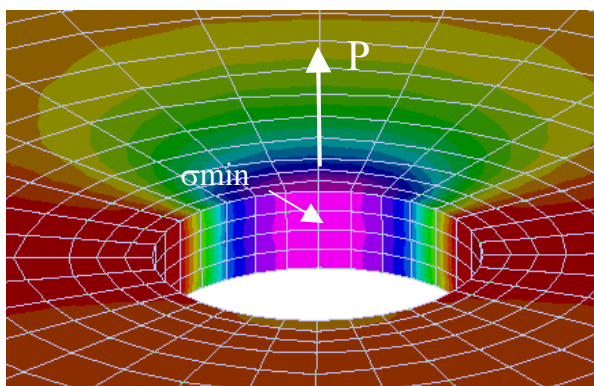
Figure 7.17 Min. principal compression stress, central applied load, ΔR=0,2 mm
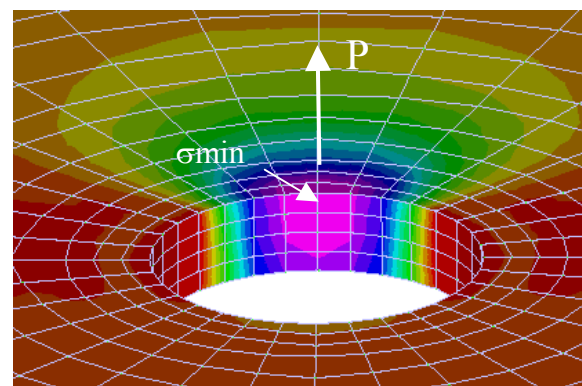
Figure 7.18   Min. principal compression stress, eccentric applied load, ΔR=0,2 mm

7.4 Semi-Finite Panel with a Bolt in a Conforming Hole

7.4.1 Introduction

In chapter 5.3.3 an analytical solution in closed form was introduced for the semi-finite panel with a bolt in a conforming hole with the help of stress concentration factors. These investigations were based on experiments. To verify the numerical determined stress distributions this analytical solution will be used.

The examined parameters are now: panel width, hole diameter or the ratio *a/b* and the distance *H* between hole center point and panel edge (see Figure 7.19). The influence of the parameters on the stress distribution will be examined in particular for the semi-finite panel. The clearance is assumed to be zero ($\Delta R = 0$).
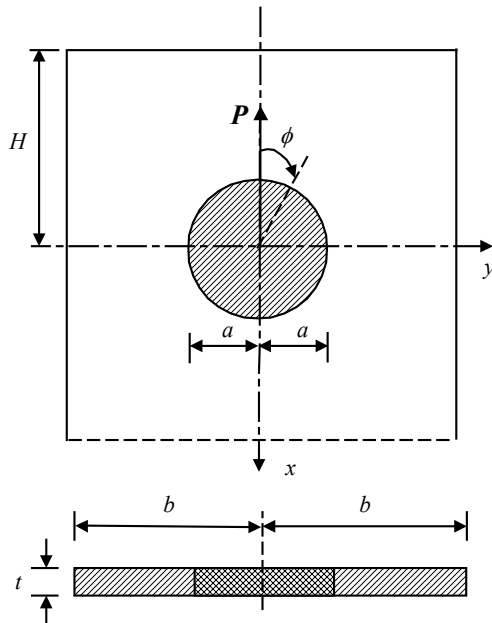
Figure 7.19 Bolted connection in a semi-finite panel

7.4.2 Influence of the Hole Diameter and the Panel Width

At first, the parameters hole diameter and panel width will be examined. Subsequently, the results will be compared with those of the infinite panel. The input parameters of the finite panel are given in Table 7.12. The hole diameter is variable and the hole is located in the center of the panel strip. The clearance is assumed to be zero ($\Delta R = 0$).

Table 7.12 Input parameters

Panel size (*2bxh*) [mm]	Hole diameter [mm]	Glass thickness *t* [mm]	Load *P* [kN]
100 x 600	variable	10	30

Figure 7.20 shows the maximum principal tensile stresses σ_{max} as a function of the ratio *a/b*. Compared are the material combinations glass-aluminium, glass-POM-C and the approximate analytical solution according to *Pilkey* and *Frocht and Hill*.
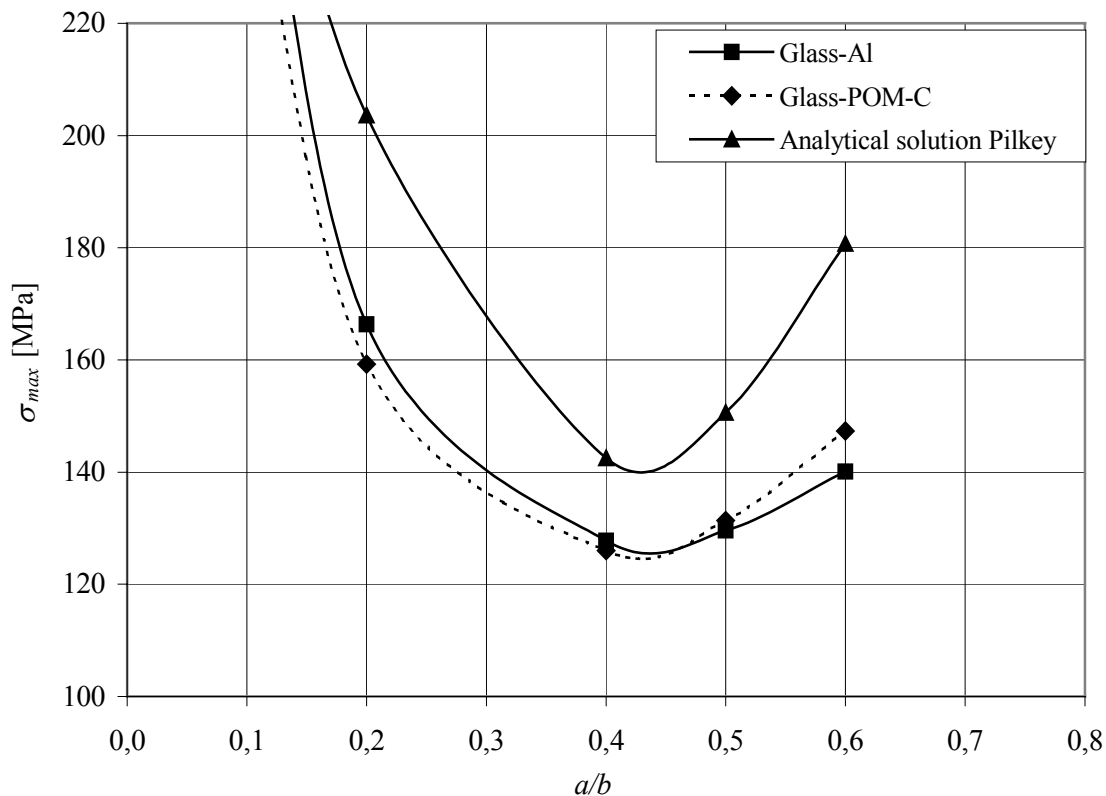
Figure 7.20 Influence of the ratio *a/b* on the principal tensile stresses

If the ratio of drill hole radius *a* and *b* lies in the range of $0,1 < a/b \leq 0,2$, the stresses increase enormously or tend to infinity. An interesting aspect is that for values $a/b > 0,2$ the stresses decrease until a minimum is reached between $a/b = 0,4$ and 0,5. Afterwards, the values rise again. This distribution was also determined by *Theocaris* (see chapter 5.3.3). An interesting aspect is the stress distribution for the material combination glass-POM-C. The tensile stresses are below those of the material combination glass-aluminium until the ratio $a/b = 0,4$ is reached, thereafter the stresses obtain higher values than the material combination glass-aluminium. This means that when the hole is located closer to the edge and a soft material like POM-C is used for the bolt the deformations and the tensile stresses are higher than using a stiffer material like aluminium.

The shape of the analytical calculated curve is similar to the numerical determined curves but they are not congruent. One reason for the deviation is that the approximate solution of *Pilkey* is based on experimental investigations made by *Forcht and Hill*, who used different materials (aluminium and steel) than in this investigation. As already explained, the influence of different materials on the stress distribution is only small unless the clearance is assumed to be zero ($\Delta R = 0$). Additionally, the experimental based solution includes friction which is not considered in the numerical analysis and therefore is responsible for the main part of the deviation. As shown in chapter 7.3.4, dependent on the friction coefficient μ_H, the tangential stresses increase up to 30% compared with the frictionless connection.

Comparing the tangential stresses of finite (width 100 mm) and infinite panel (see Figure 7.21 and Figure 7.23), a reduction in panel width results in a significant stress increase: considering the finite panel the maximum tangential stresses for the material combination glass-aluminium are about 79% higher than the values of the infinite panel and 86% higher for glass-POM-C. On the contrary the panel width has no significant influence on the radial stresses (see Figure 7.22 and Figure 7.24).
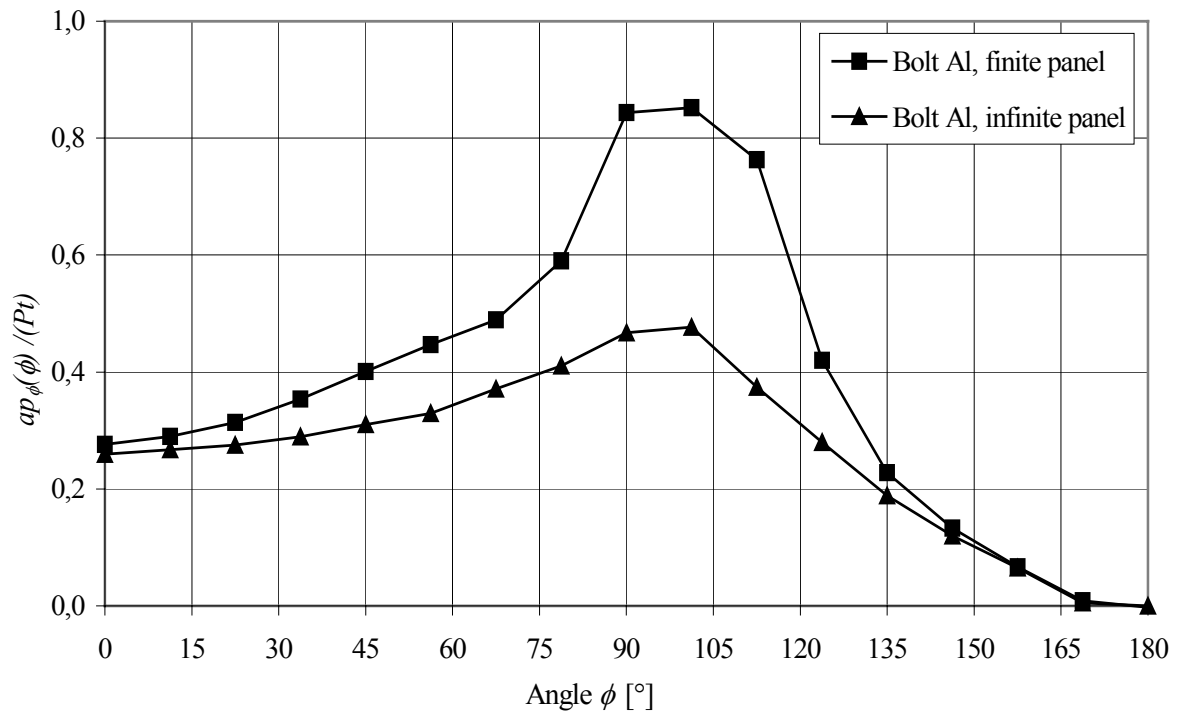
Figure 7.21 Tangential stress distributions of infinite and finite panel, material combination glass-aluminium
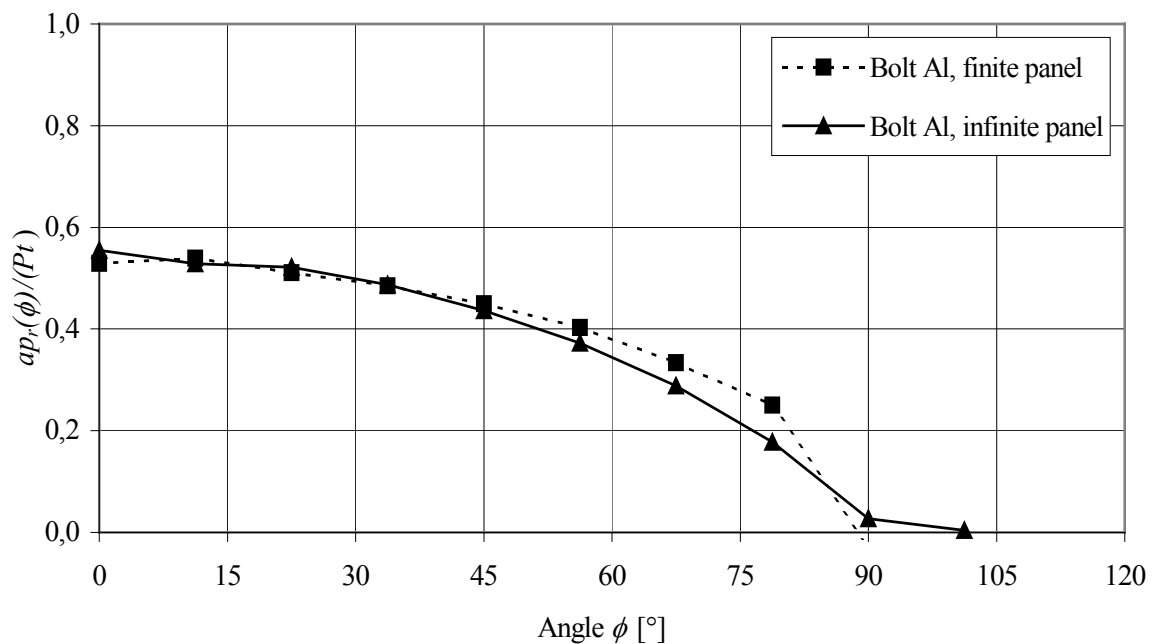
Figure 7.22 Radial stress distributions of infinite and finite panel, material combination glass-aluminium
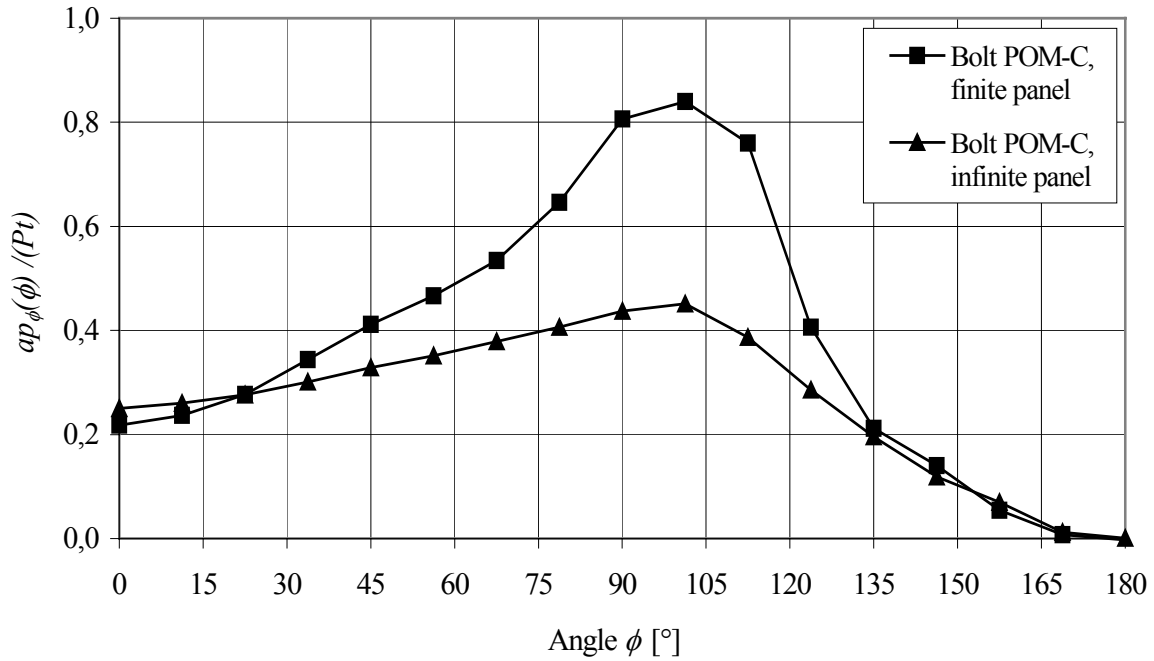
Figure 7.23 Tangential stress distributions of infinite and finite panel, material combination glass-POM-C
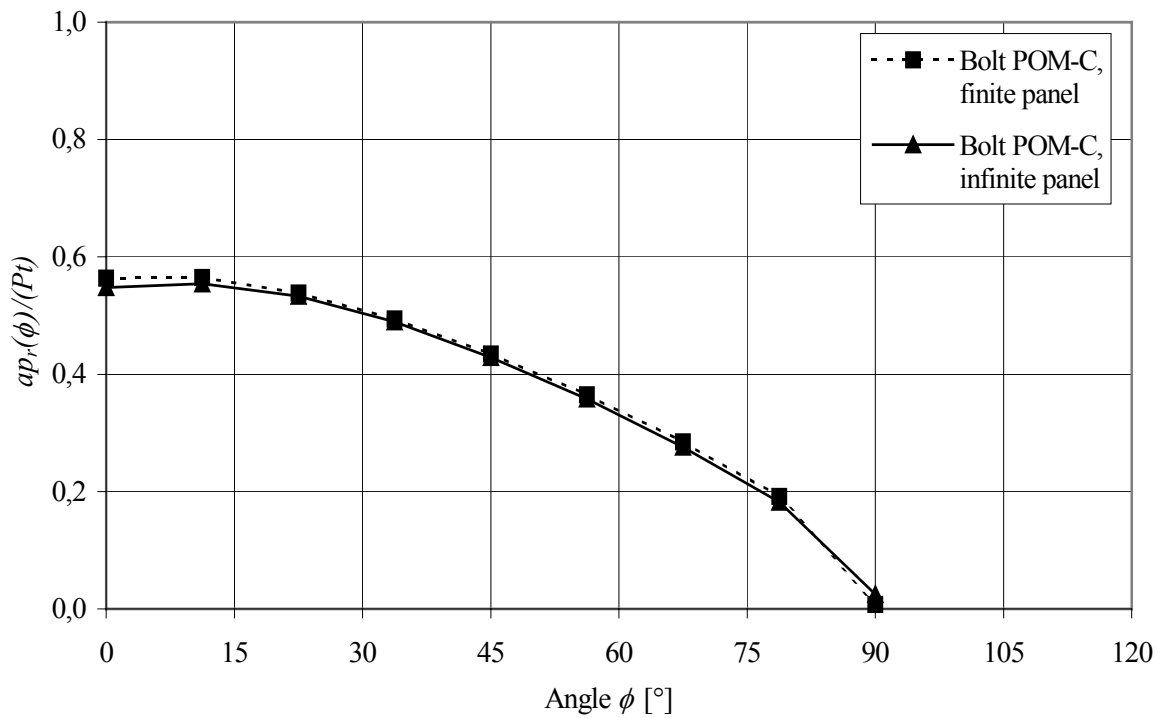
Figure 7.24 Radial stress distributions of infinite and finite panel, material combination glass- POM-C

7.4.3 Influence of the Distance between Hole and Edge

Not only the panel width but also the distance between the hole and the edge of the panel have an influence on the magnitude of the principal stresses. The following analysis is based on the parameter according to Table 7.12. The distance H is variable (see Figure 7.19). Figure 7.25 contains the distribution of the principal tensile stresses as a function of the ratio a/b, where H = 50 mm or H = 100 mm. To allow a comparison the stress distribution for the panel with the centrally located hole is given in Figure 7.25. As represented in Figure 7.25, the principal tensile stresses increase with the reduction of the distance H. If the ratio a/b for a chosen edge distance of H = 50 mm decreases additionally the stresses tend to infinity for $a/b < 0{,}4$. In the range of $0{,}4 \leq a/b \leq 0{,}5$ the values of principal tensile stresses increase only about 10% compared with the values of the panel with a central hole.

However, having a distance H = 100 mm, the values approach almost the stress values of the panel with the centrally located hole.
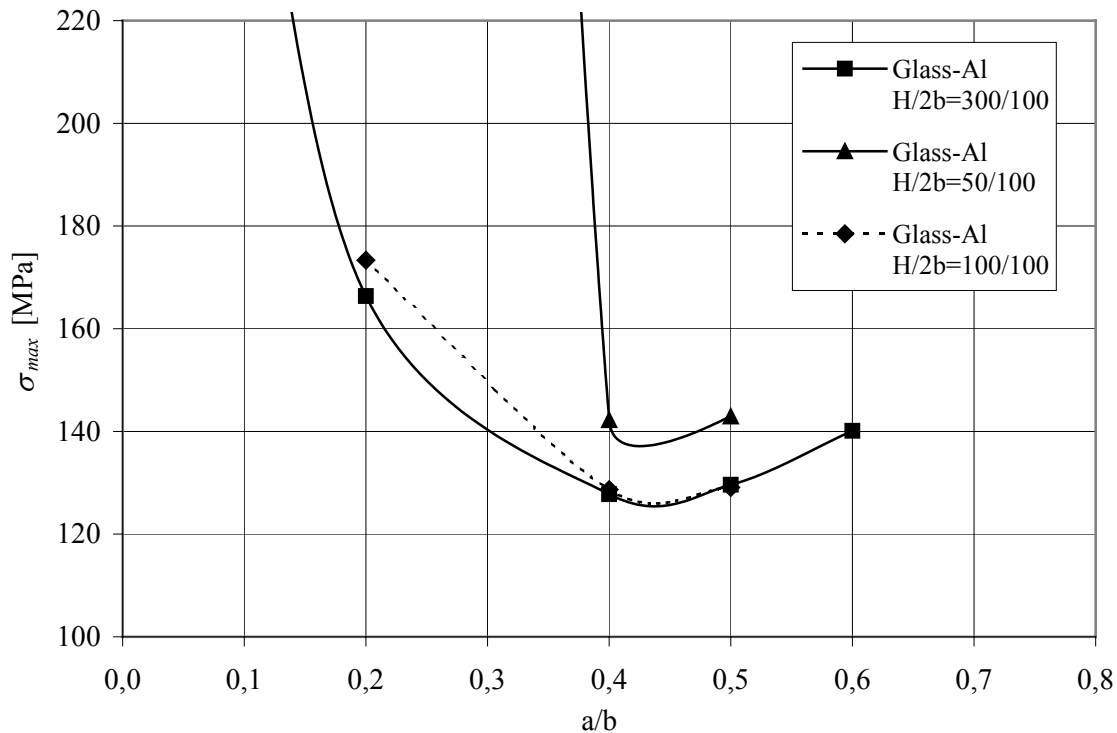
Figure 7.25 Distribution of the principal tensile stresses as a function of the ratio a/b and the distance H

Having a constant distance H, but increasing the hole diameter at the same time, the distance between hole boundary and panel edge decreases respectively. The tangential and radial stresses decrease therefore. By increasing the hole diameter from 20 to 50 mm, where the distance H = 50 mm is constant, the tangential and radial stresses decrease up to 90%. At the same time the maximum contact pressure does not occur at an angle of $\phi = 0°$ but, dependent on the ratio a/b, will be displaced up to $\phi = 45°$, for $a/b = 0{,}5$ (see Figure 7.26). In contrast, the location of the tangential stresses remains unchanged at about $\phi = 101°$.
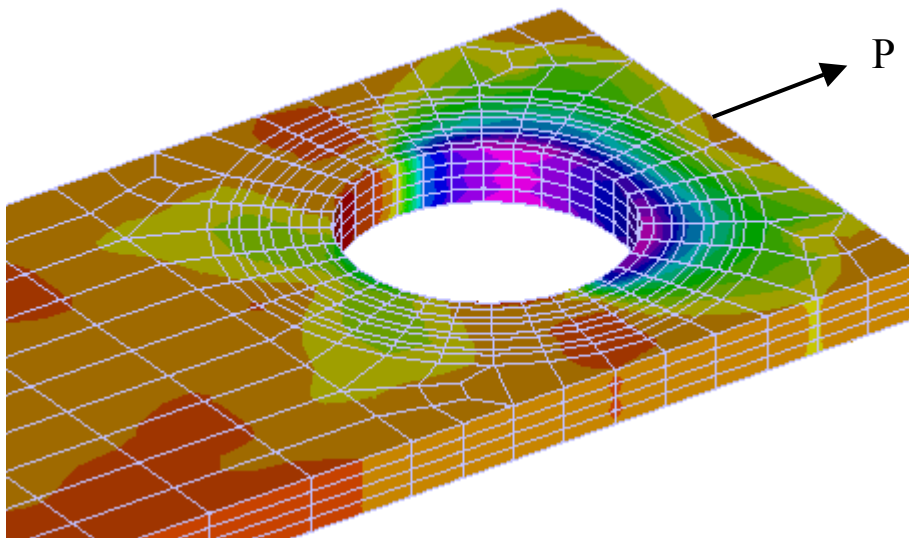
Figure 7.26 Distribution of the contact pressure, where *H*=50 mm, *a/b*=0,5

7.5 Comparison with other Research

7.5.1 Introduction

Based on the FEM-models which were developed within the parameter studies two examples of other research works will be now recalculated. The examples of the research works are based on other approaches or FEM-program. Therefore an additional verification of the own approach is possible as well as an appraisal of the methods used in these research investigations.

7.5.2 Investigations carried out by *Techen*

[Techen 1997] carried out experimental investigations with bolted connections. The gap between bolt and hole was filled with different two-component resins. The bolt fitted exactly in the hole without clearance. With the help of tension tests *Techen* determined the magnitude of the failure loads and the location of the initial crack. The initial crack was determined at an angle of $\phi = 45°$. To calculate the stresses with the help of the failure loads he carried out additionally FE-analyses but did not receive any proper results. That is why *Techen* used the analytical solution according to [Girkmann 1963] which presumes that both bolt and panel consist of the same elastic material and no clearance ($\Delta R = 0$) occurs (see chapter 5.3.2). Knowing the angle of $\phi = 45°$ and the corresponding failure load from the experiments the maximum tensile stress was then calculated.

To check the approach according to *Techen* the following example will be recalculated. [Siebert 2004] contains an analysis of this example as well. Therefore, an additional verification is possible.

The geometry and the material properties are given in Table 7.13 and Table 7.14.

Table 7.13   Input parameters

Panel size (*2bxh*) [mm]	Hole diameter [mm]	Bolt diameter [mm]	Interlayer thickness [mm]	Glass thickness *t* [mm]
300 x 500	24	16	4	12

Table 7.14   Material properties

	Interlayer resin	Bolt steel S235	Glass
Poisson's ratio ν	0,3 - 0,49	0,3	0,23
Young's modulus E	3240 MPa	210.000 MPa	70.000 MPa

Techen does not specify Poisson's ratio ν but, according to references, the limit values ν = 0,3 and ν = 0,49 are examined.

The location of the hole is given in Figure 7.27.
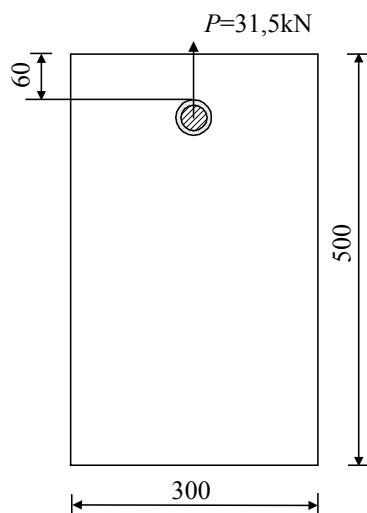
Figure 7.27   Location of the drill hole

In the following modelling is carried out according to the previous FEM-analyses. 32 elements are chosen in circumference of the hole and, using SOLID-elements additionally, 4 elements are chosen across panel thickness. The load is uniformly distributed on the bolt length. In Table 7.15 the results are listed.

Table 7.15   Result overview

Material properties resin	σ_{max} [MPa]	Angle ϕ	σ_{min} [MPa]	Angle ϕ
E=3240 MPa ν=0,49	110,76 / 90°		-149,54 / 0°	
E=3240 MPa ν=0,3	115,21 / 90°		-139,71 / 0°	
Result *Techen* E=3240 MPa ν=?	139,3 / 45°		-	
Result *Siebert* E=2000 MPa ν=0,49	113,7 / 90°		-	

Reducing Poisson's ratio ν from 0,49 to 0,3 the principal tensile stresses calculated by FE-analysis increase slightly from 111 MPa to 115 MPa. The maximum tensile stress occurs at ϕ = 90° for both cases.

The results are in good conformity to *Siebert*. Comparing these results with *Techen*, an essential larger contact area is determined. If the stress σ_{max} = 139,3 MPa and the corresponding angle ϕ = 45° determined by Techen is converted to an angle of 90°, a stress value of σ_{max} = 111,8 MPa will be calculated.

Because of these results it is assumed that either the contact area or the corresponding angle ϕ was detected too small by *Techen* and the numerical model which was developed within this thesis, determines the stresses properly.

The approximate solution for calculating the maximal tensile stresses given by *Techen* can be used as long as the connection may be assumed frictionless and the failure load including the contact angle ϕ is determined by a full scale test. However, in practice, the determination of the contact angle causes problems and leads to wrong assumptions (see *Techen*). Because of the material behaviour of glass (see chapter 2) the initial crack may not occur at the location of the maximum tensile stress but at the location with the maximum surface damage.

7.5.3 Investigations carried out by *Overend*

In his thesis [Overend 2002] examined bolted connections with different geometries by executing FE-analyses and experimental investigations. The FEM-model was verified with the help of a comparison of the numerical solution and the approximate analytical solution of the semi-finite panel with a centrally located hole (see chapter 4). The deviation between numerical and analytical solution is given with ±3%. Unfortunately, in [Overend 2002], the magnitude of the load and the material parameters are not listed and a recalculation of this example is therefore not possible. However the comparable example of a semi-finite panel and hole, which was carried out within this thesis (see chapter 7.2), led approximately to the same deviations. After that, *Overend* calculated a bolted connection using this verified FEM-model. The load was applied on the steel bolt and it was assumed that there is no clearance between bolt, bushing and hole ($\Delta R = 0$). The calculation was done with 2D and 3D-volume elements. *Overend* determined a conformity of 2D- and 3D-analysis. This statement cannot be

validated on the basis of the numerical calculations which were carried out within this thesis (see chapter 7.3.1).

Indeed, *Overend* used a different FEM-program, i.e. Lusas Finite Element Analysis System, Version 13.2 and it is presumed that this is the reason for the difference. In particular the type of contact modeling, the load application, the type of supporting and the used element types and geometries influence the results and can cause more or less differences (see chapter 6).

Furthermore, *Overend* examines bolted connections with different bushing materials (aluminium, polyamide) and different magnitudes of clearance. The calculations are computed with 2D-elements. It has to be noticed that the calculations include friction. The friction coefficient amounts μ_H = 0,25. This example will be recalculated in the following. The geometry is given in Table 7.16. The distance between the hole and the top edge is given with 31,5 mm (definition according to Figure 7.27). Material properties are not given by *Overend* therefore the parameters according to Table 7.17 are used.

Table 7.16   Input parameters

Panel size (*2bxh*) [mm]	Hole diameter [mm]	Bolt diameter [mm]	Bushing thickness [mm]	Clearance *ΔR* [mm]	Glass thickness *t* [mm]
100 x 200	37	32	2	1	6

Table 7.17   Material properties

	Bushing aluminium	Bolt steel S235	Glass
Poisson's ratio ν	0,3	0,3	0,23
Young's modulus E	70.000 MPa	210.000MPa	70.000 MPa

The load amounts 25 kN. The load is distributed uniformly on the bolt length. In the following modelling according to the previous FEM-analyses is carried out. Once again 32 elements are chosen in circumference of the hole, and using SOLID-elements additionally, 4 elements are chosen across panel thickness. The analysis is carried out by 2D-PLATE-elements as well in order to compare the results with the 2D-analysis of *Overend*. The results are given in Table 7.18.

Table 7.18   Principal stresses, friction coefficient μ_H=0,25

Element type	σ_{max} [MPa]	Angle ϕ	σ_{min} [MPa]	Angle ϕ
SOLID GAP	266,54 / 67°		-283,63 / 0°	
SOLID CONTACT	251,19 / 67°		-257,62 / 0°	
PLATE GAP	228,52 / 67-78°		-261,76 / 0-10°	
Result *Overend*	ca. 280*) / 60-80°		ca. -200*) / 0°	

*) Values are estimated out of a diagram

When using PLATE-elements the maximum tensile stress is 20% lower than the value of *Overend*. The maximum stress occurs within a range of ϕ = 67° to 78°, which is comparable with *Overend*.

In the opposite the calculation with SOLID-elements is in conformity. However, the compressive stresses are significant higher than the values of *Overend*. It is presumed that different algorithms of contact modelling, different friction modelling and different 2D-element types are the reason for that. The stress values determined by *Overend* can only be roughly estimated according to a diagram. As a consequence further inaccuracies may occur.

7.6 Summary

As shown in this chapter, partially the examined parameters have a big influence on the stress distribution in the area of the drill hole. That is why it is very important to model these parameters close to reality. Only a step-by-step verification of the numerical model - which was used in this chapter - leads to correct results. The parameters of the FEM-model itself already influence the results considerably. Furthermore, the results of different FEM-programs are not transferable in general and a verification of each FEM-program is indispensable.

The FEM-model which was verified and applied within this work corresponds very well with the analytical solutions and comparable FEM-calculations of other researchers.

In the following the results are shortly summarized once more.

Influence of different materials

Presuming a neat-fit condition (clearance $\Delta R = 0$), the values of the maximum principal tensile stresses only differ slightly despite of different material combinations (glass-aluminium, glass-POM-C). Using SOLID-elements with the material combination glass-aluminium the maximum principal tensile stresses are 5,6% (N4W) or 6,3% (MARC) higher than the values for the material combination glass-POM-C.

The maximum principal compressive stresses have approximately identical values for both material combinations.

Influence of a clearance

By increasing the clearance between bolt and hole ($\Delta R > 0$) the stresses increase as well. At the same time the location of maximum principal tensile stresses changes. With the absence of clearance ($\Delta R = 0$) the stress maximum occurs approximately perpendicular to the load direction. Otherwise, when it is assumed that $\Delta R > 0$, the stress maximum moves towards the load direction. According to the size of clearance (max. $\Delta R = 2,0$ mm was examined) the stress maximum occurs at a range between 35° and 55°, depending on the material combination. In comparison with the neat-fit connection ($\Delta R = 0$) a clearance of $\Delta R = 2,0$ mm for aluminium leads to an increase in maximum principal tensile stresses of about 66% and, for POM-C, to an increase of about 39%.

Influence of friction

The exact determination of the friction coefficient μ_H of the enlisted friction partners has to be done with experimental investigations, which can not be carried out within the scope of this thesis. To examine the influence of friction however, different friction coefficients are applied.

When increasing the friction coefficient μ_H it is determined that the tangential stresses p_ϕ will grow and the contact compressive stresses p_r will decrease. In comparison with the frictionless connection, the tangential stresses with a friction coefficient $\mu_H = 1,0$ increase up to 30% and the radial stresses decrease up to 30%, not depending on the material combinations.

Influence of an eccentric load application

In comparison with a centrally load application the location of the maximum stress concentration is not in the midplane anymore but, as expected, on the corresponding surface of the load application. This leads to an increase in maximum principal tensile stresses of about 7,5% for the neat-fit condition ($\Delta R = 0$). The rise in maximum principal compressive stresses amounts about 7% compared to a central loading. If additional clearance is present, the principal stresses grow rapidly. With a clearance of $\Delta R = 0,2$ mm the increment of maximum principal tensile stress amounts about 35% and, for the maximum principal compressive stress, the increment even amounts about 76%.

Influence of hole diameter, panel width and distance between hole and edge

If the ratio of drill hole radius a and panel semi-width b lies in the range of $0,1 < a/b \leq 0,2$, the stresses increase enormously or tend to infinity. An interesting aspect is that for values $a/b > 0,2$ the stresses decrease until a minimum between $a/b = 0,4$ und $0,5$ is reached. Afterwards the values rise again.

A comparison with the tangential stresses of a panel of finite and infinite width shows that a reduction of the panel width influences the amount of the maximum tangential stresses essentially: Having a finite width of 100 mm the maximum tangential stresses are 80% to 86% higher than for the infinite panel. On the contrary the panel width has no significant influence on the radial stresses.

Not only the panel width but also the distance between hole and panel edge influence the amount of principal tensile stresses. By reducing the edge distance H the principal stresses increase. If, in addition, the ratio a/b decreases for a chosen edge distance of $H = 50$ mm, the stresses tend to infinity at $a/b < 0,4$. In the range of $0,4 \leq a/b \leq 0,5$ the values of principal tensile stresses only increase about 10% compared with the values of the panel with a central hole.

FEM-model and its input parameters

MARC

The contact modelling with MARC is more user friendly than modelling with GAP-elements but because of the algorithm it is very time consuming. When symmetries are used (modelling only half of the system) the analyses need still more time than with N4W GAP-elements. Furthermore, convergence problems will occur, if nodes of contacting bodies (bolt and hole) are very close to each other. That is why the contacting bodies should have different mesh sizes and meshing should be done very accurate. It is of the same importance to define the contacting bodies in proper order. A body with a finer mesh should be defined before a body with a coarser mesh. If the contacting bodies are very close to each other, the application of a bias-factor is recommended.

When modelling a bigger clearance ($\Delta R > 0,5$ mm) or friction the analysis with the MARC CONTACT function will be significantly outranged compared with the N4W GAP-elements. In cases like this the calculation with N4W GAP-elements very often cause convergence problems and it takes a lot of time to find the correct settings for a successful analysis.

N4W

In particular modelling with GAP-elements is more time consuming but very well suited for simple geometries. Additionally, the compression stiffness (penalty parameter) of the GAP-elements has to be studied because its value influences the result essentially.

In cases without clearance or friction satisfying results for the contact modelling with GAP-elements are obtained and this kind of modelling is very stable compared with the MARC CONTACT function.

General comments

The investigations show that, using PLATE-elements and 32 elements in circumference of the hole, satisfying results can be achieved for the "most simple" examined case (semi-finite panel with a circular hole). The additional effort of computation time and the amount of memory, using SOLID-elements, can be saved. Indeed it is not possible to determine the stress distribution across thickness. When using SOLID-elements it is determined that the stress distribution across thickness has its maximum on the midplane of the panel and decreases towards the surfaces.

A close to reality contact model can only be achieved by using nonlinear contact algorithms. Within this thesis, in case of modelling with 3D-volume elements (SOLID-elements), the results approached closer to the analytical solution than in case of modelling with 2D-elements. This is valid for both examined contact algorithms (N4W GAP-elements, MARC CONTACT function).

Executing nonlinear analysis, it is generally recommended to apply the load in several increments, otherwise convergence problems may occur. Within this thesis the load was applied in 10 increments. To solve the nonlinear equation systems the "Full *Newton-Raphson*-Iteration" was used.

8 Experimental Investigations on the Stress Distribution related to the Hole Area

8.1 Introduction

As derived in chapter 7, the examined parameters influence the results of the FEM-calculation. Experimental investigations will be carried out to verify the FE-analyses not only by the means of an analytical solution but the procedure will be confirmed as well. Based on the numerical parameter study of chapter 7, the parameters hole diameter, panel width, distance between edge and hole as well as the parameters bushing-material and -thickness will be examined.

Interesting as well is also the deformation behaviour of the used bushing materials (POM-C, AlMgSi0,5 F22), therefore tension tests will be executed. The bushing geometry and the influence of different temperatures will be examined in particular.

8.2 Deformation Behaviour of the Bushings

8.2.1 Specimen

In order to evaluate the material behaviour of the bushings for thermoplastics and for aluminium one material will be examined in detail for each case. These materials are often used in practice:

- Polyacetal-Copolymer (POM-C)
- Aluminium alloy AlMgSi0,5 F22

The properties of the bushing materials are given in chapter 3. The most important material properties are summarized once again in Table 8.1.

Table 8.1   Material properties of the bushings

	POM-C	**AlMgSi0,5 F22**
Density ρ	1,41 g/cm^3	2,7 g/cm^3
Poisson's ratio ν	0,35*)	0,3
Young's modulus E	3200 MPa*)	70.000 MPa

*) according to specification of the manufacturer

Two different bushing thickness t_H with two different outside diameters d_a will be examined for each material (see Figure 8.1).

Thickness of the bushing t_H = 5 mm

Geometry 1: d_i_1 = 10 mm; d_a_1 = 20 mm

Geometry 2: d_i_2 = 30 mm; d_a_2 = 40 mm

Thickness of the bushing t_H = 2,5 mm

Geometry 3: d_i_3= 15 mm; d_a_3= 20 mm

Geometry 4: d_i_4= 35 mm; d_a_4= 40 mm
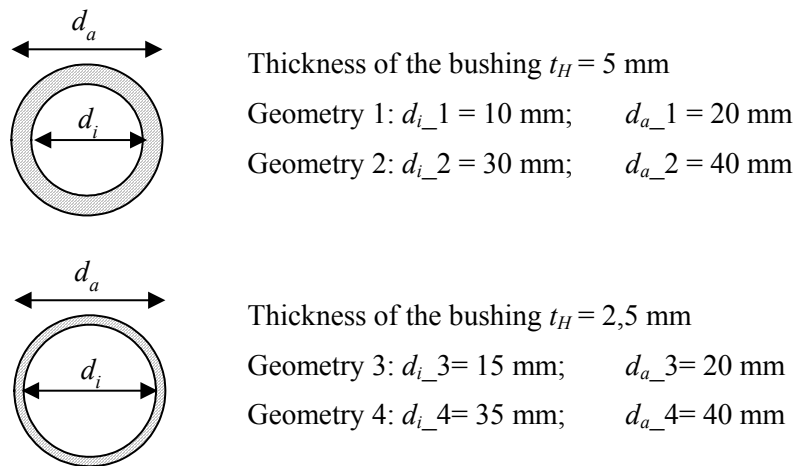
Figure 8.1   Schematic sketch of the examined bushing materials
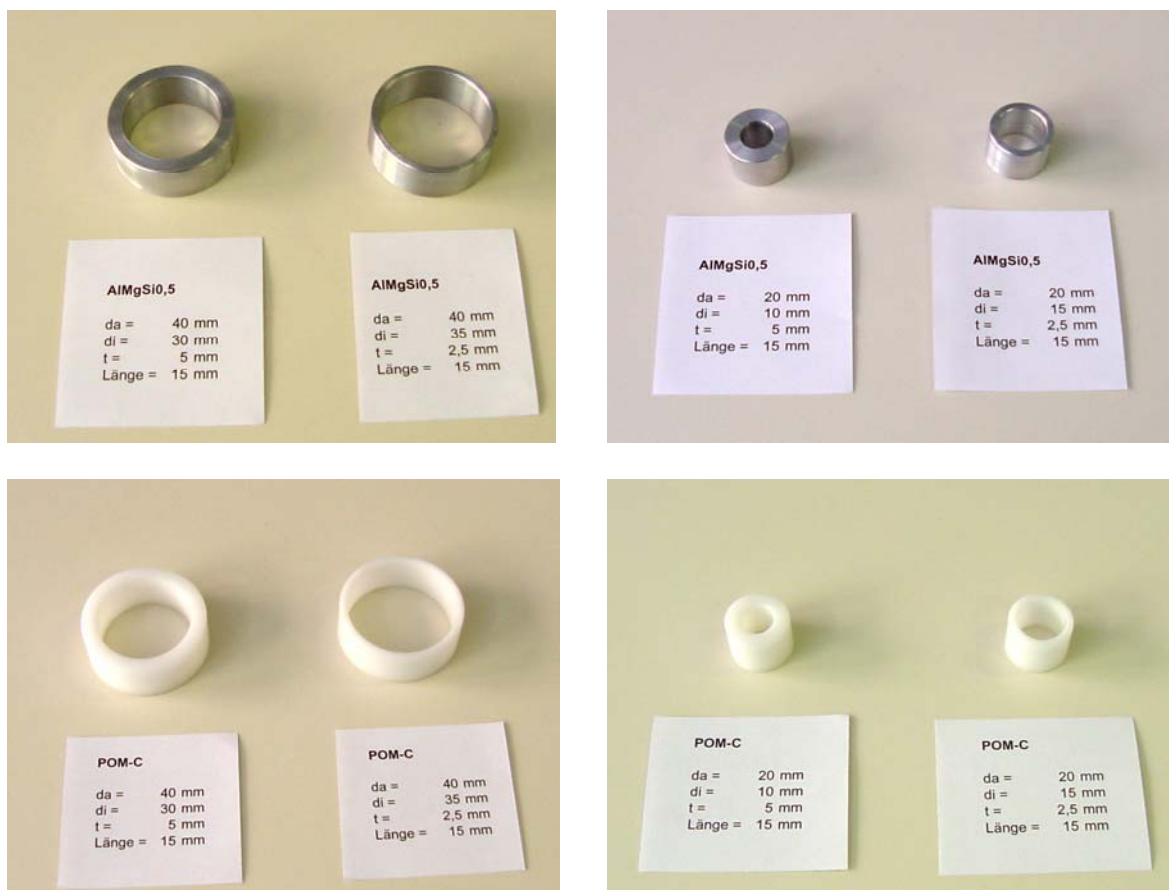
Figure 8.2   AlMgSi0,5 F22 and POM-C specimen

8.2.2 Test Set-Up and Performance

The examination of the bushings will be carried out analogous to the tests with glass specimens, which will be explained in the next section. The only difference is that, instead of glass specimen, a steel panel with the same thickness will be used in order to apply adequate loads.

The load is applied on the specimen with a constant velocity of 1 mm/min until a certain maximum load is reached. Afterwards they are unloaded. During the test performance the displacement of the bushings are determined. The test set-up and examples of the used bushings are shown in Figure 8.3.
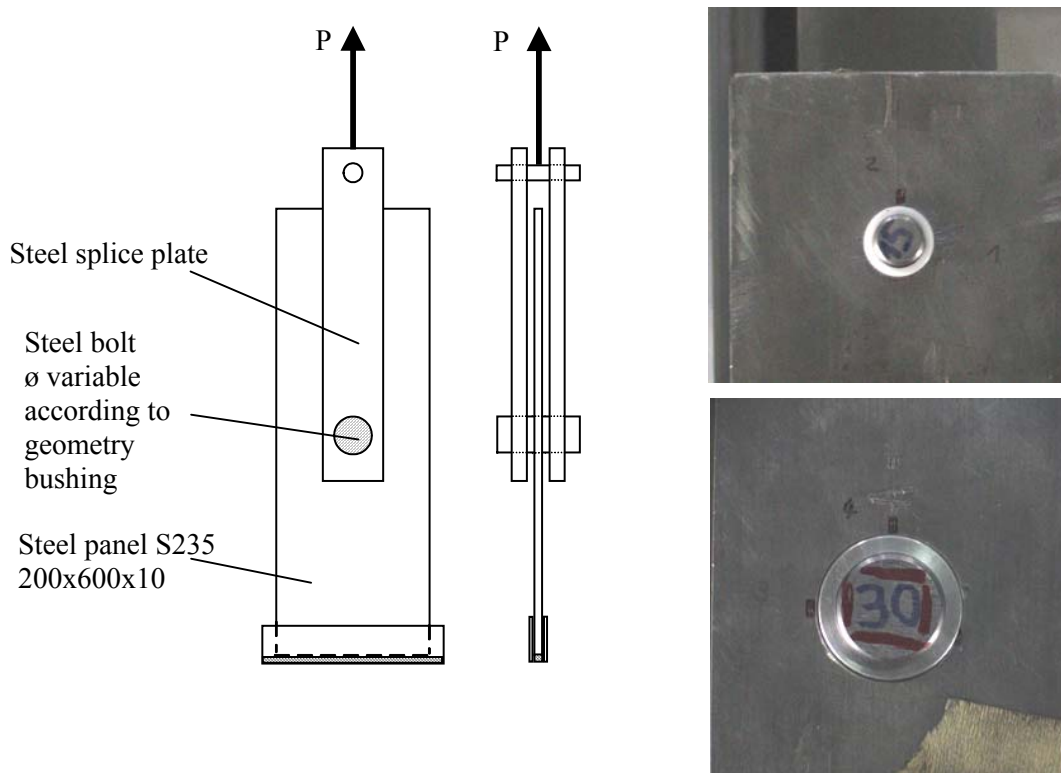
Figure 8.3   Test set-up deformation behaviour of the bushing material

At first, possible plastic deformations will be examined for each geometry and material of the bushings. Therefore different load increments (20, 25, 30, 40 and 50 kN) are applied. The bushing will be demounted after each load increment and checked if there are any permanent deformations. As far as large plastic deformations occur the load increment is not increased. Afterwards, retaining this load increment, 4 identical tests are carried out to receive reliable results about the force-deformation behaviour.

The tests are performed at room temperature (21°), and at 80°C according to the requirements of facades [DIN 18516-1]. An overview of the performed tests is given in the Appendix A.1. The force-displacement-curves of the load increment series are given in the Appendix A.1 as well.

8.2.3 Test Evaluation

To evaluate and compare the force-displacement behaviour of the different bushing materials (AlMgSi0,5 F22 und POM-C) and the bushing geometry in the following diagrams (see Figure 8.4 and Figure 8.5) force-displacement-curves are given for different bushing geometries. The load increment exemplary amounts 25 kN.

Thereafter in Figure 8.6 and Figure 8.7 force-displacement-curves are given for different bushing materials having the same outside diameter.

Figure 8.8 to Figure 8.11 contain the curves for similar parameters at 80°.
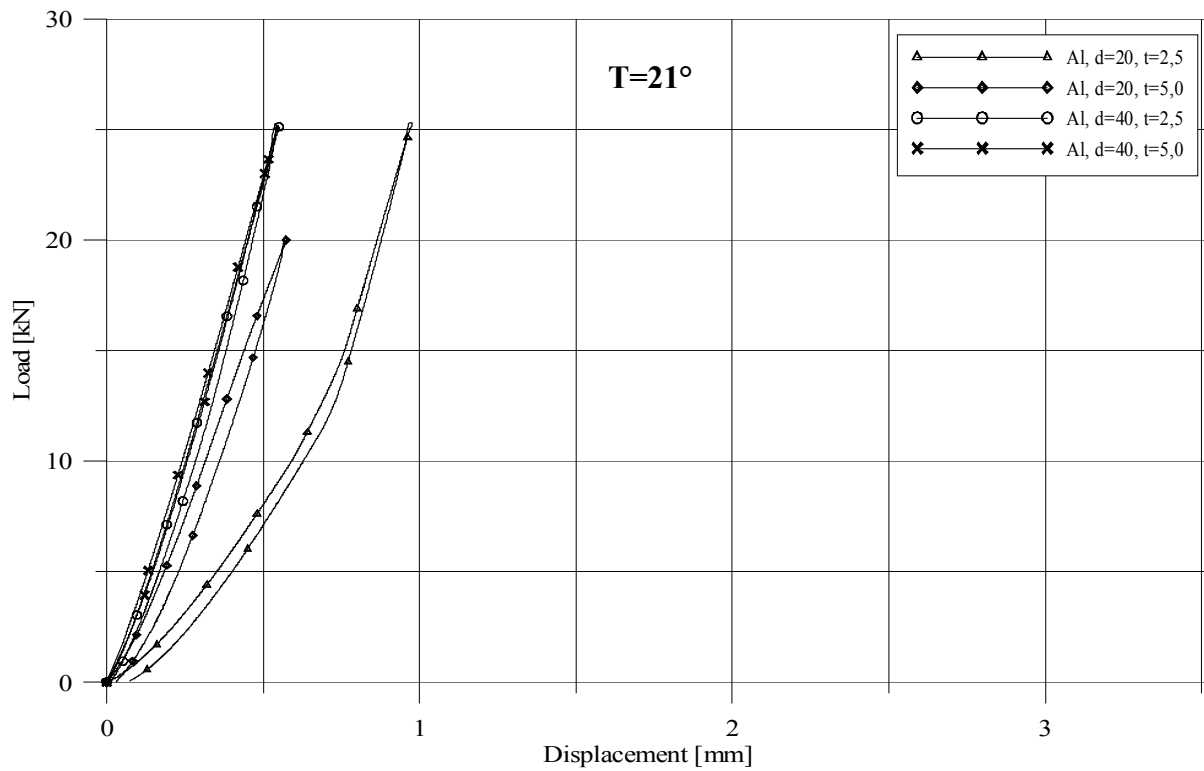
Figure 8.4   Force-displacement curve, bushing: aluminium - comparison of different geometries
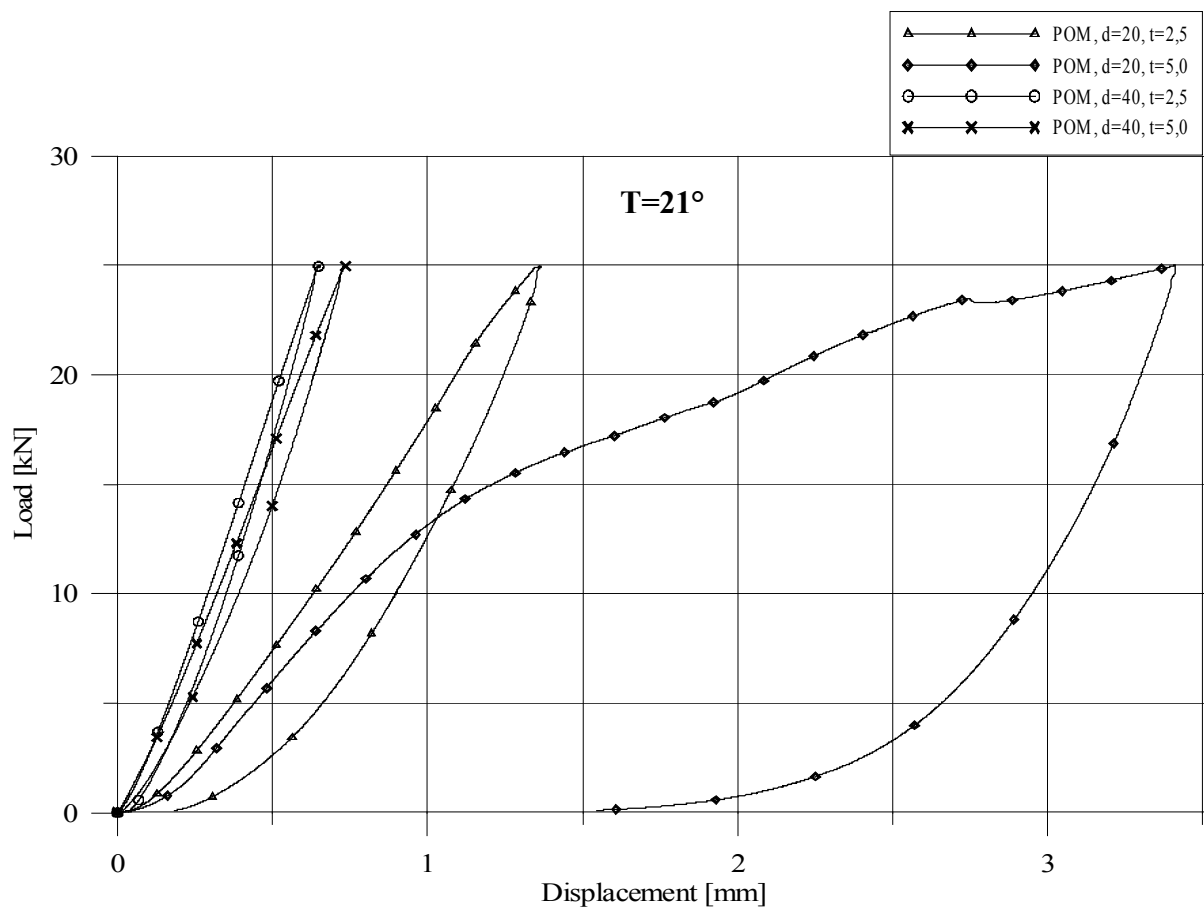
Figure 8.5   Force-displacement curve, bushing: POM-C - comparison of different geometries
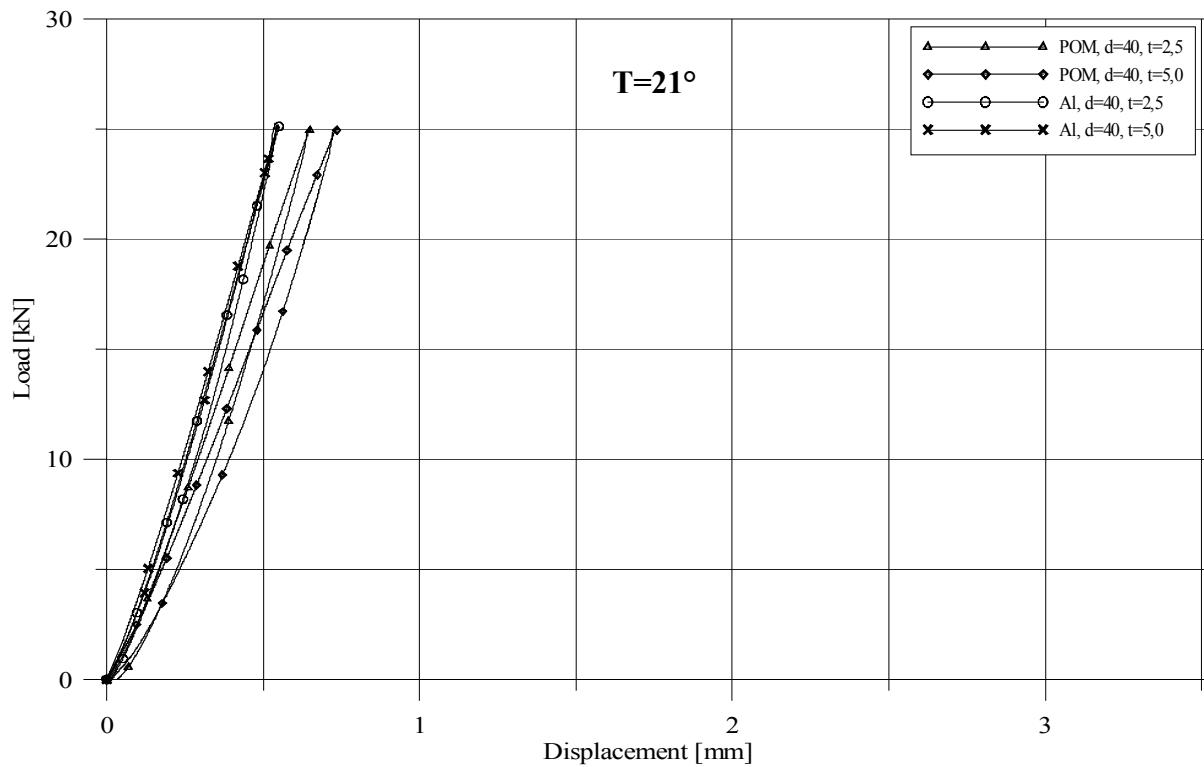
Figure 8.6   Force-displacement curve, comparison of different bushing materials d_a=40mm
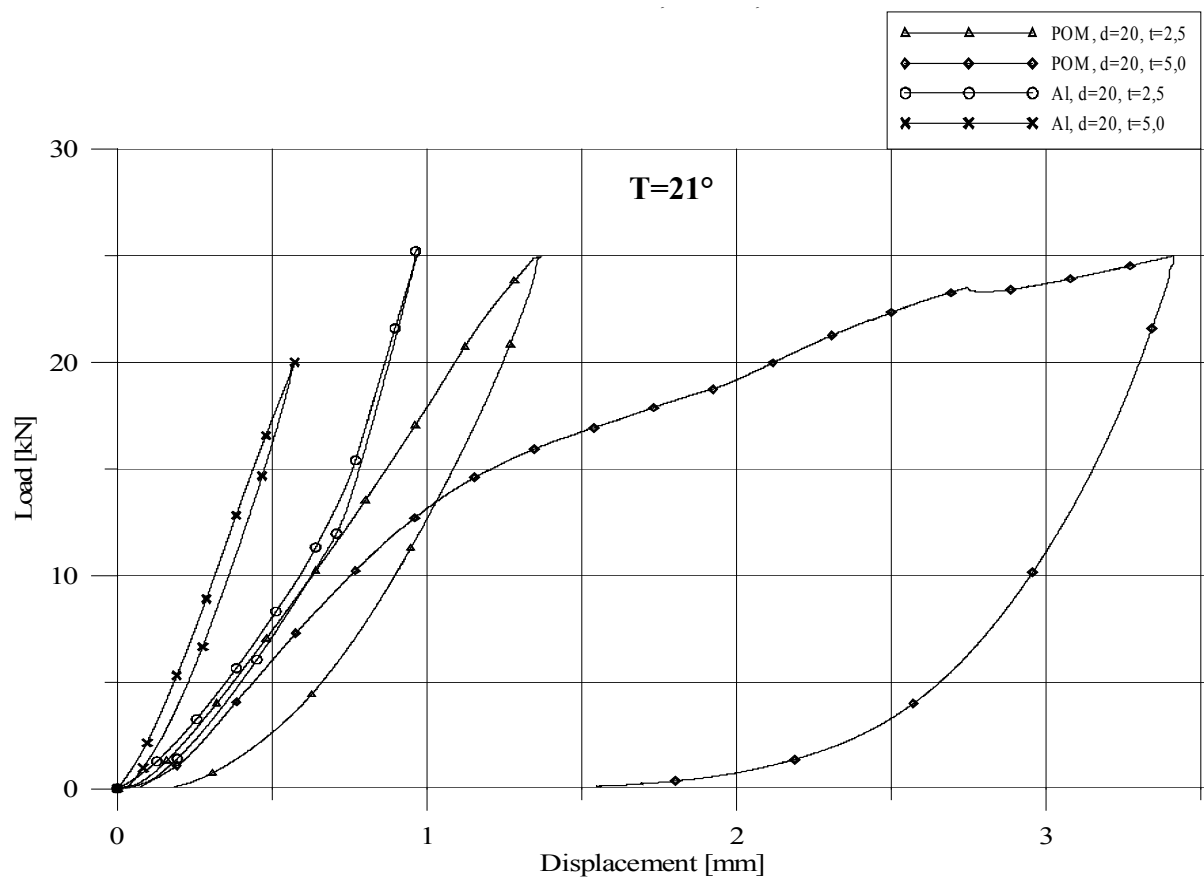
Figure 8.7   Force-displacement curve, comparison of different bushing materials d_a=20mm
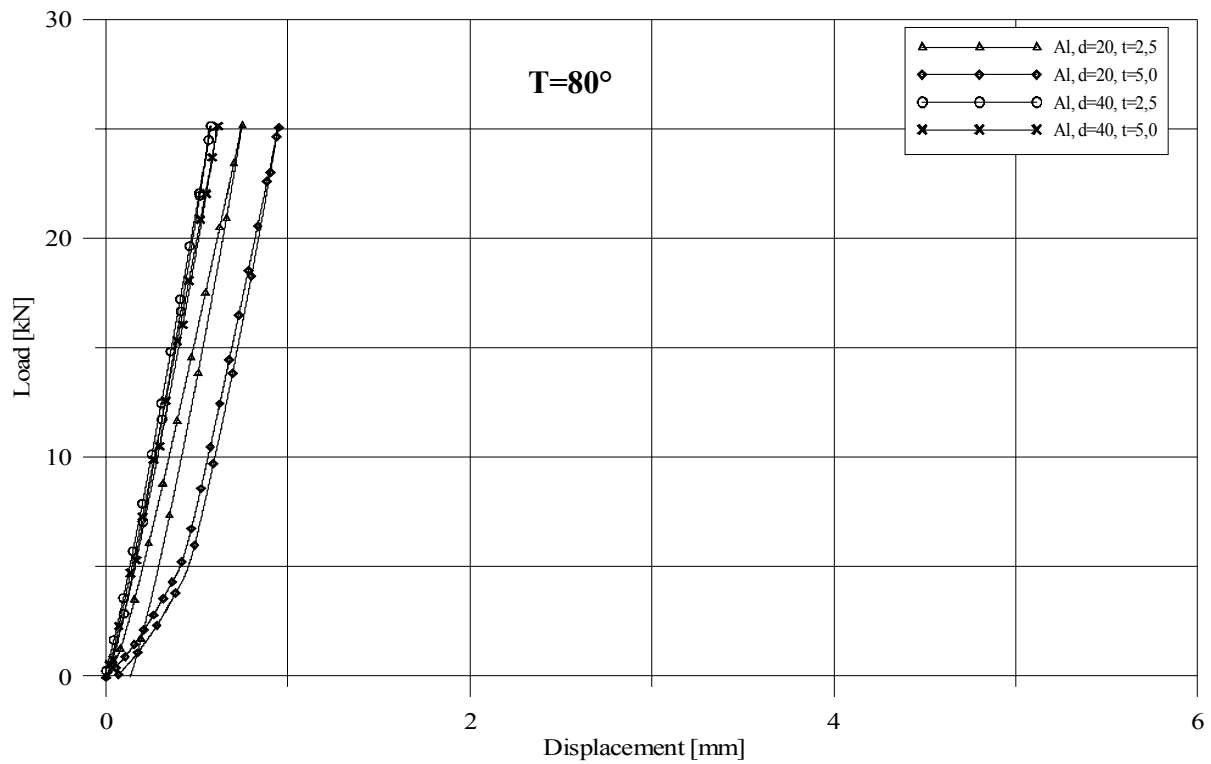
Figure 8.8   Force-displacement curve, bushing: aluminium - comparison of different geometries, T = 80°C
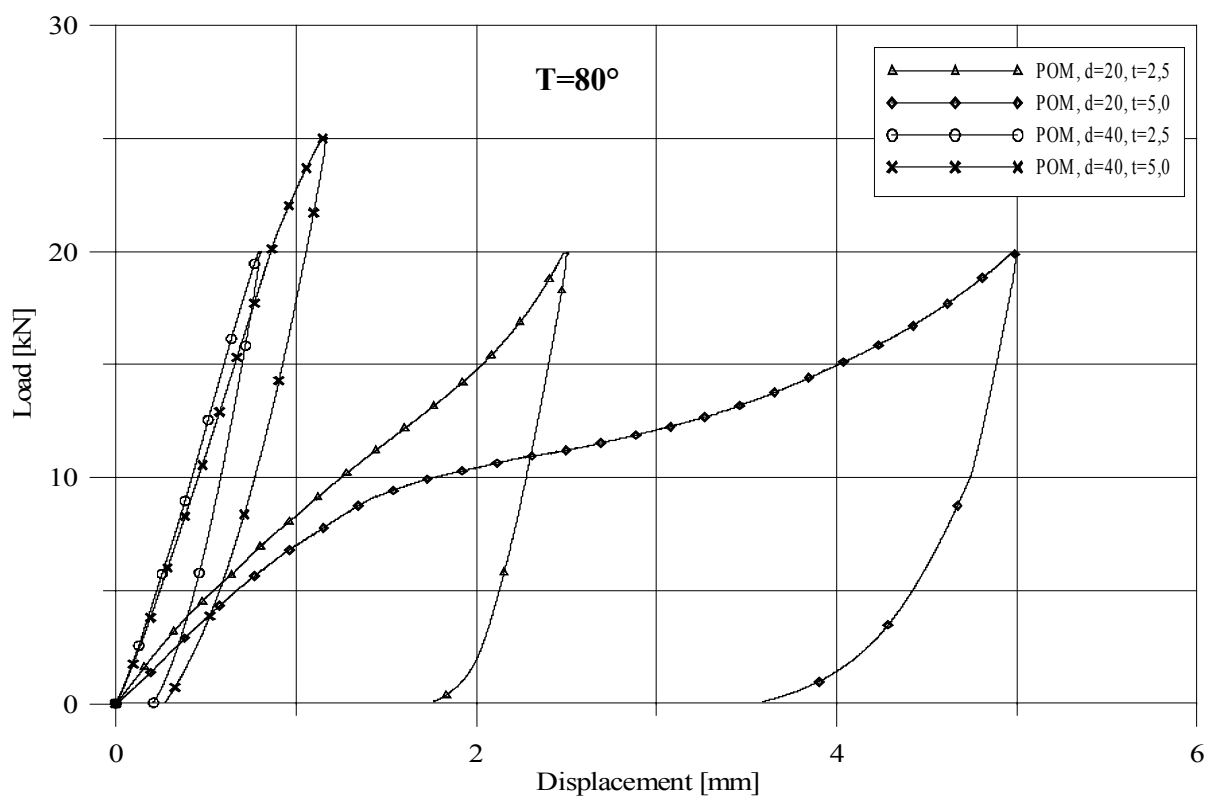
Figure 8.9   Force-displacement curve, bushing: POM-C - comparison of different geometries, T = 80°C
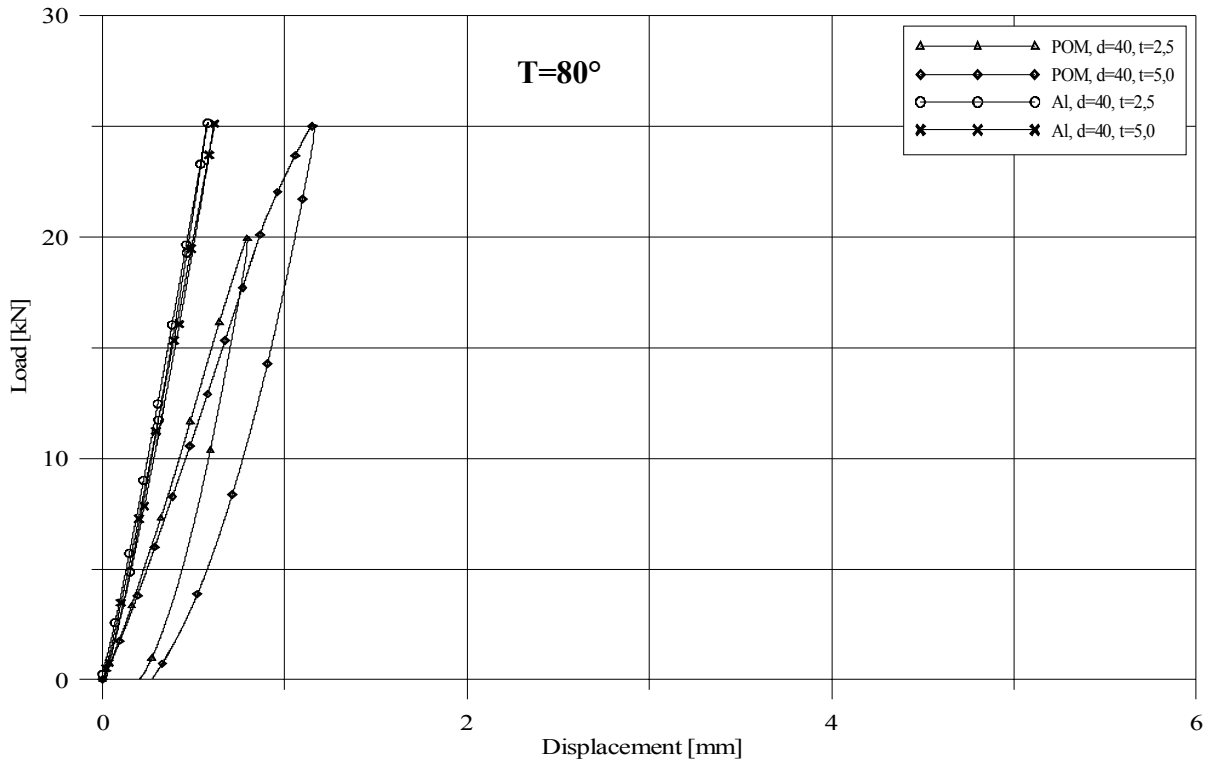
Figure 8.10 Force-displacement curve, comparison of different bushing materials d_a=40mm, T = 80°C
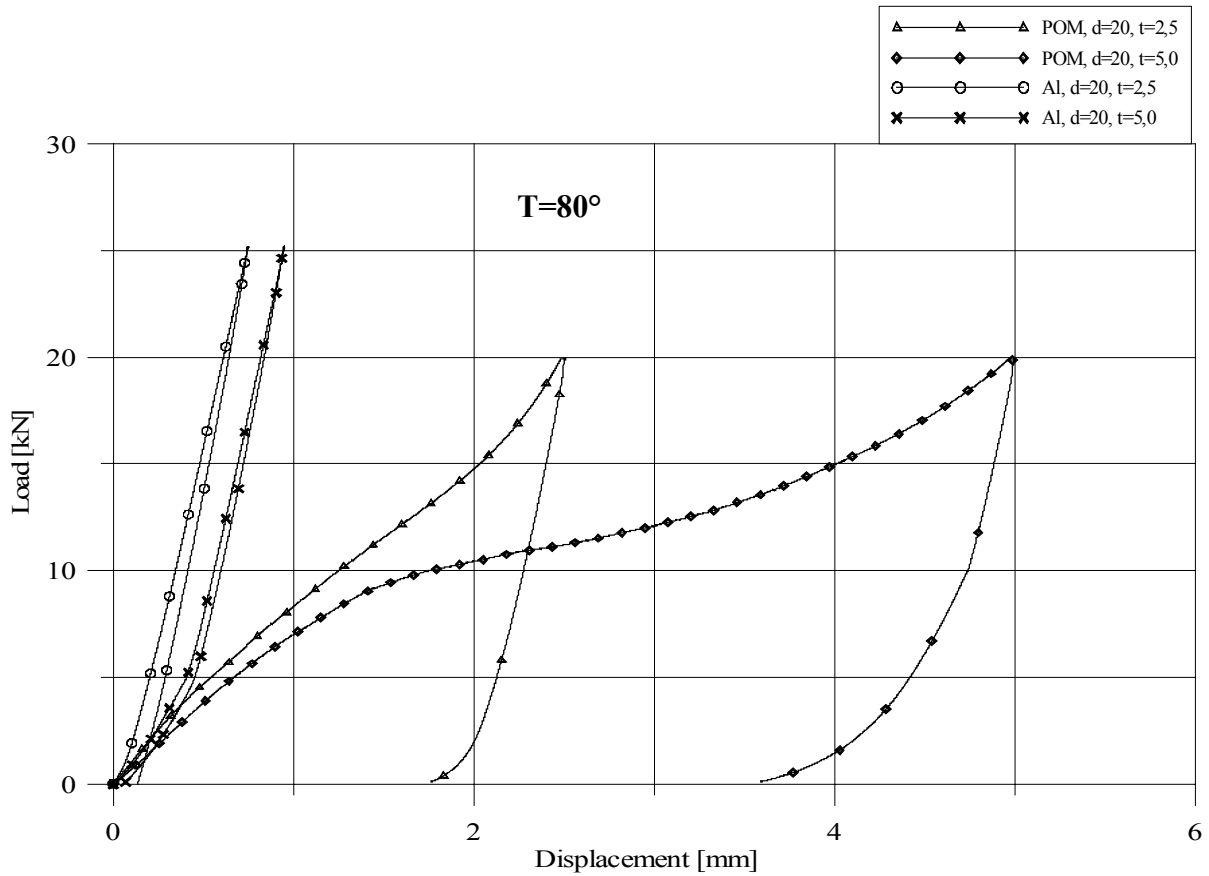
Figure 8.11 Force-displacement curve, comparison of different bushing materials, d_a=20mm, T = 80°C

8.2.4 Results

The AlMgSi0,5 F22-bushings have no visible deformations at the examined load increments (20 to 50 kN) and temperatures. Having a bushing diameter of d_a = 40 mm and thickness of 2,5 mm and 5 mm only linear elastic deformations occur independent on the temperature (see Appendix A.1, Figure A.1, Figure A.2, Figure A.9, Figure A.10). Having a bushing diameter of d_a = 20 mm and thickness of 5 mm only linear elastic deformations occur independent on the temperature as well (see Figure A.3 and Figure A.11). The bushings with 2,5 mm thickness have slightly plastic deformations (see Figure A.4 and Figure A.12). In Figure 8.4 a comparison of the force-displacements-curves at room temperature for different bushing geometries are shown. The corresponding curves at 80° are given in Figure 8.8.

The POM-C-bushings with a diameter of d_a = 40 mm show linear elastic deformations until the load increment of 30 kN is reached not depending on the bushing thickness. Slight plastic deformations occur already at 40 kN (see Figure A.5 and Figure A.6). At a temperature of 80° and a load increment of 20 kN larger plastic deformations occur and increase continuously until the maximum increment of 50 kN is reached. The bushings of 5 mm thickness show larger deformations than the ones of 2,5 mm (see Figure A.13 and Figure A.14). Having a diameter of d_a = 20 mm significant plastic deformations occur at a load increment of 20 kN (see Figure A.7 and Figure A.8). In order to compare the different bushing geometries the load is increased until an increment of 40 kN is reached. At a temperature of 80° and a load increment of 20 kN large plastic deformations occur and it takes a great effort to demount the bushings of the steel panel. That is why the load is not increased. The bushings of 5 mm thickness show again larger deformations than the ones of 2,5 mm (see Figure A.15 and Figure A.16). In Figure 8.5 a comparison of the force-displacements-curves at room temperature are shown for different bushing geometries. The corresponding curves at 80° are given in Figure 8.9. At room temperature only the POM-C-bushings with a diameter of d_a = 20 mm and a thickness of 5 mm have visible deformations (see Figure A.17). However, at 80° the 2,5 mm and the 5 mm thick bushings have visible deformations (see Figure A.18 and Figure A.19).

In Figure 8.6 and Figure 8.7 a comparison of the force-displacements-curves at room temperature are shown for the different bushing materials with the same geometry. The corresponding curves at 80° are given in Figure 8.10 and Figure 8.11.

Summary and evaluation of the different influences

AlMgSi0,5 F22

It can be assumed that bushings which have diameters between d_a = 20 mm and 40 mm and a thickness between 2,5 mm and 5 mm show a linear elastic material behaviour until a load increment of 50 kN and a temperature of 80° is reached.

POM-C

It can be assumed that bushings which have a diameter of d_a = 40 mm and a thickness between 2,5 mm and 5 mm show a linear elastic material behaviour at room temperature until a load increment of 40 kN is reached. Having a diameter of d_a = 20 mm at 20 kN plastic deformations occur for both bushing thickness. For all examined geometries significant plastic deformations occur at a load increment of 20 kN and a temperature of 80°.

8.3 Loadbearing Tests for Verifying the FEM-Model

8.3.1 Preliminary Considerations

To minimize the sources of error, which influence or alter the test results, a more or less simple test set-up is chosen. The aim is to exclude constraint stresses or eccentricities in order to receive only in-plane loads. Furthermore, monolithic glass panels are used instead of laminated glass. It is referred to [Gräf 2003], [Schuler 2003] and [Kutterer 2003] for investigations on the loadbearing behaviour of laminated glass.

The executed analytical and numerical parameter studies are valid for linear elastic material behaviour. The performed material tests, which are described in chapter 8.2, showed plastic deformations for the POM-C bushings under the application of large actions. As a result the actions for the tests are chosen in a way that the bushings only get elastic deformations. Hereby the executed tests can be recalculated by the verified FEM-model.

Based on the numerical parameter study in chapter 7, besides the parameters drill hole diameter, panel width and distance between hole and edge, the parameters bushing material and bushing thickness are examined.

The tests are recalculated by means of FEM and afterwards compared with the experimental results.

8.3.2 Specimen

Two different panel widths, 200 mm and 400 mm as well as three different drill hole diameters 20, 30 and 40 mm are examined. A centrally located hole and a hole located close to the panel edge are examined as well. An overview of the specimen and their geometries are given in Table 8.2 and Table 8.3 as well as in Figure 8.12 and Figure 8.13.

Due to the expected high local stress peaks at the edge of the drill hole, thermally toughened glass is used. The panel thickness amounts 10 mm.

Table 8.2   Specimen with a centrally located hole

Specimen no.	Size*) *2bxh* [mm]	Hole diameter [mm]	Glass thickness (mean value of 6 single values)	Comment
1	401x601,5	40,0	10,00	Drill hole has a misalignment of 0,25 mm
2	400,5x601,5	30,1	9,93	Drill hole has a misalignment of 0,25 mm
3	401x601,5	21,4	9,99	Drill hole has a misalignment of 1,0 mm
4	202x601,5	30,1	10,00	Drill hole has a misalignment of 0,2 mm

*) size determined at the specimen
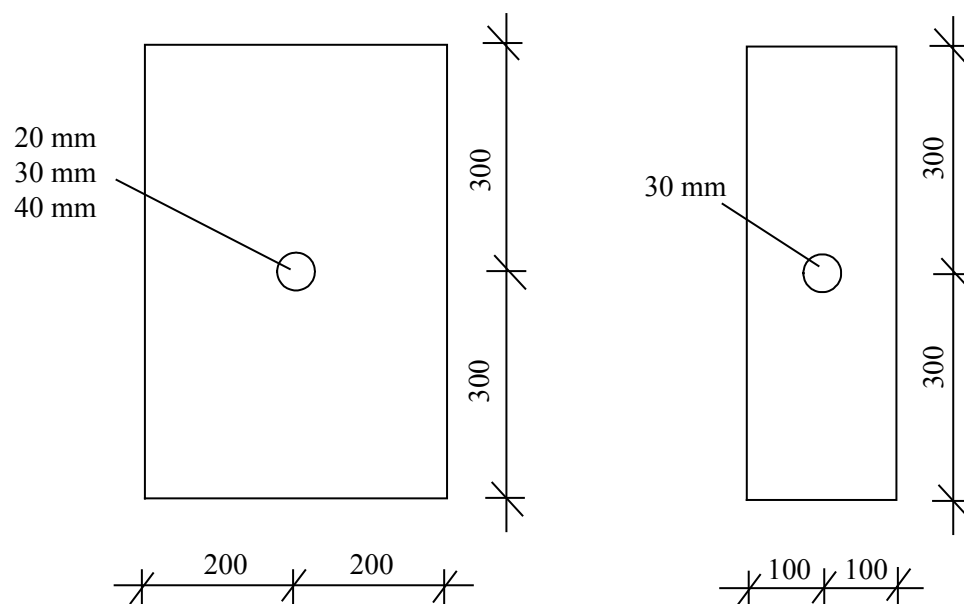
Figure 8.12 Geometry of specimen with centrally located hole

Table 8.3 Specimen with a hole located close to the panel edge

Specimen no.	Size*) *2bxh* [mm]	Hole diameter [mm]	Glass thickness (mean value of 6 single values)	Comment
1	402x602	40,0	10,96	Drill hole has a misalignment of 0,4 mm
2	401,5x602,5	30,04	10,00	Drill hole has a misalignment of 0,2 mm
3	399,5x602,5	20,0	9,99	Drill hole has a misalignment of 0,4 mm
4	202,5x602	30,0	10,00	Drill hole has a minimum misalignment

*) size determined at the specimen
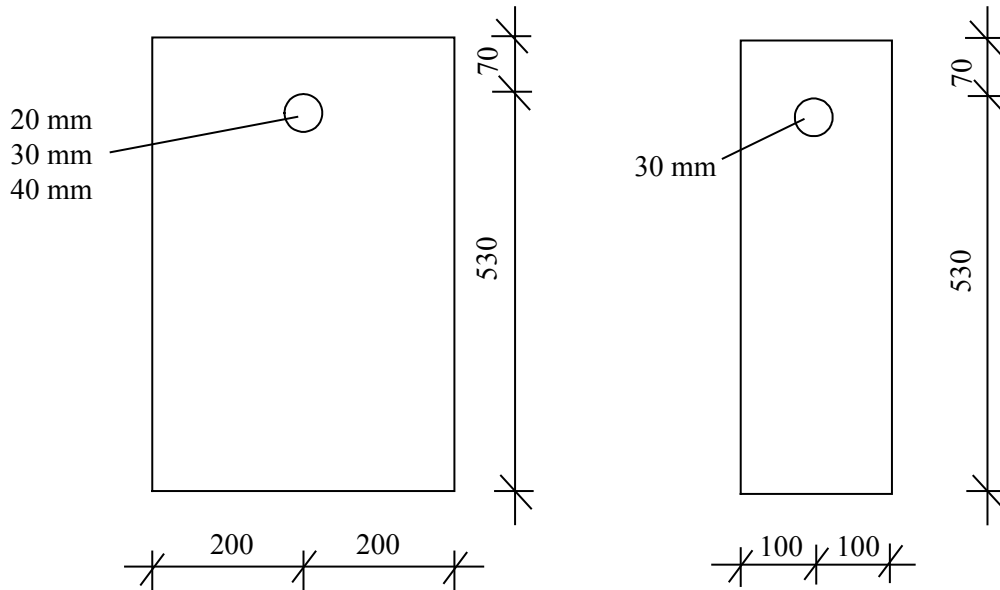
Figure 8.13 Geometry of specimen with a hole located close to the panel edge

For the bushings, the materials and geometries according to chapter 8.2 are used. In addition to the bushing outside diameters 20 mm and 40 mm, the outside diameter d_a = 30 mm is examined. An overview contains Table 8.4.

Table 8.4 Examined bushing geometries

Material of the bushing	Thickness of the bushing t_H [mm]	Outside diameter d_a [mm]
(1) AlMgSi0,5 F22 (2) POM-C	2,5 5,0	20 30 40

The geometries or the size of the bushings are measured with a digital calliper gauge and are used for the FEM-calculations. The overall clearance ΔR between drill hole and bushing is given for all specimen in Appendix A.2.

8.3.3 Measuring Technology

In order to compare the numerical (by means of FEM) and the experimental determined strains or stresses on each specimen several strain gauges are applied. To determine the stress distribution at the edge of the drill hole most accurately a high number of strain gauges is applied. The overall result ε_{DMS} is the arithmetic mean value resulting from the integration results of all strain gauge measuring grids. That is why the choice of the gauge length is decisive.

Crucial strain gradients are expected at the edge of the drill hole. Therefore, strain gauges with short measuring grids are used and the strain gauges are applied as close as possible to the edge of the drill hole in order to measure the strain distribution as accurate as possible.

The correct choice and location of the strain gauges are based on the tangential and radial stresses determined in the parameter study of chapter 7.

The following strain gauges types of the company Preusser Messtechnik GmbH are used:

- Linear strain gauges with a 1 mm long measuring grid (type FLA-1-11)

- Linear strain gauges with a 5 mm long measuring grid (type FLA-5-11)

- 0°/45°/90°-rosettes with three measuring grids, length 3 mm (type FRA-3-11)

The nominal resistance of all mentioned strain gauges amounts $120\,\Omega$. In spite of performing the experiments at almost non-varying room temperature, strain gauges with so-called "three wire technology" are used to compensate unintentional temperature influences. Temperature fluctuations may occur due to open windows or doors for example.

To determine the tangential stresses at the place perpendicular to the load direction the linear strain gauges with a 1 mm long measuring grid (identification no. L1, L2) are applied at the edge of the drill hole. Due to the symmetrical configuration it is possible to check whether the specimen is installed centrically or whether the loading happens in a central way. More strain gauges are applied at the drill hole edge in load direction ($\theta = 0°$) and at an angle of $\theta = 60°$ to determine tangential and radial stresses. Therefore 0°/45°/90°-rosettes with 3 mm long measuring grids are used (identification no. R1, R2).

In order to specify the normal stresses between the drill hole edge and the lateral edge of the panel three additional strain gauges with a 5 mm long measuring grid are applied (identification no. L3, L4, L5). One of them is applied at the backside of the panel in order to check whether the specimen is installed centrically or whether the loading happens in a central way.

The position of the strain gauges on the specimen are shown in Figure 8.14 and Figure 8.15.
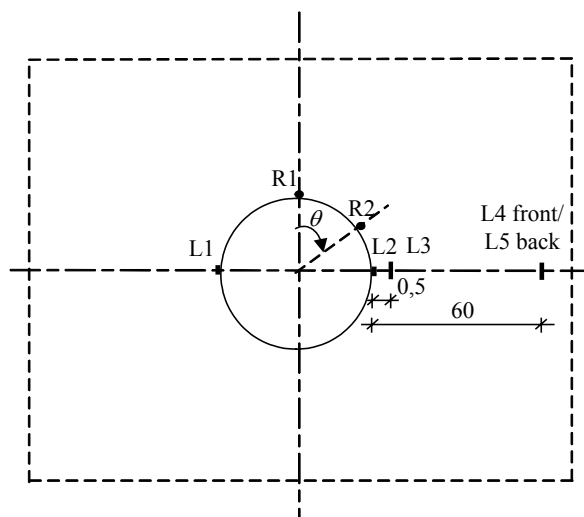
Figure 8.14   Position of the strain gauges on the specimen
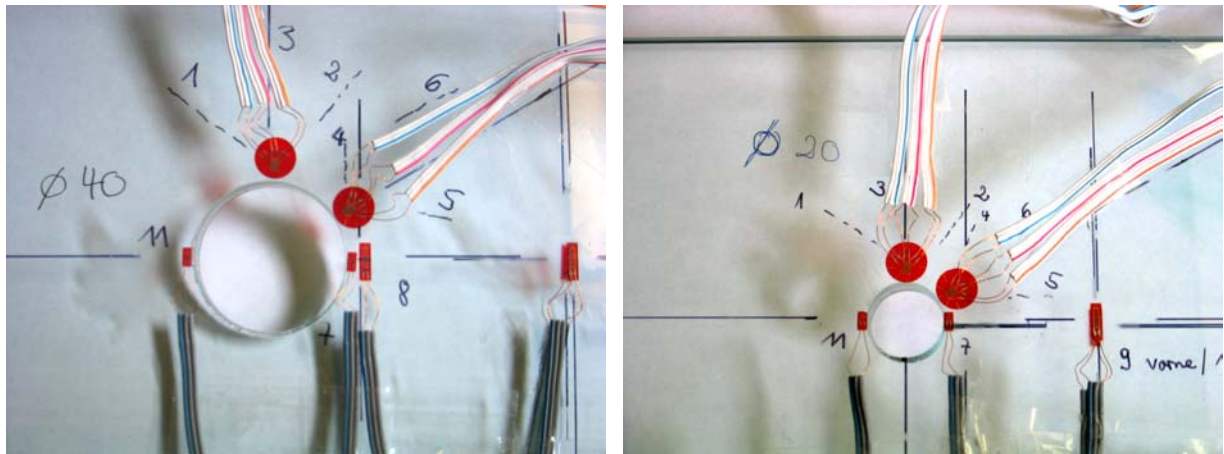
Figure 8.15 Specimen with strain gauges

The measurement signals are recorded with a digital measuring amplifier "Spider 8", transmitted directly to a PC and evaluated with the software catman 4.0, release 2.0.

The measuring grids *a*, *b* and *c* of a strain gauge rosette are connected with the measuring amplifier as three single quarter-bridges. Therefore it is possible to determine the biaxial stress state with unknown principal directions. The linear strain gauges are connected as a quarter-bridge as well.

It should be noticed that the used "three wire" device compensates resistance changes due to the temperature but not resistance changes due to the length of the cables (connecting cable between strain gauges and measuring amplifier). The *k*-factor, which is given on the strain gauge package, has to be revised with the following equation:

$$R_{new} = R_{strain\_gauge} + R_{cable}$$

$$k_{new} = \frac{k_{strain\_gauge} \cdot R_{strain\_gauge}}{R_{new}}$$

$$(8.1)$$

8.3.4 Test Set-Up and Performance

The glass panels are connected with bolts at splice plates. Between the glass drill hole and the steel bolt different bushing materials, which are described in Table 8.4, are integrated. The bushings are produced in a way that there is no clearance between steel bolt and bushing. The test-rig is shown in Figure 8.16.

At the lower edge the panels are fixed with a clamping strip. To receive a clamping, screws are used which are tightened with a torque of 8 Nm.
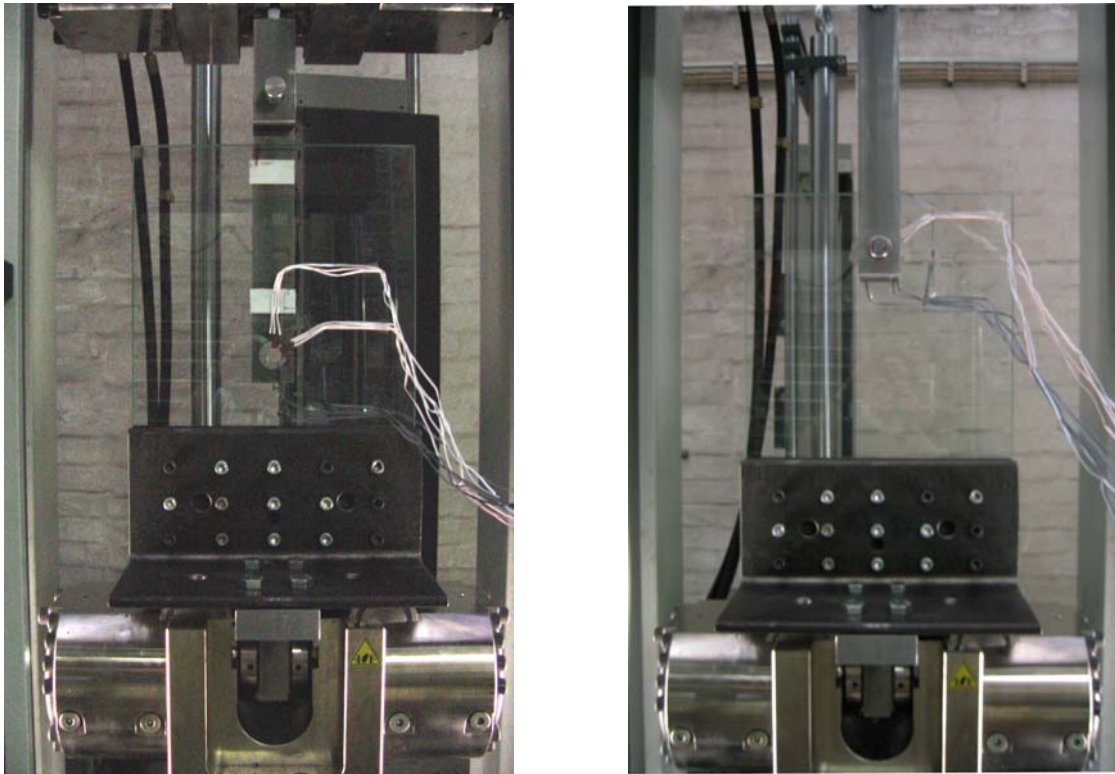
Figure 8.16 Test-rig

The loading is increased with 1 mm/min until the maximum load of 1000 N is reached. Afterwards this load level is retained for 20 sec. After this, unloaded down to 500 N and, again, the level of 500 N is retained for 20 sec. In a further step the load is increased again to 1000 N until the specimen is finally unloaded. The whole loading gradient of one experiment is shown in Figure 8.17. The tests are carried out at room temperature.

The different load levels are chosen in order to determine potential creep.
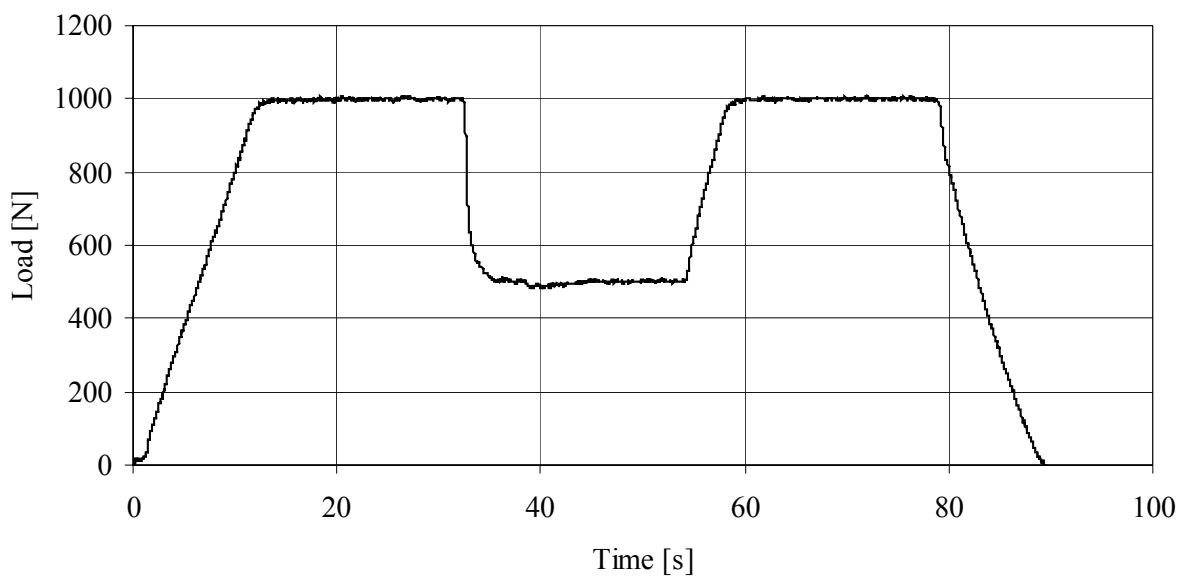
Figure 8.17 Loading gradient, protocol of the actual distribution

The strains in every experiment are determined with the help of the strain gauges. Additionally, displacement transducers are applied at the back and front side of each panel to determine any vertical misalignments during the loading. A displacement transducer is applied as well at the upper panel edge to determine any slipping of the glass panel out of the clamping strip.

A clear identification for the tests is chosen which is explained with an example (see Figure 8.18).

Test identification: Z-400-600-20-Al-2,5
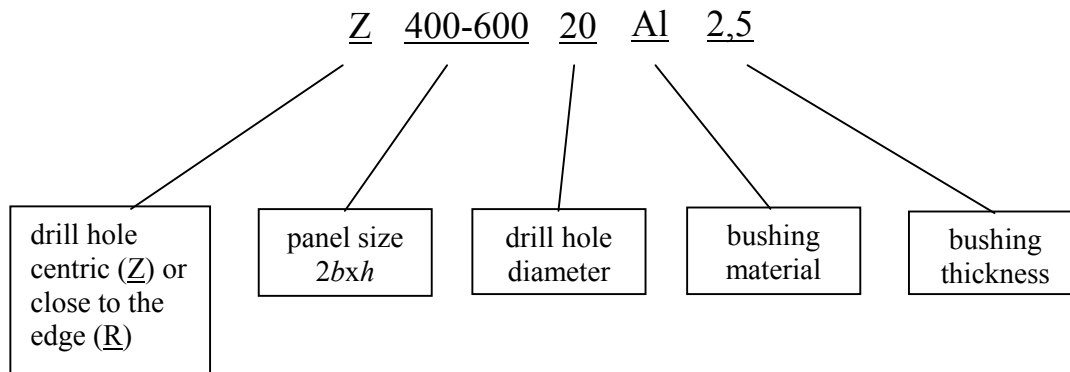
Figure 8.18 Explanation of the test identification

8.3.5 Experimental Stress Analysis

When using the experimental stress analysis with strain gauges, the correlation between strains and stresses has to be taken into consideration. This means that the material law is very important since the stresses σ have to be calculated from the measured strains ε_l.

The uniaxial stress state is given by:

$$\sigma = \varepsilon_l E \tag{8.2}$$

Having a biaxial stress state with unknown principal directions the strains ε_a, ε_b and ε_c can be measured by using the 0°/45°/90°-rosettes.

The principal stresses are calculated with the following equation:

$$\sigma_{1,2} = \frac{E}{1-v} \cdot \frac{\varepsilon_a + \varepsilon_c}{2} \pm \frac{E}{\sqrt{2}(1+v)} \cdot \sqrt{(\varepsilon_a - \varepsilon_b)^2 + (\varepsilon_c - \varepsilon_b)^2} \tag{8.3}$$

The normal stresses σ_x and σ_y and the shear stress $\tau_{x,y}$ can be calculated with the following equations (see also chapter 4):

$$\sigma_x = \frac{\sigma_1 + \sigma_2}{2} + \frac{\sigma_1 - \sigma_2}{2}\cos 2\varphi$$

$$\sigma_y = \frac{\sigma_1 + \sigma_2}{2} - \frac{\sigma_1 - \sigma_2}{2}\cos 2\varphi \qquad (8.4)$$

$$\tau_{xy} = \frac{\sigma_1 - \sigma_2}{2}\sin 2\varphi$$

8.3.6 Test Evaluation

In order to receive reliable test results for each series four identical tests are carried out. An overview of the test series is given in Appendix A.2.

The following parameters are varied:

- Drill hole diameter
- Bushing material
- Bushing thickness
- Panel width
- Location of the drill hole

However, it is not possible to determine exactly the influences of the examined parameters on the base of the test results. This will be explained in the following.

The parameter study which was described in chapter 7 showed that a clearance between bushing and drill hole influences the amount of stress significantly. Executing the tests, considerable difficulties occur. There is the problem that almost each specimen has a different clearance between bushing and drill hole. Especially this clearance is a result of manufacturing tolerances of the glass drill holes and the bushings. However, the main problem is the bad quality of the drill holes. The drill holes have misalignments up to 1 mm (see Table 8.2 and Table 8.3). The misalignments result from manufacturing the drill holes. The holes are simultaneously drilled from both sides of the panel. Misalignments occur if the drill heads are not located exactly on top of each other. Furthermore the misalignments of the specimen are located at an angle of $\theta = 0°$ and 180° which is exactly in load direction (see Figure 8.19). In the worst case this leads to an unbalanced loading in transverse direction of the panel and therefore to an increase of the maximum stresses (see eccentric loading in chapter 7.3.5).
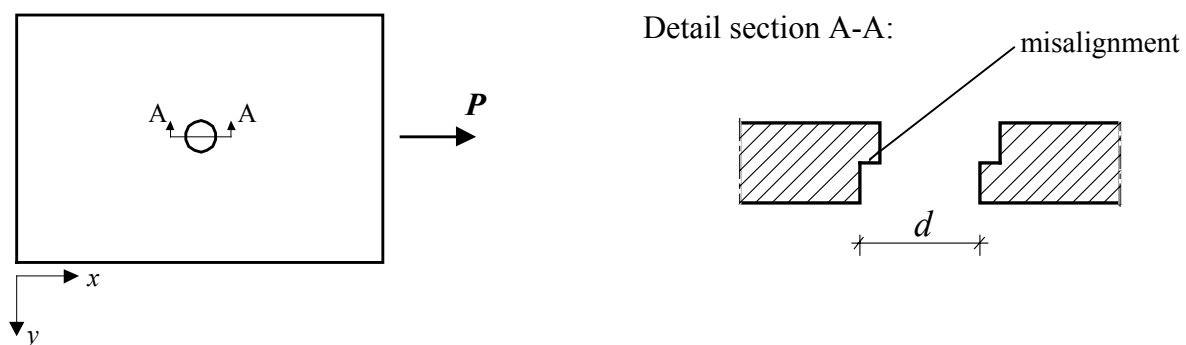
Figure 8.19 Sketch misalignment in the drill hole

For the test evaluation, this means that the test results additionally contain the parameter clearance which varies for almost every specimen. That is why the maximum stresses as well

as the contact angles and areas change. Thus the stress distributions of the specimen can not be compared. Examples of this phenomenon are given in Figure 8.20 to Figure 8.22. The stress distributions show that the stresses decrease from the edge of the drill hole towards the edge of the panel and that bigger hole diameters lead to smaller stresses. An influence of the bushing material and bushing thickness can not be observed clearly. The influence of the drill hole location can not be determined definitely.

The measured overall clearance ΔR between drill hole and bushing of all specimen is given in Appendix A.2.
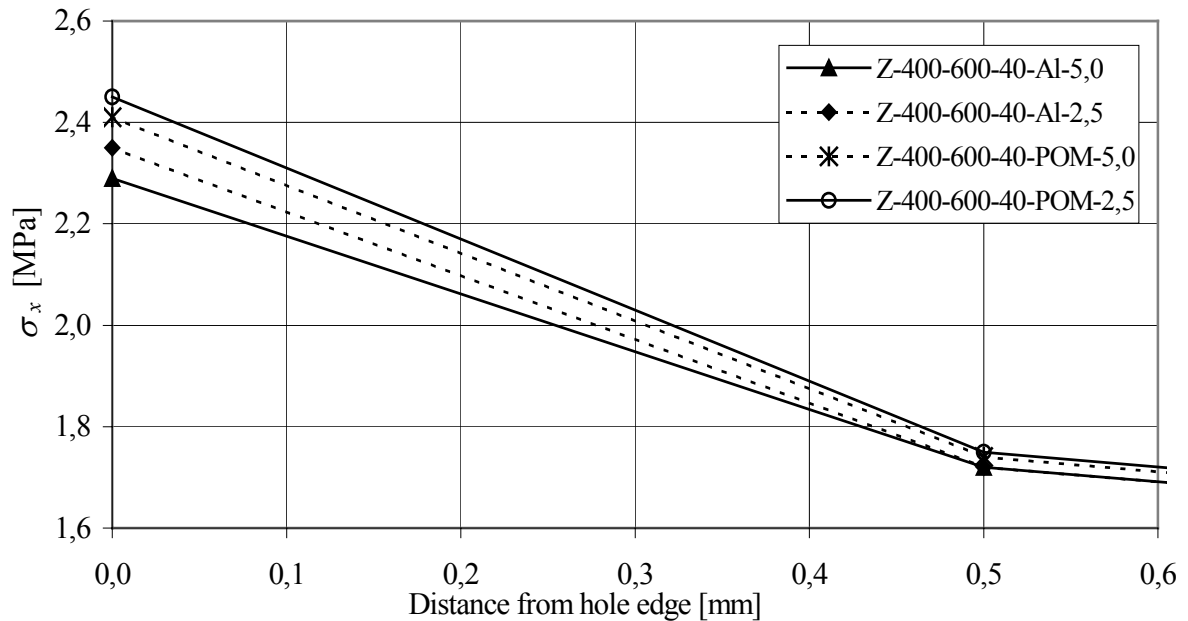
Figure 8.20 Tensile stress distribution for the hole diameter 40 mm
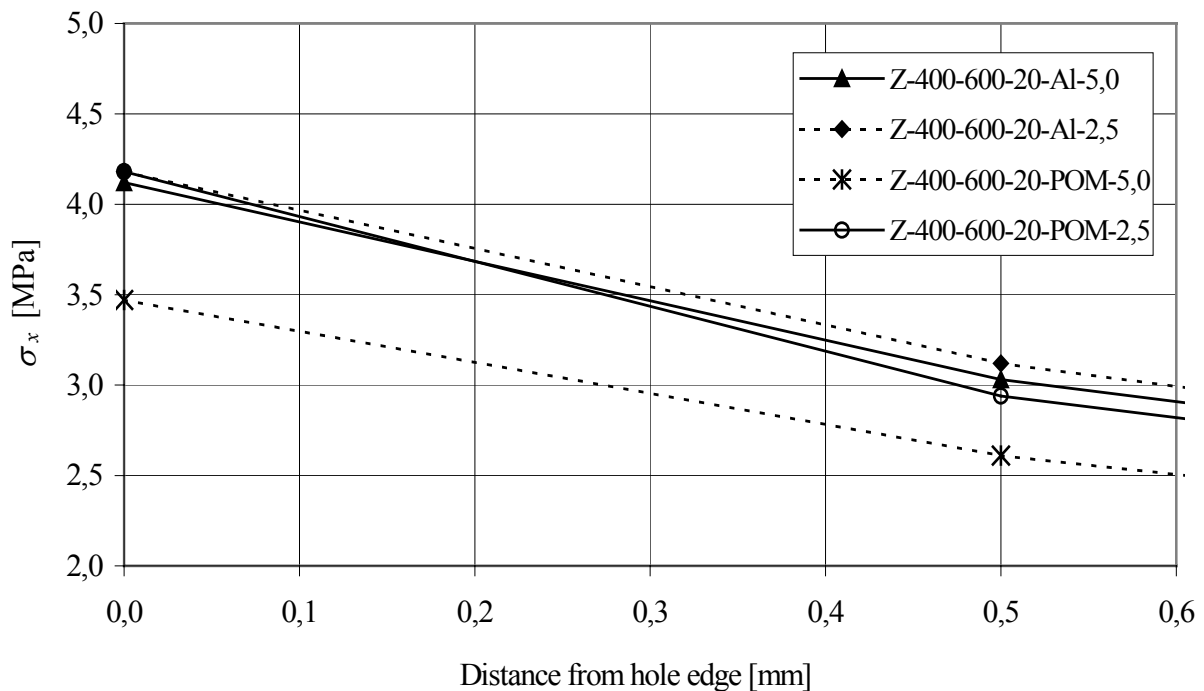
Figure 8.21 Tensile stress distribution for the hole diameter 20 mm
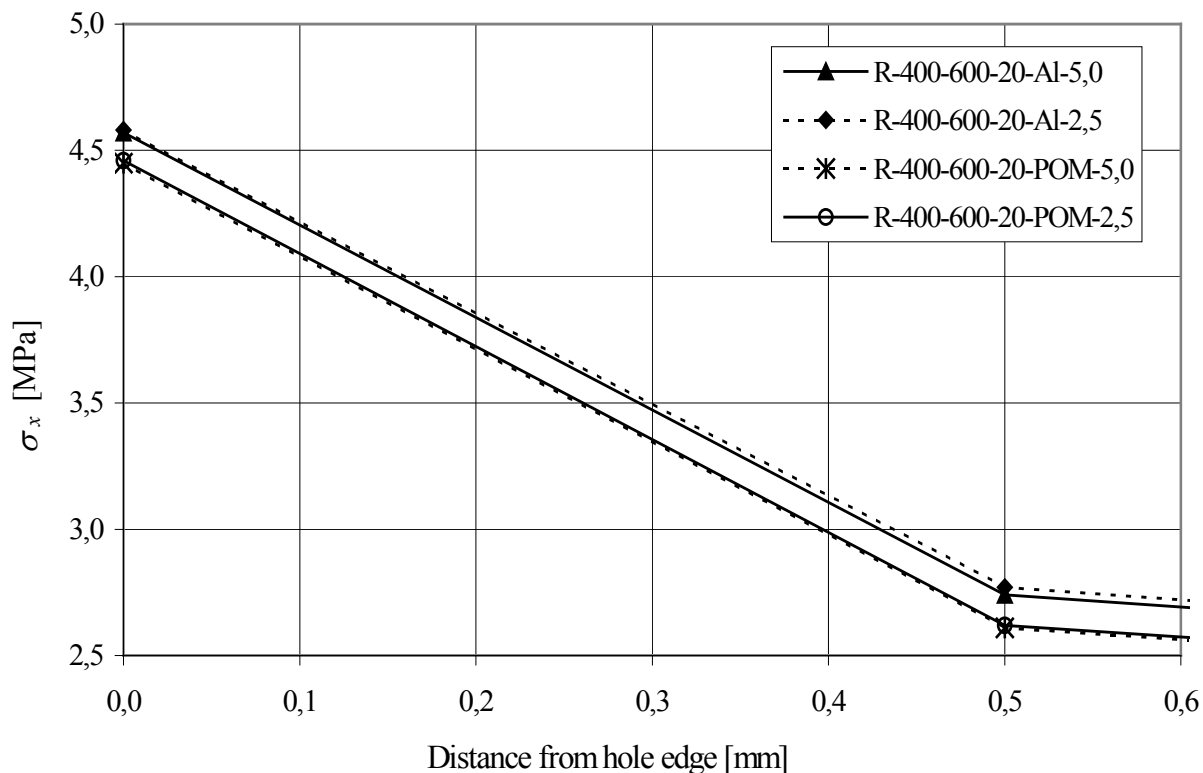
Figure 8.22 Tensile stress distribution for the hole diameter 20 mm, hole close to the edge

In practice, such tolerances appear. Additional tolerances occur when laminated glass is used due to the misalignment of the single panels. As a result the existence of a clearance or tolerances must be taken into consideration for design. To compensate such clearance the drill hole can be grouted with a suitable filling compound (see chapter 3).

This result leads to the conclusion that the tests suit mainly for the verification of the FEM-model and not for determining the influences of the different parameters on the stress distribution.

In the following, the specimen are modelled with an appropriate FEM-model and the stresses are calculated. Afterwards, the numerical and experimental determined stresses are compared.

8.4 Stress Determination by means of FEM

8.4.1 Introduction

The FEM-model verified in chapter 7 is used to recalculate the tests. Therefore SOLID-elements are used. An overview of the modelling parameters is given in Table 8.5 and the material properties are listed in Table 8.6

Table 8.5   FEM modelling parameters

Used element type of all components (glass-bushing-bolt):	SOLID-elements (CHEXA)
Element mesh around the hole:	Concentric circles Aspect ratio radial 1:1
Elements in circumference of the drill hole: Elements across panel thickness:	32 4
Analysis:	Nonlinear
Material behaviour:	Linear elastic

Table 8.6   Material properties

	Bushing POM-C	**Bushing AlMgSi0,5 F22**	**Bolt steel S235**	**Glass**
Density ρ	1,41 g/cm^3	2,7 g/cm^3	7,85 g/cm^3	2,5 g/cm^3
Poisson's ratio ν	0,35*)	0,3	0,3	0,23
Young's modulus E	3200 MPa*)	70.000 MPa	210.000MPa	70.000 MPa

*)according to specification of the manufacturer

The contact analysis is executed with MARC CONTACT.

8.4.2 Preliminary Considerations

First of all the test set-up has to be converted into a FEM-model or a static model. The aim is to represent the system very accurate but minimize the computation time at the same time.

It is examined whether the eccentric loading due to the steel splices has to be considered or whether the influence of the bolt deformation is negligible. Therefore the load could be distributed uniformly over the bolt length. The support of the bolt corresponds to a single beam with cantilever. The loads are applied on the cantilever (see Figure 8.23).

To reach maximum safety the deformation of the bolt is determined for the smallest diameter $d = 10$ mm. Applying a load of $P = 1000$ N the deformation of the bolt amounts around $7 \cdot 10^{-4}$ mm at the midspan. Due to this very small deformation of the bolt, it is assumed that the loads are transmitted uniformly to the bushing. The loads in the FEM-model are then distributed uniformly over the bolt length. The influence of the misalignment is examined in chapter 8.4.4.

Section through the test-rig:
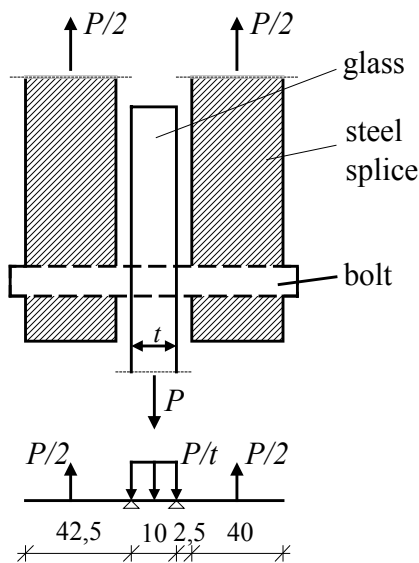
Figure 8.23 Static system for calculating the deformation of the bolt

To compare the numerical with the experimental determined stresses in the FEM-model the stresses are read out at the locations of the applied strain gauges (see Figure 8.14). It has to be considered that the amount of the measured value of the strain gauge is the mean value of the overall measuring grid length. Furthermore, there is the possibility that the corresponding location of strain gauges in the FEM-model is not lying within a finite element. Therefore, not only the nodal but also the elemental values has to be taken into consideration and the stresses have to be averaged. Thus, deviations up to 10% between numerical and experimental determined values are in conformity.

8.4.3 Summary of the Experimental Results and Evaluation of the FEM-Model

At first, the stresses determined in the test series are compared with the FEM-results. The results are listed in the Appendix A.2, Tables A.2.1 to A.2.10.

According to Table 8.7 the following stresses are determined. The location and description of the strain gauges are shown in Figure 8.14 and Figure 8.15.

Table 8.7   Determined stresses

Rosette R1:	Max. principal compressive stress
Rosette R2:	Max. principal tensile stress
Linear strain gauges L1 to L5:	Max. tensile stresses

As supposed, the deviations between numerical and experimental stresses of specimen with a misalignment are bigger. Especially the compressive stresses measured at rosette R1 differ up to 25% compared to the numerical value (see Table A.2.4). The tensile stresses at rosette R2 show slightly smaller deviations. In general, the results of the linear strain gauges correspond very well with the numerical values. That is why it is assumed that the stresses are increased only in the closest surroundings of the misalignment.

It has to be noticed that the change of the stress gradients in radial direction is bigger at the rosettes than in the areas of the linear strain gauges. That is why the results of the rosettes may vary more due to the averaged values of the measuring grid.

Specimen R-200-600-30 (see Table A.2.10) has only a very small misalignment which is hardly to measure. As a result, the deviations between the measured results of rosette R1 and R2 and the numerical calculated stresses are 10% at most.

Therefore it is presumed that the modelling by FEM is executed correctly.

The following results according to the tests can be summarized:

- The maximum tensile stress arises always at the edge of the drill hole and decreases in direction of the panel edge.

- Specimen with POM-C bushings have lower compressive stresses at the location of rosette R1 than with AlMgSi0,5 F22-bushings.

- Using 5 mm thick bushings the compressive stresses measured at rosette R1 are lower than using 2,5 mm thick bushings. However, this influence is very small.

- A reduction of the drill hole diameter from 40 mm to 20 mm or a reduction of the ratio a/b from 0,1 to 0,05 leads to an increase in tensile and compressive stresses.

- The tensile and compressive stresses are higher in case specimen have the drill hole close to the edge than specimen that have a centrally located drill hole.

To confirm these results the above mentioned parameters are examined numerically with the verified FEM-model.

8.4.4 Parameter Examination by means of FEM

In the following the influences of the different parameters are described. The evaluation of the analyses is executed according to chapter 7. The parameters are step-by-step changed, since only one parameter is changed at once in the calculations.

Misalignment influence

As mentioned in the previous chapter, the stresses of the specimen with misalignments differ significantly from the numerical determined stresses. Therefore it will be examined whether the numerical stress values are approximate to the experimental values or not. The misalignment is simulated by applying an eccentric loading in the FEM-model. According to chapter 7, the load is only applied on one end of the bolt.

In Table 8.8 the results of the FE-analysis with and without misalignment are compared with the experimental stress analysis. The specimen having the largest misalignment (1,0 mm) Z-400-600-20-xxx and a 5 mm thick aluminium bushing is chosen because, in this case, the largest deviations occur (see Appendix A.2, Table A.2.4). Using an aluminium bushing, the deformations of the bushing is smaller compared with a POM-C bushing which is softer. Therefore materials like POM or materials with comparable properties are more suited for compensating non-uniform loadings.

In case of eccentric loading in Table 8.8 the stress values are given for the panel front and back side.

Table 8.8   Principal stresses, comparison between experimental stress analyses and FE-analyses

Test identification according to chapter 8.3	Experimental stress analysis [MPa]		FE-Analysis without misalignment [MPa]	FE-Analysis eccentric loading panel front side [MPa]	FE-Analysis eccentric loading panel back side [MPa]
Z-400-600-20-Al-5,0	R1	-38,37	-28,84	-31,64	-26,07
	R2	3,75	2,94	3,29	2,81
	L1	4,03	3,70	3,98	3,41
	L2	4,12	3,70	3,98	3,41
	L3	3,03	2,83	3,03	2,62
	L4/L5	0,30	0,28	0,31	0,25

If the numerical stress values of the panel front side (equivalent to loading plane) are compared with the experimentally determined stresses the deviations are significantly lower than in the case of applying the loads uniformly (see Table 8.8). The results of the linear strain gauges correspond very well with numerical values, the deviations amount between 0% and 3%. The compressive stresses determined at the position of rosette R1 are still not corresponding with the experimental data but the deviations are reduced from 25% (uniform loading) to 17% (eccentric loading).

The executed numerical analysis shows that with an eccentric loading, the stress values approach the stresses determined in the experiments. A misalignment leads to a non-uniform load transmission. By modelling the misalignment more precise, it is presumed that the calculation of the compressive stresses at the location of rosette R1 can be improved.

Influence of different bushing materials and bushing thickness

The geometry of specimen Z-400-600-40 is taken to examine the parameter "different bushing materials". In order to compare the results for the AlMgSi0,5 F22 bushings and the POM-C bushings the same geometries are used. The clearance for all calculations is assumed constantly with $\Delta R = 0,7$ mm. The output values of the numerical calculations are determined at the same positions according to the experimental stress analysis.

Table 8.9   Principal stresses, comparison of different bushing materials and thickness t

Stress position	Bushing material AlMgSi0,5 F22 t=5mm [MPa]	Bushing material POM-C t=5mm [MPa]	Bushing material AlMgSi0,5 F22 t=2,5mm [MPa]	Bushing material POM-C t=2,5mm [MPa]
R1	-10,16	-7,56	-10,41	-8,38
R2	2,06	2,06	2,11	2,11
L1	2,13	2,13	2,19	2,19
L2	2,13	2,13	2,19	2,19
L3	1,60	1,60	1,64	1,64
L4/L5	0,31	0,31	0,31	0,31

As shown in Table 8.9 the results from the experimental stress analysis can be confirmed. Using POM-C bushings lower compressive stresses (position rosette R1) are obtained than for the AlMgSi0,5 F22 bushings. Vice versa, the results of the tensile stresses reveal no influence of the different bushing materials.

An increase of the bushing thickness from 2,5 mm to 5 mm leads to a slight decrease of the tensile and compressive stresses in the area of the drill hole.

Figure 8.24 shows the dimensionless tangential stress distributions for bushing materials and thickness. In spite of a clearance ΔR = 0,7 mm the influence of the different materials on the tangential stresses is not significant.
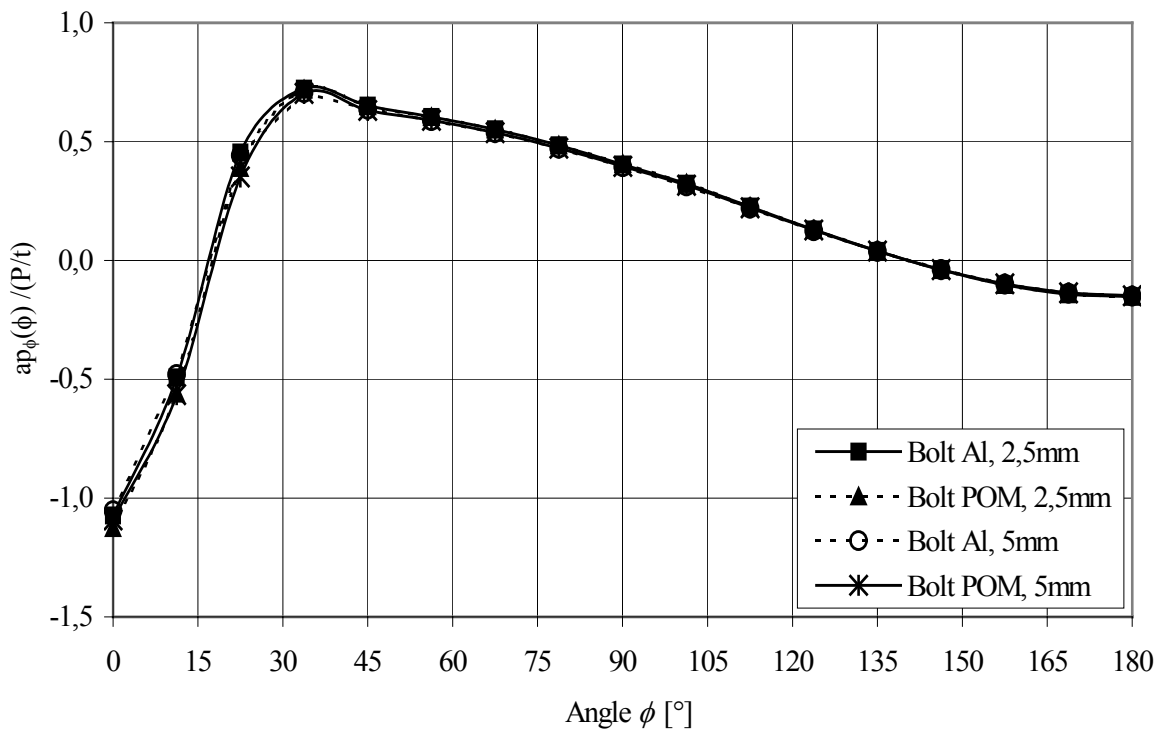
Figure 8.24 Tangential stress distribution, comparison of different bushing materials and thickness t

Figure 8.25 shows the corresponding dimensionless radial stress distributions. Using the AlMgSi0,5 F22 bushings the maximum radial stresses (compressive stresses) are slightly higher and the stresses decline faster than in case of the glass panels with POM-C bushings.
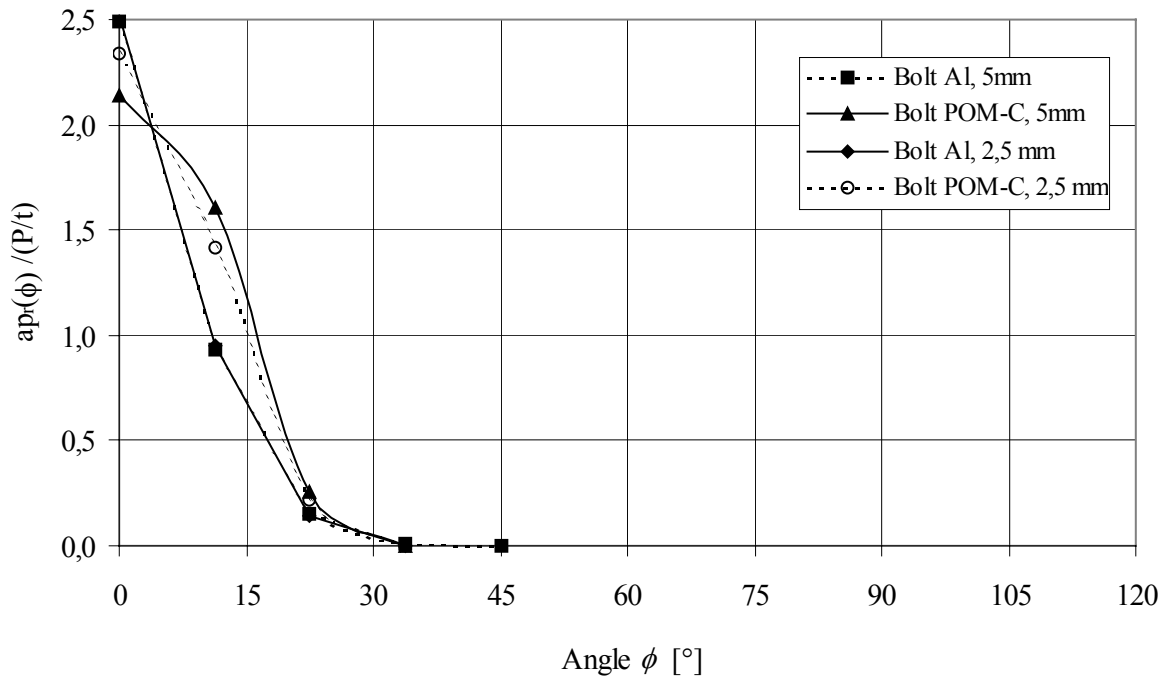
Figure 8.25 Radial stress distribution, comparison of different bushing materials and thickness t

Influence of the hole diameter

The geometries of the specimen Z-400-600-40 are Z-400-600-20 are used to examine the parameter "drill hole diameter". The bushings consists of AlMgSi0,5 F22 and have a thickness of 5 mm. The clearance for all calculations is assumed constantly with $\Delta R = 0,7$ mm. The output values of the numerical calculations are determined at the same positions according to the experimental stress analysis.

The results from the experimental stress analysis can be confirmed here as well. Table 8.10 contains the corresponding stress values for the drill hole diameters 20 mm and 40 mm. A decrease of the drill hole diameter from 40 mm to 20 mm leads to a significant increase of the compressive stresses at the position R1 (approx. 140%). The tensile stresses increase noticeable as well (approx. 74%).

Table 8.10   Principal stresses, comparison of different hole diameters

Stress position	Hole diameter 40 mm [MPa]	Hole diameter 20 mm [MPa]
R1	-10,16	-24,43
R2	2,06	3,14
L1	2,13	3,70
L2	2,13	3,70
L3	1,60	2,83
L4/L5	0,31	0,28

Influence of panel width and distance between hole and edge

The experimental investigations show that, for specimen with the drill hole close to the edge, higher tensile and compressive stresses arise than for specimen with centrally located drill holes. Therefore, in the numerical analyses, panels with centrally located drill holes are compared with panels having the drill hole close to the edge. The hole diameter of the drill holes amount 30 mm. The geometries of specimen Z-400-600-30 and R-400-600-30 are used. To examine the influence of the panel width the geometry of the specimen Z-200-600-30 and R-200-600-30 with a width of 200 mm are chosen. The bushing thickness amounts 5 mm. The clearance for all calculations is assumed constantly with $\Delta R = 0,7$ mm. The results are given in Table 8.11.

Table 8.11   Principal stresses, comparison of distance drill hole / panel edge and panel width

Stress position	Z-400-600-30-Al-5,0 [MPa]	Z-200-600-30-Al-5,0 [MPa]	R-400-600-30-Al-5,0 [MPa]	R-200-600-30-Al-5,0 [MPa]
R1	-10,79	-10,82	-15,21	-15,27
R2	2,35	2,55	2,96	3,03
L1	2,72	3,18	3,35	3,64
L2	2,72	3,18	3,35	3,64
L3	1,90	2,17	2,51	2,68
L4/L5	0,29	0,31	0,40	0,32

The results confirm that the reduction of the panel width and the distance between the drill hole and panel edge lead to higher compressive and tensile stresses. Comparing the 400 mm wide panel and a centrally located drill hole (Z-400-600-30-Al-5,0) with the 200 mm wide panel and a drill hole close to the edge (R-200-600-30-Al-5,0) the compressive stresses at position R1 increase approx. 42% and the tensile stresses increase approx. 34%.

Summary

With the additional examination of the experimental results by the means of FEM the influences determined in the experimental investigations could be verified and the accuracy of the FEM-model was demonstrated.

9 Conclusion and Outlook

9.1 General Consideration

To calculate the loadbearing of bolted connections in glass panels exact knowledge of the contact mechanisms and the parameters which influence the stress distribution around the hole is necessary. In this thesis analytical and numerical solutions for the calculation of bolted connections under the application of in-plane loads are developed.

At first, analytical solutions based on contact mechanics are shown. Starting from the *Hertz* theory it is determined whether this theory is applicable for bolted glass connections under the application of in-plane loads. In the following, advanced solutions of contact between a bolt and a conforming hole in an infinite or a finite panel are derived. After that the numerical solutions are verified with the analytical ones.

In the next step the influences of different parameters on the stress distribution around the hole are numerically and experimentally examined.

In the following the essential results are summarized.

9.2 Summary of the Investigations

Analytical approaches

Hertz assumed that the two bodies in contact are elastic half-spaces and the contact area is small compared with the dimensions of each body and with the relative radii of the curvature of the surfaces. With the help of this simplification, he established the hypotheses that the contact area is elliptical and therefore can be described by a polynomial of second order. In addition, the surfaces are assumed to be frictionless so that only a normal pressure is transmitted between them. Relative displacements in the *x-y*-plane and possibly resulting tangential forces are neglected.

This approximation is complied as long as the radii of curvature of the bodies are appreciable bigger than the size of the contact area. If the contacting bodies have approximately similar surface geometries (bolt in a hole) under the application of load, the size of the contact area grows rapidly and the arc of contact occupies a main part of the circumference of the hole. Therefore *Hertz's* treatment is invalid.

Further analytical approaches are applied to find appropriate stress distributions for both bolt and panel with a hole. The most precise analytical approximate solution is obtained for a linear-elastic connection in an infinite panel, whereas bolt and panel consist of identical materials and the contact is assumed to be frictionless. This solution is used for verifying the FEM-model.

Influence of different bolt and bushing materials

The assumption that different bushing materials (e.g. plastic POM-C or aluminium alloy) have a considerable influence on the magnitude of radial and tangential stresses and on their distribution around the hole can not be validated for the neat-fit condition (clearance $\Delta R = 0$).

Despite of different material combinations (glass-aluminium, glass-POM-C) the values of the maximum principal tensile stresses differ only slightly. The maximum principal compressive stresses for both material combinations have approximately identical values.

Influence of a clearance

By increasing the clearance between bolt and hole ($\Delta R > 0$) the stresses increase as well and the material combination is getting of importance. At the same time the location of maximum principal tensile stresses changes. With the absence of clearance ($\Delta R = 0$) the stress maximum occurs approximately perpendicular to the load direction. Otherwise, when $\Delta R > 0$ is assumed, the stress maximum moves towards the load direction. According to the size of clearance (max. $\Delta R = 2{,}0$ mm was examined) the stress maximum moves up to 50°. This also results in different stress increments for both material combinations (glass-aluminium, glass-POM-C). In comparison with the neat-fit connection ($\Delta R = 0$), a clearance of $\Delta R = 2{,}0$ mm leads to an increase in maximum principal tensile stresses of about 66% for aluminium and, for POM-C, to an increase of about 39%.

Influence of friction

The exact determination of the friction coefficient μ_H of the enlisted friction partners has to be done with experimental investigations which can not be carried out within the scope of this thesis. To examine the influence of friction however different friction coefficients are applied.

When increasing the friction coefficient μ_H it is principally determined that the tangential stresses p_ϕ will grow and the contact compressive stresses p_r will decrease. In comparison with the frictionless connection, with a friction coefficient $\mu_H = 1{,}0$, the tangential stresses increase up to 30% and the radial stresses decrease up to 30%, not depending on the material combinations.

Influence of an eccentric load application

In comparison with a centrally load application the location of the maximum stress concentration is not in the midplane anymore but, as expected, on the surface. For the neat-fit condition ($\Delta R = 0$), this leads to an increase in maximum principal tensile stresses of about 7,5% and in maximum principal compressive stresses of about 7% as compared to a centrally loading. If additional clearance is present, the principal stresses grow rapidly. With a clearance of $\Delta R = 0{,}2$ mm the increment of maximum principal tensile stress amounts about 35% and, for the maximum principal compressive stress, the increment even amounts about 76%.

Influence of hole diameter, panel width and distance between hole and edge

If the ratio of drill hole radius a and panel width b lies in the range of $0{,}1 < a/b \leq 0{,}2$ the stresses increase enormously or tend to infinity. An interesting aspect is, that for values $a/b > 0{,}2$, the stresses decrease until a minimum is reached between $a/b = 0{,}4$ und $0{,}5$. Afterwards, the values rise again.

A comparison with the tangential stresses of a panel of finite and infinite width shows that a reduction of the panel width influences the amount of the maximum tangential stresses essentially: having a finite width of 100 mm the maximum tangential stresses are 80% to 86% higher than for the infinite panel. On the contrary the panel width has no significant influence on the radial stresses.

Not only the panel width but also the distance between hole and panel edge influence the amount of principal tensile stresses. By reducing the edge distance H the principal stresses increase. If the ratio a/b decreases for a chosen edge distance of $H = 50$ mm the stresses tend to infinity at $a/b < 0{,}4$. In the range of $0{,}4 \leq a/b \leq 0{,}5$ the values of principal tensile stresses increase only about 10% compared with the values of the panel with a central hole.

9.3 Final Remark

Partially, the examined parameters have a big influence on the stress distribution around the drill hole. That is why it is very important to model these parameters numerically close to reality.

Only a step-by-step verification of the numerical model - which was done for example within the scope of this thesis - obtains correct results. Already the parameters of the FEM-model itself influence the results considerably. Furthermore, the results of different FEM-programs are not transferable and a verification of each FEM-program is indispensable.

9.4 Future Research

Within the scope of this work different coefficients of static friction μ_H for the examination of the parameter "friction" were used to determine the influence on the stress distribution. As shown, the influence of friction is not negligible and it is a complex physical phenomenon which depends on a variety of parameters. To determine exact coefficients according to the used material combinations and the surrounding conditions it is proposed to investigate experiments in future research. Furthermore, for its numerical representation more comprehensive theories than *Coulomb's* friction model should be examined and these will continue to be topics of research.

The investigations of this work were made with regard to in-plane loads. In practice several load cases have to be superimposed. Thus, the combination of in-plane and transverse loading must be examined as well.

So far the material behaviour of the bushing materials was presumed to be linear-elastic. As it was determined in the experimental investigations of this work the POM-C interlayer showed plastic deformations at temperatures around 80°C. Therefore, based on the results of this thesis, numerical investigations subjected to the plastic material behaviour are suggested.

The examinations are yet limited to drill holes with a cylindrical shape. Since point-supports and drillings with a conical shape are often used in architecture as well, further research is necessary.

References

[AbZ Z-30.3-6]   Allgemeine bauaufsichtliche Zulassung Z-30.3-6 05.12.2003, DIBt Berlin.

[AbZ Z-70.2-99]   Allgemeine bauaufsichtliche Zulassung Z-70.2-99 07.09.2004, DIBt Berlin.

[AbZ Z-30.2-112]   Allgemeine bauaufsichtliche Zulassung Z-70.2-112 15.06.2005, DIBt Berlin.

[Albrecht 2004]   Albrecht, N.: Untersuchung von Lastabtragungsmechanismen im Lochbereich zur Vordimensionierung punktgestützter Glastafeln. Dissertation, TH Karlsruhe 2004.

[Bathe 1990]   Bathe, K.-J.: Finite-Elemente-Methoden. Springer Verlag Berlin, Heidelberg, New York, London, Paris, Tokio, Hongkong 1990.

[Becker 1984]   Becker, F.: Untersuchungen zum Langzeitverhalten der Thermoplaste POM und PA66 unter ruhender und schwingender Belastung. Dissertation, Technische Universität Berlin 1984.

[Bernard, Daudeville 2003] Bernard F., Daudeville L.: On the Design of Mechanical Joints in Tempererd Glass Structures. Glass Processing Days 2003, proceedings pp. 754-757.

[Bernard, Daudeville 2004] Bernard F., Daudeville L.: Load Bearing Capacity of Connections in Tempered Glass Structures. Structural Engineering International 2/2004, pp. 107- 110.

[Bickley 1928]   Bickley, W.G.: The Distribution of Stress Round a Circular Hole in a Plate. Philos. Trans. Roy. Soc. London 227, 383, 1928.

[Bronstein et al 1993] Bronstein, I.N., Semendjajew, N.E: Taschenbuch der Mathematik, B. G. Teubner Verlagsgesellschaft, Stuttgart Leipzig, Verlag Harri Deutsch Thun und Frankfurt/Main, 1991.

[Burmeister 1998a]   Burmeister, A.: Konzentrierte Lasteinleitung im konstruktiven Glasbau. Seminar "Glas im konstruktiven Glasbau". FH München, 1998.

[Burmeister 1998b]   Burmeister, A.: Bemessung punktgelagerter Fassaden-konstruktionen. Darmstädter Statik-Seminar "Glas im Bauwesen". Bericht-Nr. 13, 1998.

[Carré, Daudeville 1999] Carré, H.; Daudeville, L.: Load Bearing Capacity of Tempered Structural Glass. Journal of Engineering Mechanics 125, Vol. 8, 1999, pp. 914-921.

[Ciavarella, Decuzzi 2001a] Ciavarella M, Decuzzi P.: The state of stress induced by the plane frictionless cylindrical contact. I. The case of elastic similarity. Int. J. of Solids and Structures. Vol. 38, 2001, pp. 4507-4523.

[Ciavarella, Decuzzi 2001b]   Ciavarella M, Decuzzi P.: The state of stress induced by the plane frictionless cylindrical contact. II. The general case (elastic dissimilarity). Int. J. of Solids and Structures. Vol. 38, 2001, pp. 4525-4533.

[Czichos, Habig2003]   Czichos, H., Habig, K-H.: Tribologie Handbuch. Reibung und Verschleiß. Vieweg Verlag Wiesbaden, 2003.

[DASt 2003]   Deutscher Ausschuss für Stahlbau (DASt): Experimentelle und analytische Untersuchungen an neuartigen Stahl-Glas-Verbindungen im Hinblick auf zukünftige Einsatzgebiete und Bemessungskonzepte. Forschungsbericht, Stahlbau Verlags- und Service GmbH 2003.

[DIBt 2001]   DIBt: Merkblatt „Anforderungen an begehbare Verglasungen; Empfehlungen für das Zustimmungsverfahren", Fassung März 2000, DIBt Mitteilungen 2/2001.

[DIN 1055-1]   DIN 1055-1:07-1978; Lastannahmen - Lagerstoffe, Baustoffe und Bauteile, Eigenlasten und Reibungswinkel.

[DIN 1055-100]   DIN 1055-100: Teil 100:03-2001: Einwirkungen auf Tragwerke - Grundlagen der Tragwerksplanung, Sicherheitskonzept und Bemessungsregeln.

[E DIN V 18008-1]   E DIN V 18008-1:04-2005: Glas im Bauwesen; Bemessungs- und Konstruktionsregeln; Teil1: Grundlagen, Definition und Terminologie.

[E DIN V 18008-2]   E DIN V 18008-2:06-2005: Glas im Bauwesen; Bemessungs- und Konstruktionsregeln; Teil 2: Mechanisch gehaltene ausfachende Verglasungen.

[DIN 1249-3]   DIN 1249-3:02-1980: Flachglas im Bauwesen; Spiegelglas, Begriff, Maße.

[DIN 1249-10]   DIN 1249-10:08-1990: Flachglas im Bauwesen; Chemische und physikalische Eigenschaften.

[DIN 1249-11]   DIN 1249-11:09-1986: Flachglas im Bauwesen; Glaskanten; Begriff, Kantenformen und Ausführung

[DIN 1249-12]   DIN 1249-12:09-1990: Flachglas im Bauwesen; Einscheiben-Sicherheitsglas; Begriff, Maße, Bearbeitung, Anforderungen.

[DIN 2257-1]   DIN 2257-1:11-1982: Begriffe der Längenprüftechnik: Einheiten, Tätigkeiten, Prüfmittel, Messtechnische Begriffe.

[DIN 1259-1]   DIN 1259-1:09-2001: Glas - Teil 1: Begriffe für Glasarten und Glasgruppen.

[DIN 1259-2]   DIN 1259-2:09-2001: Glas - Teil 2: Begriffe für Glaserzeugnisse.

[DIN 4113-1]   DIN 4113-1:1980-05: Aluminiumkonstruktionen unter vorwiegend ruhender Belastung; Berechnung und bauliche Durchbildung.

[DIN 4426]   DIN 4426:09-2001: Sicherheitstechnische Anforderungen an Arbeitsplätze und Verkehrswege, Planung und Ausführung.

[DIN 7724]   DIN 7724:01-1988: Kunststoff-Formmassen; Celluloseester (CA, CP, CAB)-Formmassen; Einteilung und Bezeichnung.

[DIN 16780-2]   DIN 16780-2:10-1990: Kunststoff-Formmassen; Thermoplastische Formmassen aus Polymergemischen; Herstellung von Probekörpern und Bestimmung von Eigenschaften.

[DIN 16781-2]   DIN 16781-2:01-1989:Kunststoff-Formmassen; Polyoxymethylen (POM)-Formmassen; Herstellung von Probekörpern und Bestimmung von Eigenschaften.

[DIN 18800-1]   DIN 18800-1:11-1990: Stahlbauten; Bemessung und Konstruktion.

[DIN 18516-1]   DIN 18516-1:12-1999: Außenwandbekleidungen, hinterlüftet; Teil 1: Anforderungen, Prüfgrundsätze.

[DIN 18516-4]   DIN 18516-4:02-1990: Außenwandbekleidungen, hinterlüftet; Einscheiben-Sicherheitsglas. Anforderungen, Bemessung, Prüfung.

[DIN 55303-7]   DIN 55303-7:03-1996: Statistische Auswertung von Daten Teil 7: Schätz- und Testverfahren bei zweiparametriger Weibull-Verteilung.

[DIN EN 572-1]   DIN EN 572-1:09-2004: Glas im Bauwesen - Basiserzeugnisse aus Kalk-Natronsilicatglas - Teil 1: Definitionen und allgemeine physikalische und mechanische Eigenschaften.

[DIN EN 572-2]   DIN EN 572-2:09-2004: Glas im Bauwesen - Basiserzeugnisse aus Kalk-Natronsilicatglas - Teil 2: Floatglas.

[DIN EN 1288-1]   DIN EN 1288-1:09-2000: Glas im Bauwesen - Bestimmung der Biegefestigkeit von Glas - Teil 1: Grundlagen.

[DIN EN 1288-2]   DIN EN 1288-2:09-2000: Glas im Bauwesen - Bestimmung der Biegefestigkeit von Glas - Teil 2: Doppelring-Biegeversuch an plattenförmigen Proben mit großen Prüfflächen.

[DIN EN 1288-3]   DIN EN 1288-3:09-2000: Glas im Bauwesen - Bestimmung der Biegefestigkeit von Glas - Teil 3: Prüfung von Proben bei zweiseitiger Auflagerung (Vierschneiden-Verfahren).

[DIN EN 1288-4]   DIN EN 1288-4:09-2000: Glas im Bauwesen - Bestimmung der Biegefestigkeit von Glas - Teil 4: Prüfung von Profilbauglas; Deutsche Fassung EN 1288-4:2000.

[DIN EN 1288-5]   DIN EN 1288-5:09-2000: Glas im Bauwesen - Bestimmung der Biegefestigkeit von Glas - Teil 5: Doppelring-Biegeversuch an plattenförmigen Proben mit kleinen Prüfflächen.

[DIN EN 1863-1]	DIN EN 1863-1:03-2000: Glas im Bauwesen - Teilvorgespanntes Kalknatronglas.
[DIN EN 1748-1]	DIN EN 1748-1-1:12-2004: Spezielle Basiserzeugnisse Borosilicatgläser; Teil 1-1: Definitionen und allgemeine physikalische und mechanische Eigenschaften.
[DIN EN 1990]	DIN EN 1990:10-2002: Eurocode: Grundlagen der Tragwerksplanung.
[DIN EN 1991-1-1]	DIN EN 1991-1-1:10-2002: Eurocode 1: Eurocode 1: Einwirkungen auf Tragwerke - Teil 1-1: Allgemeine Einwirkungen auf Tragwerke; Wichten, Eigengewicht und Nutzlasten im Hochbau
[DIN EN 1991-1-3]	DIN EN 1991-1-3:09-2004: Eurocode 1 - Einwirkungen auf Tragwerke - Teil 1-3: Allgemeine Einwirkungen, Schneelasten
[DIN EN 1991-1-4]	DIN EN 1991-1-4:07-2005: Eurocode 1: Einwirkungen auf Tragwerke - Teil 1-4: Allgemeine Einwirkungen, Windlasten;
[DIN EN 1991-1-5]	DIN EN 1991-2-5:07-2004: Eurocode 1: Einwirkungen auf Tragwerke - Teil 1-5: Allgemeine Einwirkungen - Temperatureinwirkungen;
[DIN EN 1991-1-6]	DIN EN 1991-1-6:09-2005: Eurocode 1: Einwirkungen auf Tragwerke - Teil 1-6: Allgemeine Einwirkungen, Einwirkungen während der Bauausführung
[DIN EN 10008-1]	E DIN EN 10008-1:11-2001: Nichtrostende Stähle - Teil 1: Verzeichnis der nichtrostenden Stähle; 01-11-00.
[DIN EN 12150-1]	DIN EN 12150-1:11-2000: Glas im Bauwesen - Thermisch vorgespanntes Kalknatron-Einscheibensicherheitsglas - Teil 1: Definition und Beschreibung.
[DIN EN 12337-1]	DIN EN 12337-1:11-2000 Chemisch vorgespanntes Kalknatronglas - Teil 1: Definition und Beschreibung.
[DIN EN 12543-5]	DIN EN 12543-5:08-1998: Glas im Bauwesen - Verbundglas und Verbund-Sicherheitsglas - Teil 5: Maße und Kantenbearbeitung.
[DIN EN 12600]	DIN EN 1260011-2002: Glas im Bauwesen - Pendelschlagversuch - Verfahren für die Stoßprüfung und Klassifizierung von Flachglas.
[DIN EN 13024-1]	DIN EN 13024-1:08-2002: Glas im Bauwesen - Thermisch vorgespanntes Borosilicat-Einscheibensicherheitsglas - Teil 1: Definition und Beschreibung.
[prEN 13474-1]	prEN 13474-1:07-2005: Glass in building - Determination of the strength of glass panes - Part 1: Glass and glass products for fenestration
[prEN 13474-3]	pr EN 13474-3:07-2005: Glass in building - Determination of the strength of glass panes - Part 3: General method of calculation and determination of strength of glass by testing

[DIN EN ISO 527-1]   DIN EN ISO 527-1:1996-04: Kunststoffe - Bestimmung der Zugeigenschaften - Teil 1: Allgemeine Grundsätze.

[DIN EN ISO 527-2]   DIN EN ISO 527-2:1996-07: Kunststoffe - Bestimmung der Zugeigenschaften - Teil 2: Prüfbedingungen für Form- und Extrusionsmassen.

[DIN EN ISO 604]   DIN EN ISO 604:02-1997: Kunststoffe. Bestimmung von Druckeigenschaften.

[DIN EN ISO 899-1]   DIN EN ISO 899-1:2003-10: Kunststoffe - Bestimmung des Kriechverhaltens - Teil 1: Zeitstand-Zugversuch.

[DIN EN ISO 6721-2]   DIN EN ISO 6721-2:1996-12: Kunststoffe - Bestimmung dynamisch-mechanischer Eigenschaften - Teil 2: Torsionspendel-Verfahren.

[Domininghaus 1997]   Domininghaus, H.: Die Kunststoffe und ihre Eigenschaften. Springer Verlag 1997.

[Doremus 1994]   Doremus, R.H.: Glass Science. John Wiley & Sons Inc., 1994.

[Dundurs 1975]   Dundurs, J.: Properties of elastic bodies in contact. In: de Pater, A.D., Kalker, J.J.: Mechanics of Contact between Deformable Bodies. Delft University Press, Delft 1975.

[Edwards 1951]   Edwards R.H.: Stress Concentrations Around Spheroidal Inclusions and Cavities. Trans ASME, Vol.75, 1951

[Emonds et al. 2003]   Emonds, M. Gulati, S.T., Kaonpää A.: Effect of Coolants on Edge Quality of Float Glass. Glass Processing Days 2003, proceedings pp. 54-59.

[Emonds el al. 2005]   Emonds, M. Gulati, S.T., Kaonpää A.: Biaxial Strength of Float Glass Plates with Center Hole. Glass Processing Days 2005, proceedings pp. 54-59.

[Epple 2001]   Datenblatt zu Epple-Easy 5610 der Firma Epple & Co. GmbH, Herrenberg.

[ETAG No. 002 1998]   ETAG No. 002: Guidline for Technical European Approval of Structural Sealant Gazing Systems (SSGS), Part 1. Version July 1998.

[Exner 2001a]   Exner G.: Die Festigkeit von Glas, in Lohmeyer, S.: Werkstoff Glas III: Sachgerechte Auswahl, optimaler Einsatz, Gestaltung und Pflege. expert-Verlag, 2001.

[Exner 2001b]   Exner G.: Erlaubte Biegespannung in Glasbauteilen im Dauerlastfall, in Lohmeyer, S.: Werkstoff Glas III: Sachgerechte Auswahl, optimaler Einsatz, Gestaltung und Pflege. expert-Verlag, 2001.

[Exner 2001c]   Exner G.: Abschätzung der erlaubten Biegespannung in vorgespannten Glasbauteilen, in Lohmeyer, S.: Werkstoff Glas III: Sachgerechte Auswahl, optimaler Einsatz, Gestaltung und Pflege. expert-Verlag, 2001.

[Fink 2000]   Fink, A.: Ein Beitrag zum Einsatz von Floatglas als dauerhaft tragender Konstruktionswerkstoff im Bauwesen. Dissertation. Institut für Statik, Technische Universität Darmstadt 2000.

[Flügge 1962]   Flügge, W.: Handbook of Engineering Mechanics. McGraw-Hill Book Company New York Toronto London 1962.

[Frocht, Hill 1940]   Frocht, M.M., Hill, H.N.: Stress Concentration Factors Around a Central Circular Hole in a Plate Loaded Through Pin in the Hole. Journal of Applied Mechanics, Vol. 62, 1940, pp. A5-A9.

[Girkmann 1963]   Girkmann, K.: Flächentragwerke. Springer Verlag Wien - New York 1963.

[Gladwell 1980]   Gladwell, G.M.L.: Contact problems in the classical theory of contact mechanics. Sijthoff & Noordhoff International PublishersB.V., Alphen aan den Rijn, 1980.

[Goodier 1933]   Goodier, J.N.: Concentration of Stress Around Spherical and Cylindrical Inclusions and Flaws. Trans. ASME, Vol. 55, 1933.

[Gräf 2003]   Gräf, H.: Untersuchungen zum Tragverhalten von Verbundsicherheitsglas bei linienförmiger und punktförmiger Lagerung. Technische Universität München, Dissertation. Berichte aus dem Konstruktiven Ingenieurbau Nr. 2/03.

[Gross et al 1990]   Gross, D., Schnell, W.: Formel- und Aufgabensammlung zur Technischen Mechanik II, Verlag Bibliographisches Institut & F.A. Brockhaus AG, Mannheim 1990.

[GS-BAU-18 2001]   Grundsätze für die Prüfung und Zertifizierung der bedingten Betretbarkeit oder Durchsturzsicherheit von Bauteilen bei Bau- oder Instandhaltungsarbeiten. Prüfgrundsätze GS-BAU-18 des Hauptverbandes der gewerblichen Berufgenossenschaften HVBG, Ausgabe Februar 2001.

[Güsgen 1998]   Güsgen, J.: Bemessung tragender Bauteile aus Glas. Dissertation RWTH Aachen 1998.

[Gulati et al. 2001] Gulati, S., Roe, T., Vitkala, J.: Importance of Edge Finish on Thermal Tempering. Glass Processing Days 2001, proceedings pp. 72-78.

[Hertz 1882]   Hertz, H.: Über die Berührung fester elastischer Körper und über die Härte, Zeitschrift über reine und angewandte Mathematik 92, 1882, pp. 156-171.

[Hess 2000]   Hess, R.: Glasträger. Forschungsbericht Nr. 20. Institut für Hochbautechnik, Department für Architektur ETH Zürich 2000.

[Ho, Chau 1997]   Ho K.C., Chau K.T.: An Infinite Plane loaded by a Rivet of different Material. Journal of Solid and Structures Vol 34, No. 19, 1997, pp. 2477-2496.

[Hof 2005] Hof, P.: Rechnerische und experimentelle Untersuchungen zur Spannungsermittlung an Glasscheiben mit Hilfe der Weißlicht-Korrelations-Methode. Dissertation. Institut für Statik, Technische Universität Darmstadt 2005.

[Hoffmann 1987] Hoffmann, K.: Einführung in die Technik des Messens mit Dehnungsmessstreifen. Hottinger Baldwin Messtechnik GmbH 1987.

[HVG 1987] Hüttentechnische Vereinigung der Deutschen Glasindustrie (HVG): Festigkeit von Glas. Grundlagen und Prüfverfahren. Fordbildungskurs 1987.

[Iyer 2001] Iyer, K: Solutions for contact in pinned connections. Int. J. of Solids and Structures. Vol. 38, 2001. pp. 9133-9148.

[Jebsen-Marwedel 1980] Jebsen-Marwedel, H., Brückner, R. (Hrsg.): Glastechnische Fabrikationsfehler: "Pathologische" Ausnahmezustände des Werkstoffes Glas und ihre Behebung; Eine Brücke zwischen Wissenschaft, Technologie und Praxis. 3. Aufl., Springer-Verlag Berlin Heidelberg New York, 1980.

[Johnson 1996] Johnson K.L.: Contact Mechanics. Cambridge University Press, Cambridge 1996.

[Kalker 1990] Kalker, J.J.: Three-dimensional elastic bodies in rolling contact. Kluwer Academic Publishers, Dordrecht 1990.

[Keil 1995] Keil, S.: Beanspruchungsermittlung mit Dehnungsmeßstreifen. Cuneus Verlag, Zwingenberg 1995.

[Kerkhof 1970] Kerkhof, F.: Bruchvorgänge in Gläsern. Verlag der Deutschen Glastechnischen Gesellschaft, Frankfurt (Main) 1970.

[Kerkhof 1977] Kerkhof, F.: Bruchmechanik von Gas und Keramik. In: Sprechsaal 110 (1977), pp. 392-397.

[Klinkenberg et al 1998] Klinkenberg, A., Jäger, B., Saal H.: Untersuchungen zur statisch optimalen Halterposition bei punktgestützten Glastafeln. Stahlbau 67 (1998), Heft 4, pp. 275-280.

[Knight 1935] Knight, R.C: The Action of Rivet in a Plate of Finite Breadth. Phil. Mag. S.7 Vol.19 No. 127 March 1935, pp. 517-540.

[Komzsik 2001] Komzsik, L.: MSC.Nastran Numerical Methods, User's Guide. MSC.Software Corporation 2001.

[Kosteas 1996] Kosteas, D.: Betriebsverhalten und Bemessung von Aluminiumkonstruktionen, in Stahlbauhandbuch Band 1, Teil B. Stahlbau-Verlagsgesellschaft mbH Köln 1996.

[Køppen, Munck 2005] Køppen, K, Munck, M.: Bolted Connections in Toughened Glass. Master Theses, Department of Civil Engineering, Technical University of Denmark, 2005.

[Kühlmeyer 2001] Kühlmeyer, M.: Statistische Auswertungsmethoden für Ingenieure. Springer-Verlag Berlin Heidelberg 2001.

[Kutterer, Görzig 1997]   Kutterer, M., Görzig, R.: Glasfestigkeit im Bohrungsbereich. Institut für leichte Flächentragwerke, Universität Stuttgart 1997.

[Kutterer 2003]   Kutterer, M.: Verbundglasplatten, Näherungslösungen zur Berücksichtigung von Schubverbund und Membrantragwirkung. Dissertation, Institut für Leichtbau Entwerfen Konstruieren, Universität Stuttgart 2003.

[Laufs 2000]   Laufs, W.: Ein Bemessungskonzept zur Festigkeit thermisch vorgespannter Gläser, Dissertation. Lehrstuhl für Stahlbau, RWTH Aachen 2000.

[Lee 1992]   Lee, S. H.: MSC/Nastran Handbook for Nonlinear Analysis, Version 67. The McNeal-Schwendler Corporation, Los Angeles, Ca. 1992.

[Lewen 1991]   Lewen, B.: Das nichtlineare viskoelastische Verhalten von Kunststoffen am Beispiel der Zeit-Temperatur-Verschiebung und der Querkontraktionszahl. Dissertation RWTH Aachen 1991.

[Lin et al. 1997]   Lin, S., Hills, A., Nowell D.: Stresses in a flat plate due to a loose pin pressing against a cracked hole. Journal of Strain Analysis Vol 32, No.2 1997, pp. 145-156.

[Lohmeyer 1987]   Lohmeyer, S.: Werkstoff Glas I: Sachgerechte Auswahl, optimaler Einsatz, Gestaltung und Pflege. expert-Verlag, 1987.

[Lohmeyer 2001]   Lohmeyer, S.: Werkstoff Glas III: Sachgerechte Auswahl, optimaler Einsatz, Gestaltung und Pflege. expert-Verlag, 2001.

[Macneal 1992]   Macneal R. H.: Finite Elements: Their Design and Performance. Marcel Dekker, Inc. New York - Basel - Hong Kong 1992.

[Mauthe 1999]   Mauthe, P: Hilti HIT HY50, Relevante Produkteigenschaften für den Einsatz im Glasbau.

[Menges 1990]   Menges, G.: Werkstoffkunde Kunststoffe. Carl Hanser Verlag 1990.

[MSC.MARC 2003a]   MSC.MARC: Volume A. Theory and User Information. MSC.Software Corporation 2003.

[MSC.MARC 2003b]   MSC.MARC: Volume B. Element Library. MSC.Software Corporation 2003.

[MSC.MARC 2003c]   MSC.MARC: Volume C. Program Input. MSC.Software Corporation 2003.

[MSC.MARC 2003d]   MSC.MARC: Volume D. User Subroutines and Special Routines. MSC.Software Corporation 2003.

[MSC.MARC 2003e]   MSC.MARC: Volume E. Demonstration Problems. MSC.Software Corporation 2003.

[MSC.Nastran 2004]   MSC.Nastran: Quick Reference Guide. MSC.Software Corporation 2004.

[MSC.Nastran1997]   MSC.Nastran: Common Questions and Answers. MSC.Software Corporation 1997.

[MSC.vN4W 2004a]   MSC.visualNastran   for   Windows: Solver   Guide   2004.
                      MSC.Software Corporation 2004.

[MSC.vN4W 2004b]   MSC.visualNastran for Windows: Nonlinear+ Solver Guide 2004.
                      MSC.Software Corporation 2004.

[MSC.vN4W 2004c]   MSC.visualNastran for Windows: Nonlinear+ Examples 2004.
                      MSC.Software Corporation 2004.

[Noble, Hussain 1969] Noble, B., Hussain M.A.: Exact Solution of Certain Dual Series
                      for Indentation and Inclusion Problems. Int. Engng. Sci. Vol.7,
                      1969, pp. 1149-1161.

[Overend 2002]   Overend, M.: The Appraisal of Structural Glass Assemblies. PhD
                      Theses, Department of Civil Engineering, University of Surrey
                      2002.

[Panait 2004]   Panait, A.: Étude expérimentale et numérique des problémes de
                      contact unilatéral et de frottement sec dans les assemblages
                      verriers. Thèse, Université de Marne la Vallèe 2004.

[Persson 1964]   Persson, A.: On the stress distribution of cylindrical elastic bodies
                      in contact; Chalmers Tekniska Hogskola, Göteburg 1964.

[Peterson 1953]   Peterson, R. E.: Stress Concentration Design Factors. John Wiley
                      & Sons, Inc. 1953.

[Pilkey 1994]   Pilkey, W., D.: Formulas for Stress, Strain and Structural
                      Matrices. John Wiley & Sons, Inc. 1994.

[Pilkey 1997]   Pilkey, W., D.: Peterson's Stress Concentration Factors. John
                      Wiley & Sons, Inc. 1997.

[Reetz 2000]   Reetz, S.: Modellieren und Berechnen von gebrochenen
                      Verbundglasscheiben   mit   dem   Finite-Elemente-Programm
                      MARC, Diplomarbeit. Lehrstuhl für Stahlbau, Technische
                      Universität München 2000.

[Richter 1974]   Richter, H.: Experimentelle Untersuchungen zur Rißausbreitung
                      in Spiegelglas im Geschwindigkeitsbereich 10^{-3} bis $5*10^3$ mm/s,
                      Freiburg, Institut für Festkörpermechanik 1974, Wiss. Ber. Nr. 9.

[Rossmanith 1982]   Rossmanith, H.-P.: Finite Elemente in der Bruchmechanik.
                      Springer Verlag, Wien - New York 1982.

[Savin 1956]   Savin, G.: Spannungserhöhung am Rande von Löchern. VEB
                      Verlag Technik Berlin 1956.

[Schieder 1998]   Schieder, M.: Beitrag zur elasto-plastischen Bemessung
                      orthotroper   Platten.   Technische   Universität   München,
                      Dissertation. Berichte aus dem Konstruktiven Ingenieurbau Nr.
                      3/98.

[Schmitt et al. 1983] Schmitt, R. W.; Blank, K.; Schönbrunn, G.: Experimentelle
                      Spannungsanalyse zum Doppelringverfahren, in: Sprechsaal 116
                      (1983) Nr. 5, Seiten 397-405 und Druckfehlerberichtigung
                      Sprechsaal 116(1983) Nr.8, Seite 669.

[Schneider, Shen 1998]   Schneider, J., Shen, X.: Festigkeit gebohrter Gläser - FE Analysen und Experimentelle Untersuchungen, in Darmstädter Statik-Seminar: Glas im Bauwesen. Bericht-Nr. 13, 1998.

[Schneider 2001a]   Schneider, J.: Festigkeit und Bemessung punktgelagerter Gläser und stoßbespruchter Gläser, Dissertation. Institut für Statik, Technische Universität Darmstadt 2001.

[Schneider 2001b]   Schneider, J.: Glass Strength of Annealed and Tempered Structural Glass in the Area of Drilled Holes. Glass Processing Days 2001, proceedings pp. 193-197.

[Scholze 1988]   Scholze, H.: Glas: Natur, Struktur und Eigenschaften. Springer-Verlag, 1988.

[Schuler 2003]   Schuler, C: Einfluss des Materialverhaltens von Polyvinylbutyral auf das Tragverhalten von Verbundsicherheitsglas in Abhängigkeit von Temperatur und Belastung. Dissertation. Berichte aus dem Konstruktiven Ingenieurbau Nr. 3/03.

[Sedlacek et al. 1999]   Sedlacek, G. Blank, K., Laufs, W., Güsgen, J.: Glas im konstruktiven Ingenieurbau. Ernst und Sohn Verlag, Berlin 1999.

[Shen 1997]   Shen, X.: Entwicklung eines Bemessungs- und Sicherheitskonzeptes für den Glasbau. Forschrittsberichte VDI Reihe 4, Nr. 138, 1997.

[Siebert 1999]   Siebert, G.: Beitrag zum Einsatz von Glas als tragendes Bauteil im konstruktiven Ingenieurbau. Technische Universität München, Dissertation. Berichte aus dem Konstruktiven Ingenieurbau Nr. 5/99.

[Siebert 2001]   Siebert, G.: Entwurf und Bemessung von tragenden Bauteilen aus Glas, Ernst und Sohn Verlag, Berlin 2001.

[Siebert 2004]   Siebert, B.: Beitrag zur Berechnung punktgelagerter Gläser. Technische Universität München, Dissertation. Berichte aus dem Konstruktiven Ingenieurbau Nr. 2/04.

[Standfest 2000]   Standfest, A.: Untersuchungen an tragenden Glasrohren mit der Finite-Elemente-Methode, Eine Einführung in das FE-Program MARC, Diplomarbeit. Lehrstuhl für Stahlbau, Technische Universität München 2000.

[Summerer 1999]   Summerer, S.: FE-Analyse von auf Punkthalter gelagerten Glastragwerken, Diplomarbeit. Lehrstuhl für Stahlbau, Technische Universität München 1999.

[Techen 1997]   Techen, H.: Fügetechnik für den konstruktiven Glasbau, Dissertation. Institut für Statik, Technische Universität Darmstadt 1997.

[Techen 1998]   Techen, H.: Fügetechnik von Glaskonstruktionen. In Darmstädter Statikseminar - Glas im Bauwesen, Architektur und Konstruktion. Institut für Statik, Technische Universität Darmstadt 1998.

[Theocaris 1956]   Theocaris, P. S.: The Stress Distribution in a Strip Loaded in Tension by Means of a Central Pin. Journal of Applied Mechanics Vol. 23, 1956, pp. 85-90.

[Timoshenko, Goodier 1951]   Timoshenko, S.; Goodier, J.N.: Theory of Elasticity. McGraw-Hill Book Company New York Toronto London 1951.

[TRAV 2003]   Technische Regeln für die Verwendung von absturzsichernden Verglasungen(TRAV). Fassung Januar 2003. DIBt Mitteilungen 2/2003.

[TRLV 1998]   Technische Regeln für die Verwendung von linienförmig gelagerten Verglasungen (TRLV). Fassung September 1998. DIBt Mitteilungen 6/1998.

[eTRPV 2005]   Technische Regeln für die Bemessung und Ausführung punktförmig gelagerter Verglasungen. Entwurf August 2005.

[Weißmann 2004]   Weißmann, R.: Kantenfestigkeit und Kantenqualität von Architekturglas in 5. OTTI-Symposium Zukunft Glas 2004.

[Werkle 2001]   Werkle, H.: Finite Elemente in der Baustatik. Vieweg & Sohn Verlagsgesellschaft mbH, Braunschweig / Wiesbaden 2001

[Wilikins et al. 1976]   Wilikins, B. J. S. / Dutton, R.: Static Fatigue Limit with Particular Reference to Glass. Journal of The American Ceramic Society, Vol. 59, No. 3-4, 1976.

[Wörner et al. 2001]   Wörner, J.-D., Schneider, J., Fink, A.: Glasbau. Grundlagen, Berechung, Konstruktion. Springer-Verlag 2001.

[Wriggers 2001]   Wriggers, P.: Nichtlineare Finite-Elemente-Methoden. Springer-Verlag Berlin Heidelberg 2001.

[Wriggers 2002]   Wriggers, P.: Computational Contact Mechanics, John Wiley & Sons, LTD 2002.

[Young 1989]   Young, C.: Roak's Formulas for Stress and Strain, McGraw-Hill Inc. 1989.

[Zienkiewicz 1984]   Zienkiewicz O. C.: Methode der finiten Elemente. Carl Hanser Verlag, München - Wien 1984.

List of Symbols

Chapter 2 and 3:

a	Depth of a crack
c	Specific heat capacity
E	Young's modulus
E_d	Design value of the load
f	Correction function depending on specimen, crack geometry, loading
f_k	Characteristic strength of the material
k_{mod}	Factor for load duration
$K_{I,II,III}$	Stress intensity factors for crack mode *I, II, III*
R_d	Design value of the resistance
α_t	Average thermal expansion coefficient
γ_M	Partial safety factor, material
λ	Thermal conductivity
ν	Poisson's ratio
ρ	Density
σ_0	Tensile stress at the place of the crack normal to the crack-plane
σ_{Be}	Bending strength
σ_{Re}	Residual stress
$\sigma_{test,Be}$	Test bending strength

Chapter 4:

a	Hole radius
b	Semi-width of the panel
c	Shorter distance between panel edge and hole center
A, B, C, D	Constants of integration
E	Young's modulus
G	Shear modulus
p_x	Surface load in *x*-direction (load per unit length)
p_y	Surface load in *y*-direction (load per unit length)
r	Radius, generally
t	Thickness of the panel

u, v, w	Displacement in x-, y-, z-direction
x, y	Cartesian coordinate axes
ε_x^0, ε_y^0, γ_{xy}^0	Strain components of a panel without a hole
φ	Angle between the normal and the x-axis
θ	Angle between vector r and x-axis
ν	Poisson's ratio
Φ	Stress function
η, ξ	Principal axes
σ_N	Nominal stress
σ_x^0, σ_y^0, τ_{xy}^0	Stress components of a panel without a hole
σ_ξ^0, σ_η^0, $\tau_{\xi\eta}^0$	Stress components of a panel without a hole related to the principal axes
σ_1^0, σ_2^0, τ_1^0, τ_2^0, τ_3^0	Principal stresses of a panel without a hole
σ_x, σ_y, τ_{xy}	Stress components of a panel with a hole
σ_r, σ_θ, $\tau_{r\theta}$	Stress components in polar coordinates

Chapter 5:

a	Radius
A, B	Positive constants
b	Semi-width of the panel
$\bar{b}$	Semi-contact-width of two cylindrical bodies
c	Semi-contact-width of two bodies
D_i	Diameter of a cylindrical body i
E	Young's modulus
F	Load
F^*	Load per unit length
h	Distance of two points lying on the surfaces of two bodies in contact, before a load is applied
H	Distance between panel edge and hole center
j	Semi-axis of an ellipse
k	Semi-axis of an ellipse
K	Stress concentration factor
N	Normal force
p_0	Maximum contact pressure

$p_r(\phi)$	Radial contact stress
$p_\phi(\phi)$	Tangential contact stress
$p(x, y)$	Contact compressive stress distribution
P	Load per unit thickness
q	Dimensionless compressive stress function
q_{max}	Dimensionless maximum contact compressive stress
r	Radius
R	Friction force
R_i, R_i'	Principal radii of curvature of a body i
ΔR	Radial difference, clearance
t	Panel thickness
u_r	Radial component of displacement
v_ϕ	Tangential component of displacement
w_i	Displacement of a body i due to contact pressure
x, y, z	Cartesian coordinate axes
α	Semi-angle of the contact segment
α^*	*Dundurs* material parameter
β^*	*Dundurs* material parameter
δ	Total displacement between two bodies due to contact pressure
ϑ	Angle
μ	Friction coefficient
ν	Poisson's ratio
ϕ	Angle
σ_I, σ_{II}	Principal stresses at the hole boundary
ψ	Angle

Chapter 6:

$\mathbf{C}$	Vector of constraints
g_N	Gap-function
$\mathbf{F}$	Vector of external nodal loads
K_a, K_t	Penalty values
$\mathbf{K}$	Global stiffness matrix
$\mathbf{K}^0$	Initial tangential stiffness matrix
$\mathbf{K}^i$	Tangential stiffness matrix of the iteration step i

$\mathbf{K}_S$ Secant stiffness matrix

N_I Dimensionless form function

$\mathbf{P}$ Vector of external nodal loads

$\mathbf{R}^i$ Vector of internal loads of the iteration step i

$\Delta\mathbf{R}^i$ Difference vector (non balanced load vector) of the iteration step i

u, v, w Displacement in x-, y-, z-direction

U   Strain energy

U_0 Initial Gap opening

$\mathbf{U}^i$ Vector of nodal displacements of the iteration step i

$\Delta\mathbf{U}^i$ Nodal displacement increments of the iteration step i

W   Potential of all loads

ε_N Penalty parameter

$\mathbf{\Lambda}$ Vector of *Lagrange* multipliers

Π Energy potential

Chapter 7 and 8:

a Hole radius

b Semi-width of the panel

E Young's modulus

H Distance between panel edge and hole center

$p_r(\phi)$ Radial contact stress

$p_\phi(\phi)$ Tangential contact stress

P Load

ΔR Radial difference, clearance

t Panel thickness

t_H Bushing thickness

μ Friction coefficient

ν Poisson's ratio

ϕ Semi-angle of the contact segment

σ_{min} Minimum compressive stress

σ_{max} Maximum tensile stress

Appendix to Chapter 8

A.1 Material Tests

Table A1.1   Overview test series AlMgSi0,5 F22

Test series	Bushing geometry identification according to chapter 8.2	Temperature [°C]	Load increments [kN]	Number of samples	Figure
M.1-20_1 to M.1-20_5	1	20	20, 25, 30, 40, 50	5*)	Figure A.3
M.1-20_6 to M.1-20_9	1	20	50	4	-
M.2-20_1 to M.2-20_5	2	20	20, 25, 30, 40, 50	5*)	Figure A.1
M.2-20_6 to M.2-20_9	2	20	50	4	-
M.3-20_1 to M.3-20_5	3	20	20, 25, 30, 40, 50	5*)	Figure A.4
M.3-20_6 to M.3-20_9	3	20	50	4	-
M.4-20_1 to M.4-20_5	4	20	20, 25, 30, 40, 50	5*)	Figure A.2
M.4-20_6 to M.4-20_9	4	20	50	4	-
M.1-80_1 to M.1-10_5	1	80	20, 25, 30, 40, 50	5*)	Figure A.11
M.1-80_6 to M.1-10_9	1	80	50	4	-
M.2-80_1 to M.2-10_5	2	80	20, 25, 30, 40, 50	5*)	Figure A.9
M.2-80_6 to M.2-10_9	2	80	50	4	-
M.3-80_1 to M.3-10_5	3	80	20, 25, 30, 40, 50	5*)	Figure A.12
M.3-80_6 to M.3-10_9	3	80	50	4	-
M.4-80_1 to M.4-10_5	4	80	20, 25, 30, 40, 50	5*)	Figure A.10
M.4-80_6 to M.4-10_9	4	80	50	4	-

*) one test per load increment

Table A1.2   Overview test series POM-C

| Test series	Bushing geometry identification according to chapter 8.2	Temperature [°C]	Load increments [kN]	Number of samples	Figure
M.1-20_1 to M.1-20_4	1	20	20, 25, 30, 40	4*)	Figure A.7
M.1-20_5 to M.1-20_8	1	20	40	4	-
M.2-20_1 to M.2-20_4	2	20	20, 25, 30, 40	4*)	Figure A.5
M.2-20_6 to M.2-20_8	2	20	40	4	-
M.3-20_1 to M.3-20_4	3	20	20, 25, 30, 40	4*)	Figure A.8
M.3-20_6 to M.3-20_8	3	20	40	4	-
M.4-20_1 to M.4-20_4	4	20	20, 25, 30, 40	4*)	Figure A.6
M.4-20_6 to M.4-20_8	4	20	40	4	-
M.1-80_1	1	80	20	1*)	Figure A.15
M.1-80_2 to M.1-10_5	1	80	20	4	-
M.2-80_1 to M.2-10_5	2	80	20, 25, 30, 40, 50	5*)	Figure A.13
M.2-80_6 to M.2-10_9	2	80	50	4	-
M.3-80_1	3	80	20	1*)	Figure A.16
M.3-80_2 to M.3-10_5	3	80	20	4	-
M.4-80_1 to M.4-10_5	4	80	20, 25, 30, 40, 50	5*)	Figure A.14
M.4-80_6 to M.4-10_9	4	80	50	4	-

*) one test per load increment
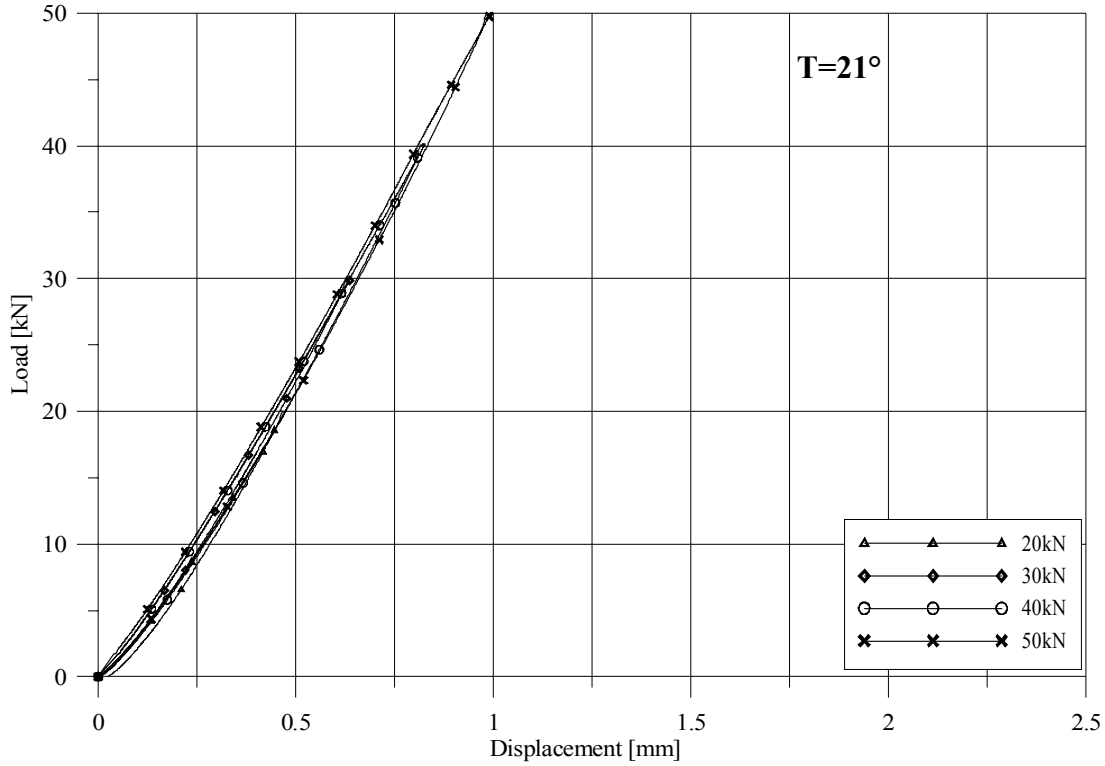
Figure A.1   Force-displacement-curve bushing Al; geometry d_a=40mm, t_H=5mm
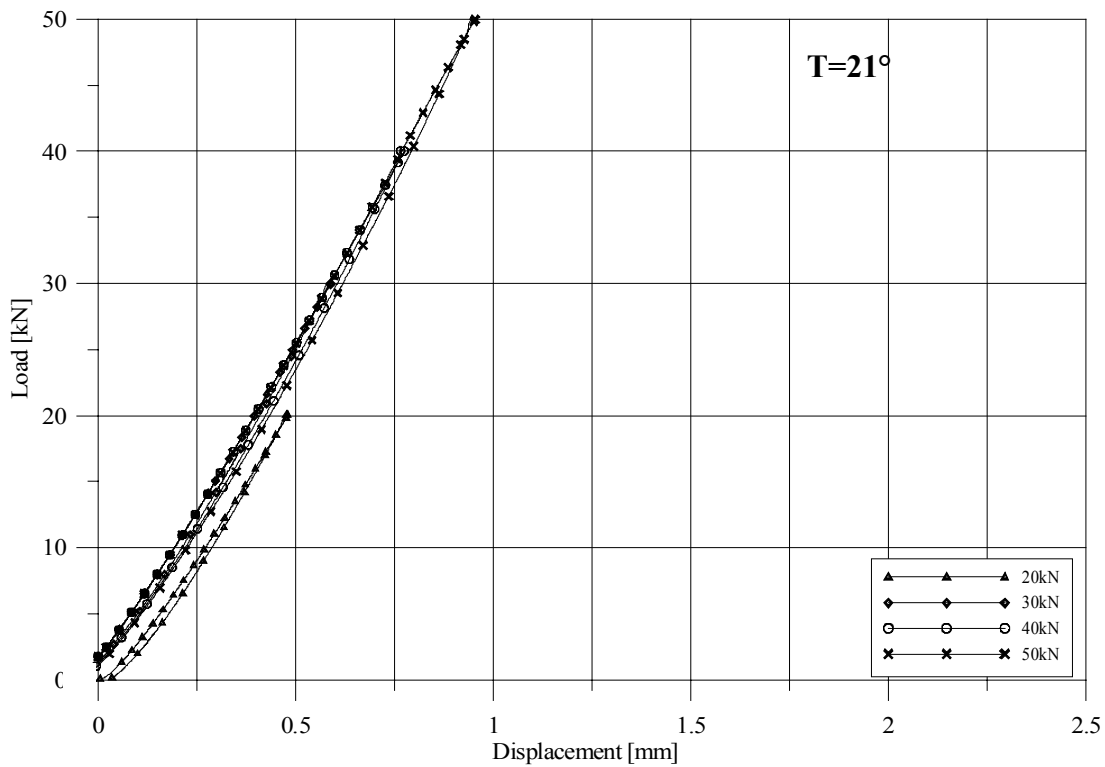

Figure A.2   Force-displacement-curve bushing Al; geometry d_a=40mm, t_H=2,5mm
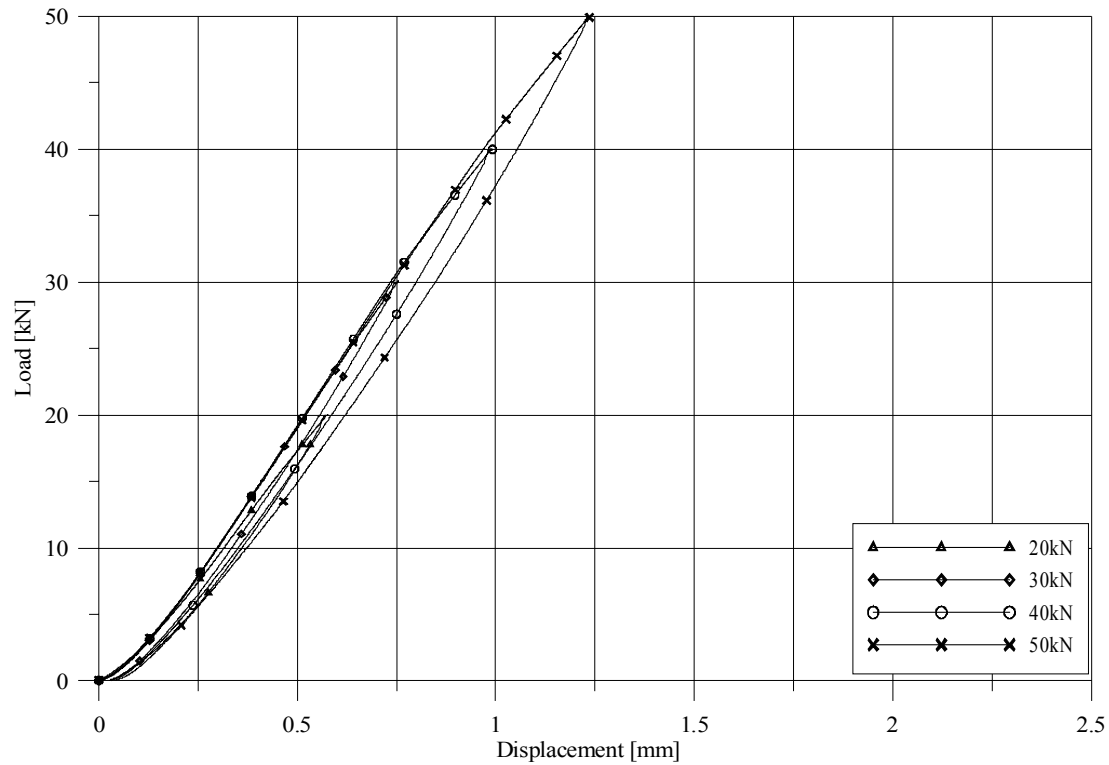
Figure A.3 Force-displacement-curve bushing Al; geometry d_a=20mm, t_H=5mm
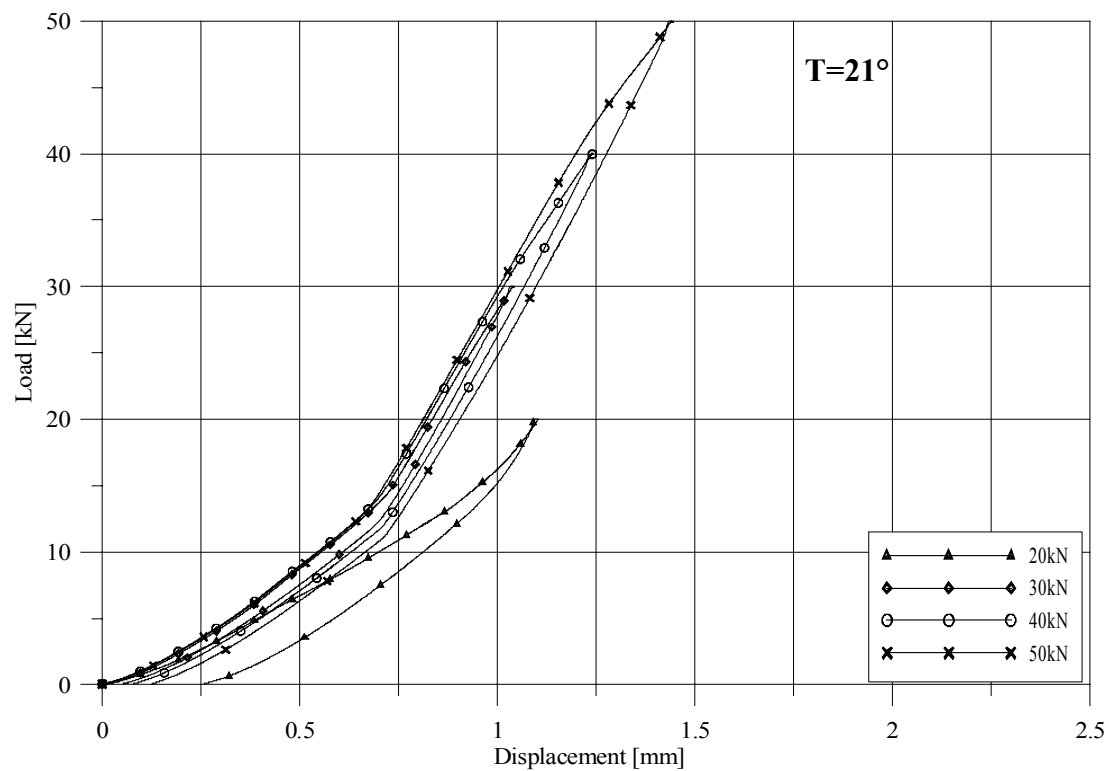
Figure A.4 Force-displacement-curve bushing Al; geometry d_a=20mm, t_H=2,5mm
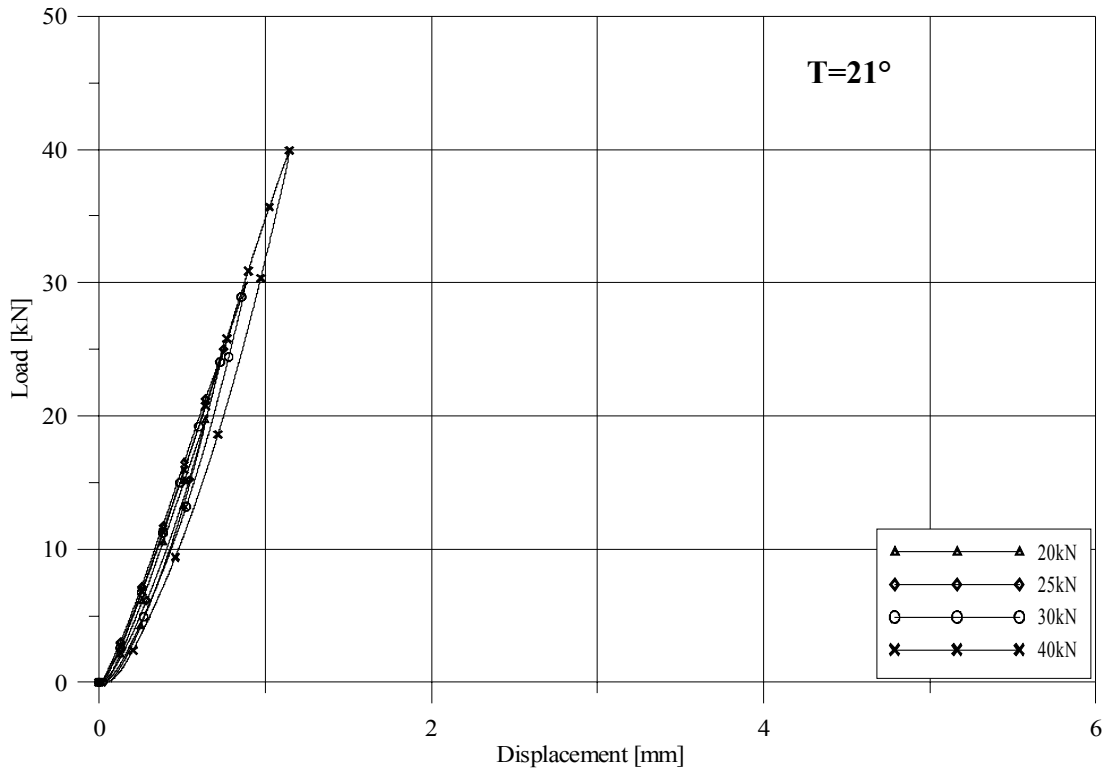
Figure A.5   Force-displacement-curve bushing POM-C; geometry d_a=40mm, t_H=5mm
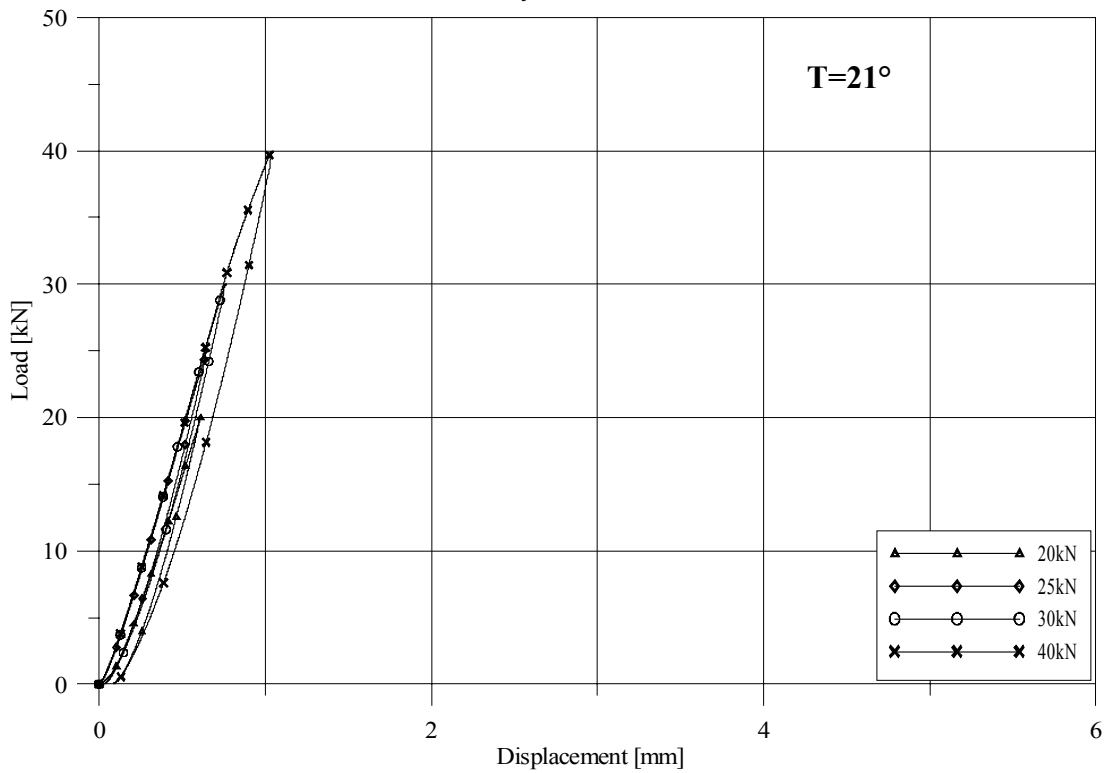
Figure A.6   Force-displacement-curve bushing POM-C; geometry d_a=40mm, t_H=2,5mm
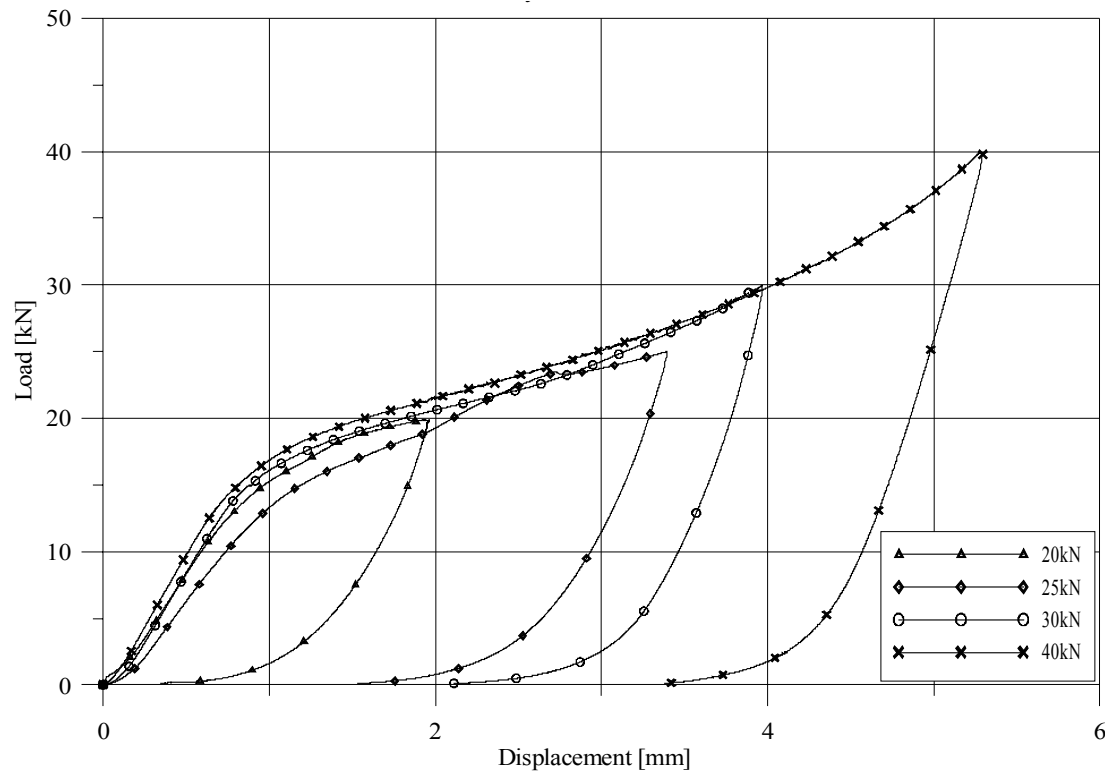
Figure A.7   Force-displacement-curve bushing POM-C; geometry d_a=20mm, t_H=5mm
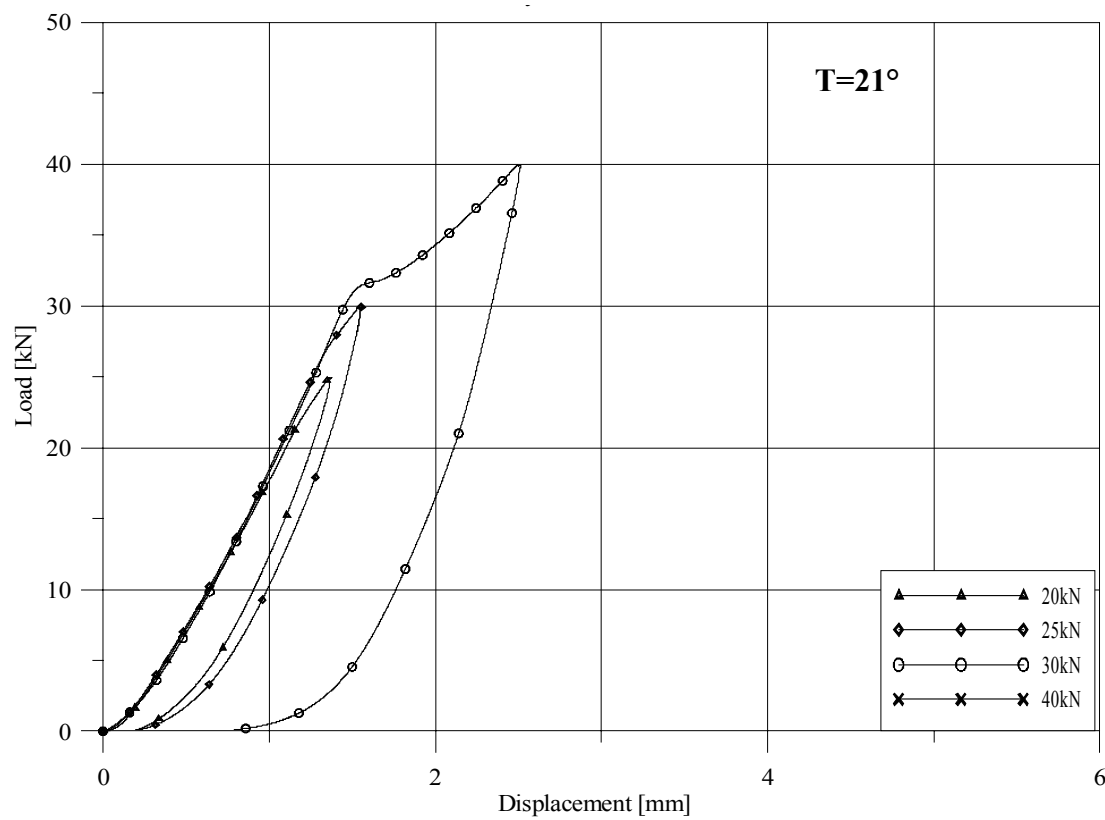
Figure A.8   Force-displacement-curve bushing POM-C; geometry d_a=20mm, t_H=2,5mm
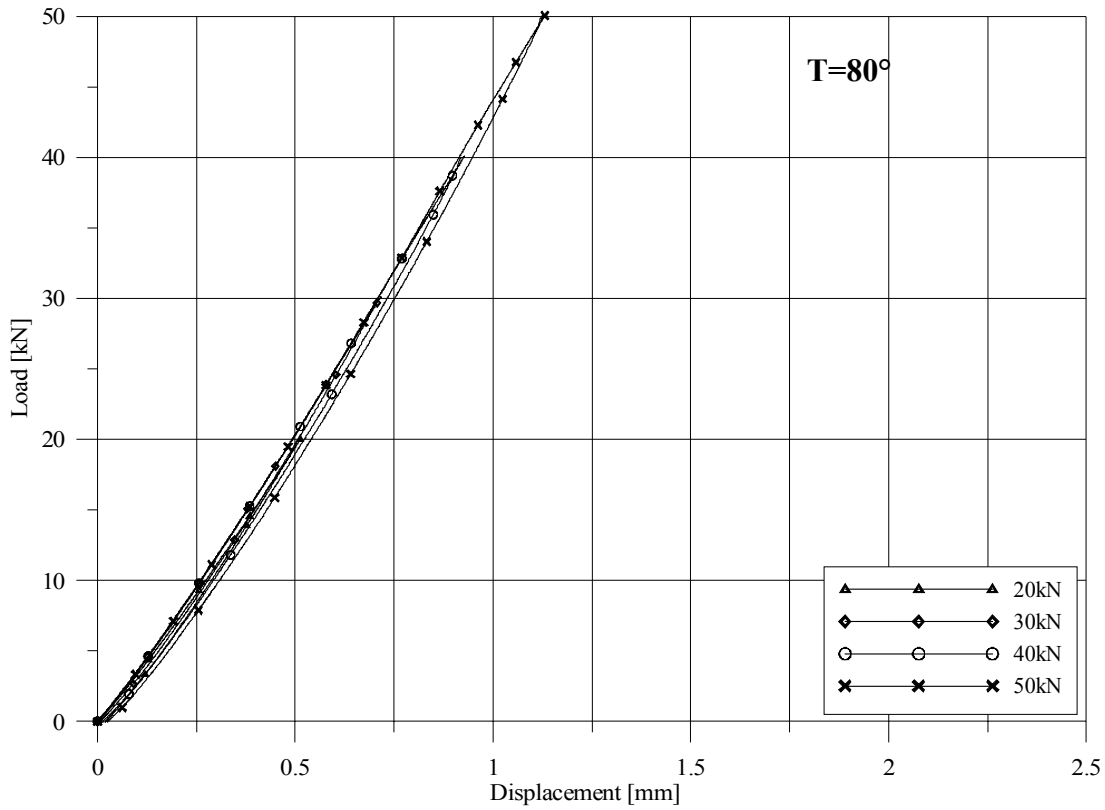
Figure A.9   Force-displacement-curve bushing Al; geometry d_a=40mm, t_H=5mm
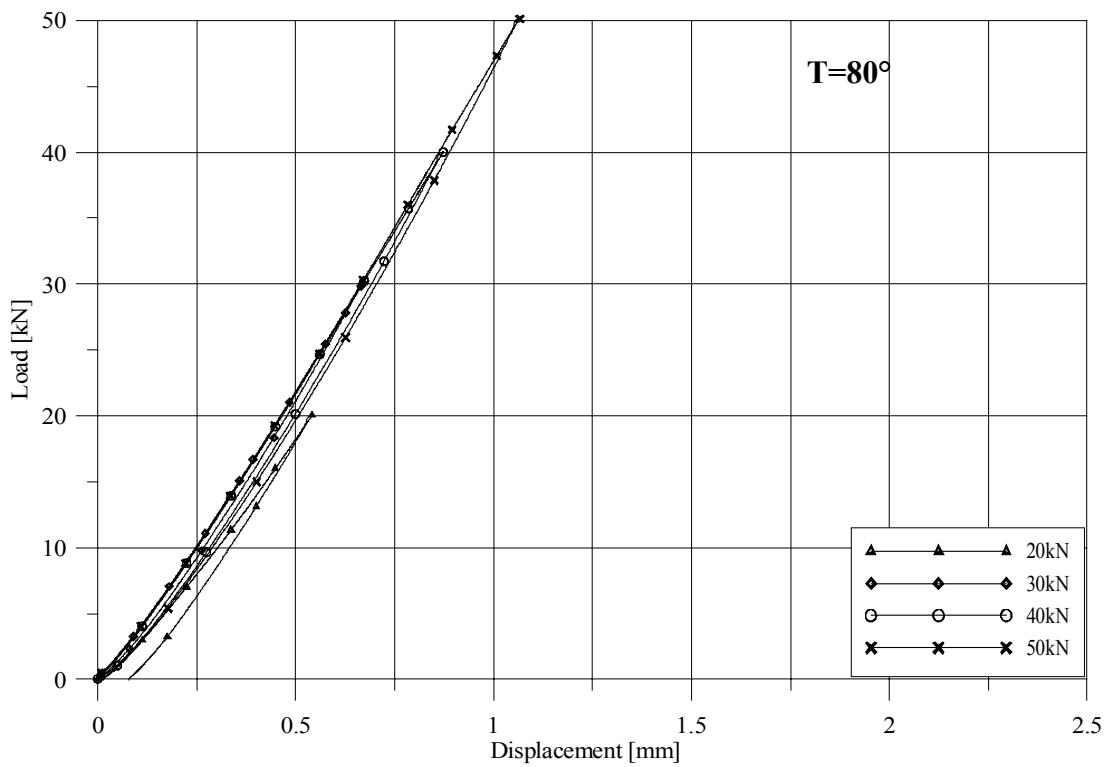
**Figure A.10**   Force-displacement-curve bushing Al; geometry d_a=40mm, t_H=2,5mm
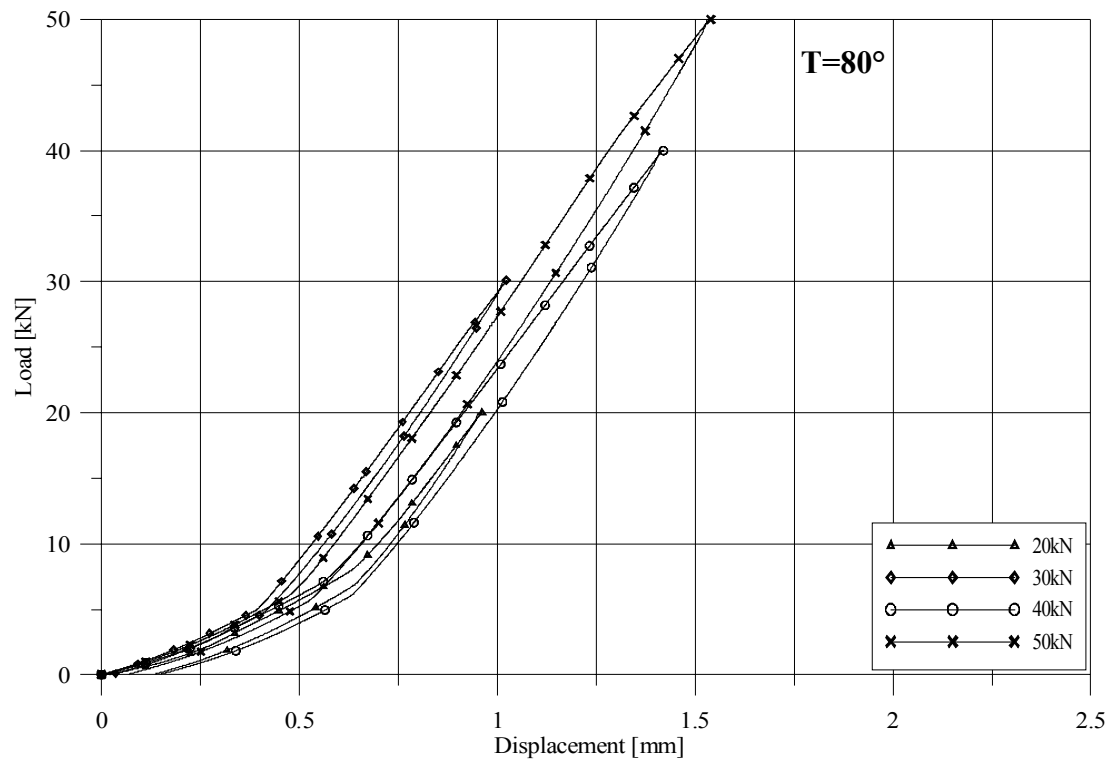
**Figure A.11**   Force-displacement-curve bushing Al; geometry d_a=20mm, t_H=5mm
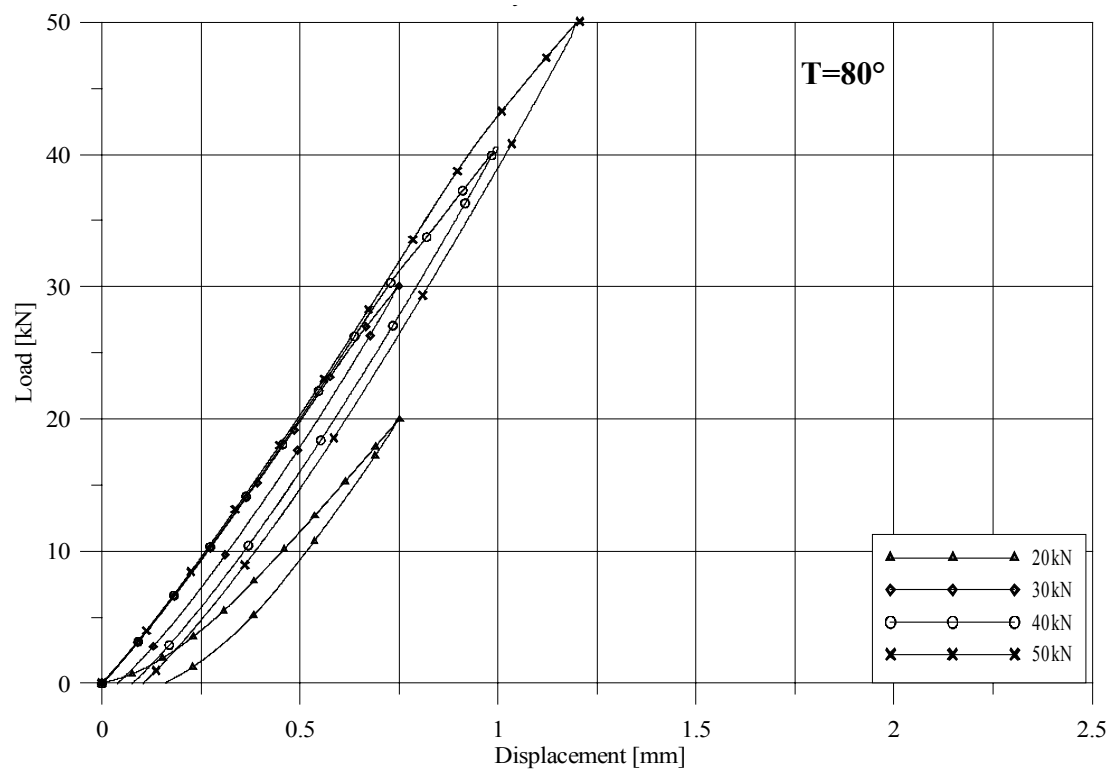
Figure A.12   Force-displacement-curve bushing Al; geometry d_a=20mm, t_H=2,5mm
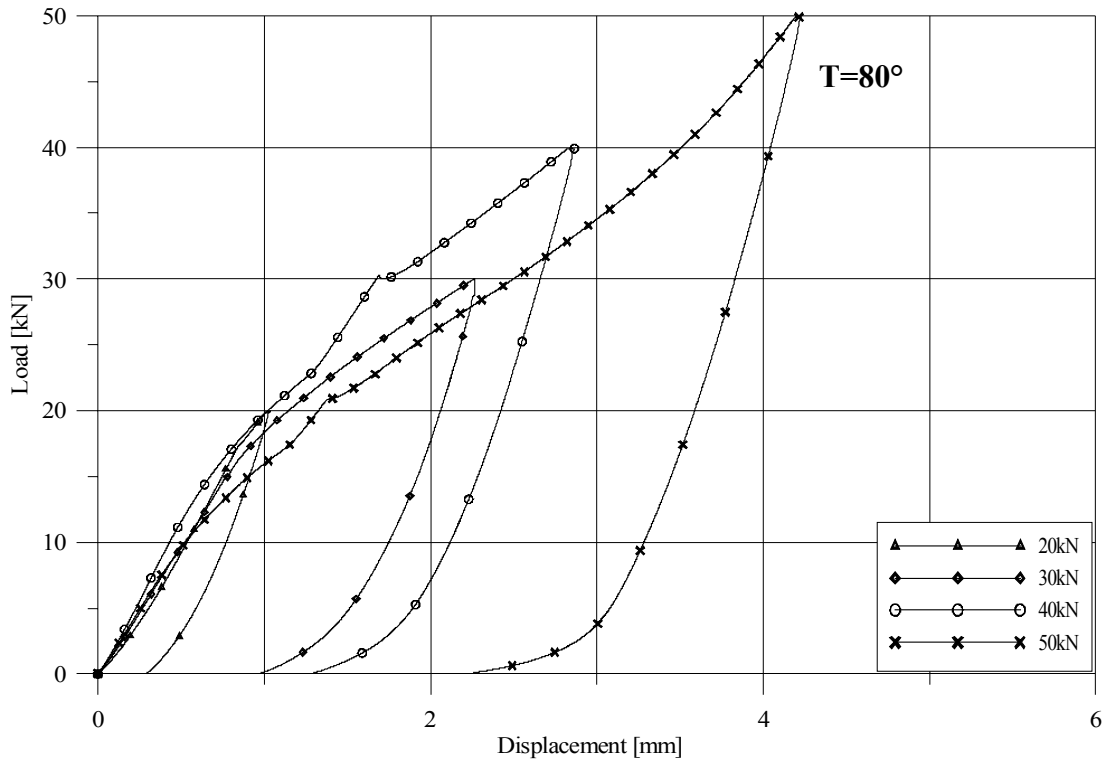
Figure A.13   Force-displacement-curve bushing POM-C; geometry d_a=40mm, t_H=5mm
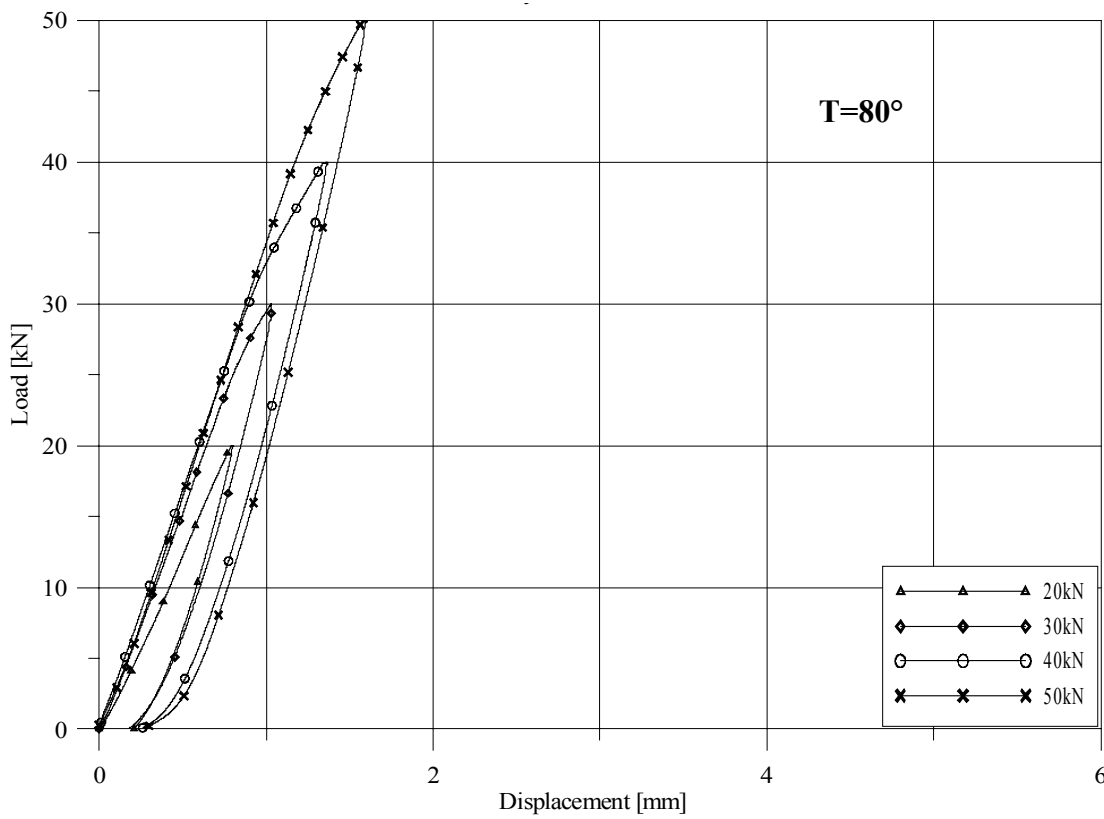
**Figure A.14**   Force-displacement-curve bushing POM-C; geometry d_a=40mm, t_H=2,5mm
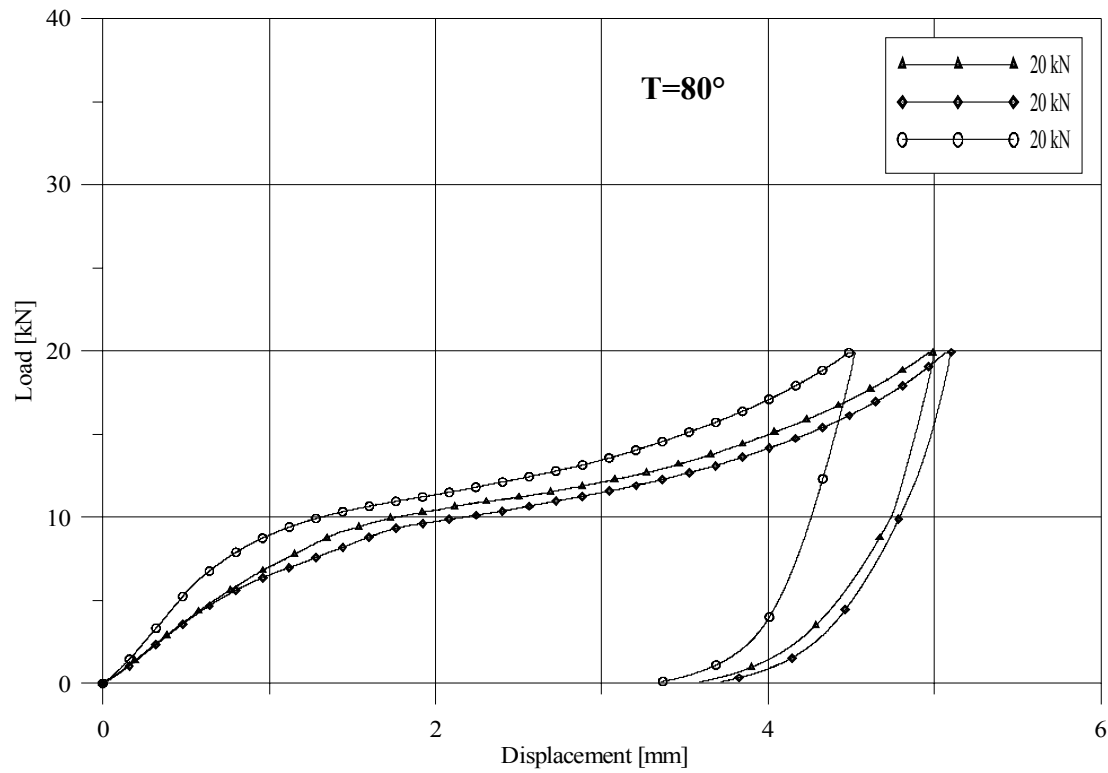
**Figure A.15**   Force-displacement-curve bushing POM-C; geometry d_a=20mm, t_H=5mm
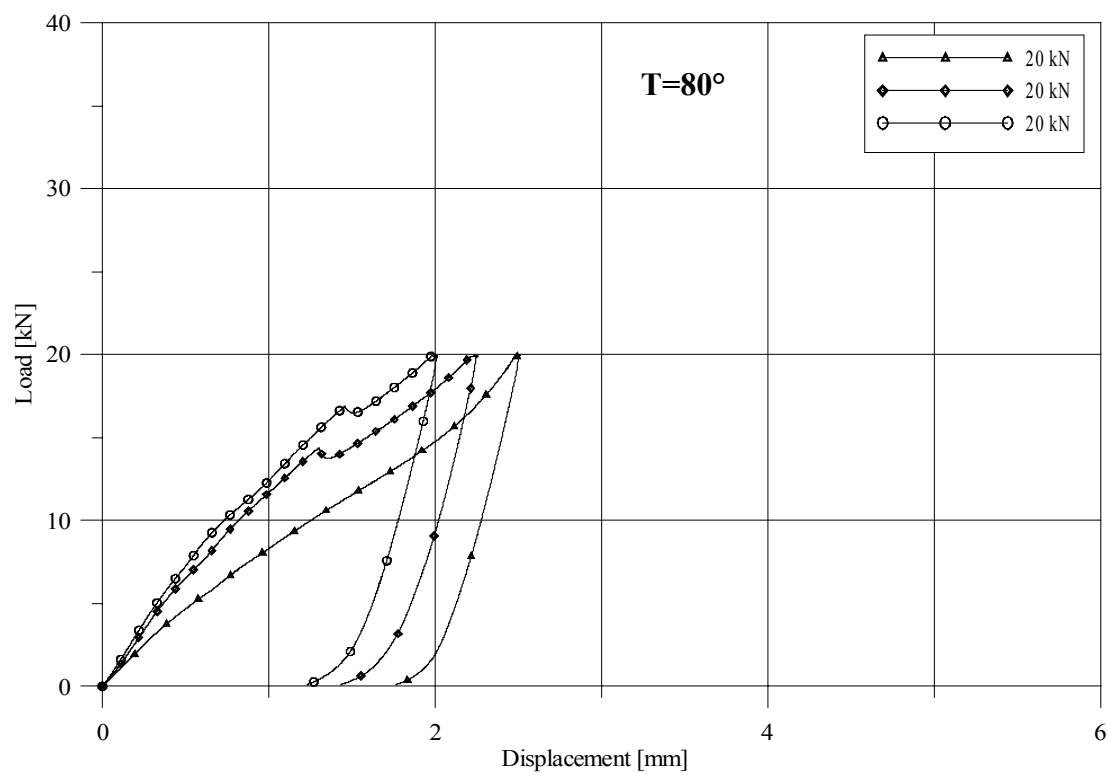
Figure A.16   Force-displacement-curve bushing POM-C; geometry d_a=20mm, t_H=2,5mm
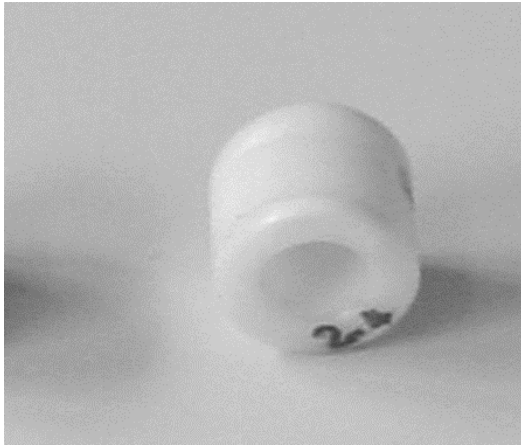
Figure A.17 POM-C bushing d_a=20mm, t_H=5mm, 21°C, load increment 25kN
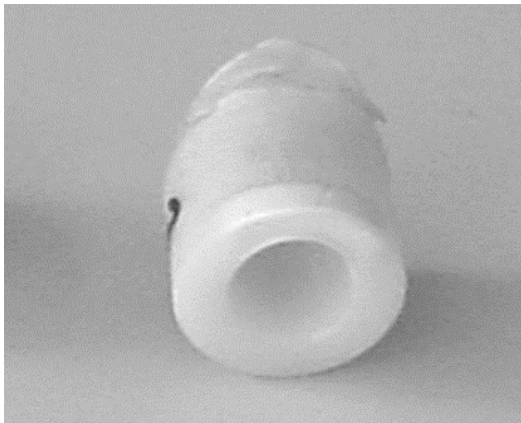
Figure A.18 POM-C bushing d_a =20mm, t_H =5mm, 80°C, load increment 20 kN
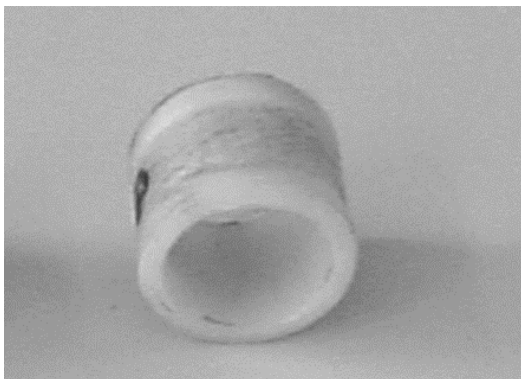
Figure A.19 POM-C bushing d_a=20mm, t_H=2,5mm, 80°C, load increment 20 kN

A.2   Loadbearing Tests

Table A.2.1   Overview test series with centrally located hole

Test series identification according to chapter 8.3	Explanation	Clearance ΔR [mm]
Z-400-600-40-Al-5,0	Panel size 400x600 mm, hole d=40 mm, aluminium-bushing, thickness t=5 mm	0,70
Z-400-600-40-Al-2,5	Panel size 400x600 mm, hole d=40 mm, aluminium-bushing, thickness t=2,5 mm	0,75
Z-400-600-40-POM-5,0	Panel size 400x600 mm, hole d=40 mm, POM-C-bushing, thickness t=5 mm	0,70
Z-400-600-40-POM-2,5	Panel size 400x600 mm, hole d=40 mm, POM-C-bushing, thickness t=2,5 mm	0,85
Z-400-600-30-Al-5,0	Panel size 400x600 mm, hole d=30 mm, aluminium-bushing, thickness t=5 mm	0,85
Z-400-600-30-Al-2,5	Panel size 400x600 mm, hole d=30 mm, aluminium-bushing, thickness t=2,5 mm	0,70
Z-400-600-30-POM-5,0	Panel size 400x600 mm, hole d=30 mm, POM-C-bushing, thickness t=5 mm	0,70
Z-400-600-30-POM-2,5	Panel size 400x600 mm, hole d=30 mm, POM-C-bushing, thickness t=2,5 mm	0,75
Z-400-600-20-Al-5,0	Panel size 400x600 mm, hole d=20 mm, aluminium-bushing, thickness t=5 mm	1,25
Z-400-600-20-Al-2,5	Panel size 400x600 mm, hole d=20 mm, aluminium-bushing, thickness t=2,5 mm	1,05
Z-400-600-20-POM-5,0	Panel size 400x600 mm, hole d=20 mm, POM-C-bushing, thickness t=5 mm	1,10
Z-400-600-20-POM-2,5	Panel size 400x600 mm, hole d=20 mm, POM-C-bushing, thickness t=2,5 mm	1,10
Z-200-600-30-Al-5,0	Panel size 200x600 mm, hole d=30 mm, aluminium-bushing, thickness t=5 mm	0,80
Z-200-600-30-Al-2,5	Panel size 200x600 mm, hole d=30 mm, aluminium-bushing, thickness t=2,5 mm	0,70
Z-200-600-30-POM-5,0	Panel size 200x600 mm, hole d=30 mm, POM-C-bushing, thickness t=5 mm	0,80
Z-200-600-30-POM-2,5	Panel size 200x600 mm, hole d=30 mm, POM-C-bushing, thickness t=2,5 mm	0,85

Table A.2.2   Test results and FE-analysis, Z-400-600-40-xxx

Test identification according to chapter 8.3	Experimental stress analysis [MPa]		FE-analysis [MPa]	Deviation [%]
Z-400-600-40-Al-5,0	R1	-13,10	-10,16	22%
	R2	2,39	2,06	14%
	L1	2,27	2,13	6%
	L2	2,29	2,13	7%
	L3	1,72	1,60	7%
	L4/L5	0,32	0,31	3%
Z-400-600-40-Al-2,5	R1	strain gage failure	-10,55	
	R2	2,45	2,12	13%
	L1	2,34	2,19	6%
	L2	2,35	2,19	7%
	L3	1,72	1,64	5%
	L4/L5	0,32	0,31	3%
Z-400-600-40-POM-5,0	R1	strain gage failure	-7,79	
	R2	2,51	2,14	15%
	L1	2,39	2,22	7%
	L2	2,41	2,22	8%
	L3	1,74	1,67	4%
	L4/L5	0,32	0,32	0%
Z-400-600-40-POM-2,5	R1	strain gage failure	-8,73	
	R2	2,51	2,15	14%
	L1	2,44	2,22	9%
	L2	2,45	2,22	9%
	L3	1,75	1,67	5%
	L4/L5	0,32	0,32	0%

Table A.2.3 Test results and FE-analysis, Z-400-600-30-xxx

Test identification according to chapter 8.3		Experimental stress analysis [MPa]	FE-analysis [MPa]	Deviation [%]
Z-400-600-30-Al-5,0	R1	-12,98	-11,00	15%
	R2	2,61	2,35	10%
	L1	2,71	2,73	1%
	L2	2,73	2,73	0%
	L3	1,90	1,90	0%
	L4/L5	0,32	0,30	6%
Z-400-600-30-Al-2,5	R1	-12,19	-10,84	11%
	R2	2,68	2,35	12%
	L1	2,73	2,73	0%
	L2	2,75	2,73	1%
	L3	1,93	1,90	2%
	L4/L5	0,32	0,30	6%
Z-400-600-30-POM-5,0	R1	-8,95	-7,81	13%
	R2	2,63	2,32	12%
	L1	2,72	2,75	1%
	L2	2,74	2,75	1%
	L3	1,91	1,90	1%
	L4/L5	0,32	0,30	6%
Z-400-600-30-POM-2,5	R1	-12,05	-10,26	15%
	R2	2,84	2,38	16%
	L1	2,72	2,78	2%
	L2	2,74	2,78	1%
	L3	1,94	1,93	1%
	L4/L5	0,32	0,30	6%

Table A.2.4   Test results and FE-analysis, Z-400-600-20-xxx

Test identification according to chapter 8.3		Experimental stress analysis [MPa]	FE-analysis [MPa]	Deviation [%]
Z-400-600-20-Al-5,0	R1	-38,37	-28,84	25%
	R2	3,75	2,94	22%
	L1	4,03	3,70	8%
	L2	4,12	3,70	10%
	L3	3,03	2,83	7%
	L4/L5	0,30	0,28	7%
Z-400-600-20-Al-2,5	R1	-37,61	-29,26	22%
	R2	3,64	3,10	14%
	L1	4,09	3,89	5%
	L2	4,18	3,89	7%
	L3	3,12	2,95	6%
	L4/L5	0,30	0,28	7%
Z-400-600-20-POM-5,0	R1	-21,64	-16,53	24%
	R2	3,19	2,51	21%
	L1	3,41	3,18	7%
	L2	3,47	3,18	9%
	L3	2,61	2,40	8%
	L4/L5	0,30	0,28	7%
Z-400-600-20-POM-2,5	R1	-26,71	-20,00	25%
	R2	3,69	3,16	14%
	L1	4,13	3,86	7%
	L2	4,18	3,86	8%
	L3	3,11	2,95	5%
	L4/L5	0,30	0,28	7%

Table A.2.5   Test results and FE-analysis, Z-200-600-30-xxx

Test identification according to chapter 8.3		Experimental stress analysis [MPa]	FE-analysis [MPa]	Deviation [%]
Z-200-600-30-Al-5,0	R1	-12,34	-10,96	12%
	R2	2,27	2,05	10%
	L1	3,28	3,17	4%
	L2	3,27	3,17	3%
	L3	2,25	2,17	4%
	L4/L5	0,32	0,31	3%
Z-200-600-30-Al-2,5	R1	-12,12	-10,86	11%
	R2	2,31	2,05	12%
	L1	3,29	3,17	4%
	L2	3,26	3,17	3%
	L3	2,29	2,17	5%
	L4/L5	0,32	0,31	3%
Z-200-600-30-POM-5,0	R1	-10,98	-9,48	14%
	R2	2,25	2,02	11%
	L1	3,24	3,17	2%
	L2	3,29	3,17	4%
	L3	2,21	2,17	2%
	L4/L5	0,32	0,30	6%
Z-200-600-30-POM-2,5	R1	-11,14	-9,52	15%
	R2	2,31	1,94	16%
	L1	3,19	2,96	7%
	L2	3,22	2,96	8%
	L3	2,25	2,00	11%
	L4/L5	0,32	0,30	6%

Table A.2.6   Overview test series with hole close to the edge

Test series identification according to chapter 8.3	Explanation	Clearance ΔR [mm]
R-400-600-40-Al-5,0	Panel size 400x600 mm, hole d=40 mm, aluminium-bushing, thickness t=5 mm	0,85
R-400-600-40-Al-2,5	Panel size 400x600 mm, hole d=40 mm, aluminium-bushing, thickness t=2,5 mm	0,85
R-400-600-40-POM-5,0	Panel size 400x600 mm, hole d=40 mm, POM-C-bushing, thickness t=5 mm	0,65
R-400-600-40-POM-2,5	Panel size 400x600 mm, hole d=40 mm, POM-C-bushing, thickness t=2,5 mm	0,50
R-400-600-30-Al-5,0	Panel size 400x600 mm, hole d=30 mm, aluminium-bushing, thickness t=5 mm	0,80
R-400-600-30-Al-2,5	Panel size 400x600 mm, hole d=30 mm, aluminium-bushing, thickness t=2,5 mm	0,80
R-400-600-30-POM-5,0	Panel size 400x600 mm, hole d=30 mm, POM-C-bushing, thickness t=5 mm	0,74
R-400-600-30-POM-2,5	Panel size 400x600 mm, hole d=30 mm, POM-C-bushing, thickness t=2,5 mm	0,76
R-400-600-20-Al-5,0	Panel size 400x600 mm, hole d=20 mm, aluminium-bushing, thickness t=5 mm	0,92
R-400-600-20-Al-2,5	Panel size 400x600 mm, hole d=20 mm, aluminium-bushing, thickness t=2,5 mm	0,72
R-400-600-20-POM-5,0	Panel size 400x600 mm, hole d=20 mm, POM-C-bushing, thickness t=5 mm	0,73
R-400-600-20-POM-2,5	Panel size 400x600 mm, hole d=20 mm, POM-C-bushing, thickness t=2,5 mm	0,68
R-200-600-30-Al-5,0	Panel size 200x600 mm, hole d=30 mm, aluminium-bushing, thickness t=5 mm	0,83
R-200-600-30-Al-2,5	Panel size 200x600 mm, hole d=30 mm, aluminium-bushing, thickness t=2,5 mm	0,77
R-200-600-30-POM-5,0	Panel size 200x600 mm, hole d=30 mm, POM-C-bushing, thickness t=5 mm	0,76
R-200-600-30-POM-2,5	Panel size 200x600 mm, hole d=30 mm, POM-C-bushing, thickness t=2,5 mm	0,78

Table A.2.7   Test results and FE-analysis, R-400-600-40-xxx

Test identification according to chapter 8.3	Experimental stress analysis [MPa]		FE-analysis [MPa]	Deviation [%]
R-400-600-40-Al-5,0	R1	-19,16	-14,74	23%
	R2	3,14	2,66	15%
	L1	2,86	2,79	2%
	L2	2,88	2,79	3%
	L3	2,31	2,23	3%
	L4/L5	0,39	0,38	3%
R-400-600-40-Al-2,5	R1	-19,25	-14,82	23%
	R2	2,94	2,66	10%
	L1	2,89	2,79	3%
	L2	2,91	2,79	4%
	L3	2,33	2,23	4%
	L4/L5	0,39	0,38	3%
R-400-600-40-POM-5,0	R1	-9,84	-8,27	16%
	R2	3,05	2,64	13%
	L1	2,82	2,79	1%
	L2	2,82	2,79	1%
	L3	2,29	2,23	3%
	L4/L5	0,39	0,38	3%
R-400-600-40-POM-2,5	R1	-10,93	-9,20	16%
	R2	2,66	2,52	5%
	L1	2,85	2,76	3%
	L2	2,87	2,76	4%
	L3	2,31	2,23	3%
	L4/L5	0,39	0,38	3%

Table A.2.8   Test results and FE-analysis, R-400-600-30-xxx

Test identification according to chapter 8.3	Experimental stress analysis [MPa]		FE-analysis [MPa]	Deviation [%]
R-400-600-30-Al-5,0	R1	-18,77	-15,03	20%
	R2	3,26	2,81	14%
	L1	3,35	3,18	5%
	L2	3,34	3,18	5%
	L3	2,48	2,39	4%
	L4/L5	0,39	0,40	3%
R-400-600-30-Al-2,5	Damage of the glass panel during installation			
R-400-600-30-POM-5,0	R1	-11,52	-9,23	20%
	R2	3,01	2,93	3%
	L1	3,48	3,36	3%
	L2	3,46	3,36	3%
	L3	2,67	2,51	6%
	L4/L5	0,38	0,37	3%
R-400-600-30-POM-2,5	R1	-13,10	-10,35	21%
	R2	3,05	2,80	8%
	L1	3,33	3,19	4%
	L2	3,32	3,19	4%
	L3	2,68	2,39	11%
	L4/L5	0,38	0,37	3%

Table A.2.9   Test results and FE-analysis, R-400-600-20-xxx

Test identification according to chapter 8.3		Experimental stress analysis [MPa]	FE-analysis [MPa]	Deviation [%]
R-400-600-20-Al-5,0	R1	-34,56	-25,23	27%
	R2	3,72	2,76	26%
	L1	4,56	4,34	5%
	L2	4,57	4,34	5%
	L3	2,74	2,58	6%
	L4/L5	0,35	0,33	6%
R-400-600-20-Al-2,5	R1	-31,75	-23,51	26%
	R2	3,69	2,78	25%
	L1	4,56	4,34	5%
	L2	4,58	4,34	5%
	L3	2,77	2,58	7%
	L4/L5	0,35	0,33	6%
R-400-600-20-POM-5,0	R1	-12,21	-10,15	17%
	R2	3,28	2,67	19%
	L1	4,43	4,36	2%
	L2	4,45	4,36	2%
	L3	2,61	2,56	2%
	L4/L5	0,35	0,33	6%
R -400-600-20-POM-2,5	R1	-15,23	-12,69	17%
	R2	3,34	2,77	17%
	L1	4,45	4,35	2%
	L2	4,46	4,35	2%
	L3	2,62	2,58	2%
	L4/L5	0,35	0,33	6%

Table A.2.10 Test results and FE-analysis, R-200-600-30-xxx

Test identification according to chapter 8.3		Experimental stress analysis [MPa]	FE-analysis [MPa]	Deviation [%]
R-200-600-30-Al-5,0	R1	-15,98	-15,81	1%
	R2	2,76	2,52	9%
	L1	3,91	3,63	7%
	L2	3,90	3,63	7%
	L3	1,42	1,34	6%
	L4/L5	0,28	0,27	4%
R-200-600-30-Al-2,5	R1	-16,22	-15,69	3%
	R2	2,81	2,52	10%
	L1	3,93	3,63	8%
	L2	3,95	3,63	8%
	L3	1,44	1,34	7%
	L4/L5	0,29	0,27	4%
R-200-600-30-POM-5,0	R1	-11,63	-10,84	7%
	R2	2,65	2,49	6%
	L1	3,84	3,63	5%
	L2	3,85	3,63	6%
	L3	1,41	1,32	6%
	L4/L5	0,29	0,28	4%
R-200-600-30-POM-2,5	R1	-14,46	-13,94	4%
	R2	2,65	2,51	3%
	L1	3,86	3,63	6%
	L2	3,88	3,63	6%
	L3	1,42	1,32	7%
	L4/L5	0,29	0,28	4%